U.PORTO

FEUP FACULDADE DE ENGENHARIA
UNIVERSIDADE DO PORTO

Multi-Scale Modelling and Analysis of Heterogeneous Solids at Finite Strains

Doctoral Thesis

Author:
F.J.P. Reis

Supervisor:
Dr. F. M. Andrade Pires

A thesis submitted in fulfilment of the requirements
for the degree of Doctor of Philosophy in Mechanical Engineering

at the

Department or Mechanical Engineering, Faculty of Engineering
University of Porto

June 2014

Abstract

The behaviour of the great majority of materials when subjected to complex loadings is strongly dependent on their microstructure. Therefore, it is widely accepted by both the scientific and industrial communities that, in order to develop new materials that are able to satisfy tight criteria, the complete understanding of the relation between the macroscopic behaviour of the material and its microstructure is vital. This will be only possible with the formulation and development of new micro-macro strategies. Within this context, *Coupled Multi-Scale Models* can be an important ally to address this challenge. The main objective of this thesis is to develop an efficient framework, which incorporates several numerical techniques to model the deformation behaviour of heterogeneous materials at finite strains and predict material failure in relevant practical problems. For this purpose, the thesis starts with a global overview of the state-of-art on the present topic. In Chapter 2, the main concepts of the *Continuum Mechanics Theory* and the *Finite Element Method* are briefly reviewed. This chapter is followed by the introduction of the underlying formulation of *First-Order Coupled Multi-Scale Models*. In Chapter 4, the first main contribution of this work is introduced: an adaptive sub-incremental strategy for the solution of the micro-scale problem. With this new strategy it is possible to significantly reduce the CPU cost required to solve the micro-equilibrium problem, which has a significant repercussion to the global CPU time which is necessary to solve coupled multi-scale problems. Due to the difficulty to enforce *Periodic* boundary conditions in RVEs with non-conform meshes, in Chapter 5, a new numerical approach to impose a *Periodic* displacement fluctuation over the boundary of the RVE based on the *Mortar* decomposition method is introduced. As demonstrated by a set of numerical examples, the new strategy is quite robust either for two or three dimensional problems. When softening regimes are attained, mesh dependence pathology is commonly observed. This pathology was addressed in Chapter 6. In order to minimize this problem, two distinct non-local approaches of integral type were suggested for micro and macro domains. While at the micro-scale the approach proposed significantly reduced the mesh dependence pathology, at the macro-scale, further work is required to enhance the numerical framework proposed. In Chapter 7, a new concept of *Periodic* boundary condition is proposed, which is able to tackle the presence of a localization band with an arbitrary shape. Despite of being an embryonic concept and, therefore, a significant amount of work still needs to be carried out, it has provided interesting indications. The document finishes with the presentation of the main conclusions of this work and, in addition, suggestions for future research are made.

Resumo

O comportamento mecânico de um material quando sujeito a diferentes solicitações é profundamente dependente da sua micro-estrutura. Por sua vez, o desenvolvimento de complexos sistemas mecânicos passa pelo aparecimento de novos materiais que cumpram apertados requisitos de projecto. O desenvolvimento de novos materiais apenas é possível com o auxílio de ferramentas numéricas. Assim, os Modelos Acoplados Multi-Escala poderão ser um aliado neste enorme desafio. É neste contexto que esta dissertação se enquadra: desenvolvimento do Método Acoplado Multi-Escala para a caracterização de materiais tendo por base a sua micro-estrutura. Face a este objectivo, esta tese inicia-se, no Capítulo 1, com uma revisão bibliográfica desta temática. De seguida, no Capítulo 2, é introduzida uma breve revisão da Teoria dos Meios Contínuos bem como do Método dos Elementos Finitos (MEF). No capítulo 3, é proposta a formulação subjacente aos Modelos Acoplados Multi-Escala, onde é dada especial atenção a aspectos computacionais. O capítulo 4 versa sobre um procedimento de incremetação automático para o método de *Newton-Raphson* implementado à micro-escala. Com este procedimento é possível reduzir significativamente o tempo computacional associado a um problema multi-escala acoplado. Face à dificuldade encontrada na construção de malhas periódicas em complexos Elementos de Volume Representativos (EVRs), no Capítulo 5 é sugerida uma nova estratégia numérica de impor condição Periódica. Como comprovado pelos diferentes resultados, esta contribuição garante claramente uma correcta imposição de um deslocamento periódico providenciando simultaneamente uma enorme flexibilidade para o utilizador deste método numérico. A patologia de dependência da malha demonstrada pelo MEF quando o regime de amaciamento do material é atingido é analisada no contexto dos modelos acoplados multi-escala no Capítulo 6. Com base em duas abordagens distintas não-locais do tipo integral para o problema à micro e macro escalas, foi possível atenuar claramente esta patologia em ambos os domínios espaciais. No entanto, enquanto que à micro-escala esta patologia foi praticamete eliminada, à macro-escala é ainda necessário algum trabalho com o intuito de aprimorar as indicações positivas que a formulação proposta originou. Face à necessidade da caracterização dos materiais em diferentes regimes, em particular no regime de amaciamento, no Capítulo 7 é introduzido um novo conceito de condição *Periódica* com a capacidade de ter em conta a presença de uma banda de localização no comportamento global do EVR . Embora seja um conceito embrionário, foram obtidas indicações positivas quanto à configuração final do EVR quando esta nova condição de fronteira é prescrita. Por último, são apresentadas as principais conclusões deste trabalho bem como sugestões de trabalhos futuros.

Agradecimentos

Ao meu orientador, Professor Dr. Francisco Manuel de Andrade Pires, o meu obrigado por me ter apoiado ao longo destes quatro anos. Para além disto, reconhecer o seu esforço para que ao longo deste período tivesse a oportunidade de participar em cursos e congressos altamente prestigiados na área da Mecânica Computacional. O meu obrigado também aos Professores Dr. José César de Sá e Dr. Pedro Ponces Camanho pelas suas sugestões e discussões sempre pertinentes relativas a modelos numéricos e claro, às belas discussões *'Benfica .VS. Porto'*.

Gostaria de também de deixar uma palavra de agradecimento para com a Fundação para a Ciência e Tecnologia (FCT) por ter suportado financeiramente este trabalho com uma bolsa de doutoramento ao longo destes quatro anos.

Aos meus colegas de gabinete e grandes amigos, Dr. Filipe Xavier Costa Andrade, Dr. Lucival Malcher, Thiago Doca e Dra. Mariana Seabra, o meu obrigado por estes quatro anos de convivência saudável, onde foi possível todos os dias discutir conceitos, ideias e sugestões. E claro, aos belos momentos passados fora do gabinente a saborear as belas "*Francesinhas*" que o Porto tem para oferecer. Gostaria de agradecer também aos colegas Shenghua Wu e Mohsen Mirkhalaf pelos belos momentos passados ao longo dos últimos 2 anos.

À minha família, sobretudo aos meus pais, Albino e Aurora, e irmã, Telma, o meu obrigado pelo enorme apoio e suporte ao longo desta etapa tão importante da minha vida.

Por último, gostaria de agradecer à minha namorada e futura esposa, Maribel, pelo seu apoio incondicional e enorme paciência demonstrada nos momentos mais duros deste longo percurso. Utilizando uma palavra que nos dias de hoje me diz muito por motivos profissionais, foste o principal "propulsor" para que um dia concluísse este desafio.

A todos, o meu muito Obrigado.

Fábio José Pinho Reis.

Contents

List of Figures

List of Tables

Dedicated to Maribel

Chapter 1

Introduction

Over the last decades, scientific and industrial communities have been sharing their resources and have been working together towards the optimized design of materials and structures. As a result of this cooperation, new materials, new technologies and new simulation tools to support design projects have been discovered and developed. Probably, it is the development of new simulations tools that has had the most significant impact. This marked evolution may be justified by two reasons: the computational capacity versus power has had a dramatic increase over the last years and both industrial and scientific communities are aware that the design of new complex structures and systems, which simultaneously need to satisfy restrictive safety, mechanical and, in some cases, economical constraints, is only possible through virtual simulations tools.

Even though significant advances have been achieved on the simulation of different phenomena, there is still the need for further developments. This is particularly true for the numerical strategies and algorithms that have been used to characterize the behaviour of materials with a generic microstructures subjected to complex loading conditions.

Basically, two distinct approaches have been followed in order to model the behaviour of materials: continuum and micromechanical approaches. In the first one, the characterization of the material is accomplished by the development of continuous constitutive equations. Commonly, these equations are established based on phenomenological assumptions or, in some cases, based on micromechanical considerations. Notable results have been obtained however, this approach seems to be close to its limits. This is mainly due to the fact that regardless of the complexity of the continuous equations, they will never contemplate and include all the phenomena that take place at the micro structural level such as: phase transformation, thermal conductivity among different phases, internal deterioration, onset of fracture and so on. The second approach starts from another point of view: by considering exclusively information from the microstructure,

analytical and semi-analytical solutions are formulated which are able to estimate the overall properties of the material. Even though considerable efforts have been directed towards the development of these analytical solutions, they still remain too simple, not covering a wide range of practical applications.

Faced with the gap between these two approaches, a new framework has been developed aiming to establish the bridge between pure continuous and micromechanical approaches: Coupled Multi-Scale Models.

1.1 Heterogeneous materials

Regardless of the kind of material (metal, composite, polymer, natural), the hypothesis of *homogeneity* might be a limiting assumption for several reasons. When we dive into the microstructure of a generic material it is possible to observe different features such as: second phases, voids, micro-cracks and inclusions. In addition, these features embedded at the microstructure might interact in a complex manner and have considerable impact on the overall properties and performance of the material.

Traditionally, a metal alloy such as a carbon-steel alloy is considered isotropically homogeneous and, in fact, for simple applications this assumption is admissible. However, when it is necessary to design and construct a structural component, which during its active live will possibly be subjected to critical external loading conditions bringing the material close to its limits, we verify that there are significant deviations between the predicted behaviour and the experimentally observed. This happens mainly due to the fact that, there is a strong dependence of the overall properties and global performance of the material on phenomena that take place at its microstructure. Thus, in these cases, it is imperative to perform structural analyses which take into account information from the microstructure of the material. Within the context of heterogeneous materials, it is also important to remark that, since ancient times, we have been manipulating virgin materials aiming to improve its properties by the introduction of a second phase/constituent into the microstructure of the virgin material. In fact, this is what has been done with composites materials. One of the advantages of composites materials relies on the fact that it is possible to define a specific material for each particular application by manipulating the fibers, the matrix and the manufacture process.

Faced with this undoubtedly relevant evidence, several analytical approaches have been suggested to quantify the overall properties of heterogeneous materials exclusively by the analysis of its microstructure. The simplest analytical strategy is the *rule of mixtures*. This strategy assumes that the overall properties are calculated as a volume average of

the corresponding microscopic value of each constituent phase, which is weighted by the respective volume fraction. In this case, only the spatial configuration of the constituents and their particular properties are considered, ignoring completely all the other aspects.

A different analytical approach, which is suitable for materials with a regular repetitive microstructure pattern, was suggested by Eshelby [7]. The global elastic properties of the heterogeneous material are obtained by the analytical solution of a boundary value problem of an infinite isotropic matrix containing a circular or ellipsoidal inclusion. This analytical approach, widely known as the *effective medium approach* has been generalized and extended in order to incorporate others aspects such as plasticity and interaction among inclusions ([8], [9], [10], [11]).

Based on the original work of Eshelby [7], Hill [12] has proposed a new analytical approach: *the self-consistent approach*. The fundamental idea was to introduce incremental solutions for a composite, which is characterized by an inclusion embedded into an infinite homogeneous matrix, and imposing that the properties of the matrix are the same as the composite. With this analytical framework, Hill [12] obtained closed-forms for Bulk and shear moduli which have provided reasonable results for composites with a regular microstructure. Even though the *self-consistent approach* has undergone some developments, the results obtained still remain unsatisfactory due to the fact that the composites that can be analysed are quite simple, not being representative of a real composite material.

The *variational bounding methods* have gained importance on the development of analytical methods to obtain advanced properties of composites. Within this context, pioneer work was carried out by Hashin and Shtrikman [13], who obtained upper and lower bounds on the values of overall elastic moduli for materials with irregular microstructure. Some extensions of this original work have been published i.e. [14–18].

Another approach for analytical methods is provided by the *mathematical asymptotic homogenization theory*. This method was initially proposed by Bensoussan et al. [19] and Sanchez-Palencia [20]. This theory is based on the principle of scale separations, which means that macro and micro level are naturally distinct. Mathematically, the asymptotic homogenization theory applies an asymptotic expansion to the displacement and stress fields which are dependent on the natural length parameter (ratio between the characteristic size of the heterogeneities and the size of the macrostructure). A more detailed discussion of this analytical approach may be found in [21–23]. An extensive overview of the analytical methods mentioned can be found in [24].

More recently, the *numerical homogenization* procedure has gained a notable popularity within the composite community. The basic idea is to solve the equilibrium problem of

a *Representative Volume Element* (RVE) [25] when it is subjected to admissible kinematical boundary conditions (Periodic and Uniform Tractions constraints) and then, compute the overall properties by homogenization over the RVE's domain. Compared with classical analytical approaches, this numerical framework stands out mainly because it allows to model different phenomena at the microstructure without restrictions. Some examples of this approach can be found in [26–29] among several others.

1.2 Multi-scale modelling

Despite the notable contributions and results, which have resulted exclusively from micromechanical analysis, there is still a significant and pronounced gap between the micromechanical results and the real behaviour of the macroscopic structure. This fact is more noticeable when we need to analyse the behaviour of the material whenever it goes beyond the elastic domain. Undoubtedly we recognize that, in parallel with the macroscopic deformation of the solid, there are inherent evolutions at the microstructure such as phase transformations, internal deterioration, onset of fracture, propagation of the micro-cracks that need to be taken into account throughout the analysis for the appropriate design of the component.

The characterization of these phenomena exclusively by means of analytical and semi-analytical approaches, which solely take into account information from the virgin microstructure of the material is far from being ideal.

In recent years a promising numerical tool has attracted considerable amount of efforts: *Coupled Multi-Scale Modelling*. The underlying principles and concepts, which constitute the coupled multi-scale theory, were introduced by [30], [31], [32] , [33] and [34]. This micro-macro modelling procedure defines the stress-strain relation at each macroscopic point through a homogenization procedure, which involves a solution of a boundary problem over a statistically *Representative Volume Element* (RVE). In practice, considering the finite element method, this numerical approach consists in solving simultaneously two boundary problems: the macroscopic problem and the micro boundary value problem at each macroscopic integration *Gauss* point. Compared with the different approaches mentioned previously, this numerical solution stands out due to the following reasons:

- There is no constraint with regard to geometry of the microstructure. Complex and arbitrary geometries can be easily incorporated into a RVE;
- The framework is suitable to model non-linear and time dependent problems;

- With appropriate algorithms it is possible to include interaction among the different constituents of the microsctructure as well as to characterize the internal deterioration and phase transformations [35];
- Large deformation can be trivially modelled either at macro or micro-scales;
- Regardless of the phenomena incorporated at the microstructure and their complexity, the overall response at macro-scale is always a consequence of the microstructure.

Relevant contributions to this field have been made by several authors. Among others, the work performed by Miehe et al. [36], Miehe and Koch [37] where a crystal plasticity framework at small and finite strains was established and the work of Kouznetsova et al. [38], who have proposed a second order coupled-multi scale scheme in order to introduce the effect of the size of the RVE and its constituents should be highlighted. More recently, Özdemir et al. [39, 40] have enhanced the coupled multi-scale model in order to incorporate thermal effects.

With regard to practical applications, Massart et al. [41, 42] using a coupled multi-scale model, which includes an internal damage variable, performed structural analysis of masonry walls. A similar study was carried out by Mercatoris et al. [43]. More recently, Coenen et al. [44] based on classical plate and shells theory has formulated a coupled multi-scale framework that is able to solve problems involving heterogeneous thin sheets. In addition to these examples, several others may be found in the literature i.e. [45–48].

One drawback of this numerical framework is the fact that this formulation is rather computationally expensive. However, this problem may be minimized by employing parallel computations [49, 50] and by applying selective usage [51], where in some non-critical parts at the macro-scale, instead of the fully multi-scale analysis, closed-forms or continuum constitutive laws are adopted.

Notwithstanding the promising capabilities of coupled multi-scale models have shown, some issues inherent with their youth have been raised. In particular, when they are used to characterize complex materials over the line which defines the initiation of the softening regime verified at the macroscopic specimen. In this case, the current formulation of *First-Order Coupled Multi-Scale Models* fails mainly for three reasons. The first one is due to the fact that the RVE loses its representativeness when this structural regime is reached. Several efforts have been directed towards this topic where the work of Gitman et al. [52, 53] should be pointed out. The second reason is inherent with the mesh dependence pathology that is verified under these conditions. It is noteworthy

to mention that since in a coupled multi-scale model at least two spatial scales are included on the analysis, this pathology may be observed at both scales. With regard to this issue, the work of Wu et al. [54] should be highlighted. The third is related to the necessity of extending *First-Order Coupled Multi-Scale Models* with strategies that are able to properly model the presence at both scales of localization bands or discontinuities (depending on the nomenclature considered). Among several others, the work carried out by Belytschko et al. [55], Song and Belytschko [56], Souza and Allen [57], Coenen et al. [58], Nguyen et al. [59], Nguyen et al. [60], Nguyen et al. [61] and Verhoosel et al. [62] should be highlighted. In addition to the transition of scales, it is still necessary to pay attention to the kinematical boundary condition enforced at the RVE level in the presence of a localization band. In the literature, according to the author's knowledge only the work carried out by Coenen et al. [63] has addressed this issue. As a matter of fact, some authors advocate that the enhancement of the scale transition with parameters, which define a localization band at both domains, dramatically minimizes the mesh dependence pathology verified at both scales.

The main objective of this thesis is to develop an efficient framework, which incorporates several numerical techniques, to model the deformation behaviour of heterogeneous materials at finite strains and predict material failure in relevant practical problems.

1.3 Outline

In order to facilitate the understanding and reading of the present document, in this section, the main architecture of it is introduced chapter by chapter.

Chapter 2

In Chapter 2, the fundamental concepts of the *Continuum Solid Mechanics* theory are introduced as well as the main definitions of the *Finite Element Method* (FEM). These concepts will be widely used in the following chapters of this document.

Chapter 3

In Chapter 3, the concepts of First-order coupled multi-scale models are introduced such as Homogenization, *Hill-Mandel* principles or even boundary conditions, which are kinematically admissible within the context of coupled multi-scale models. Special attention is also given to numerical and computational aspects such as *Newton-Raphson*

method applied at each spatial domain and linerization of micro and macro problems. As a matter of fact, all formulation was introduced under the finite strain assumption.

Chapter 4

In order to reduce the computational cost inherent with coupled multi-scale problems, in Chapter 4, an adaptive sub-incremental strategy is proposed for the *Newton-Raphson* method implemented at the micro-scale domain. For this purpose, *Line-Search* and *Arc-Length* methods were properly modified for the micro-equilibrium problem in order to guarantee quadratic rates of convergence at both scales. By means of some numerical examples, the new adaptive incremental approach was assessed demonstrating a significant computational cost reduction.

Chapter 5

In Chapter 5, a new enforcement of *Periodic* boundary condition was proposed based on the *Mortar* decomposition method. The main idea is to impose a periodic displacement over non-conform meshes. In other words, over meshes with an arbitrary discretization. The new concept was implemented for either two and three dimensional problems and the admissibility of the new constraint was demonstrated. In order to assess the robustness of the new enforcement, some examples were considered where outstanding results were obtained for either two or three dimensional problems.

Chapter 6

The mesh dependence pathology observed within the context of First-order coupled multi-scale models was addressed in Chapter 6. In order to minimize this pathology, which is verified at both scales, two non-local approaches of integral-type were proposed for each scale. Despite sharing the same base, the two approaches considered are significantly different: while at the micro-scale, a scalar internal variable as considered as non-local parameter, i.e. the damage associated to the constitutive model, at the macro-scale, a kinematic tensorial variable was selected, i.e. the macroscopic deformation gradient. Outstanding results were obtained at the micro-scale, where this pathology was considerably minimized. In contrast, despite positive indications, the approach implemented at the macro-scale still needs to be improved.

Chapter 7

In Chapter 7, a new concept of *Periodic* boundary condition that is able to tackle the presence of a localization band is introduced. The main idea consists on the decomposition of the total RVE domain based on the shape of the localization band. For this purpose, once again, the *Mortar* decomposition method is considered. Due to the complexity of the new concept, only a preliminary result was introduced. Nevertheless, a clearly interesting indication in terms of the final configuration of the RVE was obtained, which is in agreement with the initial expectation about this concept.

Chapter 8

This document concludes with Chapter 8 where the summary of the main achievements of this work is presented. Moreover, suggestions for future research are made.

1.4 Related publications

Most of the work of this thesis has either been published, submitted or are currently in preparation for submission in scientific journals. A list of this contributions is given herein.

- F.J.P. Reis, F.M. Andrade Pires. *An adaptive sub-incremental strategy for the solution of homogenization-based multi-scale problems*, Computer Methods in Applied Mechanics and Engineering, 257: 164-182, 2013.
- F.J.P. Reis, F.M. Andrade Pires. *A mortar based approach for the enforcement of periodic boundary conditions on arbitrarily generated meshes*, Computer Methods in Applied Mechanics and Engineering - (under review).
- F.J.P. Reis, F.M. Andrade Pires. *A Non-local method of integral type for heterogeneous media* - (in preparation).

Chapter 2

Continuum Mechanics and Finite Element Method

2.1 Introduction

A coupled multi-scale model can be viewed as an extension of the continuum solid mechanics theory and most of the definitions of this theoretical field are widely applied in the formulation of such micro-macro models. Thus, before we proceed with the introduction of a first-order coupled multi-scale model, a brief revision of continuum solid mechanics will be addressed in this chapter.

Due to the complexity inherent with solid mechanics problems, and in order to provide an engineering applicability to these models, suitable numerical tools are required. Within the context of this work, the *Finite Element Method* is considered coupled with the iterative *Newton-Raphson* method. Whereas the former numerical method is responsible to perform the spatial discretization of the problem domain and the boundary conditions, the latter is used to solve with quadratic rates of convergence a non-linear system of equations.

Before to proceed, it is relevant to emphasize once again, that the main goal of this chapter is not to provide an detailed an exhaustive introduction neither on Continuum solid Mechanics nor Finite Element Method but rather to present a short overview of these topics. Nevertheless, for those who are not familiar and do not have a strong background in these topics, several famous publications can be consulted for Continuum Solid Mechanics [6, 64–68] and for Finite Element Method [6, 65, 69–71].

2.2 Kinematics of deformation

Consider a body ($\mathcal{B}$), which in the *Euclidean* three-dimensional space $\mathcal{R}^3$, occupies the region Ω_0 with a regular boundary defined by $\partial\Omega_0$ on its initial configuration (see Figure 2.1).

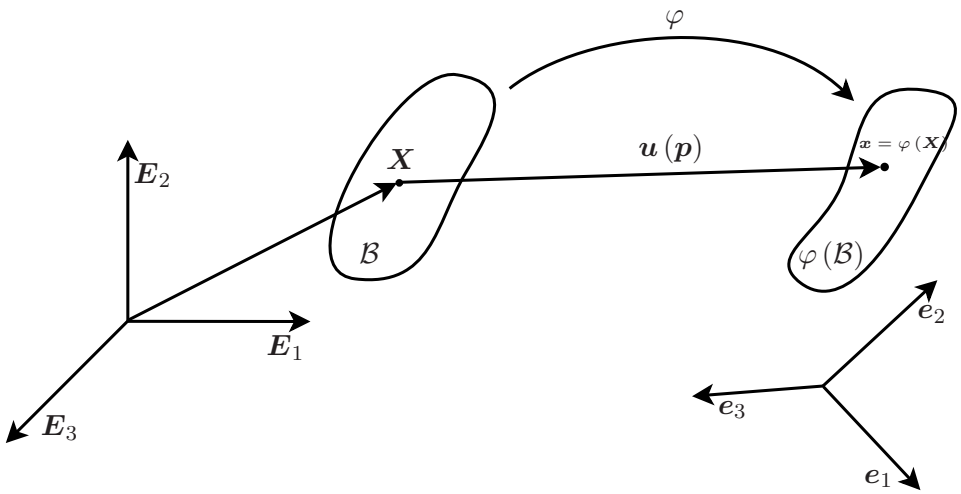

FIGURE 2.1: Deformation of a body.

After a given motion φ of the body which may include a rigid movement (i.e. translation and/or rotation) within a certain time t, the position of the material particle $\boldsymbol{p}$ at time t with initial coordinate $\boldsymbol{X}$ is given by

$$\boldsymbol{x} = \varphi\{\boldsymbol{X}, t\}, \tag{2.1}$$

where $\boldsymbol{x}$ is the position in the *Euclidean* space of the material particle $\boldsymbol{p}$. By definition, the displacement field, $\boldsymbol{u}$, of the material particle $\boldsymbol{p}$ is given by

$$\boldsymbol{u}\{\boldsymbol{X}\} = \varphi\{\boldsymbol{X}\} - \boldsymbol{X}. \tag{2.2}$$

Manipulating the previous equation, it is possible to obtain an explicit expression for the position of particle $\boldsymbol{p}$ in the deformed configuration of the solid:

$$\boldsymbol{x} = \boldsymbol{X} + \boldsymbol{u}\{\boldsymbol{X}\}. \tag{2.3}$$

The velocity field is, by definition, the derivative of the displacement with respect to time, t:

$$\dot{\boldsymbol{x}}\{\boldsymbol{X}, t\} = \frac{\partial\varphi\{\boldsymbol{X}, t\}}{\partial t}. \tag{2.4}$$

Assuming that $\varphi\{\boldsymbol{X}, t\}$ is invertible, for all instant t, the material points $\boldsymbol{X}$ can be explicitly defined by its coordinates on the deformed configuration of the solid, $\boldsymbol{x}$

$$\boldsymbol{X} = \varphi^{-1}\{\boldsymbol{x}, t\} = \boldsymbol{x} - \boldsymbol{u}\left\{\varphi^{-1}\{\boldsymbol{x}, t\}, t\right\}. \tag{2.5}$$

where φ^{-1} denotes the *reference* map. With this function at hand it is possible to define the *spatial* velocity field:

$$\boldsymbol{v}\{\boldsymbol{x}, t\} = \dot{\boldsymbol{x}}\left\{\varphi^{-1}\{\boldsymbol{x}, t\}, t\right\}. \tag{2.6}$$

Both fields $\dot{\boldsymbol{x}}$ and $\boldsymbol{v}$ represent the velocity of the solid during the deformation. However, they were established in different referentials and for this reason they are different.

With the introduction of the initial and current position of a particle, $\boldsymbol{p}$, respectively denoted by $\boldsymbol{X}$ and $\boldsymbol{x}$, it is possible to define two descriptions which may be used to characterize the motion of a solid: *material* and *spatial* descriptions. The *material* description, also called *Lagrangian* description, characterizes the deformation of the solid with reference to the initial configuration of the solid. This means that the equilibrium and dynamic equations which govern the behaviour of the solid, are explicitly dependent on the original coordinates $\boldsymbol{X}$ and time t. This description basically consists of following a material particle through the motion and analyse the variables from this point of view.

Alternatively, all fields inherent with the motion of a solid may be described using a *spatial* description or *Eulerian* description. Conversely to the *material* description, in this description all fields are functions of the spatial position $\boldsymbol{x}$. Conceptually, this description may be described as: in a fixed point of the space observe the motion of the particles of the solid.

2.2.1 Deformation gradient

Mathematically, the gradient of a generic function (either scalar or vectorial function) consists the estimation of the evolution of a function in a particular direction. This operation is widely applied within the context of *Continuum Solid Mechanics* and in this document it will be symbolically represented by ∇.

When applying this operator to the *motion function* results the deformation gradient, $\boldsymbol{F}\{\boldsymbol{X}, t\}$, which is a second order tensor. Considering the *material* configuration, this parameter is defined as

$$\boldsymbol{F}\{\boldsymbol{X}, t\} = \nabla_{\boldsymbol{p}}\varphi\{\boldsymbol{X}, t\} = \frac{\partial \boldsymbol{x}}{\partial \boldsymbol{X}}. \tag{2.7}$$

Taking into account expression (2.7) together with the relations introduced in the previous section and after a straightforward algebra manipulation, the deformation gradient, $\boldsymbol{F}\{\boldsymbol{X}, t\}$, may be re-written as:

$$\boldsymbol{F}\{\boldsymbol{X}, t\} = \boldsymbol{I} + \nabla_{\boldsymbol{p}}\boldsymbol{u}, \tag{2.8}$$

where $\boldsymbol{I}$ denotes the second order identity tensor. In the *spatial* description, the deformation gradient is given by the following expression:

$$\boldsymbol{F}\{\boldsymbol{x}, t\} = \left[\nabla_{\boldsymbol{x}}\varphi^{-1}\{\boldsymbol{x}, t\}\right]^{-1} = \left[\boldsymbol{I} - \nabla_{\boldsymbol{x}}\boldsymbol{u}\right]^{-1}. \tag{2.9}$$

As can be possible to observe from Equations (2.7) and (2.9), there are two gradient operators denoted by $\nabla_{\boldsymbol{p}}$ and $\nabla_{\boldsymbol{x}}$. The former denotes the *material* gradient operator whereas the latter corresponds to the gradient operator defined at the *spatial* configuration. As a matter of fact, in what follows, this notation will be used.

Polar decomposition of the deformation gradient

In order to distinguish pure stretches from pure rotations, it is possible to perform the polar decomposition to the deformation gradient, which gives rise to

$$\boldsymbol{F} = \boldsymbol{R}\boldsymbol{U} = \boldsymbol{V}\boldsymbol{R}, \tag{2.10}$$

where $\boldsymbol{R}$ denotes the rotation tensor meanwhile tensors $\boldsymbol{U}$ and $\boldsymbol{V}$ are the right and left stretch tensors. Note that these two tensors are symmetric positive definite second order tensors and are defined by

$$\boldsymbol{U} = \sqrt{\boldsymbol{C}}, \tag{2.11a}$$

$$\boldsymbol{V} = \sqrt{\boldsymbol{B}}, \tag{2.11b}$$

where $\boldsymbol{C}$ and $\boldsymbol{B}$ are respectively the right and left *Cauchy-Green* strain tensors, which are mathematically defined by

$$\boldsymbol{C} = \boldsymbol{F}^T\boldsymbol{F}, \tag{2.12a}$$

$$\boldsymbol{B} = \boldsymbol{F}\boldsymbol{F}^T. \tag{2.12b}$$

Decomposition of the deformation gradient

The deformation gradient can be multiplicatively decomposed into two parts: the *isochoric*, $\boldsymbol{F}_{iso}$, and *volumetric*, $\boldsymbol{F}_v$ parts [64]. Hence, the deformation gradient, $\boldsymbol{F}$, may be defined as:

$$\boldsymbol{F} = \boldsymbol{F}_{iso}\boldsymbol{F}_v. \tag{2.13}$$

In the particular case of three-dimensional spaces, $\boldsymbol{F}_{iso}$ and $\boldsymbol{F}_v$ are determined using the following expressions:

$$\boldsymbol{F}_v = (det\boldsymbol{F})^{\frac{1}{3}}\,\boldsymbol{I}, \tag{2.14}$$

$$\boldsymbol{F}_{iso} = (det\boldsymbol{F})^{-\frac{1}{3}}\,\boldsymbol{F}, \tag{2.15}$$

where the *volumetric* part only contemplates the part of the deformation gradient inherent with volume changes of the solid and the *isochoric* part is exclusively associated with the material distortion.

2.2.2 Strain measures

Different quantities may be used to characterize the straining phenomenon of a solid. Even though the different strain quantities represent the same physic phenomenon, its selection is basically a compromise between the physical phenomenon which is aimed to be modelled and the mathematical framework which will be used to.

Among others strain measures, probably the most used either in theoretical or numerical formulations are the *Lagrangian* and the *Eulerian* strain tensors. The *Lagrangian* strain tensors is mathematically expressed by

$$\boldsymbol{E}^m = \begin{cases} \frac{1}{m}\left(\boldsymbol{U} - \boldsymbol{I}\right) & , m \neq 0, \\ \ln\left[\boldsymbol{U}\right] & , m = 0, \end{cases} \tag{2.16}$$

where m is a real number and $\ln[*]$ denotes the logarithm function. The *Eulerian* strain tensors are quite similar to the *Lagrangian* strain family distinguish solely on the stretch tensor which defines it: the left stretch tensor, $\boldsymbol{V}$:

$$\boldsymbol{E}^m = \begin{cases} \frac{1}{m}\left(\boldsymbol{V} - \boldsymbol{I}\right) & , m \neq 0, \\ \ln\left[\boldsymbol{V}\right] & , m = 0. \end{cases} \tag{2.17}$$

In the present document, the *Eulerian* logarithmic strain tensor, which corresponds to the case when $m = 0$ will be used in the formulation of material constitutive models defined at the micro-scale level.

It is important to remark that in case of rigid body rotation or translations, any of the previous defined deformation tensors vanishes.

2.3 Stress measures

In this section, the different quantities to measure stress in a deformable solid and which will be used throughout the present document will be briefly reviewed.

2.3.1 *Cauchy* stress tensor

By definition, the *Cauchy* stress tensor, $\boldsymbol{\sigma}$, is given by

$$\boldsymbol{t}\{\boldsymbol{n}, t\} = \boldsymbol{\sigma}\boldsymbol{n}, \tag{2.18}$$

where $\boldsymbol{t}$ is the surface traction and $\boldsymbol{n}$ is its associated unit outward normal vector. In the literature, it is commonly used to denominate this stress tensor as *true stress tensor* due to the fact that it is defined at the deformed (current) configuration of the solid. As a particularity of this stress tensor is the fact that it is symmetric.

In line with the deformation gradient which may be split into its *volumetric* and *isochoric* counterparts, the *Cauchy* stress tensor may also decomposed into *hydrostatic* and *deviatoric* parts. The former component, also usually called as *hydrostatic pressure* or even *mean stress* is defined as

$$p = \frac{1}{3} tr(\boldsymbol{\sigma}). \tag{2.19}$$

The deviatoric stress, $\boldsymbol{s}$, is given by

$$\boldsymbol{s} = \boldsymbol{\sigma} - p\boldsymbol{I}. \tag{2.20}$$

2.3.2 *First Piola-Kirchhoff* stress tensor

While the *Cauchy* stress tensor characterize the stress in a generic point of a continuum solid with regard to the deformed configuration of the solid, in some circumstances, it is convenient to define a stress tensor considering the undeformed configuration. Thus, the *material* version of the *Cauchy* stress tensor is known as the *First Piola-Kirchhoff* stress tensor, denoted by $\boldsymbol{P}$, which is mathematically defined as

$$\boldsymbol{P} = J\boldsymbol{\sigma}\boldsymbol{F}^{-T}, \tag{2.21}$$

where J is the determinant of the deformation gradient intrinsic with the motion of the solid. In contrast with the *Cauchy* stress tensor, $\boldsymbol{P}$ is generally *unsymmetric*.

2.3.3 *Kirchhoff stress tensor*

Using the *Cauchy* stress tensor as well as the determinant of the deformation gradient, J, it is possible to define a new symmetric stress tensor: the *Kirchhoff* stress tensor, which in this document will be denoted by $\boldsymbol{\tau}$:

$$\boldsymbol{\tau} = J\boldsymbol{\sigma}. \tag{2.22}$$

2.4 Fundamental conservation principles

So far, only the parameters that are used to mathematically define the *motion* and *stresses* in a continuum solid together with forces which a generic solid may be subjected to were addressed. Nevertheless, now, it is fundamental to introduce the laws, which are explicitly dependent on the parameters previously introduced, and are responsible for governing the behaviour of the solid. For convenience, no reference will be given to the thermodynamic principles. In fact, these principles are out of the scope of this work.

2.4.1 Conservation of mass

The principle of *conservation of mass* postulates that the following expression needs to be always satisfied

$$\dot{\rho} + \rho div_{\boldsymbol{x}} \dot{\boldsymbol{u}} = 0, \tag{2.23}$$

where ρ is the density of the solid and $div_{\boldsymbol{x}}(*)$ denotes the *spatial* divergence operator.

2.4.2 Momentum balance principle

Using a *spatial* description of the *motion* of a continuum solid, the momentum balance principle is defined by the following system of equations:

$$\begin{cases} div_{\boldsymbol{x}}\boldsymbol{\sigma} + \boldsymbol{b} = \rho\ddot{\boldsymbol{u}} & , \text{ in } \varphi(\mathcal{B}), \\ \boldsymbol{t} = \boldsymbol{\sigma}\boldsymbol{n} & , \text{ on } \varphi(\partial\mathcal{B}), \end{cases} \tag{2.24}$$

where $\boldsymbol{t}$ is the traction vector field on the deformed boundary of the solid, $\varphi(\partial\mathcal{B})$, and $\boldsymbol{n}$ is the outward unit vector normal to $\varphi(\partial\mathcal{B})$. In the first expression of the above equation system, $\boldsymbol{b}$ denotes the body force per unit deformed volume.

The above system can be equivalently re-written in the *material* configuration (or *Lagrangian* description) . In this case, this principle is defined by:

$$\begin{cases} div_{\boldsymbol{p}}\boldsymbol{P} + \overline{\boldsymbol{B}} = \overline{\rho}\ddot{\boldsymbol{u}} & , \text{ in } \mathcal{B} \\ \boldsymbol{T} = \boldsymbol{P}\boldsymbol{N} & , \text{ on } \partial\mathcal{B} \end{cases} \tag{2.25}$$

where $\boldsymbol{P}$ is the *First Piola-Kirchhoff* stress tensor, $\boldsymbol{B}$ is the body force measured per unit reference volume and $div_{\boldsymbol{p}}$ denotes the *material* divergence operator. In this version of the momentum balance principle, the density is also described assuming the reference configuration of $\mathcal{B}$. In the last expression of the previous system of equations, $\boldsymbol{T}$ denotes the boundary traction force per unit reference area and $\boldsymbol{N}$ is the unit outward vector normal to the undeformed boundary of $\mathcal{B}$.

Remark 2.1. The equations introduced above, which represent the momentum balance principle are also widely known as the Strong Equilibrium Equations.

2.5 Weak equilibrium. The principle of virtual work

Having stated the *strong equilibrium equations* in the previous section, in the present one, their corresponding *weak* form will be introduced. The *weak* form of the *strong equilibrium equations* results from the application of the *Principle of Virtual Work*.

For this purpose, consider again a generic solid $\mathcal{B}$ which occupies the region $\Omega_0 \subset \mathcal{R}^3$ with boundary $\partial\Omega_0$ in its reference configuration and subjected to body forces in its interior and surface tractions on its boundary.

2.5.1 Spatial version

The spatial version of the *Virtual Work Principle* states that the solid is in equilibrium if and only if the following expression is verified:

$$\int_{\varphi(\Omega_0)} \left[\boldsymbol{\sigma} : \nabla_x \boldsymbol{\eta} - (\boldsymbol{b} - \rho\ddot{\boldsymbol{u}}) . \boldsymbol{\eta}\right] dV - \int_{\varphi(\partial\Omega_0)} \boldsymbol{t}.\boldsymbol{\eta} dA = 0 \ \ \forall\, \boldsymbol{\eta} \in \mathcal{V}, \tag{2.26}$$

where $\boldsymbol{b}$ and $\boldsymbol{t}$ are respectively the body force per unit deformed volume and the external traction forces acting over the deformed boundary of the solid per unit area; $\boldsymbol{\eta}$ denotes

the admissible virtual displacements field belonging to the *space of virtual displacement* of $\mathcal{V}$.

2.5.2 Material version

The corresponding *material* version of Equation (2.26) states that the solid is in equilibrium if and only if the *First Piola-Kirchhoff* stress tensor satisfies:

$$\int_{\Omega_0} \left[\boldsymbol{P} : \nabla_{\boldsymbol{p}} \boldsymbol{\eta} - (\boldsymbol{B} - \overline{\rho}\ddot{\boldsymbol{u}}) . \boldsymbol{\eta} \right] dV - \int_{\partial\Omega_0} \boldsymbol{T} . \boldsymbol{\eta} dA = 0 \ \ \forall\, \boldsymbol{\eta} \in \mathcal{V}. \tag{2.27}$$

The previous equation is established by introducing into Equation (2.26) the following relations

$$\boldsymbol{\sigma} = \frac{1}{J} \boldsymbol{P} \boldsymbol{F}^T, \tag{2.28a}$$

$$\nabla_{\boldsymbol{x}} \boldsymbol{a} = \nabla_{\boldsymbol{p}} \boldsymbol{a} \boldsymbol{F}^{-1}. \tag{2.28b}$$

The second relation of Equation (2.28) holds for a generic vector field $\boldsymbol{a}$. In addition to these relations, the "bridge" between *spatial* and *material* was performed using the standard relation [72]

$$\int_{\varphi(\Omega_0)} a\left\{\boldsymbol{x}\right\} dV = \int_{\Omega_0} J\left\{\boldsymbol{p}\right\} a\left\{\varphi\left\{\boldsymbol{p}\right\}\right\} dV, \tag{2.29}$$

valid for any scalar field a.

2.5.3 Quasi-static formulation

In some cases, the inertial effects are insignificant when compared to others phenomena inherent with the deformation of the solid. Therefore, in these cases, the inertial effects can be disregarded from the formulation without loss of accuracy. This particular case is commonly called as *Quasi-Static Problem*.

Considering the spatial configuration of the solid, the equation which governs this problem is given by:

$$\int_{\varphi(\Omega_0)} \left[\boldsymbol{\sigma} : \nabla_x \boldsymbol{\eta} - \boldsymbol{b} . \boldsymbol{\eta} \right] dV - \int_{\varphi(\partial\Omega_0)} \boldsymbol{t} . \boldsymbol{\eta} dA = 0 \ \ \forall\, \boldsymbol{\eta} \in \mathcal{V}, \tag{2.30}$$

whereas the material description of the problem is given by

$$\int_{\Omega_0} \left[\boldsymbol{P} : \nabla_{\boldsymbol{p}} \boldsymbol{\eta} - \boldsymbol{B} . \boldsymbol{\eta} \right] dV - \int_{\partial\Omega_0} \boldsymbol{T} . \boldsymbol{\eta} dA = 0 \ \ \forall\, \boldsymbol{\eta} \in \mathcal{V}. \tag{2.31}$$

2.6 *Finite Element Method*

It is relatively straightforward to recognize that the equilibrium equations of a continuum solid, previously introduced, can be highly non-linear thereby, requiring an appropriate numerical method to solve them. One of those methods, which have been successfully used either by the scientific community or industry, is the *Finite Element Method*.

Basically, this numerical method requires the application of the following four fundamental steps:

- **Integral formulation of the Problem**. Describe the equilibrium of a solid through an integral equation.
- **Spatial Discretization**. This step is the basis of this method.
- **Temporal discretization**. If the external loads and prescribed displacements are dependent on time or even the constitutive model, which models the behaviour of the material, is dependent on the deformation history.
- **Solve the system of equations originated by the two steps aforementioned**. Usually, an iterative numerical method is used (i.e. *Newton-Raphson* method).

In the following, these four steps will be carefully introduced and discussed.

2.6.1 Integral formulation of the problem

The integral formulation of the problem can be obtained by applying different methods. However, the *Principle of Virtual Work* is commonly adopted. As mentioned before, the application of this method gives rise to Equation (2.30) if a spatial formulation is considered or, Equation (2.31) if the *motion* of a continuum solid is described with regard to its undeformed configuration.

2.6.2 Spatial discretization of the problem

The spatial discretization of a problem consists of subdividing the continuum domain of the problem, Ω, in a finite number of sub-domains called finite elements, Ω_e. This means that the continuum domain, Ω, has a discretized counterpart which can be conveniently defined as

$$\Omega \approx \Omega^d = \bigcup_{e=1}^{N_{elem}} \Omega_e. \tag{2.32}$$

In the previous equation, the index $(*)^d$ denotes a discretized domain and $\bigcup$ a suitable *assembly* operator.

Inside of each sub-domain, all variables of the problem (i.e. displacements, stress, etc) are determined by interpolation (Eq. 2.33) through the use of shape functions, which need to satisfy some constraints (for more details see for instance [70]):

$$a(\boldsymbol{x}) = \sum_{i=1}^{N_{node}} N_i^e(\boldsymbol{x}) a_i. \tag{2.33}$$

The previous equation defines a typical interpolation procedure for a generic field $a(\boldsymbol{x})$ defined over the domain of the element, Ω_e, where $N_i^e(\boldsymbol{x})$ denotes the shape function of the $i-th$ node of the finite element. Note that the value of this shape function is defined in a generic point $\boldsymbol{x}$ inside of the element and, a_i is the nodal value of field a. For a discretized global domain Ω^d, the procedure used is exactly the same:

$$a(\boldsymbol{x}) = \sum_{i}^{N_{point}} N_i^g(\boldsymbol{x}) a^i, \tag{2.34}$$

however, in this case, the shape function $N_i^g(\boldsymbol{x})$ is related to the entire domain and not solely to the finite element domain. Generically, the global interpolation matrix for a problem with n_{point} points is defined as

$$\boldsymbol{N}^g(\boldsymbol{x}) = \left[\begin{array}{cccc} diag[N_1^g(\boldsymbol{x})] & diag[N_2^g(\boldsymbol{x})] & ... & diag[N_{n_{point}}^g(\boldsymbol{x})] \end{array} \right], \tag{2.35}$$

where $diag[N_{n_{point}}^g(\boldsymbol{x})]$ is the diagonal matrix with dimension $n_{dim} \times n_{dim}$ (n_{dim} equal to 2 or 3 for two and three dimensional problems, respectively) with the shape function of the $i-th$ point.

The spatial discretization requires the introduction of the global discrete material gradient operator, $\boldsymbol{G}^g$, and global discrete spatial gradient operator, $\boldsymbol{B}^g$, which are the discretized versions of operators $\nabla_{\boldsymbol{p}}(*)$ and $\nabla_{\boldsymbol{x}}(*)$, respectively. Both matrices $\boldsymbol{G}^g$ and $\boldsymbol{B}^g$ need to be established for each type of problem (i.e. plane strain, plane stress, tree-dimensional problems). For plane-strain problems, $\boldsymbol{G}^g$ is defined as:

$$\boldsymbol{G}^g = \left[\begin{array}{cc:cc:c:cc} \frac{\partial N_1^g}{\partial x} & 0 & \frac{\partial N_2^g}{\partial x} & 0 & ... & \frac{\partial N_{n_{point}}^g}{\partial x} & 0 \\ 0 & \frac{\partial N_1^g}{\partial x} & 0 & \frac{\partial N_2^g}{\partial x} & ... & 0 & \frac{\partial N_{n_{point}}^g}{\partial x} \\ \frac{\partial N_1^g}{\partial y} & 0 & \frac{\partial N_2^g}{\partial y} & 0 & ... & \frac{\partial N_{n_{point}}^g}{\partial y} & 0 \\ 0 & \frac{\partial N_1^g}{\partial y} & 0 & \frac{\partial N_2^g}{\partial y} & ... & 0 & \frac{\partial N_{n_{point}}^g}{\partial y} \end{array} \right], \tag{2.36}$$

and $\boldsymbol{B}^g$ as

$$\boldsymbol{B}^g = \left[\begin{array}{cc:cc:c:cc} \frac{\partial N_1^g}{\partial x} & 0 & \frac{\partial N_2^g}{\partial x} & 0 & \dots & \frac{\partial N_{n_{point}}^g}{\partial x} & 0 \\ 0 & \frac{\partial N_1^g}{\partial y} & 0 & \frac{\partial N_2^g}{\partial y} & \dots & 0 & \frac{\partial N_{n_{point}}^g}{\partial y} \\ \frac{\partial N_1^g}{\partial y} & \frac{\partial N_1^g}{\partial x} & \frac{\partial N_2^g}{\partial y} & \frac{\partial N_2^g}{\partial x} & \dots & \frac{\partial N_{n_{point}}^g}{\partial y} & \frac{\partial N_{n_{point}}^g}{\partial x} \end{array}\right]. \tag{2.37}$$

2.6.2.1 Spatial discretization of the Virtual Work Equation

With the notation introduced above, it is straightforward to perform the spatial discretization of the virtual work equation. In fact, this procedure resumes to the substitution of the continuum domain by its discretized counterpart as well as the replacement of the continuum differential operators by matrices $\boldsymbol{G}^g$ or $\boldsymbol{B}^g$. For convenience, only the spatial discretization of the virtual work expression established following an *Eulerian* formulation (Eq. 2.30) is described here. Nevertheless, we remark that the spatial discretization of the *Virtual Work* equation defined with regard to the undeformed configuration (following a *Lagrangian* formulation - Equation (2.31)) is quite similar to the one that follows.

At the end of the spatial discretization procedure, Equation (2.30) is replaced by the following one:

$$\left\{\int_{\varphi\left(\Omega_0^d\right)}\left[\left(\boldsymbol{B}^g\right)^T\boldsymbol{\sigma}-\left(\boldsymbol{N}^g\right)^T\boldsymbol{b}\right]dV-\int_{\varphi\left(\partial\Omega_0^d\right)}\left(\boldsymbol{N}^g\right)^T\boldsymbol{t}dA\right\}^T\boldsymbol{\eta}=0\quad\boldsymbol{\eta}\in\mathcal{V}^d. \tag{2.38}$$

where $\mathcal{V}^d$ denotes the discretized version of the *virtual displacement* space, $\mathcal{V}$.

Since the above expression is satisfied for all admissible $\boldsymbol{\eta}$, the term within brackets has to disappear. Therefore, after some algebraic manipulation and some appropriate substitutions it is possible to obtain an equation which consists in a difference between the internal and external forces

$$\boldsymbol{f}^{int}-\boldsymbol{f}^{ext}=\boldsymbol{0}, \tag{2.39}$$

where these forces are defined by the following integrals:

$$\boldsymbol{f}^{int}=\int_{\varphi\left(\Omega_0^d\right)}\left(\boldsymbol{B}^g\right)^T\boldsymbol{\sigma}dV, \tag{2.40a}$$

$$\boldsymbol{f}^{ext}=\int_{\varphi\left(\Omega_0^d\right)}\left(\boldsymbol{N}^g\right)^T\boldsymbol{b}dV+\int_{\varphi\left(\partial\Omega_0^d\right)}\left(\boldsymbol{N}^g\right)^T\boldsymbol{t}dA. \tag{2.40b}$$

In current finite element procedures, the internal and external forces are computed within each finite element and then are assembled in the respective global vector:

$$\boldsymbol{f}^{int} = \bigcup_{e=1}^{n_{elem}} \left(\boldsymbol{f}_e^{int}\right), \tag{2.41a}$$

$$\boldsymbol{f}^{ext} = \bigcup_{e=1}^{n_{elem}} \left(\boldsymbol{f}_e^{ext}\right). \tag{2.41b}$$

In the previous equations, the symbol $\bigcup$ denotes an appropriated assembly operator. The element vectors of $\boldsymbol{f}_e^{int}$ and $\boldsymbol{f}_e^{ext}$ are given by:

$$\boldsymbol{f}_e^{int} = \int_{\varphi\left(\Omega_0^e\right)} \boldsymbol{B}^T \boldsymbol{\sigma} dV, \tag{2.42a}$$

$$\boldsymbol{f}^{ext} = \int_{\varphi\left(\Omega_0^e\right)} \boldsymbol{N}^T \boldsymbol{b} dV + \int_{\varphi\left(\partial\Omega_0^e\right)} \boldsymbol{N}^T \boldsymbol{t} dA. \tag{2.42b}$$

2.6.3 Temporal discretization

Besides a spatial discretization, the modelling of materials that have some kind of history dependence (e.g. strain-path or strain-rate dependent materials) also requires proper time discretization. Basically, the procedure for time discretization consists in dividing the overall time interval $[t_0, t]$ into $n+1$ steps and, for each time step, equilibrium must be satisfied.

In order to incorporate the history of the deformation into the constitutive equations which characterize the stress tensor, a set of internal variables, denoted by α, that are intrinsic with the type of material are required. Using, for instance, the *First Piola-Kirchhoff* stress tensor, for the instant t_{n+1}, this tensor is defined as

$$\boldsymbol{P}_{n+1} = \widehat{\boldsymbol{P}}\left\{\boldsymbol{F}_{n+1}, \alpha_n\right\}, \tag{2.43}$$

where $\widehat{\boldsymbol{P}}\left\{\boldsymbol{F}_{n+1}, \alpha_n\right\}$ is the *incremental constitutive functional*.

Introducing the *incremental constitutive functional* of $\boldsymbol{P}_{n+1}$ into Equation (2.31) and also performing the temporal discretization of the external forces, the *incremental mechanical quasi-static boundary value problem* is obtained which is described in what follows:

Given the set α_n of internal variables as well as the displacement field at time t_n, and knowing the forces $\boldsymbol{B}_{n+1}$ and $\boldsymbol{T}_{n+1}$ for the current time step, find the displacement field

$\boldsymbol{u}_{n+1}$ *such that*

$$\int_{\Omega_0} \left[\widehat{\boldsymbol{P}} \left\{ \boldsymbol{F}_{n+1}, \alpha_n \right\} : \nabla_{\boldsymbol{p}} \boldsymbol{\eta} - \boldsymbol{B}_{n+1}.\boldsymbol{\eta} \right] dV - \int_{\partial\Omega_0} \boldsymbol{T}_{n+1}.\boldsymbol{\eta} dA = 0 \tag{2.44}$$

is satisfied for any $\boldsymbol{\eta} \in \mathcal{V}$.

2.6.4 *Newton-Raphson* Method

In order to solve the equilibrium equation introduced in the previous section, a robust and efficient numerical method is required. Even though several methods may be used, the most popular and widely used by the computational mechanics community is the *Newton-Raphson* method. With this particular method it is possible to achieve quadratic convergence rates if it is correctly implemented.

A typical iteration j of this numerical method scheme consists in solving the linearised version of the equilibrium equation of the problem for the iterative global displacement vector, $\delta\boldsymbol{u}^{(j)}$:

$$\boldsymbol{K}^{(j-1)} \delta\boldsymbol{u}^{(j)} = -\boldsymbol{r}^{(j-1)}, \tag{2.45}$$

where $\boldsymbol{r}^{(j-1)}$ denotes the residual vector

$$\boldsymbol{r}^{(j-1)} = \boldsymbol{f}^{int} \left\{ \boldsymbol{u}_{n+1}^{(j-1)} \right\} - \boldsymbol{f}_{n+1}^{ext} \tag{2.46}$$

and $\boldsymbol{K}$ is the *global tangent stiffness matrix*:

$$\boldsymbol{K} = \left. \frac{\partial \boldsymbol{r}}{\partial \boldsymbol{u}_{n+1}} \right|_{\boldsymbol{u}_{n+1}^{(j-1)}}. \tag{2.47}$$

With the solution $\delta\boldsymbol{u}^{(j)}$ at hand, we perform the correction of the global displacement:

$$\boldsymbol{u}^{(j)} = \boldsymbol{u}^{(j-1)} + \delta\boldsymbol{u}^{(j)}. \tag{2.48}$$

This procedure is carried out until the convergence criterion is satisfied.

By definition, the global tangent stiffness is established through the linearisation of the problem. This procedure consists in finding out a closed form for the *directional derivative* of the equation which governs the equilibrium of the solid. In Appendix B.1, a summarized description of the directional derivative is introduced.

One of the main goals of the subsequent chapters of this document is to introduce a variational formulation for *coupled multi-scale models* at finite strains. The requisite of large deformations basically aims to describe the eventual presence of large rigid body

movements (rotations and translations) and therefore the stress tensor may be a functional dependent on the deformation gradient. In the following section, the linearisation of Equation (2.44) will be discussed.

2.6.4.1 Linearisation of the virtual work equilibrium equation

The typical unknown in a mechanical quasi-static equilibrium problem is the displacement field $\boldsymbol{u}$. Thus, according to the linearisation framework described in Appendix B.1, it is necessary to perform the perturbation of this field:

$$\boldsymbol{u}_\varepsilon = \boldsymbol{u} + \varepsilon\Delta\boldsymbol{u}. \tag{2.49}$$

Introducing $\boldsymbol{u}_\varepsilon$ into the definition of the deformation gradient, results the perturbed deformation gradient:

$$\boldsymbol{F}_\varepsilon = \boldsymbol{I} + \nabla_{\boldsymbol{p}}\left(\boldsymbol{u} + \varepsilon\Delta\boldsymbol{u}\right). \tag{2.50}$$

By definition, the directional derivative of Equation (2.44) is given by (for convenience, the notation associated with pseudo-time step was omitted as well as the internal variables):

$$\begin{aligned} DG\left(\boldsymbol{u}_\varepsilon, \boldsymbol{\eta}\right)[\Delta\boldsymbol{u}] &= \left.\frac{d}{d\varepsilon}\right|_{\varepsilon=0} \int_{\Omega_0} \left[\widehat{\boldsymbol{P}}\left\{\boldsymbol{F}_\varepsilon\right\} : \nabla_{\boldsymbol{p}}\boldsymbol{\eta} - \boldsymbol{B}.\boldsymbol{\eta}\right] dV - \int_{\partial\Omega_0} \boldsymbol{T}.\boldsymbol{\eta} dA \\ &= \left.\int_{\Omega_0} \frac{\partial\widehat{\boldsymbol{P}}\left\{\boldsymbol{F}_\varepsilon\right\}}{\partial\boldsymbol{F}_\varepsilon} : \frac{\partial\boldsymbol{F}_\varepsilon}{\partial\varepsilon} : \nabla_{\boldsymbol{p}}\boldsymbol{\eta} dV\right|_{\varepsilon=0} \\ &= \int_{\Omega_0} \mathbf{A} : \nabla_{\boldsymbol{p}}\Delta\boldsymbol{u} : \nabla_{\boldsymbol{p}}\boldsymbol{\eta} dV, \end{aligned} \tag{2.51}$$

where $\mathbf{A}$ is a fourth-order tensor widely known as *material* tangent modulus.

With the *material* version of the directional derivative of the equilibrium equation at hand, it is possible to obtain its *spatial* version. This is achieved introducing relations (2.28) and (2.29) into the previous equation, resulting:

$$DG\left(\boldsymbol{u}_\varepsilon, \boldsymbol{\eta}\right)[\Delta\boldsymbol{u}] = \int_{\varphi(\Omega_0)} \frac{1}{J}\mathbf{A} : \left(\nabla_{\boldsymbol{x}}\Delta\boldsymbol{u}\boldsymbol{F}\right) : \left(\nabla_{\boldsymbol{x}}\boldsymbol{\eta}\boldsymbol{F}\right) dV. \tag{2.52}$$

The previous equation can be rearranged in the following fashion

$$DG\left(\boldsymbol{u}_\varepsilon, \boldsymbol{\eta}\right)[\Delta\boldsymbol{u}] = \int_{\varphi(\Omega_0)} \frac{1}{J}\mathbf{a} : \left(\nabla_{\boldsymbol{x}}\Delta\boldsymbol{u}\boldsymbol{F}\right) : \left(\nabla_{\boldsymbol{x}}\boldsymbol{\eta}\boldsymbol{F}\right) dV, \tag{2.53}$$

where $\mathbf{a}$ is the *spatial* tangent modulus defined by the following expression

$$a_{ijkl} = \frac{1}{J} A_{imkn} F_{jm} F_{ln}. \tag{2.54}$$

Taking into account the different forms to describe the stress tensor in a solid,one can write

$$\begin{aligned} A_{imkn} &= \frac{\partial}{\partial F_{kn}} \left(\tau_{ip} F^{-1}_{mp} \right) \\ &= \frac{\partial \tau_{ip}}{\partial F_{kn}} F^{-1}_{mp} + \tau_{ip} \frac{\partial F^{-1}_{mp}}{\partial F_{kn}}, \end{aligned} \tag{2.55}$$

and, with the following relation at hand [73]

$$\frac{\partial F^{-1}_{mp}}{\partial F_{kn}} = -F^{-1}_{mk} F^{-1}_{np}, \tag{2.56}$$

we obtain

$$A_{imkn} = \frac{\partial \tau_{ip}}{\partial F_{kn}} F^{-1}_{mp} - \tau_{ip} F^{-1}_{mk} F^{-1}_{np}. \tag{2.57}$$

Finally, introducing the previous equation into (2.54) and after a straightforward algebra manipulation, we obtain a closed-form for the spatial tangent modulus, $\mathbf{a}$,

$$a_{ijkl} = \frac{1}{J} \frac{\partial \tau_{ij}}{\partial F_{km}} F^{-1}_{lm} - \sigma_{il} \delta_{jk}, \tag{2.58}$$

where δ_{jk} denotes the *Kronecker* delta.

2.6.5 Pseudo-code of finite element method

In order to conclude the presentation of the finite element method, in Table 2.1 the global structure of a finite element code in a pseudo-format is presented. We emphasize that further information as well as further details concerned to programming of a finite element code may be found in [6] where a "bridge" between theory and implementation is well described.

2.7 Conclusions

So far, the main concepts within *Continuum Solid Mechanics* and suitable numerical tools which will be widely used either to formulate or implement/program a coupled multi-scale model have been addressed and discussed throughout this chapter.

TABLE 2.1: *Newton-Raphson* algorithm for solution of the incremental Finite Element Method [6].

1. Initialize some variables for $j = 1$ (*Newton-Raphson* iteration counter)

$$\boldsymbol{u}_{n+1}^{(j)} = \boldsymbol{u}_n \qquad \boldsymbol{r}^{(j)} = \boldsymbol{f}_{n+1}^{int}(\boldsymbol{u}_n) - \lambda_{n+1}\boldsymbol{f}^{ext}$$

   where $\boldsymbol{r}$ is residual equation and λ_{n+1} is the prescribed load factor at instant t_{n+1}.

2. Increment the counter

$$j = j + 1$$

3. Compute the stiffness matrix;

$$\boldsymbol{K}_T^{(j)} = \frac{\partial \boldsymbol{r}^{(j)}}{\partial \boldsymbol{u}_{n+1}^{(j)}}$$

4. Compute the iterative displacement vector, $\delta\boldsymbol{u}^{(j+1)}$;

$$\boldsymbol{K}_T^{(j)}\delta\boldsymbol{u}^{(j+1)} = -\boldsymbol{r}^{(j)}$$

5. Update the global displacements, $\boldsymbol{u}_{n+1}^{(j+1)}$;

$$\boldsymbol{u}_{n+1}^{(j+1)} = \boldsymbol{u}_{n+1}^{(j)} + \delta\boldsymbol{u}^{(j+1)}$$

6. Update the deformation gradient, $\boldsymbol{F}_{n+1}^{(j+1)}$;

$$\boldsymbol{F}_{n+1}^{(j+1)} = \left(\boldsymbol{I} - \nabla_{\boldsymbol{x}}\boldsymbol{u}_{n+1}^{(j+1)}\right)^{-1}$$

7. Update stress tensor and internal variables;

$$\boldsymbol{\sigma}_{n+1}^{(j+1)} = \boldsymbol{\sigma}\left\{\boldsymbol{F}_{n+1}^{(j+1)}, \boldsymbol{\alpha}_n\right\} \qquad \boldsymbol{\alpha}_{n+1}^{(j+1)} = \widehat{\boldsymbol{\alpha}}\left\{\boldsymbol{F}_{n+1}^{(j+1)}, \boldsymbol{\alpha}_n\right\}$$

   where $\widehat{\boldsymbol{\alpha}}$ denotes an incremental functional which governs the evolution of $\boldsymbol{\alpha}$.

8. Compute internal forces vector, $\boldsymbol{f}^{int}\left\{\boldsymbol{u}_{n+1}^{(j+1)}\right\}$;

$$\boldsymbol{f}^{int}\left\{\boldsymbol{u}_{n+1}^{(j+1)}\right\} = \bigcup_{e=1}^{N_{elem}} \boldsymbol{f}_e^{int}\left\{\boldsymbol{u}_{n+1}^{(j+1)}\right\}$$

9. Compute the residual vector, $\boldsymbol{r}^{(j+1)}$;

$$\boldsymbol{r}^{(j+1)} = \boldsymbol{f}^{int}\left\{\boldsymbol{u}_{n+1}^{(j+1)}\right\} - \lambda_{n+1}\boldsymbol{f}^{ext}$$

10. Check the convergence.

    `IF CONV<TOL THEN` New increment `ELSE` Go to item 2) `END IF`

Chapter 3

Fundamental Principles of Coupled Multi-Scale Models

3.1 Introduction

Independently of the material, its behaviour and their global properties are deeply dependent on its microstructure. Nevertheless, this dependence may be more significant or not according to several factors such as manufacturing process, external loadings and conditions (temperature, humidity).

Aiming to incorporate the effects originated by the microstructure on the global properties of the material, some approaches as well as methods have been developed within the science and academic community. One of those methods, which has gained a notable popularity, is the *Coupled Multi-Scale Method*. The success of this tool relies on the fact that it is generic and universal for all kind of materials. This means that, having formulated a *Coupled Multi-Scale Model*, all kind of microstructures of a wide range of materials may be conveniently and properly treated.

Based on a *variational formulation*, in the present chapter, the fundamental steps necessary to formulate a *First-Order Coupled Multi-Scale Model* will be addressed and discussed.

3.2 General Concepts of Multi-Scale Constitutive Models

In this section, the main principles and governing equations employed in the development of *First-Order Coupled Multi-Scale Models* at finite strains will be briefly reviewed.

A more comprehensive account can be found in references [37, 74–78]. Before we proceed, we will introduce the notation used throughout the present document. In what follows, $\boldsymbol{x}$ will denote a generic infinitesimal point at the deformed macro-scale domain and $\boldsymbol{y}$ represents an infinitesimal point at the deformed fine scale. For example, following this notation, $\boldsymbol{A}\{\boldsymbol{x}\}$ and $\boldsymbol{A}\{\boldsymbol{y}\}$ denote a generic parameter, field or tensor respectively defined at the coarse and fine scales. In turn, capital letters $\boldsymbol{X}$ and $\boldsymbol{Y}$ denote coordinates of a generic point at the undeformed macro and micro domains respectively. The notation used is schematically represented in Figure 3.1.

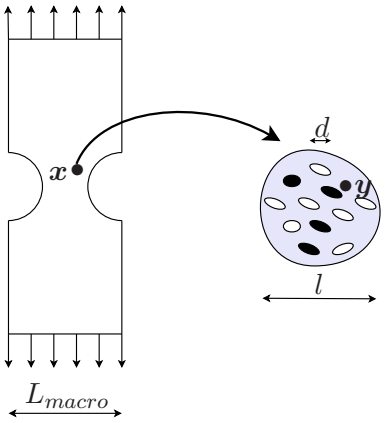

FIGURE 3.1: Definition of scales.

The development of a coupled multi-scale model starts from the assumption that, in a generic solid it is possible to identify and distinguish different scales. In fact, this assumption is valid for the majority of natural and engineering materials. Based on this aspect and in order to taken into account information from the different spatial scales, the coupled multi-scale model assumes that at any point $\boldsymbol{x}$ (macro-scale) there is an associated *Representative Volume Element* (RVE) that satisfies the *scale separation* principle. This statement implies that, the average size of the singularities and heterogeneities present in the RVE, d (Figure 3.1), is much smaller than the characteristic length of the RVE, l. It is noteworthy mentioning that this last parameter has to be smaller than the characteristic size of the macro-scale, L. These three parameters are related by the following inequality:

$$d \ll l \ll L. \tag{3.1}$$

In addition, in order to ensure that at the micro-scale the continuum hyphothesis is applicable, l must be large enough when compared with the atomic structures. Some publications have shed some light on the effects that these parameters have on the global response of the RVE. Relevant and notable contributions on this topic can be found in references [52, 79–83] and more recently in [84].

3.2.1 Averaging procedures

Within the context of coupled multi-scale models, the averaging procedures play a critical role on the definition of stress and deformation quantities. Hence, for a generic macroscopic point and at any instant in time t, the macroscopic deformation gradient, $\boldsymbol{F}\{\boldsymbol{x},t\}$, and the *First Piola-Kirchhoff* stress tensor, $\boldsymbol{P}\{\boldsymbol{x},t\}$, are defined as the volume average of their microscopic counterparts, $\boldsymbol{F}\{\boldsymbol{y},t\}$ and $\boldsymbol{P}\{\boldsymbol{y},t\}$ respectively, over the undeformed configuration of the RVE:

$$\boldsymbol{F}\{\boldsymbol{x},t\} = \frac{1}{V_0}\int_{\Omega_0} \boldsymbol{F}\{\boldsymbol{y},t\}\, dV = \boldsymbol{I} + \frac{1}{V_0}\int_{\Omega_0} \nabla_{\boldsymbol{p}}\boldsymbol{u}\{\boldsymbol{y},t\}\, dV, \tag{3.2}$$

$$\begin{aligned}\boldsymbol{P}\{\boldsymbol{x},t\} = \frac{1}{V_0}\int_{\Omega_0} \boldsymbol{P}\{\boldsymbol{y},t\}\, dV = \frac{1}{V_0}\int_{\partial\Omega_0} \boldsymbol{T}^{ref}\{\boldsymbol{y},t\}\otimes\boldsymbol{Y}\, dA \\ - \frac{1}{V_0}\int_{\Omega_0} \boldsymbol{B}^{ref}\{\boldsymbol{y},t\}\otimes\boldsymbol{Y}\, dV,\end{aligned} \tag{3.3}$$

where V_0 denotes the volume of the undeformed RVE, $\boldsymbol{I}$ is the second order identity tensor and Ω_0 represents the undeformed microscopic integration domain. In Equation (3.2) and in what follows, the symbol $\nabla_{\boldsymbol{p}}$ denotes the material gradient operator. Furthermore, $\boldsymbol{T}^{ref}\{\boldsymbol{y},t\}$ and $\boldsymbol{B}^{ref}\{\boldsymbol{y},t\}$ (see Equation (3.3)) denote, respectively, the reference boundary traction force and the reference body force fields of the RVE.

3.2.2 Definition of the microscopic displacement field

Without loss of generality, the displacement field at the micro-scale, $\boldsymbol{u}\{\boldsymbol{y},t\}$, may be split in the following fashion:

$$\boldsymbol{u}\{\boldsymbol{y},t\} = [\boldsymbol{F}\{\boldsymbol{x},t\} - \boldsymbol{I}]\,\boldsymbol{Y} + \widetilde{\boldsymbol{u}}\{\boldsymbol{y},t\}\,, \tag{3.4}$$

where the first term on the right hand side is the *Linear displacement* (varies linearly with $\boldsymbol{Y}$ - *reference coordinates* of the RVE) and the second one is the *displacement fluctuation* denoted by $\widetilde{\boldsymbol{u}}\{\boldsymbol{y},t\}$.

With the present definitions of the microscopic displacement field (Equation (3.4)) and the macroscopic deformation gradient (Equation (3.2)), can one define the *minimal kinematical admissible constraint*:

$$\int_{\partial\Omega_0} \widetilde{\boldsymbol{u}}\{\boldsymbol{y},t\}\otimes\boldsymbol{N}\{\boldsymbol{Y}\}\, dA = \boldsymbol{0}, \tag{3.5}$$

where $\boldsymbol{N}\{\boldsymbol{Y}\}$ denotes the outward unit vector to the undeformed boundary $\partial\Omega_0$ of the RVE.

3.2.3 Equilibrium of the RVE

Under the assumption of finite strains, the strong form of the equilibrium problem at the micro-scale is given by the following system of equations

$$\begin{cases} div\boldsymbol{P}\left\{\boldsymbol{y},t\right\}+\boldsymbol{B}^{ref}\left\{\boldsymbol{y},t\right\}=\boldsymbol{0} & \forall\ \boldsymbol{y}\in\Omega_0, \\ \boldsymbol{P}\left\{\boldsymbol{y},t\right\}\boldsymbol{N}\left\{\boldsymbol{Y}\right\}+\boldsymbol{T}^{ref}\left\{\boldsymbol{y},t\right\}=\boldsymbol{0} & \forall\ \boldsymbol{y}\in\partial\Omega_0, \end{cases} \tag{3.6}$$

where $div\,(*)$ denotes the *divergence* operator. The weak format of the micro-equilibrium problem can be defined by means of the virtual work principle, giving rise to the following expression

$$\begin{aligned} \int_{\Omega_0}\boldsymbol{P}\left\{\boldsymbol{y},t\right\}:\nabla\boldsymbol{\eta}dV-\int_{\Omega_0}\boldsymbol{B}^{ref}\left\{\boldsymbol{y},t\right\}.\boldsymbol{\eta}dV \\ -\int_{\partial\Omega_0}\boldsymbol{T}^{ref}\left\{\boldsymbol{y},t\right\}.\boldsymbol{\eta}dA=0\ \forall\ \boldsymbol{\eta}\ \in\ \mathcal{V}. \end{aligned} \tag{3.7}$$

The symbol $\mathcal{V}$ represents the space of the virtual admissible displacement fluctuation field, $\boldsymbol{\eta}$. Here, for simplicity, we have assumed that internal traction forces arising from frictional contact on crack surfaces or internal pressure of fluids contained within RVE voids have been ommited. They can, however, be incorporated into the theory.

3.2.4 *Hill-Mandel* Principle

A fundamental concept in multi-scale constitutive theories is the *Hill-Mandel* principle of *Macro-Homogeneity* [12, 85]. This principle requires the macroscopic stress power to equal the volume average of the microscopic stress power over Ω_0, establishing the bridge between scales:

$$\boldsymbol{P}\left\{\boldsymbol{x},t\right\}:\dot{\boldsymbol{F}}\left\{\boldsymbol{x},t\right\}=\frac{1}{V_0}\int_{\Omega_0}\boldsymbol{P}\left\{\boldsymbol{y},t\right\}:\dot{\boldsymbol{F}}\left\{\boldsymbol{y},t\right\}dV, \tag{3.8}$$

which can be equivalently re-written in terms of the RVE boundary traction force, $\boldsymbol{T}^{ref}\left\{\boldsymbol{y},t\right\}$, and body force, $\boldsymbol{B}^{ref}\left\{\boldsymbol{y},t\right\}$, fields:

$$\int_{\partial\Omega_0}\boldsymbol{T}^{ref}\left\{\boldsymbol{y},t\right\}.\boldsymbol{\eta}dA=0\ \ \forall\,\boldsymbol{\eta}\ \in\ \mathcal{V}, \tag{3.9}$$

$$\int_{\Omega_0}\boldsymbol{B}^{ref}\left\{\boldsymbol{y},t\right\}.\boldsymbol{\eta}dV=0\ \ \forall\,\boldsymbol{\eta}\ \in\ \mathcal{V}. \tag{3.10}$$

With the previous result at hand, a crucial conclusion can be drawn from the *Hill-Mandel* principle: the body and traction forces are, in fact, reaction forces associated

to the enforced kinematical constraints applied to $\widetilde{\boldsymbol{u}}\{\boldsymbol{y},t\}$ at the boundary of the RVE, $\partial\Omega_0$.

3.2.5 Macroscopic equilibrium problem

A generic multi-scale constitutive model is obtained from the solution of the RVE equilibrium problem (Equation (3.7)) in which the constraints associated to the *Hill-Mandel* principle are taken into account, for a given macroscopic deformation gradient. After finding the solution for $\widetilde{\boldsymbol{u}}\{\boldsymbol{y},t\}$, the macroscopic stress tensor, $\boldsymbol{P}\{\boldsymbol{x},t\}$, is computed according to the averaging relation (3.3). At the macro-scale, the equilibrium of the problem is therefore defined by:

$$\begin{aligned}\int_{\Theta_0}\left[\frac{1}{V_0}\int_{\Omega_0}\boldsymbol{P}\{\boldsymbol{y},t\}\,dV\right]:\nabla_{\boldsymbol{p}}\boldsymbol{\zeta}dV-\int_{\Theta_0}\boldsymbol{B}^{ref}\{\boldsymbol{x},t\}.\boldsymbol{\zeta}dV\\-\int_{\partial\Theta_0}\boldsymbol{T}^{ref}\{\boldsymbol{x},t\}.\boldsymbol{\zeta}dA=0\;\forall\;\boldsymbol{\zeta}\in\mathcal{U},\end{aligned}\tag{3.11}$$

where Θ_0 corresponds to the undeformed macroscopic integration domain where the macroscopic equilibrium equation needs to be satisfied and $\mathcal{U}$ is the space of the virtual displacement at the macro-scale domain, $\boldsymbol{\zeta}$. In turn, $\boldsymbol{T}^{ref}\{\boldsymbol{x},t\}$ and $\boldsymbol{B}^{ref}\{\boldsymbol{x},t\}$ denote the external traction force and the body force fields respectively defined over the undeformed configuration of the macroscopic solid. The solution of a multi-scale constitutive model, in the present context, requires the nested solution of equations (3.7) and (3.11), which establish the equilibrium at both scales.

3.2.6 Admissible kinematical boundary conditions

Three distinct kinematical boundary constraints have been most commonly adopted within multi-scale constitutive models: *Linear*, *Periodic* and *Uniform Traction* boundary conditions. In what follows, a brief revision of these three boundary constraints will be introduced.

3.2.6.1 Linear Boundary Condition

The *Linear* boundary condition assumes that at the boundary of the RVE, the displacement fluctuation field is null:

$$\widetilde{\boldsymbol{u}}\{\boldsymbol{y},t\}=\boldsymbol{0}\quad\forall\quad\boldsymbol{y}\in\partial\Omega.\tag{3.12}$$

Thus, the *minimal kinematical admissible constraint* (Equation (3.5)) as well as the first *Hill-Mandel*'s condition (Equation (3.9)) are automatically satisfied. Nevertheless, the second *Hill-Mandel*'s condition (Equation (3.10)) is only satisfied if $\boldsymbol{B}^{ref}\left\{\boldsymbol{y},t\right\}=\boldsymbol{0}$, revealing that the deformation of the RVE occurs in the absence of body forces and accelerations.

3.2.6.2 Periodic Boundary Condition

This kinematical constraint requires that the boundary of the RVE is always divided into positive, Γ^{+} and negative parts Γ^{-}, such that each point $\boldsymbol{y}^{+}\in\Gamma_{i}^{+}$ has its counterpart point $\boldsymbol{y}^{-}\in\Gamma_{i}^{-}$ with associated outward normal vector $\boldsymbol{n}^{+}=-\boldsymbol{n}^{-}$ (Figure 3.2). Thus,

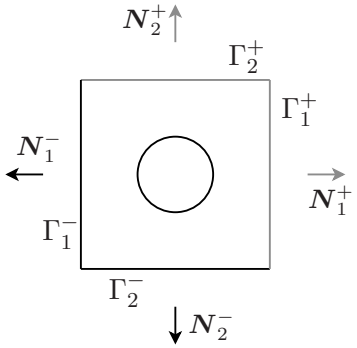

FIGURE 3.2: Decomposition of the boundary of the RVE for *Periodic* boundary condition.

the *Periodic* boundary condition is expressed by a periodic displacement fluctuation field and an anti-periodic traction field:

$$\widetilde{\boldsymbol{u}}\left\{\boldsymbol{y}^{+},t\right\}=\widetilde{\boldsymbol{u}}\left\{\boldsymbol{y}^{-},t\right\}, \tag{3.13}$$

$$\boldsymbol{T}^{ref}\left\{\boldsymbol{Y}^{+},t\right\}=-\boldsymbol{T}^{ref}\left\{\boldsymbol{Y}^{-},t\right\}. \tag{3.14}$$

With the two relations above introduced, we trivially conclude that the first *Hill-Mandel*'s condition (Equation (3.9)) and the *minimal kinematical admissible constraint* (Equation (3.5)) are satisfied. Similar to what happens with *Linear* boundary conditions, the *Hill-Mandel* condition inherent with volume body forces (Equation (3.10)) is only satisfied if $\boldsymbol{B}^{ref}\left\{\boldsymbol{y},t\right\}=\boldsymbol{0}$.

3.2.6.3 Uniform Traction Condition

The *Uniform Traction* boundary constraint is based on the *minimal kinematical admissible constraint* (Equation 3.5)) which is recovered here for convenience:

$$\int_{\partial\Omega_0} \widetilde{\boldsymbol{u}}\left\{\boldsymbol{y},t\right\} \otimes \boldsymbol{N}\left\{\boldsymbol{Y}\right\} dA = \boldsymbol{0}. \tag{3.15}$$

Once again, the *Hill-Mandel* condition associated with body forces (Equation (3.10)) is only satisfied if $\boldsymbol{B}^{ref}\left\{\boldsymbol{y},t\right\} = \boldsymbol{0}$. Under the assumption of the minimally constraint for the displacement fluctuation field and taking into account expression (3.9) related to the *Hill-Mandel* principle, it is possible to demonstrate that the traction over the RVE's border is uniform and equal to the traction of the average stress:

$$\boldsymbol{P}\left\{\boldsymbol{y},t\right\}\boldsymbol{N}\left\{\boldsymbol{y},t\right\} = \boldsymbol{P}\left\{\boldsymbol{x},t\right\}\boldsymbol{N}\left\{\boldsymbol{y},t\right\}. \tag{3.16}$$

It is for this reason that this boundary condition, which starts from the assumption of the *minimal kinematical admissible constraint*, is known as *Uniform Traction* Boundary Condition [86].

3.2.7 Remarks on the different boundary conditions

The boundary conditions previously introduced can be hierarchically sorted starting by the lowest constraint condition to the highest one. In this context, results the following order which starts with the *Uniform Traction* boundary condition followed by *Periodic* boundary condition and ended with *Linear* constraint. It is also noteworthy to mention that, among these three boundary constraints, some authors argue that *Periodic* boundary condition is the one which converges faster to the theoretical/effective solution. In others words, this means that for the same RVE size, it is the *Periodic* boundary condition which origins the closest result to the effective value [87, 88]. Note that, in the limit, when the size of the RVE reaches a certain dimension, the results obtained with the three above mentioned boundary constraints will coincide.

It is also noteworthy to mention a relevant aspect concerned to the *Uniform Traction* boundary constraint. Since this kinematical constraint is based on the *minimal kinematical admissible constraint* (Equation 3.5)) in some cases, particularly when large deformations of the RVE are involved, *spurious* effects may appear as reported by [63]. As a consequence, in these situations the result obtained are unrealistic not having a physical meaning.

Remark 3.1. As previously pointed out, in order to satisfy the *Hill-Mandel* principle, the body forces, $\boldsymbol{B}^{ref}\left\{\boldsymbol{y},t\right\}$, need to be equal to zero for both *Linear*, *Periodic* and

Uniform Traction boundary conditions. Therefore, Equation (3.3) can be re-written as:

$$\boldsymbol{P}\{\boldsymbol{x},t\} = \frac{1}{V_0}\int_{\Omega_0} \boldsymbol{P}\{\boldsymbol{y},t\}\, dV = \frac{1}{V_0}\int_{\partial\Omega_0} \boldsymbol{T}^{ref}\{\boldsymbol{Y},t\} \otimes \boldsymbol{Y}\, dA. \tag{3.17}$$

3.3 Numerical approximation

In this section, several numerical aspects required for the computational implementation of *First-Order Coupled Multi-Scale Models* within a generic non-linear implicit finite element framework at finite strains will be discussed.

3.3.1 The incremental equilibrium problem

In general, the constitutive characterization of the RVE constituents and phases can be performed by means of conventional internal variable-based dissipative constitutive models, which are described by a set of ordinary differential equations. Among others, the elasto-plastic and visco-plastic models are very often adopted for the task. For these cases, numerical approximations based on *Euler*-type methods (for more details see [6, 89–91]) to integrate the constitutive equations of the model are widely used.

Considering a typical time interval (or pseudo-time), $[t_n, t_{n+1}]$, and knowing the set of internal variables $\boldsymbol{\beta}_n\{\boldsymbol{y}\}$ at t_n, the updated stress tensor at the fine-scale domain, $\boldsymbol{P}_{n+1}\{\boldsymbol{y}\}$ at t_{n+1}, is a function of the microscopic deformation gradient $\boldsymbol{F}_{n+1}\{\boldsymbol{y}\}$. This relation can be symbolically represented by:

$$\boldsymbol{P}_{n+1}\{\boldsymbol{y}\} = \hat{\boldsymbol{P}}\left\{\boldsymbol{F}_{n+1}\{\boldsymbol{y}\}, \boldsymbol{\beta}_n\{\boldsymbol{y}\}\right\}, \tag{3.18}$$

where $\hat{\boldsymbol{P}}$ denotes a generic algorithm intrinsic with the constitutive model selected.

The last expression leads to the definition of the incremental version of the homogenized stress tensor:

$$\boldsymbol{P}_{n+1}\{\boldsymbol{x}\} = \frac{1}{V_0}\int_{\Omega_0} \hat{\boldsymbol{P}}\left\{\boldsymbol{F}_{n+1}\{\boldsymbol{y}\}, \boldsymbol{\beta}_n\{\boldsymbol{y}\}\right\} dV. \tag{3.19}$$

Based on the definition of the deformation gradient and considering once more the definition of the microscopic displacement field (Equation (3.4)), the previous equation can be re-written as

$$\boldsymbol{P}_{n+1}\{\boldsymbol{x}\} = \frac{1}{V_0}\int_{\Omega_0} \hat{\boldsymbol{P}}\left\{\boldsymbol{F}_{n+1}\{\boldsymbol{x}\} + \nabla_{\boldsymbol{p}}\widetilde{\boldsymbol{u}}_{n+1}\{\boldsymbol{y}\}, \boldsymbol{\beta}_n\{\boldsymbol{y}\}\right\} dV. \tag{3.20}$$

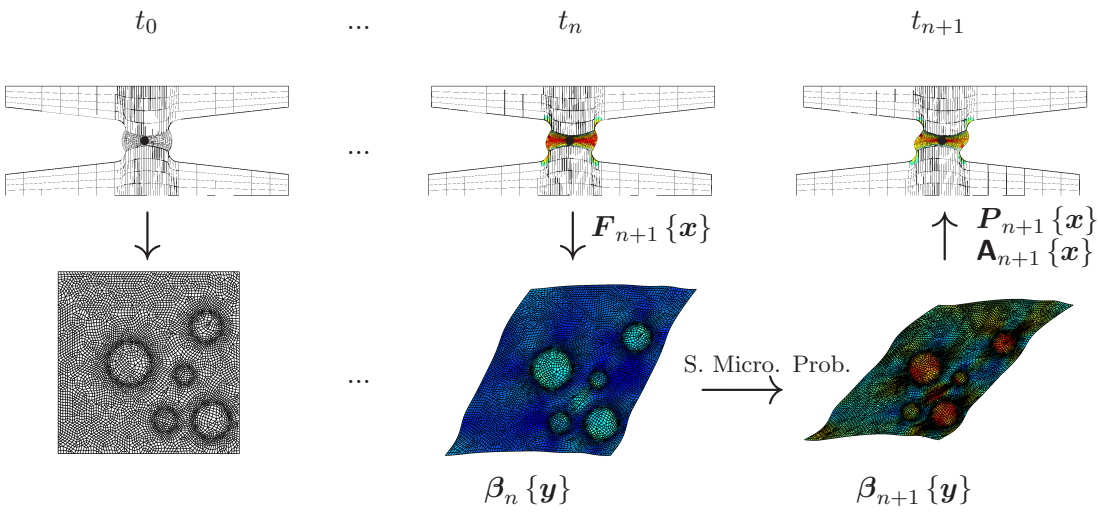

FIGURE 3.3: Schematic illustration of a homogenization-based coupled multi-scale model.

Taking into account the constraints imposed by the *Hill-Mandel* principle (Equations (3.9) and (3.10)), the final time-discrete version of the micro-equilibrium problem (Equation (3.7)) is simply given by:

$$\int_{\Omega_0} \hat{\boldsymbol{P}}\left\{\boldsymbol{F}_{n+1}\{\boldsymbol{x}\} + \nabla_{\boldsymbol{p}}\widetilde{\boldsymbol{u}}_{n+1}\{\boldsymbol{y}\}, \boldsymbol{\beta}_n\{\boldsymbol{y}\}\right\} : \nabla\boldsymbol{\eta} dV = 0 \;\forall\; \boldsymbol{\eta} \in \mathcal{V}. \tag{3.21}$$

On the other hand, the temporal discretization of Equation (3.11) follows the same strategy as used in a conventional solid mechanical problem, distinguishing solely on the approach used to determine the stress tensor in a generic point at the macro-scale. Therefore, considering once again the time interval $[t_n, t_{n+1}]$, the discrete time version of Equation (3.11) is given by:

$$\begin{aligned}\int_{\Theta_0} \left[\frac{1}{V_0}\int_{\Omega_0} \hat{\boldsymbol{P}}\left\{\boldsymbol{F}_{n+1}\{\boldsymbol{x}\} + \nabla_{\boldsymbol{p}}\widetilde{\boldsymbol{u}}_{n+1}\{\boldsymbol{y}\}, \boldsymbol{\beta}_n\{\boldsymbol{y}\}\right\} dV\right] : \nabla_{\boldsymbol{p}}\boldsymbol{\zeta} dV \\ - \int_{\Theta_0} \boldsymbol{B}^{ref}_{n+1}\{\boldsymbol{x}\}.\boldsymbol{\zeta} dV - \int_{\partial\Theta_0} \boldsymbol{T}^{ref}_{n+1}\{\boldsymbol{x}\}.\boldsymbol{\zeta} dA = 0 \;\forall\; \boldsymbol{\zeta} \in \mathcal{U}.\end{aligned} \tag{3.22}$$

In order to make the temporal discretization (which has to be performed simultaneously at both spatial domains) as clear as possible, a schematic representation of a *First-Order Coupled Multi-Scale* model is presented in Figure 3.3.

In this context, in the course of the macro-scale solution governed by Equation (3.22), the macroscopic stress tensor, $\boldsymbol{P}_{n+1}\{\boldsymbol{x}\}$, at a point $\boldsymbol{x}$ is extracted from the RVE by subjecting the RVE to the macroscopic deformation gradient, $\boldsymbol{F}_{n+1}\{\boldsymbol{x}\}$. In addition to $\boldsymbol{P}_{n+1}\{\boldsymbol{x}\}$, it is also necessary to extract the macroscopic tangent, $\mathbf{A}_{n+1}\{\boldsymbol{x}\}$, which will be described in Section 3.3.2.6. Since there is no explicit constitutive formulation at the

macro-scale, the set of internal variables, $\boldsymbol{\beta}_n \{\boldsymbol{y}\}$, is only known for each microstructural point through the micro-scale constitutive formulation.

Remark 3.2. It is noteworthy to mention that, in this work, a *Total Lagrangian* formulation was adopted and, as a consequence, all parameters and variables are defined with regard to the initial configuration in both spatial domains.

3.3.2 Finite element approximation

The final step required to numerically implement a *First-Order Coupled Multi-Scale Model* consists in performing the spatial discretization at both domains: macro and micro. For this purpose, the well established *Finite Element Method* is considered.

3.3.2.1 Micro-scale discretization.

The finite element discretized version of Equation (3.21) is obtained by replacing the functional set $\mathcal{V}$ with a discrete counterpart, $\mathcal{V}^d$, composed by the finite element shape functions of a mesh d, and the domain Ω_0 is replaced with an approximated counterpart Ω_0^d, composed by the assembly of finite element domains,

$$\int_{\Omega_0^d} \boldsymbol{G}^T \hat{\boldsymbol{P}} \left\{ \boldsymbol{F}_{n+1} \{\boldsymbol{x}\} + \boldsymbol{G}\widetilde{\boldsymbol{u}}_{n+1} \{\boldsymbol{y}\}, \boldsymbol{\beta}_n \{\boldsymbol{y}\} \right\} . \boldsymbol{\eta} dV = 0 \; \forall \; \boldsymbol{\eta} \; \in \; \mathcal{V}^d, \tag{3.23}$$

where $\boldsymbol{G}$ denotes the global discrete gradient matrix containing the shape functions derivatives and $\hat{\boldsymbol{P}}$ is the incremental constitutive model at the RVE level that computes the array of *First Piola-Kirchhoff* stress components, $\boldsymbol{P}_{n+1} \{\boldsymbol{y}\}$. Since the previous equation is satisfied for all admissible vectors $\boldsymbol{\eta}$, Equation (3.23) can be reduced to the following expression:

$$\boldsymbol{f}^{int} \{\boldsymbol{u}_{n+1} \{\boldsymbol{y}\}\} = \boldsymbol{0}. \tag{3.24}$$

where $\boldsymbol{f}^{int} \{\boldsymbol{u}_{n+1} \{\boldsymbol{y}\}\}$ is the internal force vector.

The *Newton-Raphson* method is adopted due to its quadratic asymptotic rate of convergence for the solution of the problem at the fine scale. However, this requires the proper linearization of the microscopic discretized variational equilibrium Equation (3.24), which in the present case leads to:

$$\boldsymbol{f}^{int} \{\boldsymbol{u}_{n+1} \{\boldsymbol{y}\}\}^{(j)} + \boldsymbol{K}_T \{\boldsymbol{u}_{n+1} \{\boldsymbol{y}\}\}^{(j)} \delta\widetilde{\boldsymbol{u}} \{\boldsymbol{y}\}^{(j+1)} = \boldsymbol{0}, \tag{3.25}$$

where $\boldsymbol{K}_T \{\boldsymbol{u}_{n+1} \{\boldsymbol{y}\}\}$ denotes the RVE global stiffness matrix. In the previous equation, (j) denotes the iteration number of the *Newton-Raphson* method at the micro-scale

and $\delta\widetilde{\boldsymbol{u}}\{\boldsymbol{y}\}^{(j+1)}$ is the unknown iterative nodal displacement fluctuation vector. With $\delta\widetilde{\boldsymbol{u}}\{\boldsymbol{y}\}^{(j+1)}$ at hand, the total displacement fluctuation field for $(j+1)$ is given by:

$$\widetilde{\boldsymbol{u}}_{n+1}^{(j+1)}\{\boldsymbol{y}\} = \widetilde{\boldsymbol{u}}_{n+1}^{(j)}\{\boldsymbol{y}\} + \delta\widetilde{\boldsymbol{u}}^{(j+1)}\{\boldsymbol{y}\}\,. \tag{3.26}$$

3.3.2.2 Micro-scale discretized kinematical constraints.

It is noteworthy mentioning that Equation (3.25) is generic and does not take into account the constraints enforced on the boundary. Thus, in the following, a generic numerical framework will be introduced, which can be used to solve the equilibrium problem at the micro-scale for a wide variety of admissible kinematical boundary conditions.

Without loss of generality, the displacement fluctuation field $\widetilde{\boldsymbol{u}}\{\boldsymbol{y}\}$ may be decomposed in its respective *free* $\widetilde{\boldsymbol{u}}^{f}\{\boldsymbol{y}\}$, *independent* $\widetilde{\boldsymbol{u}}^{i}\{\boldsymbol{y}\}$, *dependent* $\widetilde{\boldsymbol{u}}^{d}\{\boldsymbol{y}\}$ and *prescribed* $\widetilde{\boldsymbol{u}}^{p}\{\boldsymbol{y}\}$ counterparts:

$$\widetilde{\boldsymbol{u}}\{\boldsymbol{y}\}^{T} = \left\{\begin{array}{c:c:c:c} \widetilde{\boldsymbol{u}}^{f} & \widetilde{\boldsymbol{u}}^{i} & \widetilde{\boldsymbol{u}}^{d} & \widetilde{\boldsymbol{u}}^{p} \end{array}\right\}^{T}. \tag{3.27}$$

The *free* sub-domain corresponds to the degrees of freedom in the interior of the RVE and all others are related with the degrees of freedom at the boundary of the RVE. The sub-domain $\widetilde{\boldsymbol{u}}^{d}$ is associated with $\widetilde{\boldsymbol{u}}^{i}$ and can generically be expressed by a linear relation between these two parts:

$$\widetilde{\boldsymbol{u}}^{d}\{\boldsymbol{y}\} = \boldsymbol{\alpha}.\widetilde{\boldsymbol{u}}^{i}\{\boldsymbol{y}\}\,. \tag{3.28}$$

In the previous equation, $\boldsymbol{\alpha}$ denotes the dependency matrix, which is defined according to the boundary constraint adopted.

At the fine scale, the internal forces are a consequence of the displacement fluctuation field, $\widetilde{\boldsymbol{u}}\{\boldsymbol{y}\}$, and, therefore, the same decomposition can be performed:

$$\boldsymbol{f}\{\boldsymbol{y}\}^{T} = \left\{\begin{array}{c:c:c:c} \boldsymbol{f}^{f} & \boldsymbol{f}^{i} & \boldsymbol{f}^{d} & \boldsymbol{f}^{p} \end{array}\right\}^{T}. \tag{3.29}$$

Introducing the previous two relations (Equations (3.27) and (3.29)) into Equation (3.25) and performing the same decomposition to the global stiffness matrix of the RVE, results:

$$\left\{\begin{array}{c:c:c:c} \boldsymbol{f}^{f} & \boldsymbol{f}^{i} & \boldsymbol{f}^{d} & \boldsymbol{f}^{p} \end{array}\right\}_{n+1}^{(j)} + \left[\begin{array}{c:c:c:c} \boldsymbol{k}^{ff} & \boldsymbol{k}^{fi} & \boldsymbol{k}^{fd} & \boldsymbol{k}^{fp} \\ \hdashline \boldsymbol{k}^{if} & \boldsymbol{k}^{ii} & \boldsymbol{k}^{id} & \boldsymbol{k}^{ip} \\ \hdashline \boldsymbol{k}^{df} & \boldsymbol{k}^{di} & \boldsymbol{k}^{dd} & \boldsymbol{k}^{dp} \\ \hdashline \boldsymbol{k}^{pf} & \boldsymbol{k}^{pi} & \boldsymbol{k}^{pd} & \boldsymbol{k}^{pp} \end{array}\right]_{n+1}^{(j)} \left\{\begin{array}{c:c:c:c} \delta\widetilde{\boldsymbol{u}}^{f} & \delta\widetilde{\boldsymbol{u}}^{i} & \delta\widetilde{\boldsymbol{u}}^{d} & \delta\widetilde{\boldsymbol{u}}^{p} \end{array}\right\}^{(j+1)} = \{\boldsymbol{0}\}\,. \tag{3.30}$$

With Equation (3.28) at hand and knowing that $\widetilde{\boldsymbol{u}}^p = \{\mathbf{0}\}$, Equation (3.30) can be re-written as:

$$\begin{aligned}&\left[\begin{array}{c:c} \boldsymbol{k}^{ff} & \boldsymbol{k}^{fi}+\boldsymbol{k}^{fd}\boldsymbol{\alpha} \\ \hdashline \boldsymbol{k}^{if}+\boldsymbol{\alpha}^T\boldsymbol{k}^{df} & \boldsymbol{k}^{ii}+\boldsymbol{k}^{id}\boldsymbol{\alpha}+\boldsymbol{\alpha}^T\boldsymbol{k}^{di}+\boldsymbol{\alpha}^T\boldsymbol{k}^{dd}\boldsymbol{\alpha} \end{array}\right]^{(j)}_{n+1} \left\{\begin{array}{c} \delta\widetilde{\boldsymbol{u}}^f \\ \hdashline \delta\widetilde{\boldsymbol{u}}^i \end{array}\right\}^{(j+1)} \\ &= -\left\{\begin{array}{c} \boldsymbol{f}^f \\ \hdashline \boldsymbol{f}^i+\boldsymbol{\alpha}^T\boldsymbol{f}^d \end{array}\right\}^{(j)}_{n+1}\end{aligned} . \tag{3.31}$$

From the solution of the previous equation system results the displacement fluctuation of the *free*, $\delta\widetilde{\boldsymbol{u}}^{f^{(j+1)}}$, and *independent*, $\delta\widetilde{\boldsymbol{u}}^{i^{(j+1)}}$, degrees of freedom. With these at hand, together with Equation (3.26), we finally obtain the total displacement fluctuation field of the RVE:

$$\widetilde{\boldsymbol{u}}^{(j+1)^T}_{n+1}\{\boldsymbol{y}\} = \left\{\begin{array}{c:c:c:c} \widetilde{\boldsymbol{u}}^f & \widetilde{\boldsymbol{u}}^i & \widetilde{\boldsymbol{u}}^d & \mathbf{0} \end{array}\right\}^{(j)^T}_{n+1} + \left\{\begin{array}{c:c:c:c} \delta\widetilde{\boldsymbol{u}}^f & \delta\widetilde{\boldsymbol{u}}^i & \boldsymbol{\alpha}\delta\widetilde{\boldsymbol{u}}^i & \mathbf{0} \end{array}\right\}^{(j+1)^T} . \tag{3.32}$$

In Appendix A.1, Equation (3.31) is particularised for *Linear*, *Periodic* and *Uniform Traction* boundary conditions.

3.3.2.3 Discretized homogenized stress tensor.

To compute the homogenized *First Piola-Kirchhoff* stress tensor, which will be sent to the macro-scale, two approaches may be used (see second and third terms of expression (3.17)). In the first one, this stress tensor is computed by volume averaging of its microscopic counterpart over the undeformed configuration of the RVE. The second approach uses the third term of expression (3.17) to compute it. The latter option is clearly simpler, and the computational burden associated is also smaller. However, in order to compute the macroscopic stress tensor, it is necessary to adapt it. As pointed out by [92], in the limit, $\boldsymbol{T}^{ref}_{n+1}\{\boldsymbol{Y}\}\,dA$ is equal to $\boldsymbol{t}_{n+1}\{\boldsymbol{y}\}\,da$, where $\boldsymbol{t}_{n+1}\{\boldsymbol{y}\}$ denotes the traction acting over the deformed boundary of the RVE. Thus, expression (3.17) can be re-written as:

$$\boldsymbol{P}_{n+1}\{\boldsymbol{x}\} = \frac{1}{V_0}\int_{\partial\Omega} \boldsymbol{t}_{n+1}\{\boldsymbol{y}\}\otimes\boldsymbol{Y}\,da. \tag{3.33}$$

Following this approach, the finite element discretization of the previous equation is trivial:

$$\boldsymbol{P}_{n+1}\{\boldsymbol{x}\} = \frac{1}{V_0}\mathbb{D}_b\mathbb{F}^{int}_{b_{n+1}}, \tag{3.34}$$

where $\mathbb{D}_b$ denotes the reference nodal coordinate matrix, which exclusively includes the nodes on the boundary of the RVE

$$\mathbb{D}_b = \left[\begin{array}{cccc} \mathbb{D}_1 & \mathbb{D}_2 & \cdots & \mathbb{D}_{n_b} \end{array} \right], \tag{3.35}$$

and $\mathbb{D}_{n_b}$ is defined as

$$\mathbb{D}_{n_b}^T = \left[\begin{array}{cccc} Y_1 & 0 & Y_2 & 0 \\ 0 & Y_1 & 0 & Y_2 \end{array} \right]^T. \tag{3.36}$$

In turn, the matrix $\mathbb{F}_{b_{n+1}}^{int}$ contains the internal nodal forces over the deformed boundary of the RVE for t_{n+1}.

In order to eliminate possible inconsistencies it is important to shed some light on the following aspects. According to the general and well established concepts of *Continuum Solid Mechanics*, the *Cauchy*, $\boldsymbol{\sigma}$, and the *First Piola-Kirchhoff*, $\boldsymbol{P}$, stress tensors are related as follows:

$$\boldsymbol{\sigma} = \frac{1}{det\left(\boldsymbol{F}\right)} \boldsymbol{P} \left[\boldsymbol{F}\right]^T. \tag{3.37}$$

Even though the philosophy under a *First-Order Coupled Multi-Scale* model is quite different from a classical continuum constitutive model, the previous relations are still valid. At the macroscopic scale, the macroscopic *Cauchy* stress tensor can be defined as

$$\boldsymbol{\sigma}\left\{\boldsymbol{x}, t\right\} = \frac{1}{det\left(\boldsymbol{F}\left\{\boldsymbol{x}, t\right\}\right)} \boldsymbol{P}\left\{\boldsymbol{x}, t\right\} . \left[\boldsymbol{F}\left\{\boldsymbol{x}, t\right\}\right]^T. \tag{3.38}$$

However, a recent study has shown that the macroscopic *Cauchy* stress tensor is not equal to the homogenized microscopic counterpart in some particular cases. This means that, in a generic case:

$$\int_{\varphi(\Omega)} \boldsymbol{\sigma}\left\{\boldsymbol{y}, t\right\} dV \neq \frac{1}{\det\left[\frac{1}{V_0}\int_{\Omega_0} \boldsymbol{F}\left\{\boldsymbol{y}, t\right\} dV\right]} \frac{1}{V_0} \int_{\Omega_0} \boldsymbol{P}\left\{\boldsymbol{y}, t\right\} dV . \left[\frac{1}{V_0}\int_{\Omega_0} \boldsymbol{F}\left\{\boldsymbol{y}, t\right\} dV\right]^T. \tag{3.39}$$

According to [93], this is a consequence of the description (*Eulerian* or *Lagrangian* description) used to characterize the deformation of the RVE when it is subjected to finite strains. Nevertheless, in a recent contribution, de Souza Neto and Feijóo [94] have proved that the inequality (3.39) is only verified when a *Uniform Boundary Condition* is adopted to model the behaviour of the RVE.

In order to avoid any possible mistake, in the present work the macroscopic *Cauchy* stress tensor, $\boldsymbol{\sigma}\left\{\boldsymbol{x}, t\right\}$, is computed using the relation (3.38).

3.3.2.4 *MSP* code

After introduction of the numerical framework, which allows the solution of the equilibrium equation of the RVE when it is subjected to different boundary conditions, in Table 3.1, the structure of a code devoted to solve exclusively the micro-equilibrium problem when a RVE is subjected to a particular deformation gradient, is introduced. The name of the code is*Micro-Scale Problem* code (***MSP***).

The ***MSP*** code was totally implemented from the scratch in *Fortran 90*® and there is a parallelized version which includes the *MUMPS* parallel solver. The utility of this code is rapidly and easily obtain homogenized properties of a heterogeneous material for a particular deformation state.

3.3.2.5 Macro-scale discretization.

The spatial discretization of the macroscopic equilibrium equation (Equation (3.22)) by means of the *finite element method* gives rise to the following expression

$$\begin{aligned}&\left\{\int_{\Theta_0^d}\overline{\boldsymbol{G}}^T\left[\frac{1}{V_0}\int_{\Omega_0^d}\hat{\boldsymbol{P}}\left\{\boldsymbol{F}_{n+1}\left\{\boldsymbol{x}\right\}+\boldsymbol{G}\widetilde{\boldsymbol{u}}_{n+1}\left\{\boldsymbol{y}\right\},\boldsymbol{\beta}_n\left\{\boldsymbol{y}\right\}\right\}dV\right]dV\right.\\&\left.-\int_{\Theta_0^d}\overline{\boldsymbol{N}}^T\boldsymbol{B}^{ref}_{n+1}\left\{\boldsymbol{x}\right\}dA-\int_{\partial\Theta_0^d}\overline{\boldsymbol{N}}^T\boldsymbol{T}^{ref}_{n+1}\left\{\boldsymbol{x}\right\}dA\right\}.\boldsymbol{\zeta}=0\;\forall\;\boldsymbol{\zeta}\in\mathcal{U}^d,\end{aligned}\tag{3.40}$$

which, in fact, is completely analogous to the discretized equilibrium equation of a conventional solid mechanics problem, apart from the approach used to compute the stress tensor. In the previous equation, $\overline{\boldsymbol{G}}$ and $\overline{\boldsymbol{N}}$ denote respectively the discrete full material gradient and the global interpolation matrix, both at the macro-scale domain. The symbol Θ_0^d denotes the discretized undeformed macroscopic domain. Once again, the well-established *Newton-Raphson* method is used to solve the previous equation (for more details see [6, 91]).

3.3.2.6 Discretized homogenized material tangent modulus.

The conventional strategy employed to compute the algorithmic consistent tangent operator consists in the direct linearization of the weak equilibrium equation problem at the macro-scale (Equation (3.11)) [95]. Even though this approach is conceptually well established, within the present context, it has not been widely used due to the complexity that this method involves. A different approach has been advocated by several

TABLE 3.1: Structure of *Micro-Scale Problem code*, ***MSP***.

1. Read the input file with information about:
   - Mesh;
   - Constitutive models and material properties;
   - Problem type - *Plane Stress* or *Plane Strain*;
   - Number of increments for the problem at the micro-scale, $N_{inc}\{\boldsymbol{y}\}$;
   - Boundary conditions;
   - Macroscopic deformation gradient.
2. Identify the nodes inside of the RVE, at the bottom, right, top and left borders and corners. Determine the dependency matrix, $\boldsymbol{\alpha}$, according to the boundary condition selected;
3. Compute the incremental *Linear* displacement vector:
$$\Delta \boldsymbol{u}^{*}\{\boldsymbol{y}\} = \frac{1}{N_{inc}\{\boldsymbol{y}\}}\left(\boldsymbol{F}\{\boldsymbol{x}\} - \boldsymbol{I}\right)\boldsymbol{Y}.$$
4. Increment the counter $N = N + 1$ (increment number);
   (a) Increment the *Newton-Raphson* iteration counter, $j = j + 1$
   (b) Update the total displacement vector:
$$\boldsymbol{u}_{n+1}^{(j)}\{\boldsymbol{y}\} = \Delta \boldsymbol{u}^{*}\{\boldsymbol{y}\} + \widetilde{\boldsymbol{u}}_{n+1}^{(j)}\{\boldsymbol{y}\}$$
   (c) Compute the global internal force vector, $\boldsymbol{f}^{int}\left\{\boldsymbol{u}_{n+1}^{(j)}\{\boldsymbol{y}\}\right\}$;
   (d) Check convergence:
   `IF CONV<TOL THEN`
   Compute and store the macroscopic stress tensor (Section 3.3.2.3).
   `IF` $N = N_{inc}\{\boldsymbol{y}\}$ `THEN`
   EXIT
   `ELSE`
   Go to 4.
   `END IF`
   `END IF`
   (e) Solve the micro-equilibrium problem (Section 3.3.2.2)
   (f) Update displacements;
$$\widetilde{\boldsymbol{u}}_{n+1}^{(j+1)}\{\boldsymbol{y}\} = \widetilde{\boldsymbol{u}}_{n+1}^{(j)}\{\boldsymbol{y}\} + \delta\widetilde{\boldsymbol{u}}^{(j+1)}\{\boldsymbol{y}\}$$
   Go to a)

authors ([36, 37, 74, 75, 92, 96, 97]), the so-called *Condensation* method, which takes into account the decomposition of the displacement field carried out at the micro-scale.[1]

The *Condensation* method starts from the basic definition of the consistent matrix, which is given by the differentiation of the *First Piola-Kirchhoff* stress tensor (Equation (3.34)) with regard to the macroscopic deformation gradient:

$$\mathbf{A}_{n+1}\{\boldsymbol{x}\} = \frac{\partial \boldsymbol{P}_{n+1}\{\boldsymbol{x}\}}{\partial \boldsymbol{F}_{n+1}\{\boldsymbol{x}\}} = \frac{\partial}{\partial \boldsymbol{F}_{n+1}\{\boldsymbol{x}\}}\left(\frac{1}{V_0}\mathbb{D}_b\mathbb{F}^{int}_{b_{n+1}}\right) = \frac{1}{V_0}\mathbb{D}_b\frac{\partial \mathbb{F}^{int}_{b_{n+1}}}{\partial \boldsymbol{F}_{n+1}\{\boldsymbol{x}\}}. \tag{3.41}$$

All details inherent with the condensation method are described in detail in Appendix A.2 which also includes particularizations of this method for *Linear*, *Periodic* and *Uniform Traction* boundary conditions.

Remark 3.3. With the *macroscopic material tangent modulus* at hand (Equation (3.41)), it is possible to compute its spatial counterpart if required. This task can be performed by using the well established relation from the *Continuum Solid Mechanics* theory (for more details [94]):

$$a_{ijkl} = \frac{1}{\det \boldsymbol{F}} A_{imkn} F_{jm} F_{ln}. \tag{3.42}$$

3.3.2.7 *CMSP* code

The numerical implementation of a coupled multi-scale model is a hard and complex task mainly by two motives: the first one is related to the equilibrium of the RVE and to the establishment of the "bridge" between fine and coarse scales; the second obstacle stems from the fact that it is necessary to manipulate with a considerable amount of data either from the macro or micro-scale.

So far, there is still no commercial code available that is able to solve coupled multi-scale problems (according to the author's knowledge). In fact, this new numerical tool has been basically confined to the academic community. However, within this community, some authors have been publishing parts of their codes [99].

In order to conclude this chapter, a summary structure of *Coupled Multi-Mcale Problem* code, ***CMSP***, in a pseudo-algorithmic format is introduced in Table 3.2. Once again, this code was implemented from the scratch and *Fortran 90*® language was used.

[1] There is a third possible approach, which is a pure numerical method, where the computation of the macroscopic tangent operator is obtained by perturbation of the macroscopic deformation gradient [98]. Nevertheless, this approach requires a huge computational cost and therefore it is not attractive from the computational point of view.

3.4 Conclusions

Throughout this chapter the fundamental ingredients required to formulate a *First-Order Coupled Multi-Scale Model* under the assumption of finite strains were reviewed. In addition, numerical schemes were described in order to numerically implement this model. Special attention was given to the imposition of the kinematical admissible boundary conditions at the micro-scale domain as well as to the derivation of the macroscopic tangent operator which is computed taking into account information from the microscopic domain.

At the end of the present chapter two codes were presented. As pointed out previously, ***MSP*** code is devoted exclusively to solve the micro-equilibrium problems i.e. subjecting the RVE to a particular deformation gradient. This code is particularly useful to obtain homogenized material properties of materials with heterogeneous micro-structures. In turn, the ***CMSP*** code is a code implemented to solve a *First-Order Coupled Multi-Scale Model* under the assumption of finite strains.

In the following chapters, new numerical schemes will be proposed in order to enhance the formulation proposed in this introductory chapter as well as to optimize and to increase the attractiveness of this model.

TABLE 3.2: Structure of *Coupled Multi-Scale Problem* code, ***CMSP***

1. Read data with information of the macro and micro domains and the number of increments for the problem at the macro-scale, $N_{inc}\{\boldsymbol{x}\}$;
2. Increment the counter $N = N + 1$ (macroscopic increment number);
3. Set up the initial values:

$$\boldsymbol{u}_{n+1}^{(0)}\{\boldsymbol{x}\} = \boldsymbol{u}_n\{\boldsymbol{x}\} \qquad \boldsymbol{r}_{n+1}^{(0)}\{\boldsymbol{x}\} = -\lambda_{n+1}\boldsymbol{f}^{ext}\{\boldsymbol{x}\}$$

where $\boldsymbol{r}_{n+1}^{(0)}\{\boldsymbol{x}\}$ is residual equation.

   (a) Increment the iteration counter of the *Newton-Raphson* method at the macro-scale, $k = k + 1$;

   (b) Assemble the global macroscopic tangent stiffness $\boldsymbol{K}_T^{(k)}\{\boldsymbol{x}\}$:

   `IF` $N = 1$ `AND` $K = 1$ THEN

   Compute $\boldsymbol{K}_T^{(k)}\{\boldsymbol{x}\}$ assuming an elastic domain for whole macroscopic structure

   `ELSE`

   Use $\boldsymbol{K}_T^{(k)}\{\boldsymbol{x}\}$ obtained at micro-scale.

   `END IF`

   (c) Compute the macroscopic incremental displacements:

$$\boldsymbol{K}_T^{(k)}\{\boldsymbol{x}\}\,\delta\boldsymbol{u}^{(k+1)}\{\boldsymbol{x}\} = -\boldsymbol{r}_{n+1}^{(k)}\{\boldsymbol{x}\}$$

   (d) Update the macroscopic displacements:

$$\boldsymbol{u}_{n+1}^{(k+1)}\{\boldsymbol{x}\} = \boldsymbol{u}_{n+1}^{(k)}\{\boldsymbol{x}\} + \delta\boldsymbol{u}^{(k+1)}\{\boldsymbol{x}\}$$

   (e) For each macroscopic integration *Gauss* point, compute the macroscopic deformation gradient:

$$\boldsymbol{F}_{n+1}^{(k+1)}\{\boldsymbol{x}\} = \boldsymbol{I} + \nabla_{\boldsymbol{p}}\boldsymbol{u}_{n+1}^{(k+1)}\{\boldsymbol{x}\}$$

   (f) Solve the microscopic equilibrium problem

   - `GO TO` point 2) of Table 3.1 - solve the micro-equilibrium problem considering **only one increment**;
   - Compute the macroscopic tangent operator (Appendix A.2) and assemble $\boldsymbol{K}_T^{(k+1)}\{\boldsymbol{x}\}$ using information from micro-scale.

   (g) Compute the macroscopic internal forces vector

   (h) Actualize the residual vector

$$\boldsymbol{r}_{n+1}^{(k+1)}\{\boldsymbol{x}\} = \boldsymbol{f}^{int}\left\{\boldsymbol{u}_{n+1}^{(k+1)}\{\boldsymbol{x}\}\right\} - \lambda_{n+1}\boldsymbol{f}^{ext}\{\boldsymbol{x}\}$$

   (i) Check the convergence.

   `IF CONV<TOL THEN`

   `IF` $N = N_{inc}^{M}\{\boldsymbol{x}\}$ `THEN`

   EXIT

   `ELSE`

   Go to 2.

   `END IF`

   `ELSE`

   Go to a)

   `END IF`

Chapter 4

An adaptive sub-incremental strategy for the solution of homogenization-based multi-scale problems

4.1 Introduction

In the past decade, the modelling of heterogeneous materials by continuous interchange of informations between scales has been a topic of extensive research. Among various approaches and techniques for the micro-macro modelling, we will focus on those where the macroscopic stress and strain tensors are defined as volume averages of their microscopic counterparts over a *Representative Volume Element* (RVE) of material [see 30–34, among others]. Due to their suitability for implementation within non-linear finite element frameworks, this class of homogenization techniques, which are collectively called computational homogenization, have emerged as a very effective way to describe complex microstructural geometries, arbitrary constitutive material behaviour and microstructural evolution. Of particular interest to the modelling of dissipative media is the so-called multilevel finite element framework (ML-FEM) or FE^2. This method is based on the nested solution of two coupled problems, one at a macro-scale and other at the micro-scale, where a micro-scale computation is conducted over a statistically representative volume element in order to extract quantities required for the macro-scale.

A considerable number of publications have focused on this multi-scale modelling approach, where we highlight the pioneering work of Miehe and co-workers, that have

established a crystal plasticity framework at both small and finite strains [36, 37] and the work of Kouznetsova and co-workers [38], that have proposed a second order multi-scale scheme to address the effect of the RVE size and its constituents. The modelling framework has been extended to incorporate thermal effects [39, 40] and include the presence of discontinuities, which are the outcome of dissipative phenomena that take place at the micro-scale [55, 56, 63]. Recently, the method has been successfully applied for stress and structural damage analysis of masonry walls [41–43, 100] and the formulation enhanced to perform the mechanical analysis of heterogeneous thin sheets [44]. Many more contributions can be found in the literature on this rapidly expanding field [see 45–48, among others]. In parallel to the development of the method, several numerical issues inherent to the formulation of multi-scale constitutive models have been extensively addressed, such as the definition of the RVE size [52, 83] or the effect of the spatial discretization at both scales [53], whose associated shortcomings have been overcome in recent years.

In the ML-FEM framework, the macroscopic equilibrium problem is solved simultaneously with one microscopic RVE problem for each point of the macroscopic finite element mesh. Therefore, as the size of the macroscopic and/or microscopic problem increases, memory storage and computational requirements can become excessive, making the solution of realistic problems extremely challenging. This is one of the major drawbacks associated with the ML-FEM, which makes it difficult to be adopted in an industrial environment. Nevertheless, various strategies have been suggested to tackle the problem, where we highlight the use of parallel processing techniques [49, 50], the selective usage [51] and the reduction of the problem at the RVE domain [101–104]. Although these approaches considerably enhance the computational efficiency of the ML-FEM framework, the robustness of the solution procedure also has an important impact on the overall computational time. For instance, if the solution of one microscopic RVE equilibrium problem cannot be found, the macroscopic solution algorithm has to be stopped and reinitiated with a reduced load increment. Therefore, the failure of the microscopic problem has a crucial repercussion on the overall computational time. Convergence difficulties at the micro-scale equilibrium problem are surely more pronounced whenever material and geometrical non- linearities are encountered in the solution. Nevertheless, similar problems appear in the solution of conventional dissipative phenomenological constitutive models, which have been significantly alleviated by using well-established numerical tools [105–108].

The present contribution proposes advanced solution procedures to improve the efficiency and robustness of multi-scale problems in the finite deformation regime including inelastic behaviour at the micro-scale. These schemes are inspired on the idea of ensuring

convergence of the solution algorithm, in the presence of several sources of non-linearity, for larger increments.

The potential lack of robustness of the *Newton- Raphson* method, which in multi-scale constitutive models can emerge either in the solution of the macro or micro-scale equilibrium problems, is the central motivation of this work. The aims of the work are twofold. First, two well-established numerical strategies, the so-called *Line Search* procedure and the *Arc-Length* method, are modified and extended for the solution of the discrete RVE boundary value problem. An adaptive strategy, where the sub-increment size is automatically defined according to the problem evolution, is proposed. This strategy helps circumventing the numerical problems that arise at the micro-scale when complex RVEs are considered, clearly improving the robustness of the solution procedure. Therefore, the finite element analysis of a single RVE under prescribed macroscopic strain histories, can be performed for significantly larger deformation gradients. As a second purpose of this contribution, the solution of fully coupled multi-scale finite element analyses of solids, within the ML-FEM framework will be addressed. Here, the solution obtained for the micro equilibrium problem with the adaptive sub-incremental strategy proposed is employed as an improved initial guess, for an additional step at the micro- scale, to ensure the consistency of the macroscopic equilibrium problem. This methodology critically reduces the computational times of the ML-FEM analyses under finite strains with inelastic material behaviour and preserves the quadratic rates of asymptotic convergence that characterize the *Newton-Raphson* scheme at the macroscopic level.

The present chapter is organized as follows. In Section 4.2, the enhanced solution procedures for multi-scale problems, are introduced and discussed in detail. The effectiveness of the numerical strategies proposed is demonstrated in Section 4.3 through the analysis of three distinct problems. Finally, in Section 4.4, the main conclusions of this contribution is introduced.

4.2 Enhanced solution procedures for multi-scale problems

The solution procedure, for the generic finite element-based framework for homogenization-based multi-scale analysis of heterogeneous solids, involves a combination two full *Newton-Raphson* methods at different scales. Although, this nested approach is well established and is the basis for most non-linear problems, additional sophistications are required to produce effective and robust solution algorithms.

In this section, two well established numerical strategies, in non-linear solid mechanics problems, the so-called *Line Search* procedure and the *Arc-Length* method, are modified

and extended for the solution of the micro-scale RVE boundary value problem. An adaptive strategy to automatically adjust the sub-increment size, taking into account the nature and evolution of the problem at the micro-scale is proposed.

4.2.1 *Line Search* Method

Different versions of the *Line Search* method emerged in 80's proposed by several authors [105, 109]. The main goal of this numerical scheme is to improve the convergence rate of iterative solution procedures. To achieve this purpose, a new variable η - commonly called *iterative step-length* - is introduced that performs a correction on the displacement field of the conventional incremental non-linear finite element problem. Thus, the displacement field is defined as:

$$\boldsymbol{u}_{n+1} = \boldsymbol{u}_n + \eta.\delta\boldsymbol{u}, \tag{4.1}$$

where $\boldsymbol{u}_n$ is the displacement field converged in the previous increment and $\delta\boldsymbol{u}$ is the iterative displacement. The total potential energy, Φ, which governs the equilibrium of a solid, is typically used to determine the new parameter, η. The truncated *Taylor's* expansion of this function is given by:

$$\Phi\left(\boldsymbol{u}+\delta\boldsymbol{u}\right) = \Phi_0\left(\boldsymbol{u}\right) + \frac{\partial\Phi}{\partial\boldsymbol{u}}\delta\boldsymbol{u} + \frac{1}{2}\delta\boldsymbol{u}^T\frac{\partial^2\Phi}{\partial\boldsymbol{u}^2}\delta\boldsymbol{u} + \ldots . \tag{4.2}$$

In the previous equation, the derivative $\partial\Phi/\partial\boldsymbol{u}$ is the equilibrium force vector, $\boldsymbol{r}\left(\boldsymbol{u}\right) = \left(\boldsymbol{f}^{int} - \boldsymbol{f}^{ext}\right)$, of a conventional finite element problem and, the second derivative of the potential Φ, is the tangent stiffness matrix, $\boldsymbol{K}_T$. The equilibrium of the solid is verified when Φ reaches a stationary value for a particular value of η. Considering a similar *Taylor's* expansion for Φ dependent on η results

$$\Phi\left(\eta+\delta\eta\right) = \Phi_0\left(\eta\right) + \frac{\partial\Phi}{\partial\eta}\delta\eta + \frac{1}{2}\delta\eta\frac{\partial^2\Phi}{\partial\eta^2}\delta\eta + \ldots , \tag{4.3}$$

where the displacement field and the external force vector are constant and only the correctional factor is unknown. From the mathematical point of view, the stationary value of Φ corresponds to:

$$s\left(\eta\right) = \frac{\partial\Phi}{\partial\eta} = \delta\boldsymbol{u}^T\left(\eta\right)\left[\boldsymbol{f}^{int}\left(\boldsymbol{u}\left(\eta\right)\right) - \boldsymbol{f}^{ext}\right] = \delta\boldsymbol{u}^T\left(\eta\right)\boldsymbol{r}\left(\boldsymbol{u}\left(\eta\right)\right) = 0. \tag{4.4}$$

In general, the previous relation is not employed since it is extremely difficult, from the numerical point of view, to satisfy. Therefore, it is replaced by an iterative scheme where

the *iterative step-length* η is computed whenever the following inequality is verified:

$$\left| \frac{s(\eta)_{n+1}^{(j),(l)}}{s_{n+1}^{(j),(0)}} \right| < \beta. \tag{4.5}$$

In the previous equation $s(\eta)_{n+1}^{(j),(l)}$ and $s_{n+1}^{(j),(0)}$ are computed by the inner product between the out-of-balance force vector $\boldsymbol{r}(\boldsymbol{u}(\eta))$ and the iterative displacement vector $\delta\boldsymbol{u}$ (see Equation (4.4)) for every $j-th$ iteration of the *Newton-Raphson* method. However, $s_{n+1}^{(j),(0)}$ is only defined once, at the beginning of the *Line Search* iterative scheme and $s(\eta)_{n+1}^{(j),(l)}$ is defined for each $l-th$ iteration. The parameter β is the *Line Search tolerance*, which according to [109, chap. 9] as well as to our experience, provides satisfactory results for values around 0.8. If inequality (4.5) is not satisfied, an extrapolation or interpolation procedure is carried out to update η and a new iteration is undertaken. For more details on how these operations are performed see [109, chap. 9].

4.2.1.1 Micro-scale *Line Search* Method.

The implementation of the *Line Search* method for the solution of the micro-equilibrium problem requires some modifications due to the specific nature of the kinematical admissible constraints enforced on the boundary of the RVE. In contrast to conventional solid mechanics problems, where the difference between internal and external forces is well defined and characterized, we realise that $\boldsymbol{f}^{ext}$ is null at the micro-scale domain for the present case. Another difference emerges as a consequence of the decomposition of the displacement field. Thus, taking into account Equations (3.27) and (3.29), the parameter $s(\eta)_{n+1}^{(j),(l)}$ is defined by:

$$\begin{aligned} s(\eta)^{(j),(l)} &= \delta\widetilde{\boldsymbol{u}}_{n+1}^{f^{(j),(l)}}\{\boldsymbol{y}\}.\boldsymbol{f}_{n+1}^{f^{(j),(l)}} + \delta\widetilde{\boldsymbol{u}}_{n+1}^{i^{(j),(l)}}\{\boldsymbol{y}\}.\boldsymbol{f}_{n+1}^{i^{(j),(l)}} \\ &\quad + \delta\widetilde{\boldsymbol{u}}_{n+1}^{d^{(j),(l)}}\{\boldsymbol{y}\}.\boldsymbol{f}_{n+1}^{d^{(j),(l)}} + \delta\widetilde{\boldsymbol{u}}_{n+1}^{p^{(j),(l)}}\{\boldsymbol{y}\}.\boldsymbol{f}_{n+1}^{p^{(j),(l)}} \\ \Leftrightarrow s(\eta)^{(j),(l)} &= \delta\widetilde{\boldsymbol{u}}_{n+1}^{f^{(j),(l)}}\{\boldsymbol{y}\}.\boldsymbol{f}_{n+1}^{f^{(j),(l)}} + \delta\widetilde{\boldsymbol{u}}_{n+1}^{i^{(j),(l)}}\{\boldsymbol{y}\}.\boldsymbol{f}_{n+1}^{i^{(j),(l)}} \\ &\quad + \boldsymbol{\alpha}\delta\widetilde{\boldsymbol{u}}_{n+1}^{i^{(j),(l)}}\{\boldsymbol{y}\}.\boldsymbol{f}_{n+1}^{d^{(j),(l)}}. \end{aligned} \tag{4.6}$$

The previous equation is valid for all admissible boundary conditions that can be formulated based on the displacement field decomposition. However, for *Linear* and *Periodic* boundary conditions, they can be dramatically simplified. We start with the simplest case: *Linear* boundary condition. The *Linear* constraint restricts the fluctuation field to the nodes in the interior of the RVE, which means that $\widetilde{\boldsymbol{u}}^{i}\{\boldsymbol{y}\}$ and $\widetilde{\boldsymbol{u}}^{d}\{\boldsymbol{y}\}$ are null. Thus, $s(\eta)$ is determined by:

$$s(\eta)^{(j),(l)} = \delta\widetilde{\boldsymbol{u}}_{n+1}^{f^{(j),(l)}}\{\boldsymbol{y}\}.\boldsymbol{f}_{n+1}^{f^{(j),(l)}} \tag{4.7}$$

The same expression for parameter $s(\eta)$ is obtained for *Periodic* boundary condition. This is due to the fact that at the boundary of the RVE there are an *anti-periodic* traction force field. In order to clarify how this numerical method can be incorporated into the *Newton-Raphson* procedure for the solution of the micro-equilibrium problem, in Table 4.1 we introduce, in pseudo-code format, the structure of the algorithm.

TABLE 4.1: The combined *Newton-Raphson/Line Search* method for solution of the non-linear micro-scale finite element equation.

Given the total macroscopic deformation gradient, $\boldsymbol{F}_{n+1}\{\boldsymbol{x}\}$, and knowing the set of internal variables of the RVE, $\boldsymbol{\beta}_n$, at time t_n, do:

1. Compute the increment of the *Linear* displacement $\Delta\boldsymbol{u}_{n+1}^{Lin}$:

$$\Delta\boldsymbol{u}_{n+1}^{Lin} = \left(\boldsymbol{F}_{n+1}\{\boldsymbol{x}\} - \boldsymbol{I}\right)\boldsymbol{Y} - \boldsymbol{u}_n^{Lin}.$$

2. Set initial guess for total displacement and iterative displacement fluctuation, $j = 0$ and $l = 0$:

$$\boldsymbol{u}_{n+1}^{(0),(0)}\{\boldsymbol{y}\} = \boldsymbol{u}_n\{\boldsymbol{y}\} + \Delta\boldsymbol{u}_{n+1}^{Lin} \quad ; \quad \delta\widetilde{\boldsymbol{u}}^{(j)}\{\boldsymbol{y}\} = \boldsymbol{0}$$

3. Set the iteration counter of the *Newton-Raphson* method, $j = j + 1$.

   (a) Set the iteration counter of the *Line Search* scheme, $l = l + 1$

      i. Update the total displacement:
      IF $(l = 1)$ THEN $\eta^{(l)} = 1$ ENDIF

$$\boldsymbol{u}_{n+1}^{(j),(l)}\{\boldsymbol{y}\} = \boldsymbol{u}_{n+1}^{(j-1),(l)}\{\boldsymbol{y}\} + \eta^{(l)}\delta\widetilde{\boldsymbol{u}}^{(j)}\{\boldsymbol{y}\}.$$
$$\widetilde{\boldsymbol{u}}_{n+1}^{(j),(l)}\{\boldsymbol{y}\} = \widetilde{\boldsymbol{u}}_{n+1}^{(j-1),(l)}\{\boldsymbol{y}\} + \eta^{(l)}\delta\widetilde{\boldsymbol{u}}^{(j)}\{\boldsymbol{y}\}.$$

      ii. Compute the internal force vector $\boldsymbol{f}^{int}\left\{\boldsymbol{u}_{n+1}\{\boldsymbol{y}\}\right\}^{(j),(l)}$.
      IF $(j \geqslant 2)$ THEN
      Compute $s_{n+1}^{(j),(l)}(\eta)$ (Equation (4.7)).
      ELSE
      GOTO (b).
      ENDIF

      iii. Check condition (4.5).
      IF condition (4.5) is verified THEN
      GOTO (b).
      ELSE
      Compute $\eta^{(l+1)}$. For more details see [109, chap. 9].
      GOTO (a).
      ENDIF

   (b) Check the convergence of the *Newton-Raphson* method.
   IF $(CONV < TOL)$ THEN

   - Compute and store the macroscopic stress tensor $\boldsymbol{P}_{n+1}\{\boldsymbol{x}\}$ (Equation (3.34)).
   - Compute and store the material tangent modulus $\mathbf{A}_{n+1}\{\boldsymbol{x}\}$ (Equation (3.41)).
   - EXIT

   ENDIF

   (c) Assemble RVE global stiffness and solve for $\delta\widetilde{\boldsymbol{u}}^{(j+1)}\{\boldsymbol{y}\}$ (Equation (3.31)).

$$\boldsymbol{f}^{int}\left\{\boldsymbol{u}_{n+1}\{\boldsymbol{y}\}\right\}^{(j),(l)} + \boldsymbol{K}_T\left\{\boldsymbol{u}_{n+1}\{\boldsymbol{y}\}\right\}^{(j)}\delta\widetilde{\boldsymbol{u}}^{(j+1)}\{\boldsymbol{y}\} = \boldsymbol{0}$$

   (d) Compute $s_{n+1}^{(j+1),(0)}$.

$$s_{n+1}^{(j+1),(0)} = \delta\widetilde{\boldsymbol{u}}_{n+1}^{f^{(j),(l)}}\{\boldsymbol{y}\}.\boldsymbol{f}_{n+1}^{f^{(j),(l)}}$$

   (e) Reset the counter l and GOTO 3.

4.2.2 Micro-Scale Incremental Procedure

The combination of the conventional *Newton-Raphson* method with a *Line Search* technique for the solution of the micro-scale problem might not guarantee convergence at this scale within just one step. This pathology is also encountered on the solution of

conventional non-linear finite element problems. The usual course of action in such cases is to apply the load in several incremental steps.

A similar approach can be devised for the micro-equilibrium problem. Within the generic finite element-based framework for multi-scale analysis previously presented, the RVE equilibrium is governed by Expression (3.24). This expression is a function of the microscopic displacement field $\boldsymbol{u}_{n+1}\{\boldsymbol{y}\}$ which is, by definition, expressed by:

$$\begin{aligned} \boldsymbol{u}_{n+1}\{\boldsymbol{y}\} &= (\boldsymbol{F}_{n+1}\{\boldsymbol{x}\} - \boldsymbol{I})\,\boldsymbol{Y} + \widetilde{\boldsymbol{u}}_{n+1}\{\boldsymbol{y}\}, \\ \Leftrightarrow \boldsymbol{u}_{n+1}\{\boldsymbol{y}\} &= \boldsymbol{u}^{Lin}_{n+1} + \widetilde{\boldsymbol{u}}_{n+1}\{\boldsymbol{y}\}, \end{aligned} \tag{4.8}$$

where $\boldsymbol{u}^{Lin}_{n+1}$ is the *Linear* displacement prescribed over the RVE.

In order to define an incremental procedure for the solution of the micro-equilibrium problem it is necessary to select a suitable parameter/variable that is incremented through the problem. Based on the definition of the microscopic displacement field (Equation (4.8)) together with the expression which governs the equilibrium of the RVE (Equation (3.24)), we have selected the *Linear* displacement $\boldsymbol{u}^{Lin}_{n+1}$. Thus, for a generic time t_{n+1} at the macro-scale, the total microscopic displacement can be incrementally defined as

$$\begin{aligned} \boldsymbol{u}^{m}_{n+1}\{\boldsymbol{y}\} &= \boldsymbol{u}^{Lin}_{n} + \lambda^{m}\Delta\boldsymbol{u}^{Lin}_{n+1} + \widetilde{\boldsymbol{u}}^{m}_{n+1}\{\boldsymbol{y}\}, \\ &= \boldsymbol{u}^{Lin}_{n} + \left(\lambda^{m-1} + \Delta\lambda^{m}\right)\Delta\boldsymbol{u}^{Lin}_{n+1} + \widetilde{\boldsymbol{u}}^{m}_{n+1}\{\boldsymbol{y}\}, \end{aligned} \tag{4.9}$$

where $\Delta\boldsymbol{u}^{Lin}_{n+1}$ is the incremental *Linear* displacement at instant $t = n+1$ defined by

$$\Delta\boldsymbol{u}^{Lin}_{n+1} = (\boldsymbol{F}_{n+1}\{\boldsymbol{x}\} - \boldsymbol{I})\,\boldsymbol{Y} - \boldsymbol{u}^{Lin}_{n}, \tag{4.10}$$

m denotes the microscopic increment number and λ^m is the *displacement factor*, which defines the prescribed *Linear* displacement at increment m. This parameter ranges between 0 and 1, which defines the beginning and end of the incremental scheme at the micro-scale. In addition, based on Equation (4.9), it is possible to define the increment of the microscopic displacement field associated with the microscopic increment m:

$$\Delta\boldsymbol{u}^{m}_{n+1}\{\boldsymbol{y}\} = \Delta\lambda^{m}\Delta\boldsymbol{u}^{Lin}_{n+1} + \Delta\widetilde{\boldsymbol{u}}^{m}_{n+1}\{\boldsymbol{y}\}, \tag{4.11}$$

Different approaches may be used to define the *incremental displacement factor* $\Delta\lambda^m$. The simplest case consists on the definition of the number of increments for each problem.

Despite its simplicity, this approach might be inefficient since, in many circumstances, it is not easy to anticipate the appropriate number of sub-increments for a specific problem.

A cutting procedure is commonly employed, where the load increment is cut in half and an attempt to solve the new incremental problem is made. This procedure is carried out as many times as required until convergence is reached. However, this strategy can lead to a significant number of increments, which can have a significant repercussion on the computational cost. In addition, in some problems involving instabilities and saddle points it may be impossible to obtain a solution.

In the following, a strategy to determine the *incremental displacement factor*, $\Delta\lambda^m$, for the problem at the micro-scale is proposed which is related to the nature and the evolution of the problem. This strategy is inspired on the standard *Arc-Length* method.

4.2.2.1 Micro-scale Arc-Length Method.

Considering the *Arc-Length* method, in addition to the microscopic displacement fluctuation field $\widetilde{\boldsymbol{u}}\{\boldsymbol{y}\}$, the *incremental displacement factor* $\Delta\lambda^m$ is also an unknown of the problem. With this assumption, Equation (3.24) can be re-defined as

$$\boldsymbol{f}^{int}\left\{\boldsymbol{u}_{n+1}^{m}\{\boldsymbol{y}\},\Delta\lambda^{m}\right\}=\boldsymbol{0}. \tag{4.12}$$

Considering the previous equation and upon its linearization results:

$$\begin{aligned}\frac{\partial \boldsymbol{f}^{int}\left\{\boldsymbol{u}_{n+1}^{m}\{\boldsymbol{y}\},\Delta\lambda^{m}\right\}}{\partial \boldsymbol{u}_{n+1}^{m}\{\boldsymbol{y}\}}\frac{\partial \boldsymbol{u}_{n+1}^{m}\{\boldsymbol{y}\}}{\partial \widetilde{\boldsymbol{u}}_{n+1}^{m}\{\boldsymbol{y}\}}\delta\widetilde{\boldsymbol{u}}\{\boldsymbol{y}\}+\frac{\partial \boldsymbol{f}^{int}\left\{\boldsymbol{u}_{n+1}^{m}\{\boldsymbol{y}\},\Delta\lambda^{m}\right\}}{\partial \boldsymbol{u}_{n+1}^{m}\{\boldsymbol{y}\}}\frac{\partial \boldsymbol{u}_{n+1}^{m}\{\boldsymbol{y}\}}{\partial\Delta\lambda^{m}}\delta\lambda=-\boldsymbol{Res}\\ \Leftrightarrow \boldsymbol{K}_{T}^{m,(j)}\delta\widetilde{\boldsymbol{u}}^{(j+1)}\{\boldsymbol{y}\}+\boldsymbol{K}_{T}^{m,(j)}\Delta\boldsymbol{u}_{n+1}^{Lin}\delta\lambda^{(j+1)}=-\boldsymbol{Res}^{(j)},\end{aligned} \tag{4.13}$$

where $\boldsymbol{K}_{T}^{m,(j)}$ is the global stiffness matrix of the RVE. Once again, the index $(*)^{m,(j)}$ denotes the iteration number of the *Newton-Raphson* method but, in this case, associated with the microscopic increment m. For convenience, we assume that $\boldsymbol{K}_{T}^{m,(j)}\Delta\boldsymbol{u}_{n+1}^{Lin}=\boldsymbol{f}^{ext}$, where $\boldsymbol{f}^{ext}$ represents the external force vector which is a consequence of the uniform deformation prescribed over the RVE. Thus, results

$$\boldsymbol{K}_{T}^{m,(j)}\delta\widetilde{\boldsymbol{u}}^{(j+1)}\{\boldsymbol{y}\}+\boldsymbol{f}^{ext}\delta\lambda^{(j+1)}=-\boldsymbol{Res}^{(j)}. \tag{4.14}$$

At this point, it is important to highlight the fact that the different boundary conditions were not yet considered. Considering the previous equation, it possible to define an explicit expression for $\delta\widetilde{\boldsymbol{u}}^{(j+1)}\{\boldsymbol{y}\}$:

$$\delta\widetilde{\boldsymbol{u}}^{(j+1)}\{\boldsymbol{y}\}=-\left[\boldsymbol{K}_{T}^{m,(j)}\right]^{-1}\boldsymbol{Res}^{(j)}-\left[\boldsymbol{K}_{T}^{m,(j)}\right]^{-1}\boldsymbol{f}^{ext}\delta\lambda^{(j+1)}. \tag{4.15}$$

Defining $\delta\boldsymbol{u}^{Ite}=-\left[\boldsymbol{K}_{T}^{m,(j)}\right]^{-1}\boldsymbol{Res}^{(j)}$ as being the iterative displacement and $\delta\boldsymbol{u}^{Tan}=-\left[\boldsymbol{K}_{T}^{m,(j)}\right]^{-1}\boldsymbol{f}^{ext}$ as the tangential displacement, we obtain a compact expression for

$\delta\widetilde{\boldsymbol{u}}^{(j+1)}\{\boldsymbol{y}\}$:

$$\delta\widetilde{\boldsymbol{u}}^{(j+1)}\{\boldsymbol{y}\} = \delta\boldsymbol{u}^{Ite} + \delta\boldsymbol{u}^{Tan}\delta\lambda^{(j+1)}. \tag{4.16}$$

Taking into account the previous definitions and knowing that $\Delta\lambda^{m,(j+1)} = \Delta\lambda^{m,(j)} + \delta\lambda^{(j+1)}$, the increment of the microscopic displacement field at the microscopic increment m (Equation (4.11)) and iteration $j+1$ is given by:

$$\begin{aligned}
\Delta\boldsymbol{u}_{n+1}^{m,(j+1)}\{\boldsymbol{y}\} &= \left(\Delta\lambda^{m,(j)} + \delta\lambda^{(j+1)}\right)\Delta\boldsymbol{u}_{n+1}^{Lin} + \Delta\widetilde{\boldsymbol{u}}_{n+1}^{m,(j)}\{\boldsymbol{y}\} + \delta\widetilde{\boldsymbol{u}}^{(j+1)} \\
&= \left(\Delta\lambda^{m,(j)} + \delta\lambda^{(j+1)}\right)\Delta\boldsymbol{u}_{n+1}^{Lin} + \left(\Delta\widetilde{\boldsymbol{u}}_{n+1}^{m,(j)} + \delta\boldsymbol{u}^{Ite} + \delta\lambda^{(j+1)}\delta\boldsymbol{u}^{Tan}\right) \\
&= \left(\Delta\lambda^{m,(j)}\Delta\boldsymbol{u}_{n+1}^{Lin} + \Delta\widetilde{\boldsymbol{u}}_{n+1}^{m,(j)}\right) + \delta\boldsymbol{u}^{Ite} + \left(\delta\boldsymbol{u}^{Tan} + \Delta\boldsymbol{u}_{n+1}^{Lin}\right)\delta\lambda^{(j+1)} \\
&= \Delta\boldsymbol{u}_{n+1}^{m,(j)}\{\boldsymbol{y}\} + \delta\boldsymbol{u}^{Ite} + \left(\delta\boldsymbol{u}^{Tan} + \Delta\boldsymbol{u}_{n+1}^{Lin}\right)\delta\lambda^{(j+1)}.
\end{aligned} \tag{4.17}$$

Since an extra unknown was added (the incremental displacement factor, $\Delta\lambda$), it is necessary to introduce an additional equation. For this purpose the well known *Arc-Length* cylinder equation is considered:

$$\left[\Delta\boldsymbol{u}_{n+1}^{m,(j+1)}\{\boldsymbol{y}\}\right]^T\Delta\boldsymbol{u}_{n+1}^{m,(j+1)}\{\boldsymbol{y}\} = l^{m^2}, \tag{4.18}$$

where l^{m^2} denotes the arc length of the cylinder at the m microscopic increment. Introducing the definition of the incremental microscopic displacement (Equation (4.17)) and after algebraic manipulations results:

$$a\delta\lambda^2 + b\delta\lambda + c = l^{m^2} \tag{4.19}$$

where the parameters a, b e c are defined by:

$$a = \left(\delta\boldsymbol{u}^{Tan} + \Delta\boldsymbol{u}_{n+1}^{Lin}\right)^T.\left(\delta\boldsymbol{u}^{Tan} + \Delta\boldsymbol{u}_{n+1}^{Lin}\right), \tag{4.20a}$$

$$b = 2\left[\left(\delta\boldsymbol{u}^{Tan} + \Delta\boldsymbol{u}_{n+1}^{Lin}\right)^T.\Delta\boldsymbol{u}_{n+1}^{m,(j)}\{\boldsymbol{y}\} + \left(\delta\boldsymbol{u}^{Tan} + \Delta\boldsymbol{u}_{n+1}^{Lin}\right)^T.\delta\boldsymbol{u}^{Ite}\right], \tag{4.20b}$$

$$c = \Delta\boldsymbol{u}_{n+1}^{m,(j)}\{\boldsymbol{y}\}^T\Delta\boldsymbol{u}_{n+1}^{m,(j)}\{\boldsymbol{y}\} + 2\Delta\boldsymbol{u}_{n+1}^{m,(j)}\{\boldsymbol{y}\}^T\delta\boldsymbol{u}^{Ite} + \delta\boldsymbol{u}^{Ite^T}\delta\boldsymbol{u}^{Ite}. \tag{4.20c}$$

Since expression (4.19) is a quadratic equation, it is possible to easily determine $\delta\lambda$ and, upon the correct selection of the appropriate root, the increment of the displacement factor is updated:

$$\Delta\lambda^{m,(j+1)} = \Delta\lambda^{m,(j)} + \delta\lambda^{(j+1)}. \tag{4.21}$$

Conceptually, the selection of the appropriate root relies on the one which originates the smallest angle between $\Delta\boldsymbol{u}_{n+1}^{m,(j)}\{\boldsymbol{y}\}$ and $\Delta\boldsymbol{u}_{n+1}^{m,(j+1)}\{\boldsymbol{y}\}$. From the mathematical point of view, the minimum value corresponds to the maximum value of the inner product between $\Delta\boldsymbol{u}_{n+1}^{m,(j)}\{\boldsymbol{y}\}$ and $\Delta\boldsymbol{u}_{n+1}^{m,(j+1)}\{\boldsymbol{y}\}$.

The length of the incremental solution l is updated at the end of a converged increment, usually taking into account the number of iterations used. Different strategies can be pursued (for more details [109]) but, in this work, the following relation was adopted:

$$l^{m+1} = l^m \frac{NITER}{NITER^{(j)}}, \tag{4.22}$$

where $NITER$ represents the ideal number of iterations and $NITER^{(j)}$ the number of iterations used by the *Newton-Raphson* method at the $m-th$ microscopic increment.

The predictor solution

In the first iteration, $j = 1$, of each increment the determination of the root that yields the minimum angle between $\Delta \boldsymbol{u}_{n+1}^{m,(0)} \{\boldsymbol{y}\}$ and $\Delta \boldsymbol{u}_{n+1}^{m,(1)} \{\boldsymbol{y}\}$ can not be done since $\Delta \boldsymbol{u}_{n+1}^{m,(0)} \{\boldsymbol{y}\}$ is equal to zero. In addition, $\delta \boldsymbol{u}^{Ite}$ is also equal to zero and, therefore, Equation (4.19) is reduced to the solution of:

$$\delta\lambda_{1,2} = \pm \frac{l^m}{\sqrt{\left(\left\{\delta \boldsymbol{u}^{Tan} + \Delta \boldsymbol{u}_{n+1}^{Lin}\right\}\right)^T . \left\{\delta \boldsymbol{u}^{Tan} + \Delta \boldsymbol{u}_{n+1}^{Lin}\right\}}}. \tag{4.23}$$

As it is possible to observe, the previous expression yields a pair of equal and symmetric roots. Within the context of a conventional finite element program, which incorporates the *Arc-Length* method, the total external factor may increase or decrease throughout a complex trajectory and, therefore, the proper selection of the root is crucial. However, at the RVE domain, since at the end of the micro-equilibrium problem all *Linear* displacement have to be completely prescribed, $\delta\lambda$ always needs to be positive.

Remark 4.1. According to the authors' experience, the roots which are obtained at each iteration (Equation (4.19)) are quite small when compared with the values which define the transition of successive increments (Equation (4.23)) (usually less than $1.0E-05$). Since this difference is not appreciable, the authors recommend to use this formulation exclusively to define the successive increments.

Introduction of the boundary conditions

The incremental scheme introduced in the previous section does not address the different admissible boundary constraints. As stressed out in Section 3.3.2.1, for each admissible boundary condition the displacement fluctuation field $\widetilde{\boldsymbol{u}}\{\boldsymbol{y}\}$ as well as the system of equations have to be established according to the basic assumptions which define it.

In this context, the modified *Arc-Length* method introduced in the previous section necessarily needs to reflect the dependence of the boundary condition with the displacement fluctuation field. This aspect is materialized on the condensation of the external force vector, $\overline{\boldsymbol{f}}^{ext}$, as well as on the computation of the tangential displacement vector, $\overline{\delta \boldsymbol{u}}^{Tan}$.

The global vector of external forces is determined by the product between the RVE global stiffness tangent matrix, $\boldsymbol{K}_T^{m,(j)}$ and the increment of the global *Linear* displacement:

$$\boldsymbol{f}^{ext} = \boldsymbol{K}_T^{m,(j)}.\Delta\boldsymbol{u}_{n+1}^{Lin}. \tag{4.24}$$

It is relevant to note that these two parameters are independent of the type of boundary condition selected. Nevertheless, the tangential displacement vector, $\overline{\delta\boldsymbol{u}}^{Tan}$, which is determined using the following expression clearly depends on the type of boundary conditions selected:

$$\overline{\delta\boldsymbol{u}}^{tan} = -\left[\boldsymbol{K}_{Bound}^{m,(j)}\right]^{-1}\overline{\boldsymbol{f}}^{ext}, \tag{4.25}$$

where, $\boldsymbol{K}_{Bound}^{m,(j)}$, denotes the boundary stiffness matrix used to solve the equilibrium problem at micro-scale (Equations (A.2) and (A.4) for *Linear* and *Periodic* boundary conditions respectively) and $\overline{\boldsymbol{f}}^{ext}$ is the condensated external force vector. The condensation procedure of $\overline{\delta\boldsymbol{u}}^{Tan}$ and $\overline{\boldsymbol{f}}^{ext}$ is performed according to the decomposition defined by expressions (3.27) and (3.29).

4.2.2.2 Micro-scale Improved Initial Guess for ML-FEM.

The solution of the micro-equilibrium problem using the incremental strategy instead of a single step, leads to the loss of consistency of the macroscopic equilibrium problem. The updated macroscopic tensor $\boldsymbol{P}_{n+1}\{\boldsymbol{x}\}$, which is computed after the sub-division of the time-step into a number of sub-steps at the micro-scale, is not consistent with the macroscopic constitutive tangent operator. This inconsistency leads to the loss of quadratic rate of asymptotic convergence of the macroscopic equilibrium problem.

The problem of loss of consistency between the numerical integration scheme, employed to solve the local problem with the use of sub-steps, and the consistent tangent matrix has been the subject of study in conventional non-linear finite element problems. This problem has similarities with the present context since the solution of the RVE problem can be interpreted as the stress-update procedure of a non-linear algorithm. In particular, under the assumption of small deformations, a sub-stepping framework was proposed by [110] which guarantees the consistency of the problem by properly defining a tangent matrix, dependent on m sub-matrices associated with m sub-steps used during the state-update framework. Even though remarkable results were obtained, its applicability is still restricted to a limited number of problems. This is mainly due to the fact that this framework has not been extended (according to the authors' knowledge) to finite strains and, in addition, the degree of complexity associated with its numerical implementation is considerable.

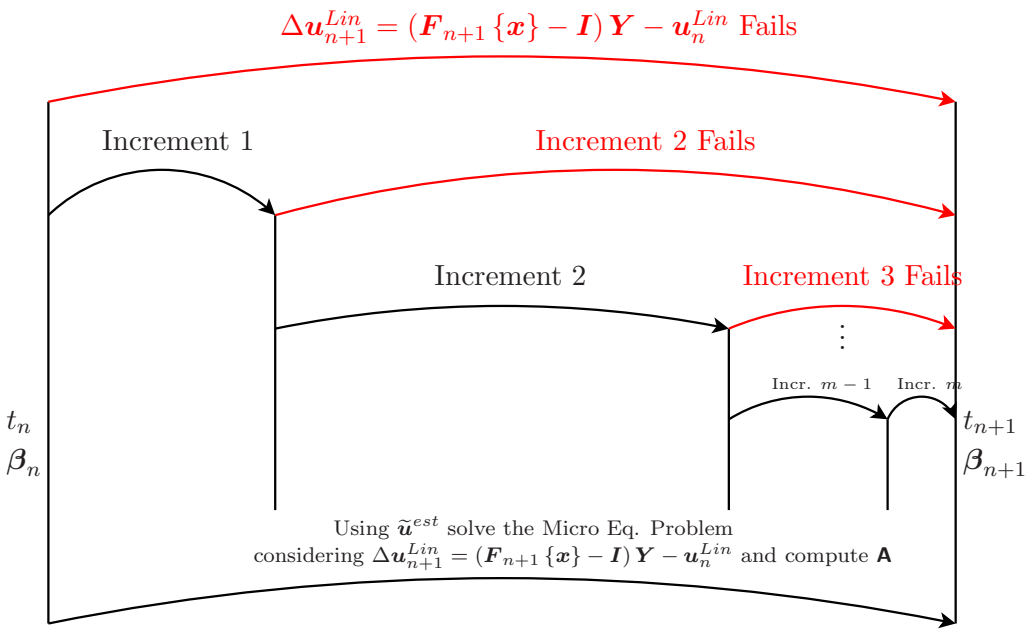

FIGURE 4.1: Improved initial guess scheme for the ML-FEM where the microscopic increments are automatically determined.

In the particular case of the ML-FEM framework, the inconsistency issue may be circumvented by using a similar strategy as proposed by [111]. Generically, this strategy consists in performing an additional increment, which starts from instant t_n considering all the internal variables as well as the parameters that define the configuration of both scales at this instant. Then, the guess for the displacement fluctuation vector $\widetilde{\boldsymbol{u}}^{est}$ to be employed by the *Newton-Raphson* method is the displacement fluctuation vector, which resulted from the previously converged sub-stepping scheme. In this additional step, the deformation of the RVE is driven by the total increment of the *Linear* displacement, $\Delta \boldsymbol{u}_{n+1}^{Lin}$. This strategy is schematically represented at the bottom of Figure 4.1.

Finally, it is important to highlight the fact that, in [111], the sub-increments are defined by the direct decomposition of the macroscopic deformation gradient which, in turn, is always the half of the last step (i.e., 1.0, 0.5, 0.25, etc.). However, within the framework presented in this contribution, the successive increments are defined by an algorithm (Section 4.2.2.1), which can assume any real value (say, 1.0, 0.837, 0.654), that is, any combination is possible. This is, in fact, a direct consequence of the *Arc-Length* algorithm since it is driven by the evolution of the problem.

Remark 4.2. It is important to emphasize that, if the final step it is not performed, the problem at the macro-domain still converges. However, the convergence rates are not quadratic, leading to a greater number of iterations at this level.

In Table 4.2, a summary of the new incremental scheme to solve the micro-equilibrium problem is presented in a pseudo-code format.

TABLE 4.2: The incremental strategy combined with the *Newton-Raphson/Arc-Length* scheme for solution of the non-linear micro-equilibrium problem.

Whenever the standard *Newton-Raphson* method fails to converge, for the prescribed *Linear* displacement in one increment, the following procedure should be applied. Given the total macroscopic deformation gradient, $\boldsymbol{F}_{n+1}\{\boldsymbol{x}\}$, and knowing the set of internal variables $\boldsymbol{\beta}_n$ at t_n, do:

1. Compute the incremental *Linear* displacement:

$$\Delta \boldsymbol{u}_{n+1}^{Lin} = \left(\boldsymbol{F}_{n+1}\{\boldsymbol{x}\} - \boldsymbol{I}\right)\boldsymbol{Y} - \boldsymbol{u}_{n}^{Lin}$$

2. Set the counter of the incremental procedure, $m = m + 1$;

3. Assemble the RVE global stiffness and compute the external force vector;

$$\boldsymbol{f}^{ext} = \boldsymbol{K}_{T}^{m}.\Delta \boldsymbol{u}_{n+1}^{Lin}$$

4. Perform the condensation of the stiffness matrix and external force vector according to the boundary condition selected;

5. Compute the condensated tangential displacement vector:

$$\overline{\delta \boldsymbol{u}}^{Tan} = -\left[\boldsymbol{K}_{Bound}^{m}\right]^{-1}\overline{\boldsymbol{f}}^{ext};$$

6. Compute the incremental factor:

$$\delta\lambda = abs\left[\frac{l^{m}}{\sqrt{\left(\delta \boldsymbol{u}^{Tan} + \Delta \boldsymbol{u}_{n+1}^{Lin}\right)^{T}.\left(\delta \boldsymbol{u}^{Tan} + \Delta \boldsymbol{u}_{n+1}^{Lin}\right)}}\right]$$

7. Update the incremental and total displacement factor:

$$\Delta\lambda^{m} = \delta\lambda \quad ; \quad \lambda^{m} = \lambda^{m-1} + \Delta\lambda^{m}$$

8. Define the increment of the microscopic displacement field and the total microscopic displacement field:

$$\Delta \boldsymbol{u}_{n+1}^{m} = \left(\Delta \boldsymbol{u}_{n+1}^{Lin} + \delta \boldsymbol{u}^{Tan}\right)\Delta\lambda^{m} \quad ; \quad \boldsymbol{u}_{n+1}^{m}\{\boldsymbol{y}\} = \boldsymbol{u}_{n+1}^{m-1}\{\boldsymbol{y}\} + \Delta \boldsymbol{u}_{n+1}^{m}$$

9. Solve the micro-equilibrium problem **with** $\lambda = Constant$:

$$\boldsymbol{f}^{int}\left\{\boldsymbol{u}_{n+1}^{m,(j)}\{\boldsymbol{y}\}\right\} + \boldsymbol{K}_{T}\left\{\boldsymbol{u}_{n+1}^{m,(j)}\{\boldsymbol{y}\}\right\}\delta\widetilde{\boldsymbol{u}}\{\boldsymbol{y}\}^{m,(j+1)} = \boldsymbol{0}$$

IF (*Fails*) THEN:

- Redefine l, $l^{m} = 0.5l^{m}$
- GOTO (3).

ELSEIF (*Converge*) THEN:

IF ($\lambda^{m} = 1$) THEN

- Compute and store the macroscopic stress tensor $\boldsymbol{P}_{n+1}\{\boldsymbol{x}\}$ (Equation (3.34));
- Consider $\widetilde{\boldsymbol{u}}^{est}$ as the initial guess for the *Newton-Raphson* method and using β_n compute the tangent operator tensor $\mathbf{A}_{n+1}\{\boldsymbol{x}\}$ (exclusively for coupled multi-scale problems) by using Equation (3.41).
- EXIT

ELSE

- Update l according to the number of iterations used (Expression (4.22));
- GOTO (2).

ENDIF

ENDIF

4.2.3 Solution Procedure

In the previous sections, we have addressed different numerical techniques that can be used, either separately or combined, with the *Newton-Raphson* method to build a more advanced solution procedure for multi-scale models. These strategies can be used in two main contexts: for the analysis of a single RVE under prescribed macroscoscopic strain histories or for fully coupled multi-scale analysis with the ML-FEM framework.

For the ML-FEM analysis there are several well established solution strategies available for the macro-scale problem which are addressed in detail in the literature [6, 65, 106, 107], but fall outside of the scope of this work.

4.3 Numerical results

In this section, the effectiveness of the numerical strategies addressed in this document will be investigated through the analysis of three distinct problems. In the first one, a honeycomb RVE will be subjected to a purely compressive deformation gradient, which simultaneously triggers material and geometrical non-linearities. Then, a square RVE containing a circular void at the center will be subjected to a wide range of macroscopic deformation gradients. Finally, a homogenization-based multi-scale problem, whose associated macro-structure is a plane-strain specimen commonly employed for the characterization of ductile materials, will be presented.

4.3.1 Hexagonal honeycomb RVE

The main goal of this numerical example is to assess the ability of the proposed numerical schemes to solve a problem where both material and geometrical non-linearities take place. It is worth mentioning that this kind of problems can be extremely challenging using conventional solution strategies. In fact, without resorting to improved numerical tools, the solution of problems involving phenomena like softening, snap-through and snap-back may be extremely inefficient and computationally expensive.

The two dimensional honeycomb RVE presented in Figure 4.2 was discretized with the eight-noded isoparametric quadrilateral element, amounting to a total of 1804 elements. This element was used with a four-*Gauss* point reduced numerical integration rule (2×2 *Gauss* points instead of 3×3) to avoid the phenomenon of volumetric "locking". Each segment has a length equal to 0.1 mm and a thickness of 0.01 mm. For the present example, a plane strain condition was assumed. With regard to the material, an

hyperelastic *Ogden* constitutive model was selected. The material parameters are listed in Table 4.3.

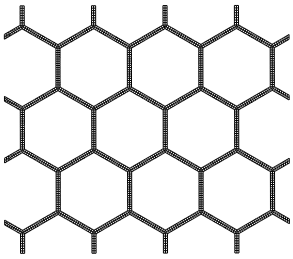

FIGURE 4.2: Mesh of the hexagonal honeycomb RVE.

TABLE 4.3: Properties for the honeycomb RVE.

Parameter	**Value**
μ_1	$5MPa$
α_1	2
μ_2	$2MPa$
α_2	-2
Bulk Modulus, B	$50MPa$

In order to trigger geometrical instabilities (i.e., causing buckling effects), the RVE is subjected to a purely compressive deformation gradient

$$\boldsymbol{F} = \begin{bmatrix} 1.0 & 0.0 \\ 0.0 & 0.85 \end{bmatrix}. \tag{4.26}$$

Only the *Linear* boundary condition has been assumed. Note that providing a detailed comparison between the physical behaviour of foams with homogenization-based RVE analysis is out of the scope of this contribution. A discussion related to this issue may be found in [112]. Our intention here is rather to show the enhancement achieved in the convergence when the proposed numerical schemes are adopted. It is also relevant to mention that, for this particular example, the parameter $NITER^{(j)}$ used in the Arc-Length method was set to 5. With regard to the maximum number of *Line Search* iterations, it was set to 5. Moreover, since the main goal is to follow a complex path inherent with the compression of an unstable RVE rather than to obtain exclusively the final configuration/point of its deformation, the displacement factor λ was set to 0.01 at the beginning of the problem.

In Figure 4.3(a), the evolution of the P_{22} component of the homogenized *First Piola-Kirchhoff* stress tensor is plotted as a function of the displacement factor λ. It is easy to conclude that the evolution obtained is highly non-linear incorporating some regions which make its characterization quite complex and difficult to follow from the numerical

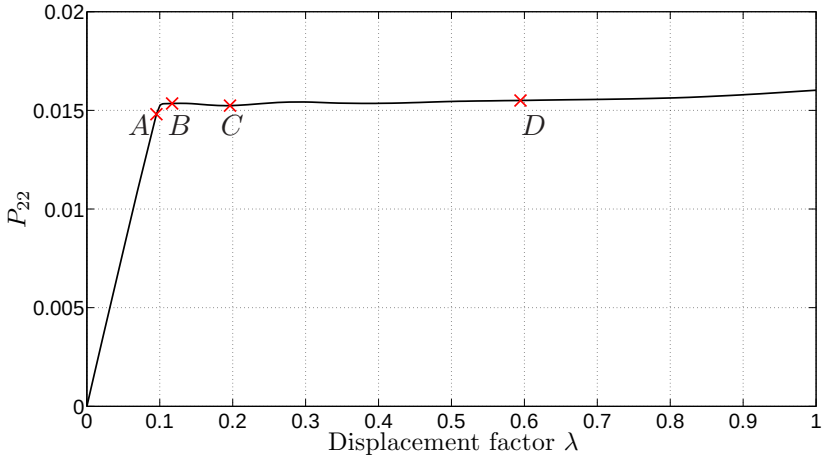

(a) Evolution of P_{22}.

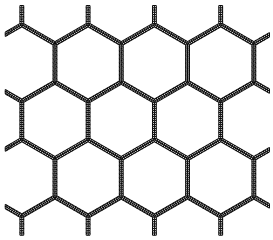

(b) Initial configuration.

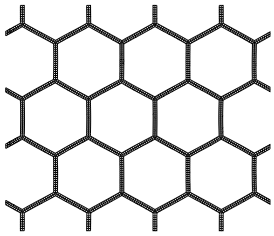

(c) Point A ($\lambda = 0.0892$).

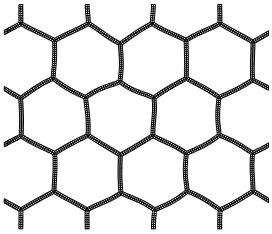

(d) Point B ($\lambda = 0.134$).

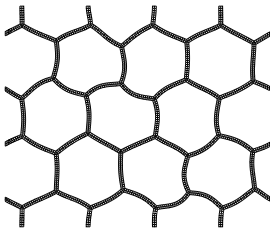

(e) Point C ($\lambda = 0.196$).

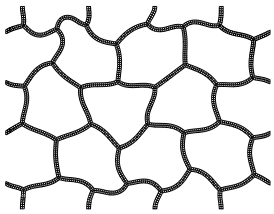

(f) Point D ($\lambda = 0.596$).

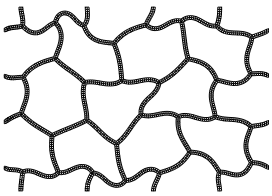

(g) Final configuration ($\lambda = 1.00$).

FIGURE 4.3: Deformation evolution of the foam RVE.

point of view. The first aspect is concerned with the presence of a severe "*knee*", which defines the transition between the linear behaviour, and the "*plateau*" (transition between points A and B). In fact, this transition is well-know for promoting the failure of the *Newton-Raphson* scheme whenever this class of problems is analysed. From the physical point of view, the transition between the linear and "*plateau*" regimes is a consequence of the *buckling* phenomena of the ligaments which are illustrated in Figures 4.3(d) and 4.3(e).

The second source of non-linearity appears in the "*plateau*" region. With a more closer inspection to the curve it is possible to see that P_{22} increases and decreases slightly with the applied displacement, resembling a smooth "*snap-through*" effect (between points B

and D). These effects are a consequence of the loss of the stiffness of the RVE inherent with the buckling phenomena followed by a stiffening of the RVE which results from the bending of the ligaments. It is important to note that more severe "*snap-through*" may take place at the RVE domain and these effects are similar to the ones which occur on conventional macro-scale problems.

Due to the presence of different sources of non-linearity in this problem, two different solution procedures were used to solve the problem. Both employ the incremental division of the *Linear* displacement (described in Section 4.2.2) and the use of the *Line Search* method described (Section 4.2.1). Nevertheless, one of the solution procedures is combined with the modified *Arc-Length* technique.

The solution procedure which incorporates the modified *Arc-Length* technique has shown a remarkable ability to follow the equilibrium path with reasonably sized load increments. A total number of 62 increments was used. On the other hand, when trying to solve the same problem without the *Arc-Length* technique enormous difficulties were encountered, particularly in the transition from the elastic region to the "*plateau*" and whenever there was a drop on P_{22} followed by an increase, failing to converge in most circumstances and requiring an excessive number of increments to achieve the final solution.

4.3.2 RVE with a circular void at its center

The main goal of this example is to show that the convergence of the micro-equilibrium problem can be achieved for larger macroscopic deformation gradients with the use of the numerical strategies proposed in this contribution. To this end, a square RVE with a circular void at center corresponding to a void volume fraction of 12.5%, is modelled by a non-linear constitutive law and is subjected to a wide range of admissible deformation states in the volumetric and pure shear strain directions. In order to promote different deformations states, the RVE is subjected to the following deformation gradient:

$$\boldsymbol{F} = \begin{bmatrix} 1.0 + \alpha \times 0.05 & \beta \times 0.05 \\ 0.0 & 1.0 + \alpha \times 0.05 \end{bmatrix}, \tag{4.27}$$

where α and β are parameters which can range between 0 and 1. In the limit, when $\alpha = 1$ and $\beta = 0$ the RVE is subjected to a pure bi-axial traction. In turn, $\alpha = 0$ and $\beta = 1$ corresponds to a pure shear deformation state.

The RVE was discretized using 320 quadratic quadrilateral elements (8-noded) with reduced integration (2×2) and *plane strain* condition was considered (Figure 4.4). A *von Mises* elasto-plastic constitutive model was adopted with *Young*'s modulus $E = 70\ GPa$,

Poisson ratio $v = 0.3$, initial yield stress $\sigma_0 = 243\ MPa$ and linear hardening modulus $H = 0.2\ GPa$.

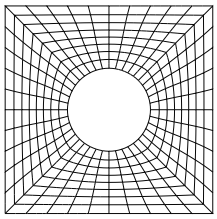

FIGURE 4.4: Mesh of the RVE: 320 quadratic quadrilateral elements (8-noded) with reduced integration.

Similar to the previous example, the maximum number of *Line Search* iterations was set to 5. However, for this example, the ideal number of iterations for the modified *Arc-Length* method coupled with the *Incremental* scheme, $NITER^{(j)}$, was set to 8.

4.3.2.1 RVE with a circular void at the center - *Line Search.*

We start by presenting the numerical results obtained when only the *Line Search* strategy is employed to solve the equilibrium of the RVE (that is, the incremental strategy is inactive). A limit number of 15 iterations for the *Newton-Raphson* method has been considered in the present study, that is, if convergence has not been attained within 15 iterations, it is considered that convergence has not been achieved.

The results obtained for different deformation states associated with *Linear* and *Periodic* boundary conditions are respectively given in Figures 4.5(a) and 4.5(b). The dark region corresponds to combinations of α and β where the solution was found applying the standard *Newton-Raphson* method. Nevertheless, the light grey region corresponds to combinations of α and β where the equilibrium problem is only solved when the *Line Search* method is used. Close observation to the diagrams shows that the total number of deformation states that can be solved with the combined *Newton-Raphson*/*Line Search* method is significantly higher when compared to the number of cases solved exclusively by the *Newton-Raphson* scheme. Note that this conclusion is valid either for *Linear* or *Periodic* boundary conditions.

In Table 4.4, the convergence rates for the strain state associated with parameters $\alpha = 0.1$ and $\beta = 0.2$, for both boundary conditions analysed in this work are presented. In this table, the values in bold highlight the effect that the *Line Search* approach has on the solution of the problem. While the standard *Newton-Raphson* scheme diverges after a certain number of iterations (4 for *Linear* and 3 for *Periodic*), with the correction

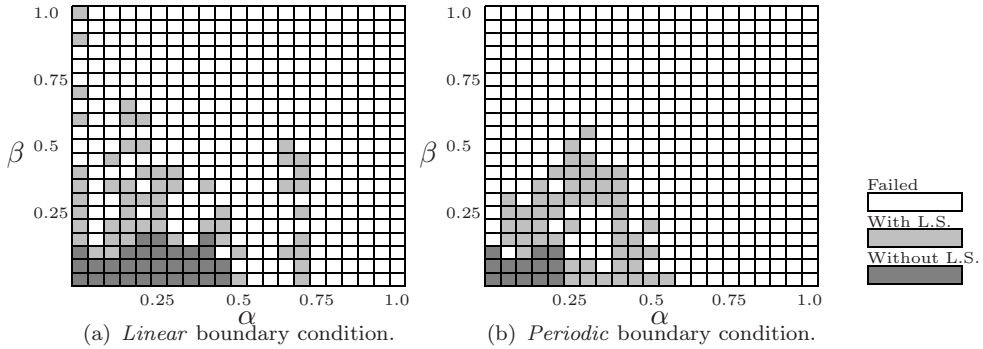

(a) *Linear* boundary condition. (b) *Periodic* boundary condition.

FIGURE 4.5: Map of results obtained when only the *Line Search* technique is used.

carried out by the *Line Search* method, the combined *Newton-Raphson/Line Search* scheme is able to solve the problem.

TABLE 4.4: Convergence rates for $\alpha = 0.1$ and $\beta = 0.2$.

Linear Boundary Condition			*Periodic* Boundary Condition		
W/out *L. S.*	W/ *L. S.*	*L. S.* Iter.	W/out *L. S.*	W/ *L. S.*	*L. S.* Iter.
0.931960	0.931960	0	44.8259	44.8259	0
0.697790	0.697790	0	76.0714	76.0714	0
1.48615	**0.640464**	2	208.246	**87.6270**	2
99.7177	**0.521248**	2	*Diverg.*	**80.6496**	3
Diverg.	**0.429722**	2		**74.6134**	2
	0.293908	1		**60.6393**	1
	$0.279117E-1$	0		7.83018	0
	$0.165097E-2$	0		1.27382	0
	$0.494053E-4$	0		0.243087	0
	$0.250414E-8$	0		$0.260192E-02$	0
				$0.334930E-06$	0

4.3.2.2 RVE with a circular void at the center - Modified *Arc-Length* method.

In this case, only the modified *Arc-Length* method coupled with the incremental strategy proposed in this work is assessed under the same conditions of the previous example. For this case, it is necessary to define in advance the maximum number of admissible increments to solve the problem. According to the authors' experience, 10 increments (including the extra step to guarantee the consistency of a coupled multi-scale model) is a reasonable value. This means that if the problem needs more than 10 increments to achieve solution, it is considered that convergence has not been attained. In Figures 4.6(a) and 4.6(b) it is plotted, in colour coded tables, the number of steps required by the incremental algorithm for attaining convergence for different strain states, when *Linear* and *Periodic* boundary conditions are enforced. Each color corresponds to a specific number of increments used and, in turn, the unfilled region is associated to deformation states where more than 10 increments are necessary to solve the equilibrium of the RVE.

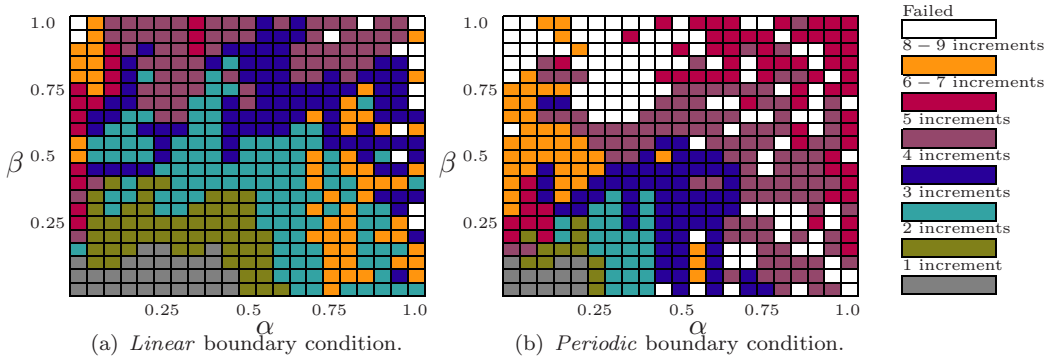

(a) *Linear* boundary condition. (b) *Periodic* boundary condition.

FIGURE 4.6: Map of results obtained when exclusively the modified *Arc-Length* method coupled with the incremental scheme is used.

Analysing Figures 4.6(a) and 4.6(b), it is possible to conclude that, with the incremental approach introduced in this work, the solution of the RVE problem can be found for a wider range of deformation states. Nevertheless, this result is more pronounced for *Linear* boundary condition. It is important to note that the solution of the micro-equilibrium problem without the proposed incremental algorithm is only achieved for a small range of deformation gradients represented by the one step region of Figures 4.6(a) and 4.6(b) (the grey region). It is also possible to conclude that the beneficial effect of the incremental approach is more noticeable when the prescribed deformation gradient has a dominant strength component.

The solution of the problem could also be obtained using the incremental strategy with a fixed number of increments, without the use of the modified *Arc-Length* technique. In this case, all increments would have the same size, which results from the division of the total increment by the maximum number of increments defined for the problem. This strategy is clearly not very efficient since it is not related to the nature of the problem and its evolution. On the other hand, the solution presented here with the modified *Arc-Length* technique coupled with the incremental strategy is able to efficiently solve the problem. Although it is necessary to solve an additional system of equations for the calculation of the tangential displacement, $\delta \boldsymbol{u}^{Tan}$, as well as the increment displacement factor, $\Delta\lambda^m$, since the tangential displacement field is also used to update the total microscopic displacement field, the number of iterations required to attain convergence within each increment is significantly smaller. In addition, since the increment size is adaptively determined, this approach can increase or decrease the size depending on the nature of the problem, leading to a more efficient and robust solution.

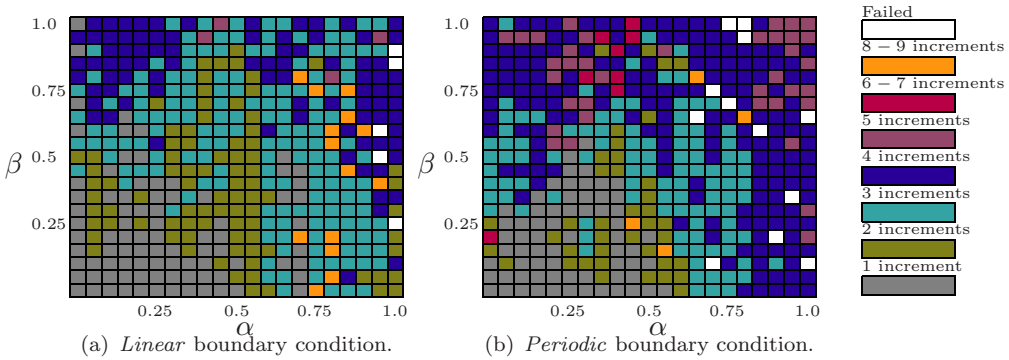

(a) *Linear* boundary condition. (b) *Periodic* boundary condition.

FIGURE 4.7: Map results obtained when both *Line Search* and modified *Arc-Length* schemes are used.

4.3.2.3 RVE with a circular void at the center - *Line Search* & Modified *Arc-Length* method.

In this case, both numerical schemes introduced in this document are combined to solve the problem under analysis in this sub-section. It is also important to remark that the assumptions inherent to each numerical scheme are also kept for this case.

Figures 4.7(a) and 4.7(b) show, for *Linear* and *Periodic* assumption respectively, the number of sub-steps required for achieving convergence for different strain states, defined by parameters α and β. Performing a simple comparison with the results presented in 4.3.2.2, we observe that when the incremental approach is used in conjunction with the combined *Newton-Raphson/Line Search* method, the number of increments is remarkably lower. Note that, in case of *Periodic* boundary condition, for almost the complete range of deformation states triggered by (4.27), it is possible to solve the micro-boundary problem. It clearly illustrates the improvements obtained with the numerical strategies proposed.

The fact that it is possible to achieve convergence of the micro-equilibrium problem for larger macroscopic deformation gradients, when using the numerical strategies addressed in this contribution, has a significant impact on the computational cost. Even though this reduction in the computational burden is, at first glance, restricted to the micro-scale, it has enormous repercussion on the global overall computation time necessary for the solution of coupled multi-scale problems, as it will be discussed in the following example.

4.3.3 Coupled multi-scale test

The purpose of this example is to illustrate the reduction on overall computational cost achieved, with the use of the numerical strategies proposed in the solution of a coupled multi-scale problem. The example consists of a tensile test where the macroscopic specimen is a flat grooved specimen. The geometry of the specimen is illustrated in Figure 4.8(a). The macrostructure was discretized with 80 quadratic quadrilateral finite elements (8-noded) with reduced (2×2) integration (Figure 4.8(b)). With regard to the RVE, the same RVE used in Section 4.3.2 was considered as well as the same material properties. Once again, plane strain condition was assumed.

The macro-structure was subjected to a prescribed vertical displacement of 0.2 mm. The loading scheme adopted in this example consists in incrementally applying a uniform vertical displacement to the top edge of the mesh considering the total number of macroscopic load increments equal to 30. Four different possibilities have been considered in the solution of the present problem: in the first case, the problem was solved using the *Newton-Raphson* method without modifications at the micro-scale; in the second case, the modified *Newton-Raphson* method with the *Line Search* scheme was adopted; the modified *Arc-Length* method coupled with the incremental approach was used in the third case and, finally, in the fourth case, the problem was solved considering both numerical schemes at the fine scale. The list of algorithmic parameters used in the solution of this problem can be found in Table 4.5.

TABLE 4.5: Algorithmic parameters used in the solution of the coupled multi-scale problem.

Algorithmic variables	Value
Maximum number of *Line Search* iterations	5
Ideal number of iterations for the modified *Arc-Length* scheme, $NITER^{(j)}$	8
Maximum number of iterations at each microscopic increment	15
Maximum number of increments at micro-scale (including the extra step to guarantee the consistency of a coupled multi-scale model)	10

As it is possible to observe in Figure 4.9, regardless of the numerical strategy adopted to solve the micro-equilibrium problem, the reaction curves are coincident. However, in order to highlight the benefits of the strategies proposed in the present work, a detailed comparison of the number of increments at the macro-scale, necessary to solve the coupled problem for *Linear* and *Periodic* boundary conditions, as well as the relative CPU time is performed[1]. In Figures 4.10 and 4.11 these two parameters are presented for *Linear* and *Periodic* boundary conditions respectively. Taking as reference the case

[1]The computation of the relative CPU time took as reference value the lowest CPU time used to solve the coupled problem for each boundary condition.

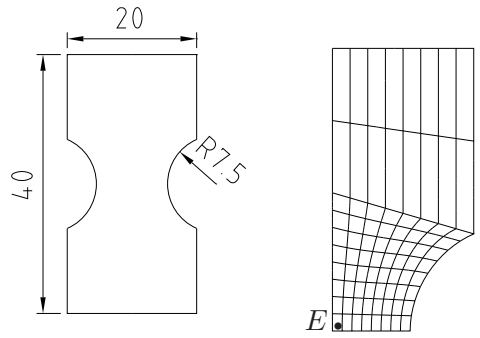

(a) Geometry (in *mm*). (b) Mesh.

FIGURE 4.8: Specimen for coupled multi-scale problem.

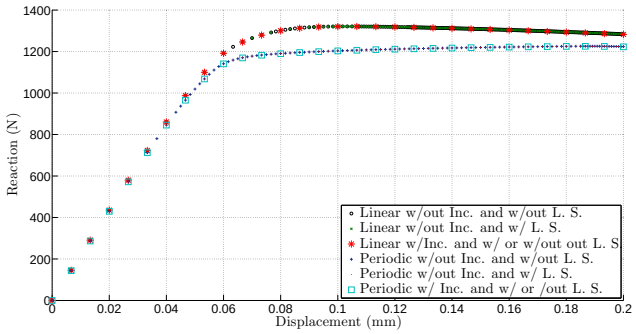

FIGURE 4.9: Reaction curves for *Linear* and *Periodic* boundary conditions obtained with different numerical strategies.

where the standard *Newton-Raphson* is used to solve the micro-equilibrium problem (labeled *W/out L.S.* and *W/out Inc. Apr.* in Figures 4.10 and 4.11), it is clear that the number of macroscopic increments and the relative CPU time significantly decreased with the numerical strategies discussed in this work.

When the conventional *Newton-Raphson* is used, 235 and 111 increments are necessary at the macro-scale to solve the coupled problem for *Linear* and *Periodic* boundary conditions respectively. This means that, due to the failure of the standard *Newton-Raphson* scheme at the micro-scale, it was necessary to cut the macroscopic load increment in half and try to solve the new macroscopic increment. This procedure was repeated whenever necessary. However, when this method is combined with the *Line Search* scheme (labeled "W/ L.S. and W./out Inc. Apr." in Figures 4.10 and 4.11), it is possible to reduce these numbers to 144 and 85 respectively. In addition, the use of this strategy has a significant influence on the reduction of the computational time, 33%/18% for *Linear*/*Periodic* boundary conditions. In turn, when the modified *Arc-Length* coupled with the incremental method was adopted (labeled "W/out L.S. and W/ Inc. Apr." in Figures 4.10 and 4.11), for both boundary conditions, the problem was solved using just 30

increments, which was the target number of macroscopic increments. The overall reduction of the computational time, for this numerical strategy was remarkable: 78%/49% for *Linear*/*Periodic* boundary conditions. When both numerical methods were simultaneously used, once more the problem was solved using just 30 macroscopic increments. The reduction of the computational time, when both strategies are combined, is equal to 78%/64% for *Linear*/*Periodic* boundary conditions, which means that there was an additional reduction for *Periodic* boundary conditions. With a deeper analysis of the results, it is possible to conclude that from the two numerical schemes proposed in this document, the modified *Arc-Length* coupled with the incremental framework is the one which leads to the more noticeable CPU reduction time. However, the implementation of both numerical schemes ensures that the problem will be always efficiently solved.

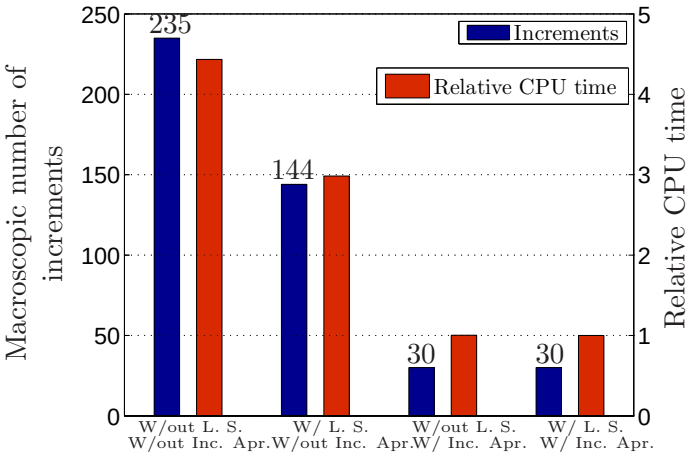

FIGURE 4.10: Number of macroscopic increments and relative CPU time for *Linear* boundary condition.

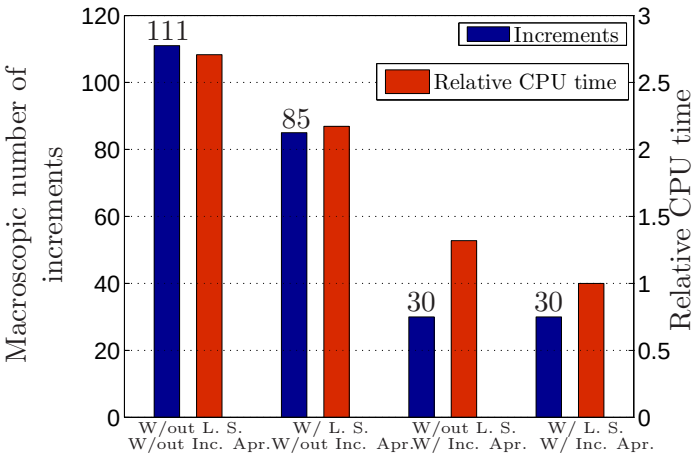

FIGURE 4.11: Number of macroscopic increments and relative CPU time for *Periodic* boundary condition.

The convergence rate of the macroscopic *Newton-Raphson* procedure at the 20^{th} macroscopic increment is listed in Table 4.6(a) when *Periodic* boundary condition is considered. In Table 4.6(b), the convergence of the residuals for the micro *Newton-Raphson* procedure, for the RVE located in point E (Figure 4.8(b)), at the 3^{rd} iteration of the 20^{th} macroscopic increment is listed. The first attempt to solve the micro-equilibrium problem, with a displacement factor of $\lambda = 1$, fails and the modified *Arc-Length* method coupled with the incremental procedure is activated. This solution procedure computes a new displacement factor, $\lambda_1 = 0.6003$, and tries to find a solution. The solution of the first microscopic increment, associated with $\lambda_1 = 0.6003$ requires seven iterations to converge resorting to the use of the *Line Search* method twice (in iterations 2 and 3). After the solution for the first microscopic increment, a new displacement factor is computed, $\lambda_2 = 1.0000$. The solution of the second microscopic increment associated with λ_2 only requires three iterations to converge and does not resort to the use of the *Line Search* technique. Finally, the total displacement fluctuation field obtained at the end of the second microscopic increment is employed, in an additional increment, as an improved initial guess by the *Newton-Raphson* method. In this last stage, the RVE is subjected to the total *Linear* displacement, which results from the total macroscopic deformation gradient.

As expected, the convergence of residuals at both macro and micro scales is quadratic as it is possible to observe in Table 4.6. This is a direct consequence of the use of the exact tangent matrices at both micro and macro scales, and the use of the final step at the micro scale to ensure the consistency of the macroscopic problem.

TABLE 4.6: ML-FEM problem: convergence rates at macro and micro domains for point E (Figure 4.8 b)) at the macroscopic increment number 20 for *Periodic* boundary condition.

(a) Macroscopic convergence

Iterations at the Macro-scale	Convergence
1	0.1026
2	$0.6745E-03$
3	$0.6915E-07$

(b) Microscopic convergence for macroscopic iteration number 3.

Incremental displacement factor, λ	Iterations	L. S. Iterations	Convergence
First attempt, $\lambda = 1$	FAILS	-	-
$\lambda_1 = 0.6003$	1	0	21.0109
	2	2	**20.4726**
	3	1	**36.4287**
	4	0	1.5292
	5	0	$0.7201E-01$
	6	0	$0.8435E-04$
	7	0	$0.2539E-09$
$\lambda_2 = 1.0000$	1	0	0.4755
	2	0	$0.1402E-02$
	3	0	$0.5414E-07$
Extra increment $\lambda = 1.0000$	1	0	0.2622
	2	0	$0.6856E-03$
	3	0	$0.1853E-07$

4.4 Conclusions

In this work, several numerical strategies have been investigated to develop more efficient and robust solution procedures for homogenization-based multi-scale constitutive models at finite strains. Firstly, the well-established *Line Search* method which is typically employed in conventional non-linear finite element problems was conveniently modified and extended in the solution of the discrete RVE boundary value problem. Finally, a new adaptive incremental approach for the solution of the micro-equilibrium problem was proposed inspired on the standard *Arc-Length* method. To ensure the consistency of the macroscopic equilibrium problem, the solution of the micro-equilibrium problem was employed as an improved initial guess, in the solution of ML-FEM problems.

The presented numerical examples have demonstrated that the proposed procedures produce a dramatic improvement in the robustness and efficiency of the *Newton-Raphson* scheme of the discrete RVE boundary value problem. The examples clearly illustrate that these procedures are able to ensure the convergence of the solution algorithm in the presence of several sources of non-linearity allowing larger macroscopic deformation gradients to be prescribed. The improvement is particularly noticeable when all the techniques are combined, nevertheless, they can also be employed separately. The proposed methodologies also dramatically reduce the overall computational cost of ML-FEM analyses, which was reduced up to four times in our analyses, and preserve the quadratic rates of asymptotic convergence that characterize the *Newton-Raphson* scheme at the macroscopic level.

Chapter 5

A new enforcement of Periodic boundary condition for arbitrary meshes based on *Mortar* decomposition method

5.1 Introduction

The design of new materials is one of the most challenging tasks in engineering science that has been continuously fostered by the increasing requirements of novel applications. Since the response of the material at the macroscopic level is a direct consequence of the material microstructural geometry and evolution, the establishment of relationships between the microstructure and the macroscopic properties of materials has attracted considerable research efforts. In recent years, a general modelling framework, the so-called multilevel finite element framework (ML-FEM) or FE^2 [36, 37, 92, 95, 96], has been developed to capture the behaviour of heterogeneous materials. The underlying idea of the method is to extract the quantities required for the macro-scale by solving a micro-scale problem over a statistically representative volume element (RVE). This modelling framework allows an effective description of complex microstructural geometries, arbitrary constitutive material behaviour and microstructural evolution. Nevertheless, some disadvantages have also been associated with the ML-FEM such as the computational cost that the solution of multi-scale problems incurs [49, 50, 103, 104, 113] or the loss of representativeness of the RVE when softening regimes are reached [52, 84].

In the ML-FEM framework, the definition of the size of the RVE problem is extremely important since it should be large enough to statistically represent the microstructure of the material. In contrast, as the size of the RVE problem increases, memory storage and computational requirements can become prohibitive. This is due to the fact that in the ML-FEM framework the macroscopic equilibrium problem is solved simultaneously with one microscopic RVE problem for each point of the macroscopic mesh. Another important feature of this technique is the definition of the boundary condition to apply for the RVE problem. There are three classic kinematical constraints: *Linear* boundary displacements, *Uniform boundary Tractions* and *Periodic* boundary fluctuations. Several numerical studies have shown [87, 88] that the *Periodic* boundary condition (PBC) is the one that converges faster to the theoretical/effective solution when the RVE size increases. This means that for the same RVE size, the PBC delivers a better estimation of the effective properties. Therefore, due to its representativeness and computational efficiency, this contribution focuses on the enforcement of PBCs for randomly generated meshes.

The classical approach for applying the PBC consists on the enforcement of an identical displacement fluctuation field for each pair of corresponding boundaries of the RVE. This forces the RVE to be discretized with a conform mesh on opposite boundaries, i.e. the finite element mesh topology has to be such that a one-to-one correspondence exists between nodes of opposing sides of the RVE boundary [37, 78]. Although for some simple RVE geometries this requirement may be easily met using commercial pre-processors or even dedicated mesh generation algorithms [114], this is not generally the case. For instance, if the microstructure does not have geometrical periodicity, which is the most frequent case for microstructures obtained from real image processing, the mesh will not probably be conform. Furthermore, this requirement is also quite restrictive within the context of the finite element method. In particular, it is extremely challenging to develop an adaptive remeshing strategy, which employs an unstructured mesh generator, that always generates a conform mesh. In addition, the introduction of discontinuities at the RVE level, which is a rapidly expanding topic [55, 56, 59, 62, 63], would also be very difficult to accommodate.

In order to circumvent the requirement of having conform meshes, several solutions have been proposed. A surface-to-surface constraint has been suggested in [115, 116], which can be found in some commercial finite element codes. In this case, the boundary of the RVE is split into master and slave parts where the nodes embedded in the slave domain are prescribed and defined by the closest nodes on the opposite edge/surface (master domain) by interpolation. Despite its simplicity, this approach suffers from lack of robustness when the master and slave edges/surfaces have a different node density. A slightly different approach was proposed in [117] and recently enhanced and optimized

in [118]. In this approach, the displacement field at two opposite sides of the RVE is interpolated by linear combinations of shape functions which need to satisfy some constraints. A different solution was proposed in [119] by introducing an independent finite element discretization of the boundary tractions.

In this work, a different strategy is proposed to enforce PBCs on RVE problems with an arbitrary finite element mesh discretization. This approach is inspired on the mortar method [1], which was originally introduced in the context of domain decomposition techniques. This method is able to efficiently enforce interface constraints over interacting non-conform domains in a variationally consistent way based on the *Lagrange* multiplier method. An essential feature of the method is the introduction of interface conditions in an integral (weak) form instead of strong, point wise constraints. Furthermore, the mortar method is able to preserve optimal convergence rates from the finite element methods as long as appropriate mortar spaces are chosen. The use of the so-called dual *Lagrange* multipliers spaces [120] allows for an efficient local elimination of the discrete *Lagrange* multipliers by static condensation. These advantages have led to the application of the mortar method in different computational fields such as contact problems [5, 121–125] and recently in fluid-solid interaction problems [126].

The present Chapter is structured as follows. In Section 5.2, the new strategy to enforce PBC is introduced where the spatial discretization of the RVE equilibrium problem based on standard and dual bases is presented, followed by details on the evaluation of the integrals, for both two and three dimensional problems. Finally, in order to demonstrate the efficiency of the method, Section 5.3 presents several numerical examples to assess the results, followed by some conclusions.

5.2 Periodic boundary condition enforcement

A new approach for the enforcement of PBCs based on the *Mortar* decomposition method will be introduced in this Section for two and three dimensional problems. The mortar discretization will be combined with the *Lagrange* multiplier method in an integral (weak) form. Spatial discretization of the RVE equilibrium problem based on standard and dual *Lagrange* multipliers will be presented followed by details on the numerical integration of the *Mortar* coefficients. Two alternative schemes are obtained: a *Force-Displacement* (where the *Lagrange* multipliers method is considered) or a *Fully-Displacement* based scheme.

Remark 5.1. In line with the standard admissible kinematical boundary conditions introduced in Section 3.2.6, the body force field will be considered null, $\boldsymbol{B}\{\boldsymbol{y}, t\} = \boldsymbol{0}$. This is a necessary assumption in order to satisfy the *Hill-Mandel* condition (3.10).

Remark 5.2. For sake of clarity, the nomenclature concerned with the time/pseudo-time in the present Chapter will be omitted since all parameters and variables, which will be used in what follows, are defined at instant t_{n+1}. Furthermore, the explicit representation of the set of internal variables in the *First Piola-Kirchhoff* stress tensor will also be dropped.

5.2.1 Mixed variational formulation

Expressing the equation that governs the RVE equilibrium problem, Equation (3.21), as a function of the displacement fluctuation field, leads to:

$$\int_{\Omega_0} \hat{\boldsymbol{P}}\left\{\boldsymbol{F}\left\{\boldsymbol{y}\right\}\right\} : \nabla_{\boldsymbol{p}} \widetilde{\boldsymbol{u}}\left\{\boldsymbol{y}\right\} dV - \int_{\partial\Omega_0} \boldsymbol{T}^{ref}\left\{\boldsymbol{y}\right\} . \widetilde{\boldsymbol{u}}\left\{\boldsymbol{y}\right\} dA = 0. \tag{5.1}$$

Due to the decomposition of the boundary of the RVE for PBC, described in Section 3.2.6.2, the previous equation can be re-written as:

$$\begin{aligned}\int_{\Omega_0} \hat{\boldsymbol{P}}\left\{\boldsymbol{F}\left\{\boldsymbol{y}\right\}\right\} : \nabla_{\boldsymbol{p}} \widetilde{\boldsymbol{u}}\left\{\boldsymbol{y}\right\} dV - \int_{\Gamma_0^+} \boldsymbol{T}^{ref}\left\{\boldsymbol{y}^+\right\} . \widetilde{\boldsymbol{u}}\left\{\boldsymbol{y}^+\right\} dA \\ - \int_{\Gamma_0^-} \boldsymbol{T}^{ref}\left\{\boldsymbol{y}^-\right\} . \widetilde{\boldsymbol{u}}\left\{\boldsymbol{y}^-\right\} dA = 0,\end{aligned} \tag{5.2}$$

where the integral over $\partial\Omega_0$ was conveniently split. Owing to the *anti-periodic* traction field (Equation (3.14)) associated to a PBC, we eliminate the integral over the negative part of the boundary, Γ_0^- , and Equation (5.2) can be simplified:

$$\int_{\Omega_0} \hat{\boldsymbol{P}}\left\{\boldsymbol{F}\left\{\boldsymbol{y}\right\}\right\} : \nabla_{\boldsymbol{p}} \widetilde{\boldsymbol{u}}\left\{\boldsymbol{y}\right\} dV + \int_{\Gamma_0^+} \boldsymbol{T}^{ref}\left\{\boldsymbol{y}^-\right\} . \left(\widetilde{\boldsymbol{u}}\left\{\boldsymbol{y}^+\right\} - \widetilde{\boldsymbol{u}}\left\{\boldsymbol{y}^-\right\}\right) dA = 0. \tag{5.3}$$

Considering relation (3.13), it is possible to define a *gap* function, $\boldsymbol{g}$, as being the difference between the displacement fluctuation of a node on the positive domain, $\widetilde{\boldsymbol{u}}\left\{\boldsymbol{y}^+\right\}$, and the displacement fluctuation of a node on the negative domain, $\widetilde{\boldsymbol{u}}\left\{\boldsymbol{y}^-\right\}$, located on opposite sides of the RVE, with the same relative coordinates:

$$\boldsymbol{g} = \|\widetilde{\boldsymbol{u}}\left\{\boldsymbol{y}\right\}\| = \widetilde{\boldsymbol{u}}\left\{\boldsymbol{y}^+\right\} - \widetilde{\boldsymbol{u}}\left\{\boldsymbol{y}^-\right\} = \boldsymbol{0}, \tag{5.4}$$

where the symbol "$\|*\|$" denotes the "*jump*" of variable "$*$". Thus, with $\boldsymbol{g}$ function at hand, it is possible to write

$$\int_{\Omega_0} \hat{\boldsymbol{P}}\left\{\boldsymbol{F}\left\{\boldsymbol{y}\right\}\right\} : \nabla_{\boldsymbol{p}} \widetilde{\boldsymbol{u}}\left\{\boldsymbol{y}\right\} dV + \int_{\Gamma_0^+} \boldsymbol{T}^{ref}\left\{\boldsymbol{y}^-\right\} . \boldsymbol{g}\, dA = 0. \tag{5.5}$$

The last term of the previous equation represents the global constraint for a PBC, which takes into account constraints (3.13) and (3.14). Thus, it is possible to conclude that the *Hill-Mandel* condition (3.9) and the *minimal kinematical constraint*, mathematically defined by Equation (3.5), are automatically satisfied.

In preparation of a mixed variational formulation, the *Lagrange* multiplier method is employed here to enforce the global constraint introduced in Equation (5.5). In fact, the use of the *Lagrange* multiplier method can be viewed as a requisite of the *Mortar* method since, the *key* idea of the method consists on a suitable spatial discretization of the *Lagrange* variable, which will be derived in Section 5.2.2. Replacing the traction force field, $\boldsymbol{T}^{ref}\{\boldsymbol{y}^{-}\}$, with the *Lagrange* multiplier vector, $\boldsymbol{\lambda}$, in Equation (5.5) results:

$$\int_{\Omega_0} \hat{\boldsymbol{P}}\{\boldsymbol{F}\{\boldsymbol{y}\}\} : \nabla_{\boldsymbol{p}} \widetilde{\boldsymbol{u}}\{\boldsymbol{y}\}\, dV + \int_{\Gamma_0^+} \boldsymbol{\lambda}.\boldsymbol{g} dA = 0. \tag{5.6}$$

It is important to mention that the vector, $\boldsymbol{\lambda}$, includes both normal and tangential tractions forces acting over the boundary of the RVE, $\partial\Omega_0$. By performing the infinitesimal variation of Equation (5.6), we finally arrive to the weak form of the equilibrium problem at the RVE level for PBC:

$$\int_{\Omega_0} \hat{\boldsymbol{P}}\{\boldsymbol{F}\{\boldsymbol{y}\}\} : \nabla_{\boldsymbol{p}}\, \delta\, \widetilde{\boldsymbol{u}}\{\boldsymbol{y}\}\, dV + \int_{\Gamma_0^+} \delta\boldsymbol{\lambda}.\boldsymbol{g} + \boldsymbol{\lambda}.\delta\boldsymbol{g} dA = 0. \tag{5.7}$$

It is possible to distinguish three terms inherent to the deformation of the RVE for PBC in Equation (5.7). The first, which corresponds to the volume integral, represents the variation of the virtual work associated with the internal forces of the different constituents/phases embedded in the RVE. The remaining two terms, represent, respectively, the enforcement of the kinematical constraints and the variation of the virtual work associated with the traction forces, $\boldsymbol{\lambda}$, acting over Γ^+.

5.2.2 Spatial discretization with the Mortar Element Method

The spatial discretization of the RVE equilibrium equation for PBC (Equation (5.7)) will be presented in this Section. The mortar element method, which is usually employed to couple fields between potentially mismatched surfaces in a weak integral sense, is employed here as an alternative spatial discretization method. Firstly, the spatial discretization of the RVE domain, Ω, is performed with the finite element method. The usual finite dimensional subspaces of solution, $\mathcal{V}^d \subset \mathcal{V}$, and weighting spaces, $\mathcal{U}^d \subset \mathcal{U}$, are introduced. Therefore, the spatial discretization of the RVE domain, Ω, using a set

of of finite elements is given by:

$$\Omega_0 \approx \Omega_0^d = \bigcup_{e=1}^{N_{elem}} \Omega_{0_e}, \tag{5.8}$$

where the index $(*)^d$ denotes the discretized version of the variable/domain $(*)$ and the symbol $\bigcup$ represents an appropriate *assembly* operator. As a consequence, we obtain the RVE surface finite dimensional subspace $\mathcal{W}^d \subset \mathcal{W}$, which is a simple trace space restriction of $\mathcal{V}^d$ to the respective RVE surfaces. In this work, for two-dimensional problems, we use bilinear finite elements (4 nodded elements) to discretize the domain of the RVE. The shape functions for the mortar approximation on the surfaces of the RVE are directly related to the shape functions on the domain due to the trace property. Therefore, the surface interpolation consists of linear line elements (2 nodded elements). In the three dimensional case, we focus on linear *Lagrangian* elements (4 nodded elements) for the domain and two dimensional linear triangular elements (3 nodded elements) for the RVE surface interpolation. Nevertheless, the approach can be extended for use with higher order elements without conceptual difficulty.

Let us assume that the positive, Γ_0^+, and negative, Γ_0^-, domains of the undeformed boundary of the RVE, $\partial\Omega_0$, are discretized by a different number of surfaces:

$$\Gamma_0^+ \approx \Gamma_0^{+,d} = \bigcup_{s=1}^{N_s^+} \Gamma_{s_0}^+, \tag{5.9a}$$

$$\Gamma_0^- \approx \Gamma_0^{-,d} = \bigcup_{s=1}^{N_s^-} \Gamma_{s_0}^-, \tag{5.9b}$$

where $\Gamma_0^{+,d}$ and $\Gamma_0^{-,d}$ denote, respectively, the discretized positive and negative domains whereas N_s^+ and N_s^- correspond to the number of elements used in the discretization of Γ_0^+ and Γ_0^-. In agreement, $\Gamma_{s_0}^+$ and $\Gamma_{s_0}^-$ denote the domain of an element at positive and negative surfaces.

Based on the above definitions, the discretized version of Equation (5.7) is given by:

$$\int_{\Omega_0^d} \boldsymbol{G}^T \hat{\boldsymbol{P}}\left\{\boldsymbol{F}\left\{\boldsymbol{y}\right\}\right\} dV \delta\, \widetilde{\boldsymbol{u}} + \bigcup_{s=1}^{N_s^+} \int_{\Gamma_{s_0}^+} \delta\boldsymbol{\lambda}_s.\boldsymbol{g}_s + \boldsymbol{\lambda}_s.\delta\boldsymbol{g}_s dA = 0, \tag{5.10}$$

where matrix $\boldsymbol{G}$ denotes the discretized version of the gradient operator, $\nabla_{\boldsymbol{p}}$. However, since opposite surfaces of the RVE may be discretized with a different number of elements, the *gap* function, $\boldsymbol{g}$, and the *Lagrange* parameter, $\boldsymbol{\lambda}$, need to be conveniently discretized in order to take into account the different densities of elements at opposite surfaces.

For a generic point p, the displacement fluctuation, $\widetilde{\boldsymbol{u}}_p$, and its local coordinates, $\boldsymbol{y}_p$, can be determined by interpolation of their nodal counterparts, $\widetilde{\boldsymbol{u}}_n$ and $\boldsymbol{y}_n$ as:

$$\begin{aligned}
&\text{On the positive surface, } \Gamma_{s_0}^{+}: \quad \widetilde{\boldsymbol{u}}_p^{+}\left\{\boldsymbol{\xi}\right\} = \textstyle\sum_{i=1}^{N_{nodes}} N_i\left\{\boldsymbol{\xi}_p\right\}\widetilde{\boldsymbol{u}}_{n_i}^{+}, \\
&\qquad\qquad\qquad\qquad\qquad\quad \boldsymbol{y}_p^{+}\left\{\boldsymbol{\xi}\right\} = \textstyle\sum_{i=1}^{N_{nodes}} N_i\left\{\boldsymbol{\xi}_p\right\}\boldsymbol{y}_{n_i}^{+}, \\
&\text{On the negative surface, } \Gamma_{s_0}^{-}: \quad \widetilde{\boldsymbol{u}}_p^{-}\left\{\boldsymbol{\zeta}\right\} = \textstyle\sum_{i=1}^{N_{nodes}} N_i\left\{\boldsymbol{\zeta}_p\right\}\widetilde{\boldsymbol{u}}_{n_i}^{-}, \\
&\qquad\qquad\qquad\qquad\qquad\quad \boldsymbol{y}_p^{-}\left\{\boldsymbol{\zeta}\right\} = \textstyle\sum_{i=1}^{N_{nodes}} N_i\left\{\boldsymbol{\zeta}_p\right\}\boldsymbol{y}_{n_i}^{-}.
\end{aligned} \tag{5.11}$$

where $N_i\left\{\boldsymbol{\xi}_p\right\}$ and $N_i\left\{\boldsymbol{\zeta}_p\right\}$ denote, respectively, the interpolation functions associated to an element at the positive and negative domains with N_{nodes} nodes. At this moment, it is convenient to introduce the nomenclature commonly used when the *Mortar* decomposition method is applied, which will be followed in this work. Hence, the surface where the global kinematical constraint is defined (surface integral of Equation (5.7)) will correspond to the *non-Mortar* domain, Γ_0^{+}, whereas the other surface, Γ_0^{-} to the *Mortar* domain. Moreover, in what follows, symbols $\boldsymbol{\xi}$ and $\boldsymbol{\zeta}$ will represent, respectively, an integration *Gauss* point at the positive/*non-Mortar* and negative/*Mortar* domains.

The *Lagrange* multipliers, which represents the traction forces acting over the boundary of the RVE, is defined at the discretized *non-Mortar* surface by means of the interpolation functions, $M_i\left\{\boldsymbol{\xi}_p\right\}$:

$$\boldsymbol{\lambda}_p\left\{\boldsymbol{\xi}\right\} = \sum_{i=1}^{N_{nodes}} M_i\left\{\boldsymbol{\xi}_p\right\}\boldsymbol{\lambda}_{n_i}, \tag{5.12}$$

where $\boldsymbol{\lambda}_{n_i}$ denotes the nodal traction forces of the *non-Mortar* segment. In order to obtain a consistent discretization of the *Lagrange* parameter, the interpolation functions, $M_i\left\{\boldsymbol{\xi}_p\right\}$, need to satisfy the *Babuska-Brezzi* (B-B) condition (for more details see [1, 127, 128]). These interpolation functions will be presented in detail, for two and three dimensional cases, in Section 5.2.4.

It is desirable to have a smooth evolution of the *gap* function, $\boldsymbol{g}$, throughout the discretized boundary of the RVE, $\partial\Omega^d$. This is achieved by establishing a relation between $\boldsymbol{\xi}$ and $\boldsymbol{\zeta}$. As can be seen in Figure 5.1 for two dimensional problems, for each integration *Gauss* point of the *non-Mortar* domain, $\boldsymbol{\xi}_p$, there is a corresponding point, $\boldsymbol{\zeta}\left\{\boldsymbol{\xi}_p\right\}$, at the *Mortar* domain, which needs to be determined with the base of interpolation functions used. Thus, for an arbitrary integration *Gauss* point $\boldsymbol{\xi}_p$, the associated *gap* function, $\boldsymbol{g}_p$, is given by:

$$\begin{aligned}
\boldsymbol{g}_p\left\{\boldsymbol{\xi}\right\} &= \widetilde{\boldsymbol{u}}_p^{+}\left\{\boldsymbol{\xi}\right\} - \widetilde{\boldsymbol{u}}_p^{-}\left\{\boldsymbol{\zeta}\right\} \\
&= \sum_{i=1}^{N_{nodes}} N_i\left\{\boldsymbol{\xi}_p\right\}\widetilde{\boldsymbol{u}}_{n_i}^{+} - \sum_{i=1}^{N_{nodes}} N_i\left\{\boldsymbol{\zeta}\left\{\boldsymbol{\xi}_p\right\}\right\}\widetilde{\boldsymbol{u}}_{n_i}^{-}.
\end{aligned} \tag{5.13}$$

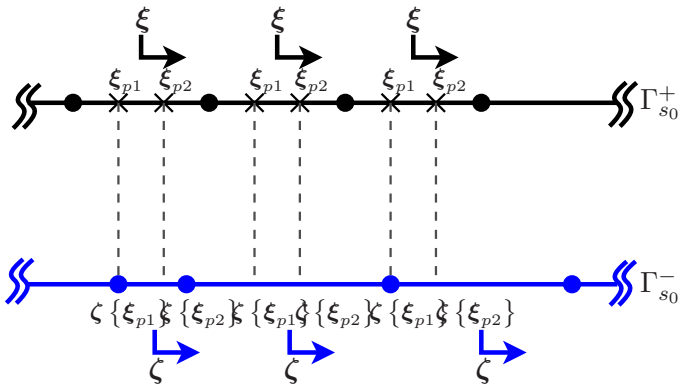

FIGURE 5.1: Relation between $\boldsymbol{\xi}_p$ and $\boldsymbol{\zeta}\{\boldsymbol{\xi}_p\}$ for two dimensional problems.

It is possible to write the previous equation in a matrix format as:

$$\boldsymbol{g}_p^T\{\boldsymbol{\xi}\} = \boldsymbol{w}_p^T \boldsymbol{B}_p, \tag{5.14}$$

where $\boldsymbol{w}_p$ is a matrix which includes the displacement fluctuations and the traction forces associated to $\boldsymbol{\xi}_p$. The matrix $\boldsymbol{B}_p$ represents an interpolation matrix for point $\boldsymbol{\xi}_p$. Both matrices are defined as follows:

$$\boldsymbol{w}_p^T = \left[\begin{array}{cccccccc} \widetilde{\boldsymbol{u}}_{n_1}^{+T} & \cdots & \widetilde{\boldsymbol{u}}_{n_{N_{nodes}}}^{+T} & \widetilde{\boldsymbol{u}}_{n_1}^{-T} & \cdots & \widetilde{\boldsymbol{u}}_{n_{N_{nodes}}}^{-T} & \boldsymbol{\lambda}_{n_1}^T & \cdots \quad \boldsymbol{\lambda}_{n_{N_{nodes}}}^T \end{array} \right], \tag{5.15a}$$

$$\boldsymbol{B}_p^T = \left[\begin{array}{cccccccc} N_1\{\boldsymbol{\xi}_p\}\boldsymbol{I} & \cdots & N_{N_{nodes}}\{\boldsymbol{\xi}_p\}\boldsymbol{I} & -N_1\{\boldsymbol{\zeta}\{\boldsymbol{\xi}_p\}\}\boldsymbol{I} & \cdots & -N_{N_{nodes}}\{\boldsymbol{\zeta}\{\boldsymbol{\xi}_p\}\}\boldsymbol{I} & \boldsymbol{0} & \cdots \quad \boldsymbol{0} \end{array} \right]. \tag{5.15b}$$

With this matrix format, it is also possible to rewrite Equation (5.12) as:

$$\boldsymbol{\lambda}_p^T\{\boldsymbol{\xi}\} = \boldsymbol{w}_p^T \boldsymbol{M}_p, \tag{5.16}$$

where matrix $\boldsymbol{M}_p$ is, once again, an interpolation matrix that includes the interpolation functions, $M_i\{\boldsymbol{\xi}_p\}$:

$$\boldsymbol{M}_p^T = \left[\begin{array}{cccccccc} \boldsymbol{0} & \cdots & \boldsymbol{0} & \boldsymbol{0} & \cdots & \boldsymbol{0} & M_1\{\boldsymbol{\xi}_p\}\boldsymbol{I} & \cdots \quad M_{N_{nodes}}\{\boldsymbol{\xi}_p\}\boldsymbol{I} \end{array} \right]. \tag{5.17}$$

The variation of the *gap* function, $\delta\boldsymbol{g}_p$, as well as the variation of the *Lagrange* parameter, $\delta\boldsymbol{\lambda}_p$, for point $\boldsymbol{\xi}_p$, can then be defined as:

$$\delta\boldsymbol{g}_p^T\{\boldsymbol{\xi}\} = \delta\boldsymbol{w}_p^T \boldsymbol{B}_p, \tag{5.18a}$$

$$\delta\boldsymbol{\lambda}_p^T\{\boldsymbol{\xi}\} = \delta\boldsymbol{w}_p^T \boldsymbol{M}_p, \tag{5.18b}$$

where $\delta \boldsymbol{w}_p^T$ consists on the variation of matrix (5.15a):

$$\delta \boldsymbol{w}_p^T = \left[\begin{array}{cccccccc} \delta \widetilde{\boldsymbol{u}}_{n_1}^{+T} & \cdots & \delta \widetilde{\boldsymbol{u}}_{n_{N_{nodes}}}^{+T} & \delta \widetilde{\boldsymbol{u}}_{n_1}^{-T} & \cdots & \delta \widetilde{\boldsymbol{u}}_{n_{N_{nodes}}}^{-T} & \delta \boldsymbol{\lambda}_{n_1}^T & \cdots & \delta \boldsymbol{\lambda}_{n_{N_{nodes}}}^T \end{array} \right]. \tag{5.19}$$

Taking into account the relations defined above and using a *Gaussian* quadrature rule to numerically evaluate the surface integral, Equation (5.10) can be re-written as:

$$\int_{\Omega_0^d} \boldsymbol{G}^T \hat{\boldsymbol{P}} \left\{ \boldsymbol{F} \left\{ \boldsymbol{y} \right\} \right\} dV \delta \widetilde{\boldsymbol{u}} + \bigcup_{s=1}^{N_s^+} \sum_{p=1}^{N_{Gauss}} \left[\delta \boldsymbol{w}_{s,p}^T \left(\boldsymbol{B}_{s,p} \boldsymbol{M}_{s,p}^T + \boldsymbol{M}_{s,p} \boldsymbol{B}_{s,p}^T \right) \boldsymbol{w}_{s,p} \right] J_p w_p = 0, \tag{5.20}$$

where J_p and w_p denote, respectively, the determinant of the Jacobian matrix and the *Gaussian* weight associated to $\boldsymbol{\xi}_p$. It is noteworthy to mention that since a total *Total Lagrange* formulation is adopted in this work, the integrals of the previous equation need to be determined over the reference configuration of the RVE. Therefore, the computation of J_p needs to account for this aspect.

Since the previous equation is satisfied for all admissible $\delta \widetilde{\boldsymbol{u}}$ and $\delta \boldsymbol{w}_p$, splitting the total displacement fluctuation field in its *interior* and *boundary* counterparts, denoted respectively by $\widetilde{\boldsymbol{u}}^i$ and $\widetilde{\boldsymbol{u}}^b$, and properly modifying matrices $\boldsymbol{B}_p$, $\boldsymbol{M}_p$ and $\boldsymbol{w}_p$, the previous equation can be conveniently expressed as a system of equations:

$$\begin{cases} \boldsymbol{f}^i \left\{ \boldsymbol{y} \right\} = \boldsymbol{0} \\ \boldsymbol{f}^b \left\{ \boldsymbol{y} \right\} + \bigcup_{s=1}^{N_s^+} \sum_{p=1}^{N_{Gauss}} \left[\left(\overline{\boldsymbol{B}}_{s,p} \overline{\boldsymbol{M}}_{s,p}^T \right) \overline{\boldsymbol{\lambda}}_{s,p} \right] J_p w_p = \boldsymbol{0} \\ \bigcup_{s=1}^{N_s^+} \sum_{p=1}^{N_{Gauss}} \left[\left(\overline{\boldsymbol{M}}_{s,p} \overline{\boldsymbol{B}}_{s,p}^T \right) \overline{\boldsymbol{w}}_{s,p} \right] J_p w_p = \boldsymbol{0}, \end{cases} \tag{5.21}$$

where $\boldsymbol{f}^i \left\{ \boldsymbol{y} \right\}$ and $\boldsymbol{f}^b \left\{ \boldsymbol{y} \right\}$ denote, respectively, the internal forces inside and at the boundary of the RVE. The matrices $\overline{\boldsymbol{M}}_p$, $\overline{\boldsymbol{B}}_p$, $\overline{\boldsymbol{w}}_p$ and $\overline{\boldsymbol{\lambda}}_p$ are defined as:

$$\overline{\boldsymbol{M}}_p^T = \left[\begin{array}{ccc} M_1 \left\{ \boldsymbol{\xi}_p \right\} \boldsymbol{I} & \cdots & M_{N_{nodes}} \left\{ \boldsymbol{\xi}_p \right\} \boldsymbol{I} \end{array} \right], \tag{5.22a}$$

$$\overline{\boldsymbol{B}}_p^T = \left[\begin{array}{cccccc} N_1 \left\{ \boldsymbol{\xi}_p \right\} \boldsymbol{I} & \cdots & N_{N_{nodes}} \left\{ \boldsymbol{\xi}_p \right\} \boldsymbol{I} & -N_1 \left\{ \zeta \left\{ \boldsymbol{\xi}_p \right\} \right\} \boldsymbol{I} & \cdots & -N_{N_{nodes}} \left\{ \zeta \left\{ \boldsymbol{\xi}_p \right\} \right\} \boldsymbol{I} \end{array} \right], \tag{5.22b}$$

$$\overline{\boldsymbol{w}}_p^T = \left[\begin{array}{cccccc} \widetilde{\boldsymbol{u}}_{n_1}^{+T} & \cdots & \widetilde{\boldsymbol{u}}_{n_{N_{nodes}}}^{+T} & \widetilde{\boldsymbol{u}}_{n_1}^{-T} & \cdots & \widetilde{\boldsymbol{u}}_{n_{N_{nodes}}}^{-T} \end{array} \right], \tag{5.22c}$$

$$\overline{\boldsymbol{\lambda}}_p^T = \left[\begin{array}{ccc} \boldsymbol{\lambda}_{n_1}^T & \cdots & \boldsymbol{\lambda}_{n_{N_{nodes}}}^T \end{array} \right]. \tag{5.22d}$$

The previous system of equations is formally equivalent to the one derived in [92] where the *Lagrange* Multiplier method was used to enforce PBC on RVE problems discretized with conform meshes. The main difference relies on the fact that, in the scheme proposed

by [92], the integrals over the boundary are replaced by simple matrices fulfilled with -1, 0 and 1 values. These matrices are responsible for linking each pair of nodes, with equal relative coordinates, at the corresponding boundaries of the RVE. Therefore, it is possible to conclude that the formulation expressed by the system of equations (5.21) has to recover, as a limiting case, the strategy proposed in [92] whenever the RVE is discretized by a conform mesh.

The previous system of equations is usually non-linear and, therefore, a suitable numerical strategy is required to solve it. Here, the well established iterative *Newton-Raphson* method was adopted, which requires the proper linearisation of (5.21). In the present case, this leads to:

$$\begin{bmatrix} \boldsymbol{K}^{ii} & \boldsymbol{K}^{ib} & \boldsymbol{0} \\ \boldsymbol{K}^{bi} & \boldsymbol{K}^{bb} & \bigcup_{s=1}^{N_s^+} \sum_{p=1}^{N_{Gauss}} \left[\overline{\boldsymbol{B}}_{s,p} \overline{\boldsymbol{M}}_{s,p}^T\right] J_p w_p \\ \boldsymbol{0} & \bigcup_{s=1}^{N_s^+} \sum_{p=1}^{N_{Gauss}} \left[\overline{\boldsymbol{M}}_{s,p} \overline{\boldsymbol{B}}_{s,p}^T\right] J_p w_p & \boldsymbol{0} \end{bmatrix}^{(j)} \begin{Bmatrix} \delta\widetilde{\boldsymbol{u}}^i \\ \delta\widetilde{\boldsymbol{u}}^b \\ \delta\boldsymbol{\lambda} \end{Bmatrix}^{(j+1)} = - \begin{Bmatrix} \boldsymbol{f}^i\{\boldsymbol{y}\} \\ \boldsymbol{f}^b\{\boldsymbol{y}\} + \bigcup_{s=1}^{N_s^+} \sum_{p=1}^{N_{Gauss}} \left[\left(\overline{\boldsymbol{B}}_{s,p} \overline{\boldsymbol{M}}_{s,p}^T\right) \overline{\boldsymbol{\lambda}}_{s,p}\right] J_p w_p \\ \bigcup_{s=1}^{N_s^+} \sum_{p=1}^{N_{Gauss}} \left[\left(\overline{\boldsymbol{M}}_{s,p} \overline{\boldsymbol{B}}_{s,p}^T\right) \overline{\boldsymbol{w}}_{s,p}\right] J_p w_p \end{Bmatrix}^{(j)}, \tag{5.23}$$

where (j) denotes the iteration number of the *Newton-Raphson* method and $\boldsymbol{K}^{**}$ the stiffness sub-matrices associated with the interior, i, and boundary, b, of the RVE. It is relevant to emphasize that with the present *Mortar* formulation, the integration *Gauss* points, $\boldsymbol{\xi}_p$ and $\boldsymbol{\zeta}\left\{\boldsymbol{\xi}_p\right\}$, are independent of the displacement fluctuation field, $\delta\widetilde{\boldsymbol{u}}$, since there is no relative displacement between adjacent surfaces of the RVE. This is an important aspect because it considerably simplifies the linearisation of the system of equations (5.21).

With the solution for $\delta\widetilde{\boldsymbol{u}}$ and $\delta\boldsymbol{\lambda}$ for $(j+1)$ at hand, the global displacement fluctuation and the traction field can be updated as follows:

$$\widetilde{\boldsymbol{u}}^{(j+1)} = \widetilde{\boldsymbol{u}}^{(j)} + \delta\widetilde{\boldsymbol{u}}^{(j+1)}, \tag{5.24a}$$

$$\boldsymbol{\lambda}^{(j+1)} = \boldsymbol{\lambda}^{(j)} + \delta\boldsymbol{\lambda}^{(j+1)}. \tag{5.24b}$$

In computational terms, we have obtained a force-displacement algorithm where both displacement fluctuation, $\widetilde{\boldsymbol{u}}$, and traction force field, represented by the *Lagrange* parameter, $\boldsymbol{\lambda}$, are unknowns of the problem.

5.2.3 Displacement based formulation

In Section 5.2.1, the enforcement of PBC was accomplished with a mixed variational formulation, which lead to a force-displacement algorithm. However, it is possible to re-formulate the problem into a weak form having the displacement fluctuation as the only unknown. This would lead to a smaller size of the system of equations, which requires less memory, and would increase the computational speed. With this objective in mind, a relation between *non-Mortar* and *Mortar* domains needs to be established, which can be derived from the last expression of (5.21):

$$\bigcup_{s=1}^{N_s^+} \sum_{p=1}^{N_{Gauss}} \left[\left(\overline{\boldsymbol{M}}_{s,p} \overline{\boldsymbol{B}}_{s,p}^T \right) \overline{\boldsymbol{w}}_{s,p} \right] J_p w_p = \mathbf{0}. \tag{5.25}$$

Considering the definition of matrices $\overline{\boldsymbol{M}}_p$ and $\overline{\boldsymbol{B}}_p$ (Equations (5.22a) and (5.22b), respectively), it is possible to write:

$$\overline{\boldsymbol{M}}_{s,p}\overline{\boldsymbol{B}}_{s,p}^{T} = \left[\begin{array}{ccc:ccc} M_1\left\{\boldsymbol{\xi}_p\right\}N_1\left\{\boldsymbol{\xi_p}\right\}\boldsymbol{I} & \cdots & M_1\left\{\boldsymbol{\xi}_p\right\}N_{N_{nodes}}\left\{\boldsymbol{\xi_p}\right\}\boldsymbol{I} & -M_1\left\{\boldsymbol{\xi}_p\right\}N_1\left\{\boldsymbol{\zeta}\left\{\boldsymbol{\xi_p}\right\}\right\}\boldsymbol{I} & \cdots & -M_1\left\{\boldsymbol{\xi}_p\right\}N_{N_{nodes}}\left\{\boldsymbol{\zeta}\left\{\boldsymbol{\xi_p}\right\}\right\}\boldsymbol{I} \\ \vdots & \cdots & \vdots & \vdots & \cdots & \vdots \\ M_{N_{nodes}}\left\{\boldsymbol{\xi_p}\right\}N_1\left\{\boldsymbol{\xi_p}\right\}\boldsymbol{I} & \cdots & M_{N_{nodes}}\left\{\boldsymbol{\xi_p}\right\}N_{N_{nodes}}\left\{\boldsymbol{\xi_p}\right\}\boldsymbol{I} & -M_{N_{nodes}}\left\{\boldsymbol{\xi_p}\right\}N_1\left\{\boldsymbol{\zeta}\left\{\boldsymbol{\xi_p}\right\}\right\}\boldsymbol{I} & \cdots & -M_{N_{nodes}}\left\{\boldsymbol{\xi_p}\right\}N_{N_{nodes}}\left\{\boldsymbol{\zeta}\left\{\boldsymbol{\xi_p}\right\}\right\}\boldsymbol{I} \end{array}\right]. \tag{5.26}$$

With the previous matrix at hand, it is possible to re-write expression (5.25) as:

$$\bigcup_{s=1}^{N_s^+} \sum_{p=1}^{N_{Gauss}} \left(\boldsymbol{a}_{s,p}^{nm} \widetilde{\boldsymbol{u}}_{s,p}^{nm} - \boldsymbol{a}_{s,p}^{m} \widetilde{\boldsymbol{u}}_{s,p}^{m} \right) J_p w_p = \boldsymbol{0}, \tag{5.27}$$

where matrices $\boldsymbol{a}_{s,p}^{nm}$ and $\boldsymbol{a}_{s,p}^{m}$ are given by:

$$\boldsymbol{a}_{s,p}^{nm} = \begin{bmatrix} M_1\left\{\boldsymbol{\xi}_p\right\} N_1\left\{\boldsymbol{\xi_p}\right\} \boldsymbol{I} & \cdots & M_1\left\{\boldsymbol{\xi}_p\right\} N_{N_{nodes}}\left\{\boldsymbol{\xi_p}\right\} \boldsymbol{I} \\ \vdots & \cdots & \vdots \\ M_{N_{nodes}}\left\{\boldsymbol{\xi_p}\right\} N_1\left\{\boldsymbol{\xi_p}\right\} \boldsymbol{I} & \cdots & M_{N_{nodes}}\left\{\boldsymbol{\xi_p}\right\} N_{N_{nodes}}\left\{\boldsymbol{\xi_p}\right\} \boldsymbol{I} \end{bmatrix}, \tag{5.28}$$

$$\boldsymbol{a}_{s,p}^{m} = \begin{bmatrix} M_1\left\{\boldsymbol{\xi}_p\right\} N_1\left\{\boldsymbol{\zeta}\left\{\boldsymbol{\xi_p}\right\}\right\} \boldsymbol{I} & \cdots & M_1\left\{\boldsymbol{\xi}_p\right\} N_{N_{nodes}}\left\{\boldsymbol{\zeta}\left\{\boldsymbol{\xi_p}\right\}\right\} \boldsymbol{I} \\ \vdots & \cdots & \vdots \\ M_{N_{nodes}}\left\{\boldsymbol{\xi_p}\right\} N_1\left\{\boldsymbol{\zeta}\left\{\boldsymbol{\xi_p}\right\}\right\} \boldsymbol{I} & \cdots & M_{N_{nodes}}\left\{\boldsymbol{\xi_p}\right\} N_{N_{nodes}}\left\{\boldsymbol{\zeta}\left\{\boldsymbol{\xi_p}\right\}\right\} \boldsymbol{I} \end{bmatrix}. \tag{5.29}$$

In turn, $\widetilde{\boldsymbol{u}}_{s,p}^{nm}$ and $\widetilde{\boldsymbol{u}}_{s,p}^{m}$ correspond to the nodal displacement fluctuation vectors, respectively, at the *non-Mortar* and *Mortar* domains associated to the integration *Gauss* point, $\boldsymbol{\xi}_p$,

$$\widetilde{\boldsymbol{u}}_{s,p}^{nm^T} = \begin{bmatrix} \widetilde{\boldsymbol{u}}_{n_1}^{nm^T} & \cdots & \widetilde{\boldsymbol{u}}_{n_{N_{nodes}}}^{nm^T} \end{bmatrix} = \begin{bmatrix} \widetilde{\boldsymbol{u}}_{n_1}^{+^T} & \cdots & \widetilde{\boldsymbol{u}}_{n_{N_{nodes}}}^{+^T} \end{bmatrix}, \tag{5.30}$$

$$\widetilde{\boldsymbol{u}}_{s,p}^{m^T} = \begin{bmatrix} \widetilde{\boldsymbol{u}}_{n_1}^{m^T} & \cdots & \widetilde{\boldsymbol{u}}_{n_{N_{nodes}}}^{m^T} \end{bmatrix} = \begin{bmatrix} \widetilde{\boldsymbol{u}}_{n_1}^{-^T} & \cdots & \widetilde{\boldsymbol{u}}_{n_{N_{nodes}}}^{-^T} \end{bmatrix}. \tag{5.31}$$

After the assembly of all integrals associated with N_s^+ elements at the discretized *non-Mortar* surface, a global expression is obtained:

$$\boldsymbol{A}^{nm}\, \widetilde{\boldsymbol{u}}^{nm} - \boldsymbol{A}^{m}\, \widetilde{\boldsymbol{u}}^{m} = \boldsymbol{0}, \tag{5.32}$$

where in this case, $\boldsymbol{u}^{nm}$ and $\boldsymbol{u}^{m}$ denote, respectively, the global vectors with the nodal displacement fluctuation at the *non-Mortar* and *Mortar* domains:

$$\widetilde{\boldsymbol{u}}^{nm^T} = \left[\begin{array}{c|c|c|c|c} \widetilde{\boldsymbol{u}}_1^{+^T} & \widetilde{\boldsymbol{u}}_2^{+^T} & \widetilde{\boldsymbol{u}}_3^{+^T} & \ldots & \widetilde{\boldsymbol{u}}_{N^+}^{+^T} \end{array} \right], \tag{5.33}$$

$$\widetilde{\boldsymbol{u}}^{m^T} = \left[\begin{array}{c|c|c|c|c} \widetilde{\boldsymbol{u}}_1^{-^T} & \widetilde{\boldsymbol{u}}_2^{-^T} & \widetilde{\boldsymbol{u}}_3^{-^T} & \ldots & \widetilde{\boldsymbol{u}}_{N^-}^{-^T} \end{array} \right]. \tag{5.34}$$

The scalars N^+ and N^- denote, respectively, the total number of nodes at the positive and negative domains. Finally, by a straightforward algebraic manipulation of Equation (5.32), we arrive at a closed form, which establishes a relation between *non-Mortar* and

Mortar displacements fields:

$$\begin{aligned} \widetilde{\boldsymbol{u}}^{nm} &= \left[\boldsymbol{A}^{nm}\right]^{-1} \boldsymbol{A}^{m} \widetilde{\boldsymbol{u}}^{m}, \\ \widetilde{\boldsymbol{u}}^{+} &= \left[\boldsymbol{A}^{nm}\right]^{-1} \boldsymbol{A}^{m} \widetilde{\boldsymbol{u}}^{-}. \end{aligned} \tag{5.35}$$

Based on the previous relation, it is possible to define the dependency matrix $\boldsymbol{\alpha}$,

$$\boldsymbol{\alpha} = \left[\boldsymbol{A}^{nm}\right]^{-1} \boldsymbol{A}^{m}, \tag{5.36}$$

which is typically introduced in the context of the *Condensation* method [78, 86, 113]. Therefore, in the following and for the sake of completeness, we will conveniently modify and extend the equations of the condensation method to include the proposed strategy.

The first step consists on the decomposition of the displacement fluctuation field, $\widetilde{\boldsymbol{u}}$, in its respective free $\widetilde{\boldsymbol{u}}^{f}$, negative $\widetilde{\boldsymbol{u}}^{-}$, positive $\widetilde{\boldsymbol{u}}^{+}$ and prescribed $\widetilde{\boldsymbol{u}}^{p}$ counterparts:

$$\widetilde{\boldsymbol{u}}^{T} = \left\{ \begin{array}{c:c:c:c} \widetilde{\boldsymbol{u}}^{f} & \widetilde{\boldsymbol{u}}^{-} & \widetilde{\boldsymbol{u}}^{+} & \widetilde{\boldsymbol{u}}^{p} \end{array} \right\}^{T}. \tag{5.37}$$

The *free* sub-domain, $\widetilde{\boldsymbol{u}}^{f}$, corresponds to the degrees of freedom in the interior of the RVE and all others are related with the degrees of freedom at the boundary of the RVE. The prescribed set, $\widetilde{\boldsymbol{u}}^{p}$, corresponds to the nodes with a null displacement fluctuation. This constraint is required in order to avoid rigid body displacements and rotations.

In the mixed variational formulation described in Section 5.2.1, the *Hill-Mandel* constraints associated to the traction forces acting over the boundary of the RVE (Equation (3.9)) as well as the *minimum kinematical constraint* (Equation (3.5)) are directly incorporated into the system of equations, which governs the equilibrium of the RVE. Nevertheless, in a displacement based scheme, this constraint is satisfied *a priori*. This means that, Equation (3.9) is a consequence of the definition of the dependency matrix (5.36). Therefore, the discretized equation that governs the equilibrium of the RVE is simply given by:

$$\begin{aligned} \int_{\Omega_0^d} \boldsymbol{G}^{T} \hat{\boldsymbol{P}} \left\{ \boldsymbol{F} \left\{ \boldsymbol{y} \right\} \right\} dV &= \boldsymbol{0}, \\ \Leftrightarrow \boldsymbol{f}^{int} \left\{ \boldsymbol{u} \left\{ \boldsymbol{y} \right\} \right\} &= \boldsymbol{0}, \end{aligned} \tag{5.38}$$

where $\boldsymbol{f}^{int} \left\{ \boldsymbol{u} \left\{ \boldsymbol{y} \right\} \right\}$ denotes the internal forces at the RVE level.

Once again, in order to solve the previous equation, which is highly non-linear in practical problems, a suitable numerical method is required. Thus, the *Newton-Raphson* method

is selected for this purpose, demanding the linearisation of (5.38), which leads to:

$$\boldsymbol{f}^{int}\left\{\boldsymbol{u}\left\{\boldsymbol{y}\right\}\right\}^{(j)} + \boldsymbol{K}_T\left\{\boldsymbol{u}\left\{\boldsymbol{y}\right\}\right\}^{(j)} \delta\widetilde{\boldsymbol{u}}^{(j+1)} = \boldsymbol{0}, \tag{5.39}$$

where $\boldsymbol{K}_T\left\{\boldsymbol{u}\left\{\boldsymbol{y}\right\}\right\}$ denotes the RVE global stiffness matrix, $\delta\widetilde{\boldsymbol{u}}$ is the unknown iterative nodal displacement fluctuation vector and "j" the iterative number of the *Newton-Raphson* method. It is important to highlight the fact that the previous equation is generic does not take into account the different admissible kinematical boundary conditions.

Performing a similar decomposition to the global stiffness matrix, $\boldsymbol{K}_T\left\{\boldsymbol{u}\left\{\boldsymbol{y}\right\}\right\}$, and internal force vector, $\boldsymbol{f}^{int}\left\{\boldsymbol{u}\left\{\boldsymbol{y}\right\}\right\}$, as described for the displacement fluctuation field, $\widetilde{\boldsymbol{u}}\left\{\boldsymbol{y}\right\}$ (Equation (5.37)), the previous equation can be re-written as follows:

$$\left\{\begin{array}{c} \boldsymbol{f}^{f} \\ \hdashline \boldsymbol{f}^{-} \\ \hdashline \boldsymbol{f}^{+} \\ \hdashline \boldsymbol{f}^{p} \end{array}\right\}^{(j)} + \left[\begin{array}{c:c:c:c} \boldsymbol{k}^{ff} & \boldsymbol{k}^{f-} & \boldsymbol{k}^{f+} & \boldsymbol{k}^{fp} \\ \hdashline \boldsymbol{k}^{-f} & \boldsymbol{k}^{--} & \boldsymbol{k}^{-+} & \boldsymbol{k}^{-p} \\ \hdashline \boldsymbol{k}^{+f} & \boldsymbol{k}^{+-} & \boldsymbol{k}^{++} & \boldsymbol{k}^{+p} \\ \hdashline \boldsymbol{k}^{pf} & \boldsymbol{k}^{p-} & \boldsymbol{k}^{p+} & \boldsymbol{k}^{pp} \end{array}\right]^{(j)} \left\{\begin{array}{c} \delta\widetilde{\boldsymbol{u}}^{f} \\ \hdashline \delta\widetilde{\boldsymbol{u}}^{-} \\ \hdashline \delta\widetilde{\boldsymbol{u}}^{+} \\ \hdashline \delta\widetilde{\boldsymbol{u}}^{p} \end{array}\right\}^{(j+1)} = \left\{\boldsymbol{0}\right\}. \tag{5.40}$$

Finally, with (5.35) at hand and knowing that $\widetilde{\boldsymbol{u}}^{p} = \left\{\boldsymbol{0}\right\}$, the previous system of equations can be condensated as:

$$\begin{array}{l} \left[\begin{array}{c:c} \boldsymbol{k}^{ff} & \boldsymbol{k}^{f-} + \boldsymbol{k}^{f+}\boldsymbol{\alpha} \\ \hdashline \boldsymbol{k}^{-f} + \boldsymbol{\alpha}^{T}\boldsymbol{k}^{+f} & \boldsymbol{k}^{--} + \boldsymbol{k}^{-+}\boldsymbol{\alpha} + \boldsymbol{\alpha}^{T}\boldsymbol{k}^{+-} + \boldsymbol{\alpha}^{T}\boldsymbol{k}^{++}\boldsymbol{\alpha} \end{array}\right]^{(j)} \left\{\begin{array}{c} \delta\widetilde{\boldsymbol{u}}^{f} \\ \hdashline \delta\widetilde{\boldsymbol{u}}^{-} \end{array}\right\}^{(j+1)} = \\ \qquad\qquad - \left\{\begin{array}{c} \boldsymbol{f}^{f} \\ \hdashline \boldsymbol{f}^{-} + \boldsymbol{\alpha}^{T}\boldsymbol{f}^{+} \end{array}\right\}^{(j)}. \end{array} \tag{5.41}$$

From the solution of the previous system of equations results the displacement fluctuation of the free, $\delta\widetilde{\boldsymbol{u}}^{f^{(j+1)}}$, and negative, $\delta\widetilde{\boldsymbol{u}}^{-(j+1)}$, degrees of freedom. With these at hand, for each "$j-th$" iteration of the *Newton-Raphson* method, the total displacement fluctuation field of the RVE is updated according to the following expression:

$$\widetilde{\boldsymbol{u}}^{(j+1)^{T}} = \left\{\begin{array}{c:c:c:c} \widetilde{\boldsymbol{u}}^{f} & \widetilde{\boldsymbol{u}}^{-} & \widetilde{\boldsymbol{u}}^{+} & \boldsymbol{0} \end{array}\right\}^{(j)^{T}} + \left\{\begin{array}{c:c:c:c} \delta\widetilde{\boldsymbol{u}}^{f} & \delta\widetilde{\boldsymbol{u}}^{-} & \boldsymbol{\alpha}\delta\widetilde{\boldsymbol{u}}^{-} & \boldsymbol{0} \end{array}\right\}^{(j+1)^{T}}. \tag{5.42}$$

Remark 5.3. The approach proposed in this contribution for the enforcement of PBC on RVE problems, with either mixed or displacement based formulations, can be easily incorporated into FE^2 multi-scale finite element codes. For this purpose, close form expressions for the macroscopic material tangent modulus,

$$\mathbf{A} = \frac{\partial \boldsymbol{P}\left\{\boldsymbol{x}\right\}}{\partial \boldsymbol{F}\left\{\boldsymbol{x}\right\}},$$

when a displacement algorithm is employed are given in Appendix A whilst for force-displacement based scheme they can be found in the literature [92].

5.2.4 Interpolation functions

A crucial feature inherent with the *Mortar* decomposition method is the selection of the interpolation function base, $M_i(\boldsymbol{\xi})$, to use over potentially mismatched surfaces (Equation (5.12)). In the literature, two admissible interpolation function bases have been commonly adopted, which satisfy the *Babuska-Brezzi* condition [1, 127]: *Standard* and *Dual* bases. In the following, these two bases will be addressed for both two and three dimensional problems.

5.2.4.1 Standard Base

The *Standard* base corresponds to the shape functions usually employed to interpolate the geometry and displacement field within the finite element method, which are widely described in the literature [70]. In this case, for both two and three dimensional problems, the *Lagrange* multipliers, $\boldsymbol{\lambda}$, are approximated with the shape functions at the boundary, $N_i(\boldsymbol{\xi})$:

$$\boldsymbol{\lambda}\{\boldsymbol{\xi}\} = \sum_{i=1}^{N_{nodes}} N_i\{\boldsymbol{\xi}\}\,\boldsymbol{\lambda}_{n_i}, \tag{5.43}$$

where $\boldsymbol{\lambda}_{n_i}$ denotes the nodal traction forces.

5.2.4.2 *Dual* base

Recently, an admissible interpolation function base has been proposed for the interpolation of the *Lagrange* multipliers, $\boldsymbol{\lambda}$, in the *Mortar* method, the so-called *Dual* base [120]. This basis of functions as to satisfy a *biorthogonality* condition besides the *Babuska-Brezzi* condition. This constraint is mathematically expressed by:

$$\int_{\Gamma_{s_0}^+} M_j\{\boldsymbol{\xi}\}\,N_i\{\boldsymbol{\xi}\}\,dA = \delta_{ji}\int_{\Gamma_{s_0}^+} N_i\{\boldsymbol{\xi}\}\,dA. \tag{5.44}$$

where δ_{ji} denotes the *Kronecker* operator. The dual shape functions are represented by $M_j\{\boldsymbol{\xi}\}$ and $N_i\{\boldsymbol{\xi}\}$ are the usual finite element shape functions, which are defined with regard to a surface parametrization $\boldsymbol{\xi}$. Due to the *biorthogonality* condition of the basis of functions, $M_j\{\boldsymbol{\xi}\}$, it will be possible to decouple the nodes where the periodicity constraint is being enforced rendering a more efficient numerical implementation than the *Standard* base.

The difference between *Standard* and *Dual* basis can be easily understood by analysing Figure 5.2, where a simple problem with non-conform meshes is schematically illustrated [1]. In Figures 5.2 (a) and (b), the light grey area at the *Mortar* domain, Γ^m, denotes a segment whose nodal displacements are influenced by the segments at the *non-Mortar* domain, Γ^{nm}, represented by the dark grey zones. When the *Standard* interpolation base is considered, all *non-Mortar* segments have influence on the nodal displacement of the *Mortar* segment. In contrast, for the *Dual* base, only the *non-Mortar* segments which are in the neighbourhood of the *Mortar* segment have influence on its nodal displacement. Thus, it is possible to conclude that the *Standard* base, Figure 5.2(a), assumes a global support whereas the *Dual* base, Figure 5.2(b), a local support. From the mathematical

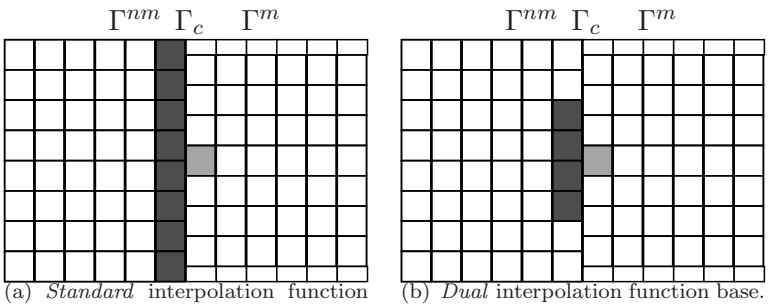

(a) *Standard* interpolation function base. (b) *Dual* interpolation function base.

FIGURE 5.2: Interpolation basis for the *Lagrange* parameters (Taken from [1]).

point of view, the difference between global and local support is materialized in matrix $\boldsymbol{A}^{nm}$, defined in Equation (5.32). Due to the global support of the *Standard* base, $\boldsymbol{A}^{nm}$ is a square matrix fulfilled of non-zero terms. However, when a *Dual* base is considered, the matrix $\boldsymbol{A}^{nm}$ becomes diagonal. This feature is very important for the numerical efficiency of the strategy presented when a displacement based scheme is adopted. In this case, the dependency matrix, $\boldsymbol{\alpha}$, can be easily obtained by inverting a diagonal matrix, $\boldsymbol{A}^{nm}$,

$$\begin{aligned} \boldsymbol{\alpha} &= [\boldsymbol{A}^{nm}]^{-1}\, \boldsymbol{A}^{m}, \\ \Leftrightarrow \boldsymbol{\alpha} &= [\boldsymbol{D}^{nm}]^{-1}\, \boldsymbol{A}^{m}. \end{aligned} \tag{5.45}$$

which is more convenient from the computational point of view.

5.2.4.3 *Dual* base - Two dimensional problems

For two dimensional problems, it is possible to find in the literature [120, 128] closed forms for the *Dual* base interpolation functions. In Table 5.1, we list the shape functions employed in this work to interpolate the geometry, the displacement field and *Lagrange* parameter for both linear and quadratic elements.

TABLE 5.1: *Dual* interpolation functions base for two dimensional problems.

	Linear Segment $\xi, \zeta \in [-1, 1]$	Quadratic Segment $\xi, \zeta \in [-1, 1]$
non-Mortar domain: Displacement field and coordinates	$N_1\{\boldsymbol{\xi}\} = \frac{1}{2}(1-\xi)$ $N_2\{\boldsymbol{\xi}\} = \frac{1}{2}(1+\xi)$	$N_1\{\boldsymbol{\xi}\} = \frac{1}{2}(1-\xi^2)$ $N_2\{\boldsymbol{\xi}\} = (1-\xi^2)$ $N_3\{\boldsymbol{\xi}\} = \frac{1}{2}(1+\xi^2)$
non-Mortar domain: *Lagrange* parameter	$M_1\{\boldsymbol{\xi}\} = \frac{1}{2}(1-3\xi)$ $M_2\{\boldsymbol{\xi}\} = \frac{1}{2}(1+3\xi)$	$M_1\{\boldsymbol{\xi}\} = \frac{5\xi^2-2\xi-1}{4}$ $M_2\{\boldsymbol{\xi}\} = \frac{3-5\xi^2}{2}$ $M_3\{\boldsymbol{\xi}\} = \frac{5\xi^2+2\xi-1}{4}$
Mortar domain: Displacement field and coordinates	$N_1\{\boldsymbol{\zeta}\} = \frac{1}{2}(1-\zeta)$ $N_2\{\boldsymbol{\zeta}\} = \frac{1}{2}(1+\zeta)$	$N_1\{\boldsymbol{\zeta}\} = \frac{1}{2}(1-\zeta^2)$ $N_2\{\boldsymbol{\zeta}\} = (1-\zeta^2)$ $N_3\{\boldsymbol{\zeta}\} = \frac{1}{2}(1+\zeta^2)$

5.2.4.4 *Dual* base - Three dimensional problems

For three dimensional problems, there are no closed forms for the *Dual* interpolation function base. This is a consequence of the shape that a surface of a three dimensional finite element may assume. Therefore, in order to circumvent this shortcoming, a numerical strategy has been proposed [129] where the interpolation functions $M\{\boldsymbol{\xi}\{\xi,\eta\}\}$ are determined according to the shape of the *non-Mortar* surface and taking into account the *biorthogonality* constraint. This strategy can be applied for either linear or quadratic tetrahedral elements and also for hexahedral finite elements.

This approach starts with the assumption that the interpolation function $M_i\left\{\boldsymbol{\xi}_p\{\boldsymbol{\xi},\boldsymbol{\eta}\}\right\}$ is determined by mapping the $N_j\left\{\boldsymbol{\xi}_p\{\boldsymbol{\xi},\boldsymbol{\eta}\}\right\}$ interpolation functions as follows:

$$M_i\left\{\boldsymbol{\xi}_p\{\xi,\eta\}\right\} = \sum_{j=1}^{N_{nodes}} b_{ij} N_j\left\{\boldsymbol{\xi}_p\{\xi,\eta\}\right\}, \tag{5.46}$$

where b_{ij} is square matrix with dimensions $[N_{nodes}, N_{nodes}]$ containing the mapping coefficients. By introducing the mapping scheme of the interpolation function, $M_i\{\boldsymbol{\xi}\{\xi,\eta\}\}$,

defined by Equation (5.46), into expression (5.44) results:

$$\begin{aligned}
&\int_{\Gamma^+_{s_0}} M_j\left\{\boldsymbol{\xi}\left\{\xi,\eta\right\}\right\} N_i\left\{\boldsymbol{\xi}\left\{\xi,\eta\right\}\right\} d\Gamma = \delta_{ji}\int_{\Gamma^+_{s_0}} N_i\left\{\boldsymbol{\xi}\left\{\xi,\eta\right\}\right\} d\Gamma,\\
\Leftrightarrow &\int_{\Gamma^+_{s_0}} \sum_{k=1}^{N_{nodes}} b_{jk} N_k\left\{\boldsymbol{\xi}\left\{\xi,\eta\right\}\right\} N_i\left\{\boldsymbol{\xi}\left\{\xi,\eta\right\}\right\} d\Gamma = D_{ji}\left\{\boldsymbol{\xi}\left\{\xi,\eta\right\}\right\},\\
\Leftrightarrow &\sum_{k=1}^{N_{nodes}} b_{jk}\int_{\Gamma^+_{s_0}} N_k\left\{\boldsymbol{\xi}\left\{\xi,\eta\right\}\right\} N_i\left\{\boldsymbol{\xi}\left\{\xi,\eta\right\}\right\} d\Gamma = D_{ji}\left\{\boldsymbol{\xi}\left\{\xi,\eta\right\}\right\},\\
\Leftrightarrow &\sum_{k=1}^{N_{nodes}} b_{jk} M_{ki}\left\{\boldsymbol{\xi}\left\{\xi,\eta\right\}\right\} = D_{ji}\left\{\boldsymbol{\xi}\left\{\xi,\eta\right\}\right\},\\
\Leftrightarrow &\boldsymbol{bM}\left\{\boldsymbol{\xi}\left\{\xi,\eta\right\}\right\} = \boldsymbol{D}\left\{\boldsymbol{\xi}\left\{\xi,\eta\right\}\right\}.
\end{aligned} \tag{5.47}$$

In the previous equation, matrix $\boldsymbol{D}\left\{\boldsymbol{\xi}\left\{\xi,\eta\right\}\right\}$ is commonly called the diagonal matrix whereas matrix $\boldsymbol{M}\left\{\boldsymbol{\xi}\left\{\xi,\eta\right\}\right\}$ is considered the mass matrix of the surface. With the previous expression at hand, we finally arrive at the definition of the coefficient matrix $\boldsymbol{b}$:

$$\boldsymbol{b} = \boldsymbol{D}\left\{\boldsymbol{\xi}\left\{\xi,\eta\right\}\right\}\left[\boldsymbol{M}\left\{\boldsymbol{\xi}\left\{\xi,\eta\right\}\right\}\right]^{-1}. \tag{5.48}$$

A detailed description of this numerical strategy is carried out in [129] where the construction of matrices $\boldsymbol{D}\left\{\boldsymbol{\xi}\left\{\xi,\eta\right\}\right\}$ and $\boldsymbol{M}\left\{\boldsymbol{\xi}\left\{\xi,\eta\right\}\right\}$ is presented in detail for surfaces with 4 nodes having an arbitrary shape. After the construction of matrix $\boldsymbol{b}$, the interpolation function $M_i\left\{\boldsymbol{\xi}_p\left\{\xi,\eta\right\}\right\}$ for a generic *Gauss* point with coordinates, $\boldsymbol{\xi}_p\left\{\xi,\eta\right\}$, can be conveniently determined using Equation (5.46).

5.2.5 Numerical integration

In this section, an integration framework is introduced to evaluate the *Mortar* coefficients included in the integrals of Equations (5.23) or (5.27), depending on the numerical scheme selected: force-displacement or fully-displacement based algorithm. This framework will be described for both two and three dimensional problems.

Before proceeding, it is important to state the two underlying requisites that we have followed in the development of the numerical integration framework. The first is concerned with the accuracy of the numerical solution. Therefore, regardless of the order of the interpolation functions considered (linear or quadratic), the strategy should always guarantee an exact result. The second is related to the generality of the approach such that the basic principles of the integration framework could be applied to both two and three dimensional problems.

5.2.5.1 Two dimensional problems

There are essentially two approaches to evaluate the integrals for two dimensional problems: *segment integration* and *projected segment*. In the following, a summarized discussion of the relative merit of each approach is introduced to justify the option that was followed in this work.

Segment integration. In this approach, the integration domain for each segment, $\Gamma^{+}_{s_0}$, at the *non-Mortar* surface, Γ^{nm}_{0}, coincides with the integration domain of the *non-Mortar* segment, as schematically illustrated in Figure 5.3(a). Despite its simplicity, this approach has some weaknesses that should be pointed out. The first one and probably the most relevant is concerned with its accuracy. When this strategy is implemented in conjunction with a *Gaussian* quadrature rule, the final solution is dependent on the number of integration points employed. As pointed out in [122], for some cases, in order to obtain an exact solution (or at least, very close to the analytical one), it is necessary to use more than 7 *Gauss* points uniformly distributed at the *non-Mortar* segment, $\Gamma^{+}_{s_0}$. The error is proportional to the number of *Mortar* segments, N^{-}_{s}, whose projections into the *non-Mortar* domain intersect the integration domain defined by the *non-Mortar* segment, $\Gamma^{+}_{s_0}$. Therefore, in order to obtain an exact result, it is necessary to know *a priori* the ideal number of integration points, which is not trivial. A possible solution to circumvent this shortcoming consists in analytically implementing this scheme. However, with this solution, a second shortcoming arises: it is necessary to particularize for each interpolation function base and for each element type the analytical integration scheme. This is particular cumbersome for three dimensional problems.

Projected segment. This approach consists in defining a *virtual integration surface*, denoted by Γ^{Int} in Figure 5.3(b), which results from the projection of the *non-Mortar* surface into the *Mortar* surface and vice-versa. After the construction of this virtual surface, the integration is no longer carried out at the *non-Mortar* domain but at the virtual integration surface, Γ^{Int}. Therefore, it is necessary to correctly map the different parameters defined at both *non-Mortar* and *Mortar* domains to the virtual surface. As a consequence, the integral over $\Gamma^{nm}_{s_0}$, present in Equations (5.23) or (5.27), is replaced by smooth sub-integrals associated to each segment of Γ^{Int}. Despite this fragmentation of the integration domain, it is always possible to obtain an exact solution using a reasonable number of integration points (i.e. 2 and 3 for linear and quadratic segments, respectively) and to guarantee the continuity of the global integral. Obviously, an analytical scheme can be also applied however, once again, it needs to be particularized for the set of interpolation functions and finite element type used.

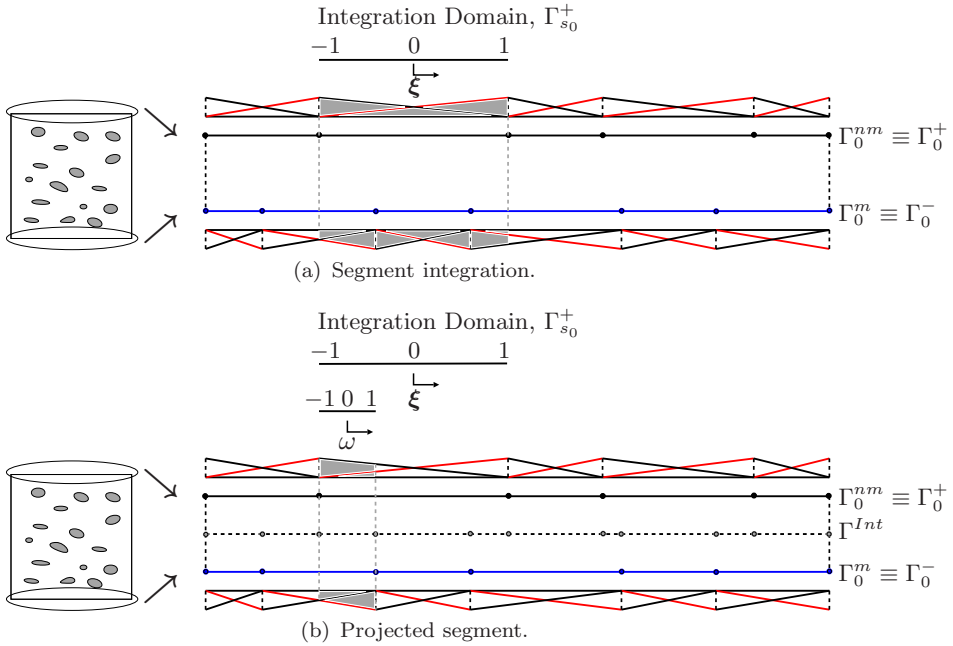

(a) Segment integration.

(b) Projected segment.

FIGURE 5.3: Definition of the integration limits for two different numerical frameworks.

Due to the higher accuracy of this approach and the fact that it can be easily extended for three dimensional problems, it will be used in this work and described in the following.

Remark 5.4. The description of the projected integration approach will made here for linear finite elements, which correspond to $2-$*noded* segments at both *non-Mortar* and *Mortar* domains, for the sake of simplicity. Nevertheless, the extension for higher order elements is straightforward. For linear elements, only two integration *Gauss* points are required to obtain an exact solution.

As previously stressed out, when the projected integration approach is considered, the integration of the *Mortar* coefficients is carried out at the *virtual integration surface*, Γ^{Int}. Each particular segment is defined by the initial and final node with coordinates $\boldsymbol{Y}_1^{Int}$ and $\boldsymbol{Y}_2^{Int}$ respectively. These nodes correspond to particular points $\xi_{1,2}$ and $\zeta_{1,2}$ at the *non-Mortar* and *Mortar* domains, respectively (Figure 5.4). At the *non-Mortar* surface, $\xi_{1,2}$ is determined by solving the following expressions:

$$\boldsymbol{Y}_1^{Int} = \boldsymbol{Y}_{s1}^{nm} + \xi_1 \left(\boldsymbol{Y}_{s2}^{nm} - \boldsymbol{Y}_{s1}^{nm}\right), \tag{5.49a}$$

$$\boldsymbol{Y}_2^{Int} = \boldsymbol{Y}_{s1}^{nm} + \xi_2 \left(\boldsymbol{Y}_{s2}^{nm} - \boldsymbol{Y}_{s1}^{nm}\right), \tag{5.49b}$$

whereas, for *Mortar* domain $\zeta_{1,2}$ are determined by:

$$\boldsymbol{Y}_1^{Int} = \boldsymbol{Y}_{s1}^{m} + \zeta_1 \left(\boldsymbol{Y}_{s2}^{m} - \boldsymbol{Y}_{s1}^{m}\right), \tag{5.50a}$$

$$\boldsymbol{Y}_2^{Int} = \boldsymbol{Y}_{s1}^{m} + \zeta_2 \left(\boldsymbol{Y}_{s2}^{m} - \boldsymbol{Y}_{s1}^{m}\right). \tag{5.50b}$$

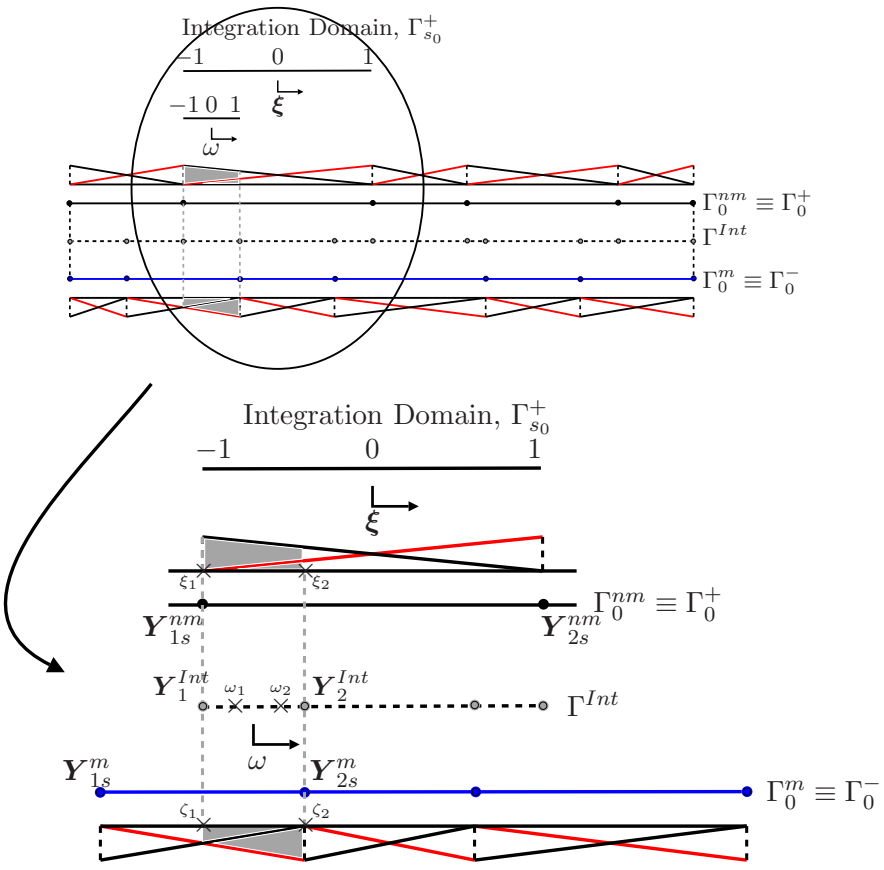

FIGURE 5.4: Schematic illustration of the projected segment strategy.

An extra coordinate system is required to numerically evaluate the integrals with the well established *Gaussian* quadrature rule. For this purpose, a local coordinate system ω ($\omega \in [-1,1]$) is introduced, which is defined for every segment of Γ^{Int}. Hence, the interpolation functions $N_i\left\{\boldsymbol{\xi}_p\right\}$, $N_i\left\{\boldsymbol{\zeta}_p\right\}$ and $M_i\left\{\boldsymbol{\xi}_p\right\}$ need to be mapped into this coordinate system, giving rise to $N_i\left\{\boldsymbol{\xi}\left\{\omega_p\right\}\right\}$, $N_i\left\{\boldsymbol{\zeta}\left\{\omega_p\right\}\right\}$ and $M_i\left\{\boldsymbol{\xi}\left\{\omega_p\right\}\right\}$ respectively. This mapping is schematically illustrated in Figure 5.4.

Since three coordinate systems are involved in the integral (which correspond to two mappings: from the global coordinates to $\boldsymbol{\xi}$ and then from $\boldsymbol{\xi}$ to ω), it is necessary to perform the "*bridge*" among these three coordinate systems by means of the *Jacobian* J:

$$J_p = \frac{\partial \boldsymbol{Y}_s}{\partial \boldsymbol{\xi}} \frac{\partial \boldsymbol{\xi}}{\partial \omega_p}. \tag{5.51}$$

Denoting $a^{nm}_{s_{ij}}$ as the (i,j) term of matrix $\boldsymbol{a}^{nm}_s$ of Equation (5.27) (this also applies for integrals of system of equations (5.23)) associated to $M_i\left\{\boldsymbol{\xi}\right\}$ and $N_j\left\{\boldsymbol{\xi}\right\}$ interpolation

functions for s *non-Mortar* segments, it is possible to write:

$$a_{s_{ij}}^{nm} = \sum_{k=1}^{N_s^{Int}} \sum_{p=1}^{2} M_i \left\{ \boldsymbol{\xi} \left\{ \omega_{k,p} \right\} \right\} N_j \left\{ \boldsymbol{\xi} \left\{ \omega_{k,p} \right\} \right\} \frac{\partial \boldsymbol{Y}_s}{\partial \boldsymbol{\xi}} \frac{\partial \boldsymbol{\xi}}{\partial \omega_{k,p}} w_p, \tag{5.52}$$

where N_s^{Int} denotes the number of virtual segments at Γ^{Int}, which define the *non-Mortar* segment, s.

Remark 5.5. For the so-called *Dual* interpolation function base and whenever $i \neq j$, the coefficient $a_{s_{ij}}^{nm}$ is null due to the *biorthogonality* constraint (Equation (5.44)).

In agreement with the previous manipulations, if we denote $a_{s_{ij}}^{m}$ as the (i, j) term of matrix $\boldsymbol{a}_s^m$ of Equation (5.27) where once again i is related with $M_i \{\boldsymbol{\xi}\}$ and, in this case, j with the interpolation functions at the *Mortar* domain, $N_j \{\boldsymbol{\zeta}\}$, it is possible to determine $a_{s_{ij}}^{m}$ by using the following expression:

$$a_{s_{ij}}^{m} = \sum_{k=1}^{N_s^{Int}} \sum_{p=1}^{2} M_i \left\{ \boldsymbol{\xi} \left\{ \omega_{k,p} \right\} \right\} N_j \left\{ \boldsymbol{\zeta} \left\{ \omega_{k,p} \right\} \right\} \frac{\partial \boldsymbol{Y}_s}{\partial \boldsymbol{\xi}} \frac{\partial \boldsymbol{\xi}}{\partial \omega_{k,p}} w_p. \tag{5.53}$$

It is important to note that the only difference between Equations (5.52) and (5.53) relies on the definition of $N_i \{\boldsymbol{\zeta} \{\omega_{k,p}\}\}$. Everything else is equal including the location of the *Gauss* points.

Finally, with $a_{s_{ij}}^{nm}$ and $a_{s_{ij}}^{m}$ at hand, the assembly of all contributions associated to all segments at both *non-Mortar* and *Mortar* domains is performed.

5.2.5.2 Three dimensional problems

The basic ingredients for integrating the *Mortar* coefficients for three dimensional problems have already been introduced in the previous section. However, some modifications are necessary to extend the *projected segment* strategy for three dimensional problems [121, 123, 130]. The main differences between two and three dimensional problems rely on: the definition of the *virtual integration surface*, Γ^{Int}, and the numerical rule employed to integrate the *Mortar* coefficients over areas with an arbitrary shape. While the *virtual integration surface*, Γ^{Int}, in two dimensional problems results from the projection of segments, in three dimensional problems, Γ^{Int} consists on a virtual plane with the projections of *non-Mortar* and *Mortar* surfaces. Since both surfaces have the same associated outward normal vector, $N^+ = -N^-$, due to the PBC enforcement, the virtual plane, Γ^{Int}, can be coincident with either the *Mortar*, Γ_0^m, or *non-Mortar*, Γ_0^{nm}, domains (see Figure 5.5(a)). Moreover, in three dimensional problems, the definition of the intersected polygon in the virtual plane (Figure 5.5(b)) is not straightforward, being

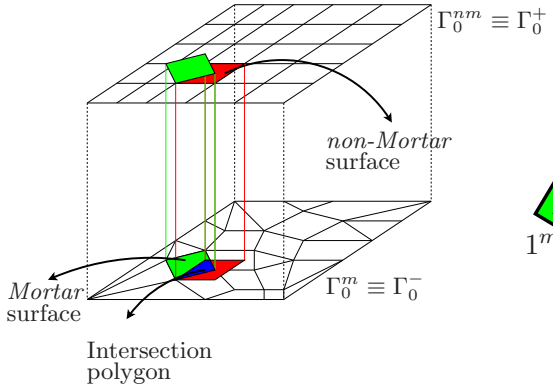

(a) Projection of the *non-Mortar* surface into *Mortar* surface and vice-versa.

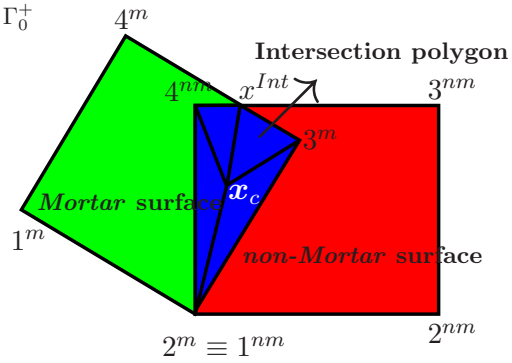

(b) Clipping.

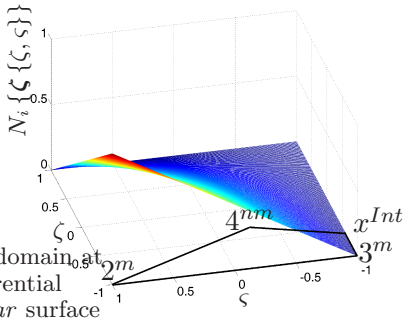

Integration domain at ζ and ς referential at the *Mortar* surface defined by points 2^m, 3^m, x^{Int} and 4^{nm}

(c) Interpolation function $N_i\{\boldsymbol{\zeta}\{\zeta,\varsigma\}\}$ defined at the *Mortar* domain.

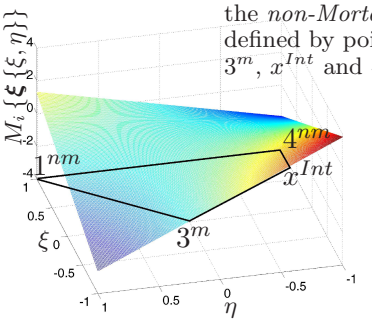

Integration domain at ξ and η referential at the *non-Mortar* surface defined by points 1^{nm}, 3^m, x^{Int} and 4^{nm}

(d) Interpolation function $M_i\{\boldsymbol{\xi}\{\xi,\eta\}\}$ defined at the *non-Mortar* domain.

FIGURE 5.5: Illustration of the numerical strategy for three dimensional problems.

necessary to use a suitable *clipping* algorithm [131]. After the definition of the intersection polygon, it is necessary to map this polygon to the spaces $\boldsymbol{\zeta}\{\zeta,\varsigma\}$ and $\boldsymbol{\xi}\{\xi,\eta\}$, as schematically illustrated in Figures 5.5(c) and 5.5(d).

With regard to the integration rule, an extension of the *Gaussian* quadrature rule is used: the *Gauss-Radau* rule [132]. Essentially, this integration method consists in dividing the intersection polygon, which results from the clipping algorithm, into n_T triangles and then, perform the integration over each triangle. The final result is obtained by summing the sub-integrals of all triangles. For sake of completeness, the numerical framework that has been used to integrate the *Mortar* coefficients for three dimensional problems is presented in Table 5.2 in *pseudo-code* format.

TABLE 5.2: Numerical framework for the integration of the *Mortar* coefficients for three dimensional problems.

1. Loop over *non-Mortar* surfaces, $s = 1, N_s^+$ (number of surfaces at *non-Mortar* domain).
   `IF` (*Dual* interpolation function base) `THEN`.
   Determine $\boldsymbol{b}$ matrix for s *non-Mortar* surface (Section 5.2.4.4).
   `ENDIF`
2. Project *non-mortar* surface, s, into *Mortar* domain;
3. Loop over *Mortar* surfaces, $r = 1, N_s^-$ (number of surfaces at *Mortar* domain);
   (a) Run a polygon algorithm to check if the *non-Mortar* surface, s, intersects *Mortar* surface, r.
   `IF` (Intersection) `THEN`
   i. Use a clipping algorithm to define the intersection polygon (Figure 5.5(a)). A detailed discussion of clipping algorithms can be found in [131].
   ii. Compute the geometric center (x_c, y_c) of the intersection polygon using the following expressions (Figure 5.5(b)):

$$x_c = \frac{\sum_{l=1}^{n_p} (x_{l+1} + x_l)(x_l y_{l+1} + y_l x_{l+1})}{A}, \tag{5.54a}$$

$$y_c = \frac{\sum_{l=1}^{n_p} (y_{l+1} + y_l)(x_l y_{l+1} + y_l x_{l+1})}{A}, \tag{5.54b}$$

   where n_p denotes the number of points of the polygon and A corresponds to the area of the intersection polygon, which can be determined by:

$$A = \frac{1}{2} \sum_{l=1}^{n_p} (x_l y_{l+1} - y_l x_{l+1}). \tag{5.55}$$

   iii. Considering the n_p points which define the intersection polygon and its center (x_c, y_c), divide the polygon into n_T triangles with $\boldsymbol{x}_T$ coordinates (Figure 5.5(b)).
   iv. For each triangle, use the *Gauss-Radau* rule [132] to define the coordinates of the integration points (ξ_T, η_T) and the respective integration weights, w_T.
   v. Calculate the global coordinates associated to (ξ_T, η_T):

$$\boldsymbol{x}_{GP} = \sum_{I=1}^{3} N_I(\xi_T, \eta_T)\, \boldsymbol{x}_{T_I}. \tag{5.56}$$

   vi. Determine the coordinates (ξ, η) for the *non-Mortar* domain and (ζ, ς) for the *Mortar* surfaces associated to $\boldsymbol{x}_{GP}$.
   vii. Evaluate the coefficients $a_{s_{ij}}^{nm}$ and $a_{s_{ij}}^{nm}$ (Figures 5.5(c) and 5.5(d)):

$$a_{s_{ij}}^{nm} = \sum_{k=1}^{n_T} A_k^{Tri} \sum_{p=1}^{N_{Gauss}} M_i\{\boldsymbol{\xi}\{\xi_{k,p}, \eta_{k,p}\}\} N_j\{\boldsymbol{\xi}\{\xi_{k,p}, \eta_{k,p}\}\} w_{k,p}, \tag{5.57a}$$

$$a_{s_{ij}}^{m} = \sum_{k=1}^{n_T} A_k^{Tri} \sum_{p=1}^{N_{Gauss}} M_i\{\boldsymbol{\xi}\{\xi_{k,p}, \eta_{k,p}\}\} N_j\{\boldsymbol{\zeta}\{\zeta_{k,p}, \varsigma_{k,p}\}\} w_{k,p}. \tag{5.57b}$$

   where A_k^{Tri} denotes the area of $k-th$ triangle.
   viii. Assemble the contributions $a_{s_{ij}}^{nm}$ and $a_{s_{ij}}^{m}$.
   `ELSE`
   `GO TO` 3.
   `ENDIF`

5.3 Numerical examples

In this section, the ability of the proposed approach, to enforce PBCs on RVE problems with arbitrary meshes at finite strains is assessed through the analysis of four numerical examples. The first two examples demonstrate that all the assumptions made during the formulation of the method are satisfied. Furthermore, the accuracy of the method and the stability of the fully linearised Newton procedure are verified. The last two examples highlight the robustness of the method and the quality of results in three dimensions.

Before proceeding, it is important to remark that all the results presented in this section were obtained with the formulation described in Section 5.2.3 combined with a linear *dual* base for the interpolation functions. This choice is advocated by the authors since it preserves the displacement based structure of FE^2 codes and it does not lead to an increase in the system size.

5.3.1 RVE with periodic configuration

As previously mentioned, the approach proposed in this work to enforce PBCs should recover, as a limiting case, the classical method whenever the RVE is discretized with a periodic mesh. In addition, the two methods should provide similar results for the same configuration/geometry of the RVE and should be relatively independent of the spatial discretization. Hence, in this example, these premises are analysed. With this objective in mind, a square RVE with a periodic configuration of voids was considered (see Figure 5.6). The RVE dimensions are $2mm \times 2mm$ and each circular void has a radius of $0,2mm$ centred in a square of $1mm \times 1mm$. This geometry was discretized with three different meshes depicted in Figure 5.6.

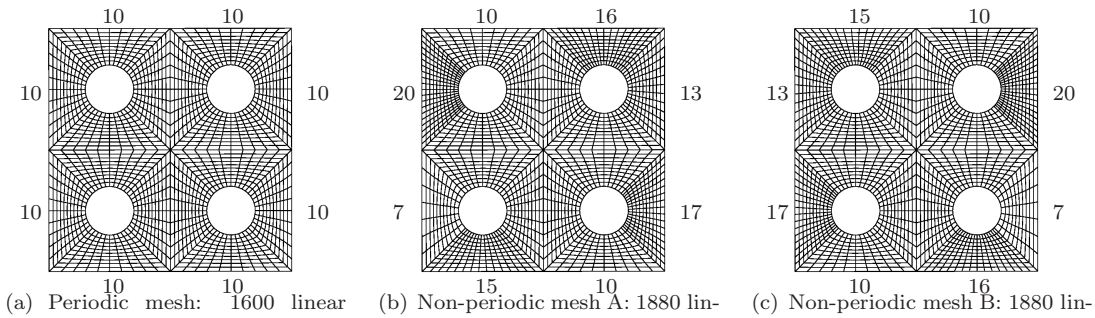

(a) Periodic mesh: 1600 linear quadrilateral elements.

(b) Non-periodic mesh A: 1880 linear quadrilateral elements.

(c) Non-periodic mesh B: 1880 linear quadrilateral elements.

FIGURE 5.6: Finite element meshes of the RVE with a periodic configuration. The numbers indicate the total number of elements at the boundary of each square.

From Figure 5.6, it is possible to conclude that the first mesh (Figure 5.6(a)) is periodic since a one-to-one correspondence exists between nodes on opposing sides of the RVE

boundary. Therefore, the classical method for applying PBCs, which consists on the enforcement of an identical displacement fluctuation field for each pair of corresponding boundaries of the RVE, is employed. The results obtained with this method will be considered as reference for this numerical example. The remaining two meshes are non-periodic (Figures 5.6(b) and (c)) having an arbitrary number of elements at the boundary. Nevertheless, we have forced mesh A (Figure 5.6(b)) to be the "mirror" of mesh B (Figure 5.6(c)) in order to assess the influence of selecting different *non-Mortar* and *Mortar* surfaces on the solution. All three meshes are discretized with linear quadrilateral elements and plane strain assumption was considered. With regard to the material constitutive model employed, a linear elastic law was considered with Young's modulus, $E = 70\,GPa$, and Poisson's ratio, $v = 0.3$. The RVE was subjected to the following macroscopic deformation gradient:

$$\boldsymbol{F}\{\boldsymbol{x}\} = \begin{bmatrix} 1.0 & 0.1 \\ 0.1 & 1.0 \end{bmatrix}. \tag{5.58}$$

The results obtained for the three different meshes at the final stage are listed in Table 5.3. In the first column, the homogenized *First Piola-Kirchhoff*, $\boldsymbol{P}\{\boldsymbol{x}\}$, is presented. The second column lists the solution of the integral (3.9), which imposes the *Hill-Mandel Principle*. Finally, the third column presents the maximum relative error of the homogenized shear component of the *First Piola-Kirchhoff* stress tensor, P_{12}. The results associated to the two non-periodic meshes are very close to the periodic mesh. This indicates that the selection of the *non-Mortar* and *Mortar* domains does not affect the quality of the result. In fact, this is an advantage of the current method when compared with other approaches commonly employed to enforce PBC for RVEs with non-conform meshes [115, 116]. In these cases, in order to obtain accurate results, it is necessary to select for master surface the one which has a higher node density. In addition, it is possible to conclude that integral (3.9) is satisfied, which demonstrates that the method proposed here to enforce PBCs is kinematically admissible when a fully displacement based algorithm is used. It is relevant to mention that when this algorithm is considered, the traction forces acting over the boundary of the RVE are a consequence of the displacement field. Finally, the maximum relative error obtained is smaller than 0.14%, which can be considered negligible.

In order to evaluate the efficiency of the proposed approach to enforce PBCs, we give an overview of the convergence behaviour in terms of the total residual norm during a non-linear Newton iteration. This is exemplified in Table 5.4 for one of the twenty equally spaced increments of the analysis. It can be observed that the approach proposed

TABLE 5.3: Numerical results for the RVE with a periodic configuration.

	$\boldsymbol{P}\{\boldsymbol{x}\}$	H-M C.	Error (%)
Periodic mesh	$\boldsymbol{P} = \begin{bmatrix} -533.834 & 3658.730 & 0.000 \\ 3658.400 & -530.483 & 0.000 \\ 0.000 & 0.000 & -99.782 \end{bmatrix}$	0.00	...
Non-periodic mesh A	$\boldsymbol{P} = \begin{bmatrix} -531.893 & 3654.430 & 0.000 \\ 3654.050 & -528.113 & 0.000 \\ 0.000 & 0.000 & -98.748 \end{bmatrix}$	$1.16E-16$	0.118%
Non-periodic mesh B	$\boldsymbol{P} = \begin{bmatrix} -531.551 & 3653.750 & 0.000 \\ 3653.040 & -528.000 & 0.000 \\ 0.000 & 0.000 & -98.651 \end{bmatrix}$	$1.19E-16$	0.136%

TABLE 5.4: Convergence behaviour in terms of the total residual norm for a representative step.

Iteration Number	**Convergence**
1	8.47687
2	0.203536
3	$0.134021E-04$
4	$0.358867E-11$

yields excellent convergence behaviour in this example as would be expected from the full linearisation of all non-linear quantities.

5.3.1.1 Non-linear constitutive model

The problem described in Section 5.3.1 was analysed again after changing the material constitutive model and the type of finite element employed. In this case, the *von Mises* elasto-plastic model was used with the same elastic parameters, with an initial yield stress, $\sigma_y = 200\ MPa$, and a constant hardening modulus, $H = 400\ MPa$. The linear quadrilateral finite element was replaced with its quadratic version with reduced integration (2×2 integration points) to avoid the phenomenon of volumetric locking observed under near incompressibility conditions. All the remaining conditions are kept the same, namely, the enforced macroscopic deformation gradient and the plane strain assumption.

In Figure 5.7, the evolution of the P_{12} term of the homogenized *First Piola-Kirchhoff* stress tensor, $\boldsymbol{P}\{\boldsymbol{x}\}$, against the prescribed load is plotted. As it is possible to observe, there is an excellent agreement between the solutions obtained with each of the different meshes. In Figure 5.8, the contours of the *von Mises* equivalent stress can be observed. Once again there are no appreciable differences. This conclusion applies not only to the

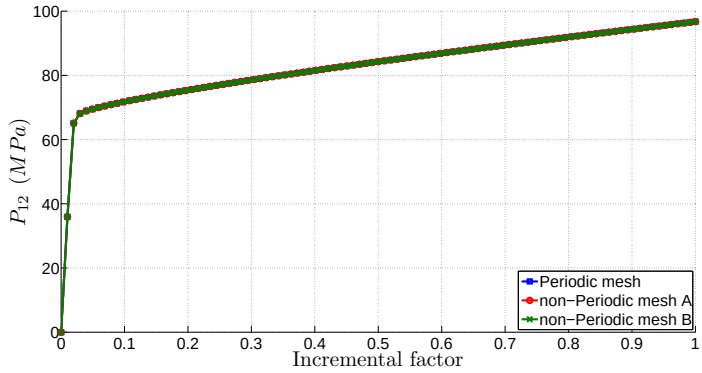

FIGURE 5.7: Evolution of the P_{12} term of the homogenized *First Piola-Kirchhoff* stress tensor, $\boldsymbol{P}\{\boldsymbol{x}\}$, for the RVE with periodic configuration modelled with an elasto-plastic constitutive model.

value of the *von Mises* equivalent stress but also to the final deformed configuration of the RVEs.

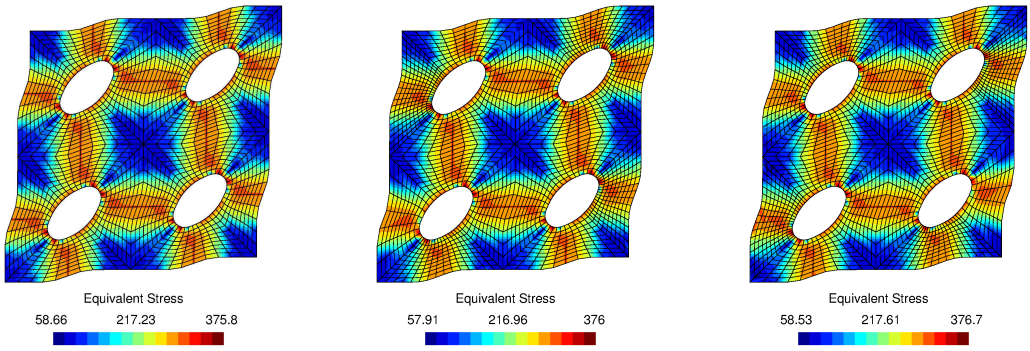

(a) Periodic mesh. (b) non-Periodic mesh A. (c) non-Periodic mesh B.

FIGURE 5.8: Contours of the *von Mises* equivalent stress for the three different meshes.

From the previous results, it is possible to conclude that the method proposed can also be used to model material non-linear constitutive behaviours at the micro structural level. It is important to remark that in this problem, the linear *dual* base for the interpolation functions was used in conjunction with quadratic finite elements. This was achieved by considering that each segment of a quadratic element is defined by a set of linear interpolation functions. This strategy has provided accurate results and has been used, with rather satisfactory results, in computational contact mechanics solution algorithms.

5.3.2 RVE with a non-periodic configuration

In this example, the convergence of average properties with increasing RVE size for different boundary conditions is analysed. Several numerical studies [87, 88] have shown

that the PBC, for a given RVE size, provides a better estimation of the average properties than the linear displacement or than the uniform traction boundary conditions. This conclusion holds if the micro structure possesses geometrical periodicity or not [87, 88]. Therefore, this evidence will be verified for non-periodic configurations by comparing the method proposed in this work, denoted *Mortar Periodic*, with two classical kinematical constraints: linear boundary displacements and uniform tractions, which correspond to the upper and lower bounds of the solution for the same RVE size.

In these analyses, the RVE micro structure is composed by circular inclusions randomly distributed in the matrix, which is typical of unidirectional fibre reinforced composite materials. The matrix-inclusion interaction is neglected. Due to the dependence of the results with the configuration of the RVE (distribution of the inclusions), for each characteristic size of the RVE, 10 randomly generated micro structures were created in order to perform a statistical analysis. The volume fraction of inclusions was set to $f = 20\%$ and the radius of all inclusions is $r = 4\ mm$. With regard to the dimension of the square RVE, 6 distinct sizes were considered: 10 mm, 20 mm, 30 mm, 40 mm, 50 mm and finally 60 mm. In what follows, the smallest RVE dimension, $L = 10\ mm$, corresponds to the reference size, L_{ref}. The generation of random micro structures with these specifications was undertaken with the algorithm proposed in [133]. In Table 5.5, the elastic material properties used in this problem are listed. All micro structures were discretized with linear triangular elements and, once again, *plane strain* condition was assumed. The macroscopic deformation gradient enforced is the same employed in the previous example.

TABLE 5.5: Material properties for the convergence analysis problem.

	Matrix	**Inclusion**
Young's Modulus, $E\ (GPa)$	$E_m = 3$	$E_{inc} = 60$
Poisson's ratio, v	$v_m = 0.3$	$v_{inc} = 0.3$

In Figure 5.9, the evolution of the homogenized shear modulus, G, is shown as a function of the RVE size for the three different boundary conditions under analysis. In Figures 5.9 (a), (b) and (c), we have plotted not only the discrete numerical values obtained for each RVE configuration but also a trend line with the average value. In Figure 5.9 (d) only the trend line with the average value for each boundary condition is plotted. In addition, we have superimposed in all Figures several solutions available in the literature, which are independent of the type of boundary condition enforced, for comparison purposes. In particular, the upper and lower *Hashin-Shtrikman* limits [13] (labelled as *"Hashin +"* and *"Hashin -"*, respectively) as well as the analytical result of G, which was obtained based on a dilute distribution of aligned fibres in the absence of matrix-inclusion interaction [24] (labelled by *"DDFA"*), are included.

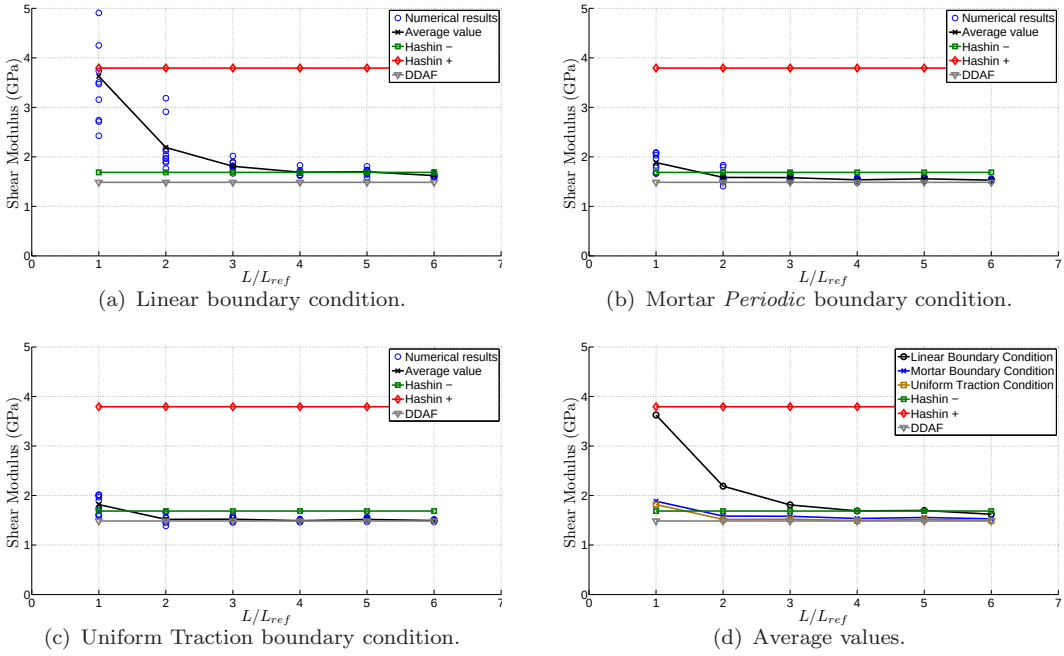

(a) Linear boundary condition.
(b) Mortar *Periodic* boundary condition.
(c) Uniform Traction boundary condition.
(d) Average values.

FIGURE 5.9: Homogenized shear modulus, G, for different boundary conditions as a function of the RVE size.

The results obtained for the homogenized shear modulus with the *Linear* boundary condition (see Figure 5.9(a)) have a significant dependence with the RVE size. For this boundary condition, the average value only stabilizes for an RVE size $L/L_{ref} \geq 4$. This behaviour is not observed for the other two two boundary constraints (Figures 5.9(b) and (c)) since the numerical results converge for the same value of G for an RVE size $L/L_{ref} \geq 2$. However, from the comparison of the evolution of the *Mortar Periodic* and *Uniform Traction* constraints it is not possible to conclude which boundary condition converges faster to the solution. Notwithstanding, we confirm that for the RVE size range analysed, the homogenized shear modulus value, G, obtained with *Mortar Periodic* constraint (Figure 5.9(b)) is within the bounds defined by the *Linear* and *Uniform Traction* boundary conditions, which is in agreement with the studies described in the literature [87, 88]. A second observation that can be made is concerned with the variability of results for the same RVE size with different boundary conditions. As it is possible to observe from Figure 5.9(a), for low values of L/L_{ref}, the numerical results clearly depend on the configuration of the RVE for *Linear* boundary condition. This observation is also applicable to *Mortar Periodic* and *Uniform Traction* boundary constraints with a significant lower dispersion of results (Figure 5.9(b) and (c)).

Comparing the analytical and numerical results in Figure 5.9(d), we observe that the *DDAF* result is quite close to the numerical ones for large values of L/L_{ref}. In contrast, it is clear that, for this particular example, the upper *Hashin-Shtrikman* bound (labelled as *"Hashin +"*) is significantly higher than all the numerical results obtained whereas

the lower bound is slight above the numerical results, which is in agreement with the result obtained in [76].

In Figure 5.10, the effective stress contour at the final configuration of the RVEs is presented for *Linear*, *Mortar Periodic* and *Uniform Traction* boundary conditions for different RVE sizes. At first glance, it is clear that the final configuration inherent with

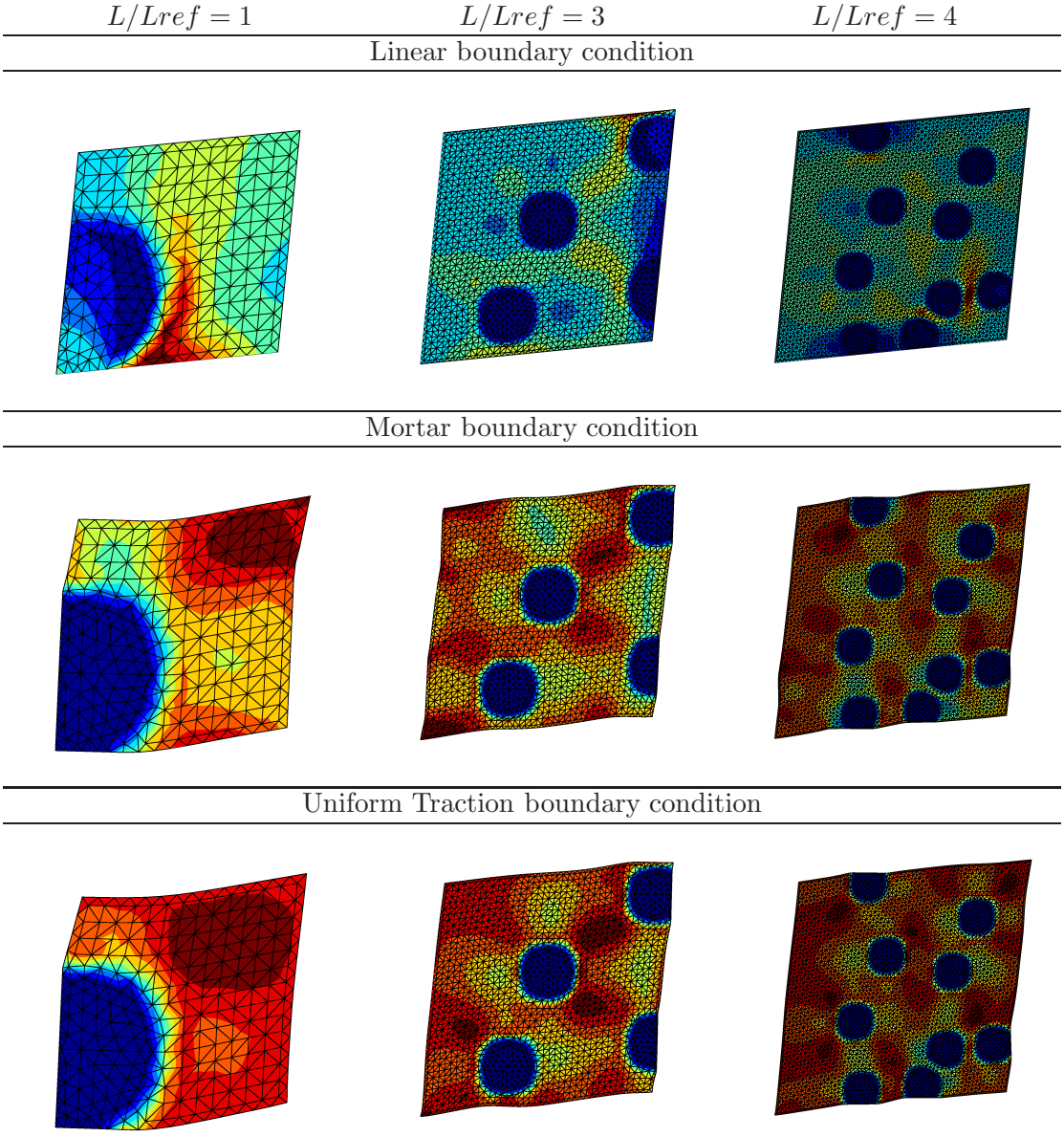

FIGURE 5.10: Final configuration of the RVE for *Linear*, *Mortar Periodic* and *Uniform traction* boundary conditions.

the *Linear* constraint is quite different from the other two due to the severe constraint enforced at the boundary of the RVE. However, when Mortar and *Uniform Traction* boundary conditions are compared, the differences at the final configuration are only noticeable for small RVE sizes ($L/L_{ref} = [1, 3]$). For larger values of L/L_{ref} ($(L/L_{ref} \geq 4)$

the RVE deformation and stress contours are nearly identical. It is also noteworthy to mention that the new boundary condition promotes, regardless of the spatial discretization, a smooth deformation pattern over the boundary of the RVE as can be observed in Figure 5.10.

5.3.3 Three dimensional RVE with a periodic configuration

In this example, we validate the approach proposed in the three dimensional setting and analyse the quality of results. To achieve this purpose, an RVE with a simple geometry was studied in order to facilitate the generation of a periodic mesh which is vital for the enforcement of the classic PBC. The results obtained with the periodic mesh will be considered as reference for this example.

The geometry of the cubic RVE is depicted in Figure 5.11. The RVE dimensions are $10mm \times 10mm \times 10mm$, the top left hole has a radius of $1mm$ and the other two holes have a radius of $1.5\,mm$. The two top holes are centred in cubes of $5mm \times 5mm \times 10mm$ and the bottom hole is centred in a cube of $10mm \times 5mm \times 10mm$. The two meshes considered for this problem are illustrated in Figure 5.11. With regard to the periodic mesh (Figure 5.11(a)), a structured mesh with 3 500 linear hexahedral elements was employed for the spatial discretization. Conversely, for the non-periodic mesh (Figure 5.11(b)), linear tetrahedral elements were used, resulting in a non-conform mesh with 68 128 elements. The substantial difference between the total number of elements used to discretize the domain, with either linear tetrahedral and hexahedral elements, is needed in order to obtain a solution with a similar accuracy. In this example, the material

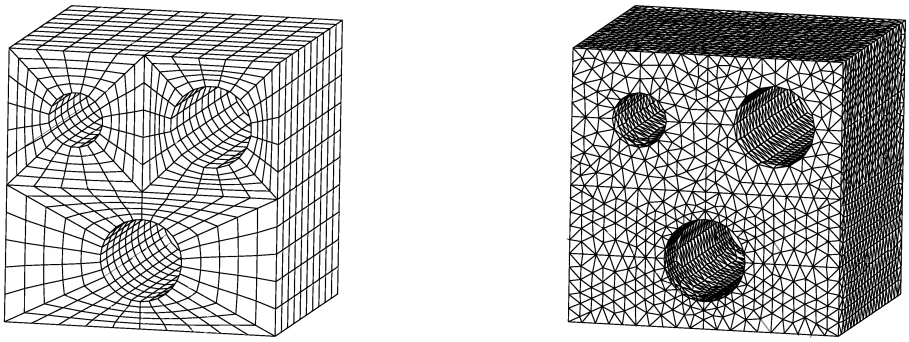

(a) Periodic mesh with 3 500 hexahedral elements and 4 433 nodes.

(b) Non-Periodic mesh: with 68 128 tetrahedral elements and 13 345 nodes.

FIGURE 5.11: Two meshes used to discretize the three dimensional RVE with a periodic configuration.

constitutive law selected is the same employed in Section 5.3.1. Furthermore, the same material properties were used and the following macroscopic deformation gradient was

considered:

$$\boldsymbol{F}\{\boldsymbol{x}\} = \begin{bmatrix} 1.0 & 0.1 & 0.0 \\ 0.1 & 1.0 & 0.0 \\ 0.0 & 0.0 & 1.0 \end{bmatrix}. \tag{5.59}$$

We start the analysis by presenting the configuration of the RVE at the end of the deformation process. From Figure 5.12, it is possible to conclude that both final configurations are quite similar. In fact, there is no visible difference between them. This is a clear indication that the new approach for the enforcement of the PBC was properly extended for three dimensional problems and successfully implemented. In Table 5.6,

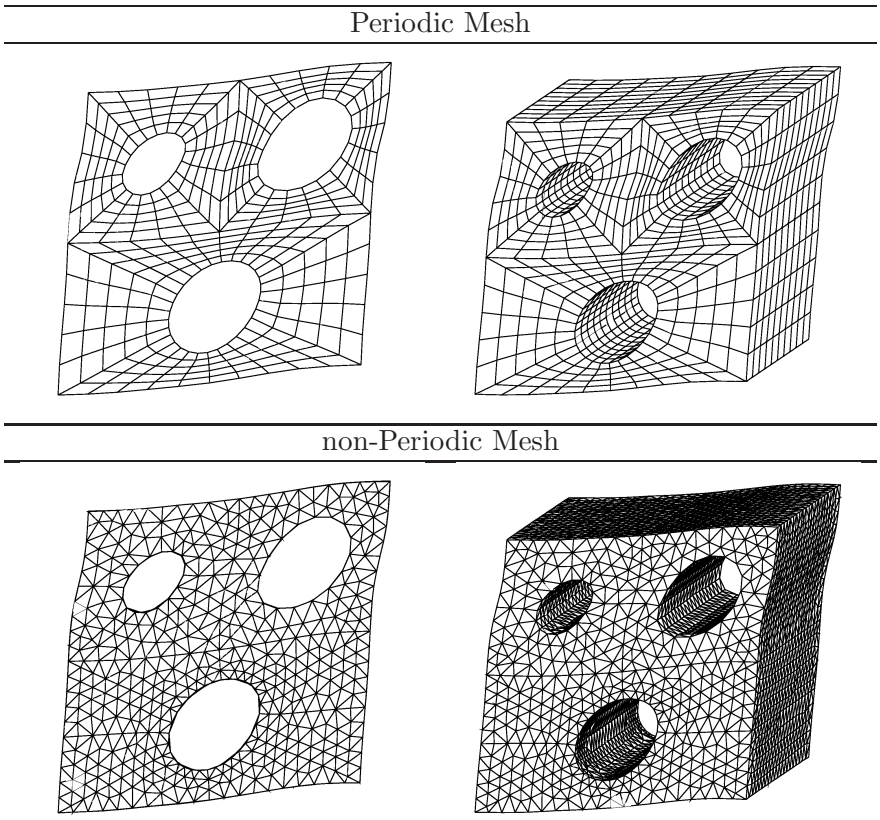

FIGURE 5.12: Final configuration of the three-dimensional RVE with different meshes.

the homogenized macroscopic *First Piola-Kirchhoff* stress tensor, $\boldsymbol{P}\{\boldsymbol{x}\}$, is listed for periodic and non-periodic meshes. From the analysis of results, we conclude that both solutions are quite close. In particular, if we consider the P_{12} component, we observe that the maximum relative error is around 0.4%. As previously pointed out, this level of error, within the context of numerical methods, can be considered negligible.

The efficiency of the proposed approach for three-dimensional problems, not reported here to avoid repetition, is similar to the one obtained for two-dimensions (see Table 5.4). Again, the typical convergence rates of the Newton Raphson method were observed.

TABLE 5.6: Homogenized *First Piola-Kirchhoff* for the three dimensional RVE with periodic configuration.

	$\boldsymbol{P}\{\boldsymbol{x}\}$	Error (%)
Periodic mesh	$\boldsymbol{P} = \begin{bmatrix} -453.485 & 3340.72 & 0.00 \\ 3348.90 & -535.197 & 0.00 \\ 0.00 & 0.00 & -97.6710 \end{bmatrix}$	$\cdots$
Non-periodic mesh	$\boldsymbol{P} = \begin{bmatrix} -455.601 & 3353.57 & 0.00 \\ 3361.86 & -538.487 & 0.00 \\ 0.00 & 0.00 & -99.9863 \end{bmatrix}$	0.383%

5.3.4 Non-periodic three-dimensional RVE with a non-conform mesh

The simulation of a complex three-dimensional RVE under an arbitrary load is carried out in this example. This problem will be used to illustrate the robustness and generality of the proposed approach for the enforcement of PBC. The geometry of the RVE is illustrated in Figure 5.13 and represents a composite material composed by undulated fibres (Figure 5.13(a)) embedded in the matrix (Figure 5.13(b)). The RVE dimensions are $10mm \times 10mm \times 10mm$ and the diameter of the fibres is $2.5\,mm$. It is important to note that the geometry of the RVE was arbitrarily created and, therefore, no detailed information about the geometry is provided. The geometry of the problem was discretized with 31 300 elements for the matrix and 15 314 elements for the fibres amounting to a total of 45 614 linear tetrahedral elements (Figure 5.13(c)). The material properties and

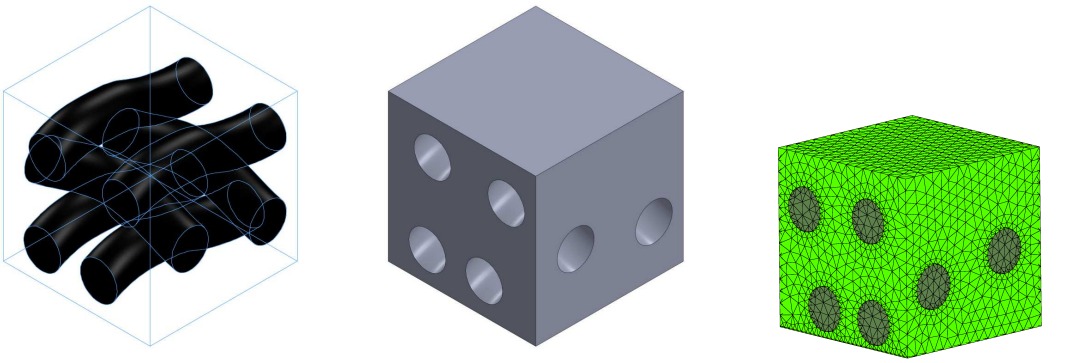

(a) Fibres. (b) Matrix. (c) Mesh with 45 614 linear tetrahedral elements.

FIGURE 5.13: Geometry and mesh of the three dimensional RVE with a non-periodic configuration.

the material constitutive behaviour employed are the same used in Section 5.3.2. In this

case, the following deformation gradient was enforced:

$$\boldsymbol{F}\{\boldsymbol{x}\} = \begin{bmatrix} 1.0 & 0.1 & 0.1 \\ 0.1 & 1.0 & 0.1 \\ 0.1 & 0.1 & 1.0 \end{bmatrix}. \tag{5.60}$$

From the analysis of Figure 5.13, it is possible to conclude that it would be extremely difficult (if not impossible), for the great majority of commercial mesh generators, to create a mesh with a one to one correspondence between nodes on opposite surfaces of the RVE. For cases like this, it is compulsory to use enhanced approaches for the enforcement of PBCs. In Figure 5.14, the effective stress contour of the RVE from different viewpoints at the end of the deformation process is shown. It is possible to observe that the approach proposed is able to accurately enforce a periodic configuration at the boundary of the RVE in spite of the non conformity of the mesh employed. In fact, all surfaces and edges assume a perfectly periodic shape at the end of the deformation process. Therefore, it is possible to conclude that the proposed formulation is robust

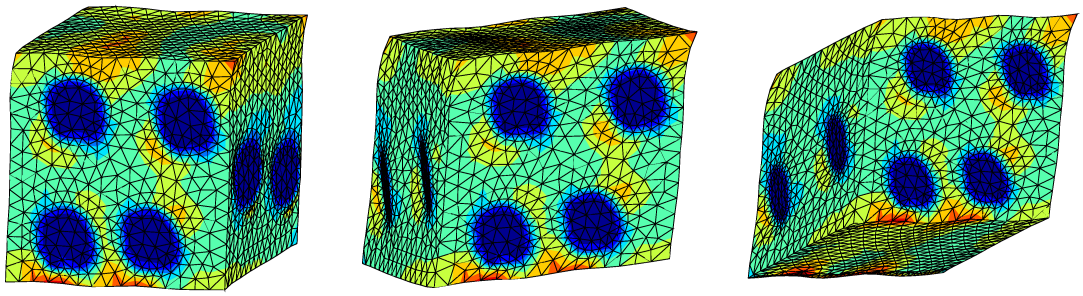

FIGURE 5.14: Effective stress contour at the final configuration of the non-periodic three-dimensional RVE with a non conform mesh.

and can be used to efficiently enforce PBC over complex non-periodic three-dimensional meshes.

5.4 Conclusions

In this contribution, a new approach for the enforcement of PBCs on complex micro-structures with non-conform meshes based on the *Mortar* decomposition method was proposed. The numerical strategy was presented for both two and three dimensional problems at finite strains. The method was formulated with a mixed variational formulation and a displacement based formulation. The description of the numerical integration framework employed to evaluate the *Mortar* coefficients was undertaken. The Newton

based finite element solution procedure for the RVE discrete equilibrium problem was presented in detail.

A comprehensive set of numerical results was presented to assess the strategy proposed and illustrate the generality of the approach. It was demonstrated that the enforcement of PBC proposed is kinematically admissible. This was achieved by analysing the traction forces acting over the boundary of the RVE, which are imposed by the *Hill-Mandel* principle. The accuracy of the method and the stability of the fully linearized Newton procedure were verified. Furthermore, the *Mortar* PBC converges to a stable solution when the size of a RVE increases as would be expected. Finally, the robustness of the method and the quality of results were confirmed, in the three dimensional setting, demonstrating the suitability of the approach for the enforcement of periodic configurations over complex RVEs with randomly generated finite element meshes.

Chapter 6

A non-local approach of integral-type within the context of a coupled multi-scale model.

6.1 Introduction

The quest to extend the range of applicability of coupled multi-scale models is one of the biggest challenge that the scientific community has faced over the last decade. While the applicability of these models is well established with sound valid arguments in the linear elastic and hardening regimes, this is not true when the structure crosses the border which defines the softening regime. It is noteworthy to mention that, in a general sense, the softening regime is a consequence of several phenomena that take place at the microstructure of the material, i.e., nucleation, growth and coalescence of voids which lead to damage accumulation, crack propagation, rupture of the matrix-fiber interface among several others. Despite significant progress on the characterization of these phenomena by means of constitutive models based on either micro-mechanical information [134, 135] or phenomenological assumptions [136], it seems that this approach is reaching its limit. Indeed, it is almost impossible to enhance these models with features which in some way replicate the different and complex phenomena that take place at the grain and phase domain of the material. Nevertheless, this difficulty may be circumvented by using coupled multi-scale models where the different phenomenon may be directly modelled: interface contact between fiber and matrix; propagation of a micro-crack which will give rise to a macro-crack; the correct characterization of the growth of a void under different stress states.

However, there are some issues which limit the applicability of coupled multi-scale models when softening regimes are reached. One of these issues is the mesh dependence pathology that these models suffer. As well established, when softening regimes are reached the loss of ellipticity of the equilibrium equations takes place which gives rise to a problem dependent on the spatial discretization considered [137–141]. It is relevant to emphasize that this issue is much more pronounced in coupled multi-scale models since at least two scales are considered.

In order to minimize this mesh dependence pathology, *non-local* approaches have been developed over the last years. Generally speaking, the main idea behind the formulation of non-local constitutive models is to introduce an intrinsic length into the standard constitutive models in order to properly define the localization zone. Two different approaches, within the context of non-local formulations, can be found in the literature: gradient-type and integral-type theories [142–145]. In the former, an additional equation is added to the structural problem - *the diffusivity equation* - and the non-local variables is considered as an additional unknown of the global problem. Thus, at the structural level a bigger problem is obtained which may have a considerable repercussion on the CPU time and, due to the presence of an extra variable, suitable constraints need to be introduced in order to have a well-posed problem. In fact, these two aspects can be critical whenever two different materials are modelled in the structure. On the other hand, this approach keeps the material constitutive level unchanged being an advantage which should be taken into account.

On the other hand, the non-local approach of integral-type follows a distinct philosophy. The non-locality effect is embedded at the material level instead of the structural domain. Hence, no modification is required at the global problem. However, whenever a new constitutive model is developed it is necessary do redefine the constitutive equations to comply with the non-local integral-type rules. Over the last decades, the non-local model of gradient-type has been the focus of many works and therefore, this approach has developed significantly with regard to its formulation. Nevertheless, the non-local method of integral-type has been recently improved for elasto-plastic materials which resulted in a more attractive model [146–148]. In this case, the extension of this model to large strains and the derivation of a closed form for the tangent material modulus are improvements which should be pointed out Andrade et al. [149].

In this chapter, a non-local approach of integral type is suggested for both macro and micro domains. Despite the fact that the formulation shares the same concepts, the numerical strategies will be rather than different due to the nature of the micro and macro equilibrium problems. Whilst at the micro-scale it is possible to find a heterogeneous media and therefore, different state variables may be considered as non-local variables,

at the macro-scale only kinematic and primary variables (i.e. macroscopic deformation gradient) are available. In fact, the possibility to considering as a non-local variable a kinematic tensor, which drives the micro-equilibrium problem, is a novelty.

The present chapter is organized in the following fashion. In Section 6.2, a brief revision of the non-local theory of integral type is introduced. For more details see references [86, 139, 142, 148]. Then, in Section 6.3 a non-local framework of integral type is proposed for heterogeneous media modelled by means of isotropic explicit damage models. In this section, particular attention is given to the numerical aspects such as the integration algorithm and definition of the tangent operator. In Section 6.4, a non-local approach for the macroscopic equilibrium problem is proposed once again based on non-local theory of integral type. Finally, in Section 6.5 these two numerical frameworks are assessed by means of a set of numerical examples.

6.2 Non-Local theory of integral type

In general, a non-local approach of integral type consists in replacing a local variable, $A\{\boldsymbol{y}\}$, which has a potential impact on the mesh dependence pathology by its non-local counterpart, $\overline{A}\{\boldsymbol{y}\}$, which is defined by the following integral:

$$\overline{A}\{\boldsymbol{y}\} = \int_{\Omega^{nl}} \beta\{\boldsymbol{y},\boldsymbol{\xi}\}\, A\{\boldsymbol{\xi}\}\, dV\{\boldsymbol{\xi}\}\,, \tag{6.1}$$

where $\beta\{\boldsymbol{y},\boldsymbol{\xi}\}$ denotes the non-local averaging operator (in some references, this operator is called as *kernel* [150]) and Ω^{nl} denotes the non-local integration domain. The operator $\beta\{\boldsymbol{y},\boldsymbol{\xi}\}$ is always defined taking into account two points with global coordinates $\boldsymbol{y}$ and $\boldsymbol{\xi}$[1] . In order to obtain an uniform evolution of $\beta\{\boldsymbol{y},\boldsymbol{\xi}\}$, this operator needs to satisfy the *normalising condition* which is given by

$$\int_{\Omega^{nl}} \beta\{\boldsymbol{y},\boldsymbol{\xi}\}\, dV\{\boldsymbol{\xi}\} = 1. \tag{6.2}$$

Aiming to satisfy the condition above defined, a regularization procedure is carried out using the following relation

$$\beta\{\boldsymbol{y},\boldsymbol{\xi}\} = \frac{\alpha\{\boldsymbol{y},\boldsymbol{\xi}\}}{\int_{\Omega^{nl}} \alpha\{\boldsymbol{y},\boldsymbol{\xi}\}\, dV\{\boldsymbol{\xi}\}}, \tag{6.3}$$

where $\alpha\{\boldsymbol{y},\boldsymbol{\xi}\}$ consists on the weighting function. In the present contribution, $\alpha\{\boldsymbol{y},\boldsymbol{\xi}\}$ is given by

$$\alpha\{\boldsymbol{y},\boldsymbol{\xi}\} = \left\langle 1 - \frac{\|\boldsymbol{y}-\boldsymbol{\xi}\|}{L^2} \right\rangle. \tag{6.4}$$

[1] In this chapter, $\boldsymbol{\xi}$ is not related to the *Mortar* integration scheme.

In the preceding equation, $\langle * \rangle$ consists on the *Macauley* brackets and L denotes the *non-local intrinsic length* which is responsible for the incorporation of a characteristic structural length into the constitutive equations. Generally speaking, this parameter is considered an intrinsic material parameter and, as a consequence, it needs to be experimentally calibrated. Typically, inverse numerical procedures are considered for this purpose [139].

Before proceeding, it may be important to shed some light on some aspects concerned to the non-local averaging operator, $\beta\{\boldsymbol{x}, \boldsymbol{\xi}\}$ (Equation (6.3)). With definition (6.3), we observe that the non-local averaging operator, $\beta\{\boldsymbol{x}, \boldsymbol{\xi}\}$, is non-symmetric [140, 141]. In other words, this means that, in some cases we may observe that

$$\beta\{\boldsymbol{x}, \boldsymbol{\xi}\} \neq \beta\{\boldsymbol{\xi}, \boldsymbol{x}\}. \tag{6.5}$$

This particular case takes place when the non-local circumference defined by the non-local intrinsic length, L, intersects the boundary of the structure. Under these conditions, we observe that the volume integral, in the denominator of Equation (6.3), is not equal for points $\boldsymbol{x}$ and $\boldsymbol{\xi}$. As a consequence, it leads to a non-symmetric tangent stiffness required in the iterative *Newton-Raphson* method, which from the CPU time is not beneficial.

In order to circumvent this issue, different definitions for the non-local averaging operator have been suggested [151]. Nevertheless, since the definition above introduced for the non-local averaging operator has been widely and successfully used in non-local approaches of integral type, it will be used in what follows.

6.2.1 Non-local averaging strategy and basic assumptions behind non-local approach

With regard to the strategies for the non-local averaging procedure expressed by Equation (6.1), there are three possibilities: *Eulerian-type*, *Lagrangian-type* and *updated Lagrangian-type*. In the former approach, the non-local integral is determined over the deformed configuration of the structure. When the second approach is considered, the integral is always defined over the initial configuration of the solid. The last can be viewed as a mixture of the other two strategies.

Since the non-local approach will be consistently integrated into a coupled multi-scale model under finite strains (i.e. *Lagrangian* approach), the same strategy for the non-local integral will be used. It is important to note that this approach has some advantages:

the integral is only numerically determined once, at the beginning of the problem and the numerical implementation is rather simple when compared to the other two strategies.

Remark 6.1. As a matter of fact, a comparative analysis among the three cited strategies was performed by Andrade et al. [148], Andrade [152] where pronounced differences among the numerical results were not observed.

Finally, it is relevant to mention an important assumption typically adopted with non-local approaches of integral type: the invariability of the kernels, $\beta\{\boldsymbol{x}, \boldsymbol{\xi}\}$. In other words, this means that $\beta\{\boldsymbol{x}, \boldsymbol{\xi}\}$ is independent of the history of the problem. From the mathematical point of view, this means that

$$\dot{\beta}\{\boldsymbol{y}, \boldsymbol{\xi}\} = 0. \tag{6.6}$$

As a matter of fact, this hypothesis has also been advocated by Andrade et al. [148].

6.3 Isotropic explicit damage model extended with a non-local approach of integral type

Under the assumption of isotropy as well as bulk and shear component of the stress tensor equally penalized by an isotropic damage variable, D, it is possible to define an isotropic damage model such that

$$\boldsymbol{\sigma}^* = (1 - D)\,\boldsymbol{\sigma}, \tag{6.7}$$

where $\boldsymbol{\sigma}^*$ denotes the effective stress tensor and $\boldsymbol{\sigma}$ denotes the *standard Cauchy* stress tensor. In case of a virgin material, D is equal to 0 whereas, in the opposite limit, when the material loses the complete stiffness capacity, variable D is equal to 1. In the literature, different definitions of effective stress tensor may be found and probably, the most widespread effective stress tensor definition was proposed by Lemaitre [136, 153]. According to Lemaitre [136, 153], the difference between the *standard* stress tensor, $\boldsymbol{\sigma}$, and the effective stress tensor, $\boldsymbol{\sigma}^*$, relies on the fact that the later reflects the internal degradation of the material. Note that the stress tensor, $\boldsymbol{\sigma}$, does not contemplate this information, assuming that the deformation of the the material occurs in the absence of internal damage.

In general, the stress tensor, $\boldsymbol{\sigma}$, and damage variable, D, can be defined by means of functionals. These functionals needs to be developed and specified according to the

material under analysis. With this hypothesis in mind, it is possible to write

$$\boldsymbol{\sigma} = \widehat{\boldsymbol{\sigma}}\left\{\boldsymbol{F}, \boldsymbol{\alpha}\right\}, \tag{6.8a}$$

$$D = \widehat{D}\left\{\boldsymbol{F}, \boldsymbol{\alpha}, \boldsymbol{\sigma}\right\}, \tag{6.8b}$$

where $\widehat{\boldsymbol{\sigma}}$ and $\widehat{D}$ denote, respectively, the stress and damage functionals. It is noteworthy to mention that, in Equation (6.8a), functional $\widehat{\boldsymbol{\sigma}}$ is independent of the damage variable whereas the damage functional, $\widehat{D}$, is a function of the stress tensor, internal variables, $\boldsymbol{\alpha}$, and a deformation quantity, which under large strain assumption is the deformation gradient $\boldsymbol{F}$. This is the main characteristic of an explicit damage model. In other words, the difference between explicit and implicit damage model relies on the fact that, in case of an implicit isotropic damage model, the functional $\widehat{\boldsymbol{\sigma}}$ is also a function of the damage variable and vice-versa. This leads to a coupled and nested model which, in general, demands far more complex algorithms to solve it. Examples of implicit damage models can be found in [134–136, 154]. Notwithstanding, it is also important to highlight the fact that the enhancement of these damage models with a non-local framework is far more complex [86, 148].

It is widely established that the introduction of a damage variable into the constitutive model promotes softening regimes and, hence, problems inherent with the loss of ellipticity of the equilibrium equations emerges. Since the source of this pathology is well identified, it is possible to remedy the problem replacing the local damage variable, D, by its non-local counterpart, $\overline{D}$. Thus, Equation (6.7) can be re-written as

$$\boldsymbol{\sigma}^{*} = \left(1 - \overline{D}\right)\boldsymbol{\sigma}, \tag{6.9}$$

where $\overline{D}$ is given by the following integral

$$\overline{D}\left\{\boldsymbol{y}\right\} = \int_{\Omega_0^{nl}} \beta\left\{\boldsymbol{y}, \boldsymbol{\xi}\right\} D\left\{\boldsymbol{\xi}\right\} dV. \tag{6.10}$$

6.3.1 Non-local explicit damage model applied to an heterogeneous media

When the behaviour of one material is studied by means of micromechanical analysis, through homogenization techniques over representative volume elements (RVEs), in order to obtain reliable results, each constituent or phase at the micro-structure needs to be properly characterized with a constitutive model. Assuming that each constituent of the micro-structure is modelled by means of (possibly different) isotropic explicit damage

models, such as the one described in Section 6.3, each constituent can individually promote the well-know mesh dependence pathology. Therefore, it is convenient to develop a strategy where an individual non-local approach may be defined for each constitutive model. In Figure 6.1, a schematic representation of a microstructure with two different phases (matrix and inclusions) is depicted where this concept is illustrated.

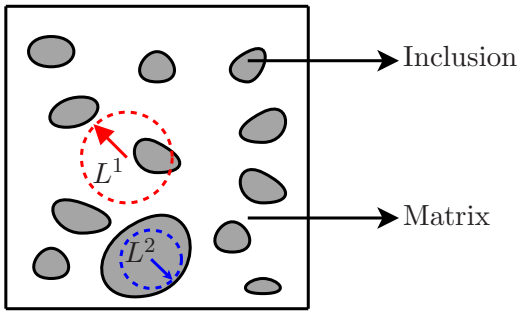

FIGURE 6.1: Schematic representation of non-local averaging scheme in an heterogeneous media.

The enhancement of each isotropic explicit damage model with a non-local approach of integral-type demands the definition of individual non-local averaging operators (kernels), $\beta^m\{\boldsymbol{y},\boldsymbol{\xi}\}$, for each $m-th$ constituent. Thus, the non-local isotropic damage variable, $\overline{D}^m$, related to $m-th$ constituent is given by

$$\overline{D}^m\{\boldsymbol{y}\} = \int_{\Omega_0^{nl,m}} \beta^m\{\boldsymbol{y},\boldsymbol{\xi}\}\, D^m\{\boldsymbol{\xi}\}\, dV^m\{\boldsymbol{\xi}\}\,. \tag{6.11}$$

It is noteworthy to mention that, due to the presence of m *kernels*, there will be m non-local characteristic lengths, L^m.

Despite of being simple to understand, two fundamental geometric considerations are required for a correct numerical implementation and to obtain reliable results, where the concept introduced. The former constraint is associated with the definition of the integration domain in an heterogeneous media. In this case, a generic point $\boldsymbol{y}$ which belongs to phase m is only affected by points $\boldsymbol{\xi}$ of the same constituent. From the geometric point of view, this means that, when the non-local circumference defined by L^m intersects a different phase, the points which belong to this second phase are not considered for the numerical integration for phase m. The later constraint is concerned with the definition of the non-local internal variable that models the behaviour of a specific phase or grain. This means that, the non-local variable at point $\boldsymbol{y}$ is exclusively affected by points $\boldsymbol{\xi}$ which are inside the non-local circumference and simultaneously belong to the same phase or grain. In these cases, each inclusion or grain should be considered as an independent solid.

Remark 6.2. As a matter of fact, it is important to emphasize that the probability of obtaining a non-symmetric homogenized operator, $\beta^m\{\boldsymbol{y},\boldsymbol{\xi}\}$, in heterogeneous media is relatively high due to the previous geometrical considerations.

6.3.2 Spatial discretization of the problem

The spatial discretization of the problem is performed by using the well-established *Gaussian* quadrature rule. Thus, for each generic point $\boldsymbol{y}$ and $\boldsymbol{\xi}$ there is one integration *Gauss* point associated [140, 146]. Based on these ideas, the discretized version of Equation (6.11) is given by

$$\overline{D}_i^m = \sum_{j=1}^{N_{Gauss}^{nl}} w_j J_j \beta_{ij}^m D_j^m, \tag{6.12}$$

where J_j denotes the determinant of the jacobian matrix associated with the $j-th$ *Gauss* point which is inside the non-local circumference and w_j is the associated weight parameter. From the previous equation, we conclude that points $\boldsymbol{y}$ and $\boldsymbol{\xi}$ are linked respectively to i and j *Gauss* points.

Based on the previous relation, it is possible to introduce the discretized version of the effective stress, $\boldsymbol{\sigma}^{*,m}$ (Equation (6.9)) for $m-th$ constituent

$$\begin{aligned}\boldsymbol{\sigma}_i^{*,m} &= \left(1-\overline{D}_i^m\right)\boldsymbol{\sigma}_i^m \\ &= \left(1-\sum_{j=1}^{N_{Gauss}^{nl}} w_j J_j \beta_{ij}^m D_j^m\right)\boldsymbol{\sigma}_i^m.\end{aligned} \tag{6.13}$$

6.3.3 Temporal discretization

The temporal discretization of the micro-equilibrium problem enhanced with a non-local approach of integral type follows the same framework as discussed in Section 3.3.1. However, in order to highlight the main differences, in Table 6.1, the fundamental steps of the algorithm developed are summarily introduced.

6.3.4 Linearization of a non-local Model

In order to conclude the numerical implementation of a non-local explicit damage model for an heterogeneous media, in the present section, the associated consistent stiffness tangent is described. Once again, it is noteworthy to mention that this tangent plays a

TABLE 6.1: Algorithm to implement a non-local explicit damage model for heterogeneous media (at micro-scale).

1. For each i *Gauss* point, determine the weight of the non-local integral related to j gauss point, β_{ij}
$$\beta_{ij}^{m} = \frac{\alpha_{ij}^{m}}{\sum_{j=1}^{N_{Gauss}^{NL}} \alpha_{ij}^{m} J_j w_j}.$$
Note that in case of the *Lagrangian* approach, the previous step is only carried out once at the beginning of the problem.

2. State-update over all integration *Gauss* points, i, (**Local Approach**);
$$\boldsymbol{\sigma}_{n+1,i}^{m} = \widehat{\boldsymbol{\sigma}}^{m}\left\{\boldsymbol{F}_{n+1,i}, \boldsymbol{\alpha}_{n,i}^{m}\right\};$$

3. Update the local damage law for all i *Gauss* points (**Local Approach**);
$$D_{n+1,i}^{m} = \widehat{D}^{m}\left\{\boldsymbol{F}_{n+1,i}, \boldsymbol{\alpha}_{n+1,i}^{m}, \boldsymbol{\sigma}_{n+1,i}^{m}\right\};$$

4. Determine the non-local damage variable for all *Gauss* points i, $\overline{D}_{n+1,i}^{m}$;
$$\overline{D}_{n+1,i}^{m} = \sum_{j=1}^{N_{Gauss}^{nl}} w_j J_j \beta_{ij}^{m} D_{n+1,j}^{m};$$

5. Compute the effective stress tensor for all integration *Gauss* points, i;
$$\boldsymbol{\sigma}_{n+1,i}^{*,m} = \left(1 - \overline{D}_{n+1,i}^{m}\right)\boldsymbol{\sigma}_{n+1,i}^{m}.$$

critical role within the context of the iterative *Newton-Raphson* method which is applied to solve the micro-equilibrium problem.

In the literature, the consistent linearization of an explicit isotropic damage model enhanced with a non-local framework of integral type has been already presented [146]. However, the range of applicability of this approach is limited: it is only valid for homogeneous media and is restricted to small deformations. In contrast, in the present work, this approach will be modified for heterogeneous media and extended to large strains. With regard to the large strain extension, the work of carried out by Andrade et al. [149] was followed.

Remark 6.3. For sake of simplicity, the nomenclature associated to the discretized time (or pseudo-time), t will be dropped. Note that when the tangent operator is determined all variables are defined at the same instant t_{n+1}.

We start the derivation of this operator by recovering the equation that governs the equilibrium problem at the micro-scale (Equation (3.24))

$$\boldsymbol{f}^{int}\{\boldsymbol{u}\} = \boldsymbol{0}, \tag{6.14}$$

which, by definition, can be re-written as

$$\boldsymbol{f}^{int}\{\boldsymbol{u}\} = \int_{\Omega^d} \boldsymbol{B}^T \boldsymbol{\sigma}^{*,m} dV. \tag{6.15}$$

In the previous equation, $\boldsymbol{B}^T$ denotes the discrete symmetric gradient operator. It is also important to note that, if the $m-th$ constituent is modelled by a constitutive model that does not have internal deterioration (i.e. in absence of internal damage), we verify that $\boldsymbol{\sigma}^{*,i} \equiv \boldsymbol{\sigma}^{i}$.

Remark 6.4. Once again, Equation (3.24) was considered for the linearization procedure, neglecting the term associated to the traction forces acting over the RVE. Note that this term is not directly affected by the introduction of the non-local technique and, hence, it has not got impact on the linearization of the problem.

The spatial discretized version of the previous equation is simply given by

$$\boldsymbol{f}^{int}\{\boldsymbol{u}\} = \sum_{i=1}^{N_{Gauss}} \boldsymbol{B}_i^T \boldsymbol{\sigma}_i^{*,m} w_i J_i, \tag{6.16}$$

where N_{Gauss} denotes the total number of *Gauss* points of the mesh (at the micro-scale) and w_i and J_i are respectively the weight and the determinant of the *Jacobian* matrix of *Gauss* point i.

By definition, the tangent stiffness matrix is given by the derivative of the internal forces with regard to the displacement field (at the micro-scale). Thus, it is possible to write

$$\begin{aligned} \boldsymbol{K}_T^{Nl} &= \frac{\partial \boldsymbol{f}^{int}\{\boldsymbol{u}\}}{\partial \boldsymbol{u}}, \\ &= \sum_{i=1}^{N_{Gauss}} \boldsymbol{B}_i^T \frac{\partial \boldsymbol{\sigma}_i^{*,m}}{\partial \boldsymbol{u}} w_i J_i. \end{aligned} \tag{6.17}$$

The derivative of the effective stress tensor, $\boldsymbol{\sigma}^{*,m}$, can be defined by the following compact expression [146, 149]

$$\begin{aligned} \frac{\partial \boldsymbol{\sigma}_i^{*,m}}{\partial \boldsymbol{u}} &= \frac{\partial \boldsymbol{\sigma}_i^{*,m}}{\partial \boldsymbol{\varepsilon}_1} \frac{\partial \boldsymbol{\varepsilon}_1}{\partial \boldsymbol{u}} + \cdots + \frac{\partial \boldsymbol{\sigma}_i^{*,m}}{\partial \boldsymbol{\varepsilon}_{N_{Gauss}}} \frac{\partial \boldsymbol{\varepsilon}_{N_{Gauss}}}{\partial \boldsymbol{u}}, \\ &= \sum_{j=1}^{N_{Gauss}} \frac{\partial \boldsymbol{\sigma}_i^{*,m}}{\partial \boldsymbol{\varepsilon}_j} \boldsymbol{B}_j. \end{aligned} \tag{6.18}$$

Denoting the derivative of the effective stress tensor, $\boldsymbol{\sigma}_i^{*,m}$, in relation to the deformation strain tensor at $j-th$ integration *Gauss* point, $\boldsymbol{\varepsilon}_j$, by $\mathbf{D}_{ij}^m$, and introducing the previous relation into Equation (6.17), it is possible to write

$$\boldsymbol{K}_T^{Nl} = \sum_{i=1}^{N_{Gauss}} w_i J_i \boldsymbol{B}_i^T \sum_{j=1}^{N_{Gauss}} \mathbf{D}_{ij}^m \boldsymbol{B}_j. \tag{6.19}$$

The fourth order tensor, $\mathbf{D}_{ij}^m$, is given by

$$\begin{aligned} \mathbf{D}_{ij}^m &= \frac{\partial}{\partial \boldsymbol{\varepsilon}_j} \left[\left(1 - \overline{D}_i^m\right) \boldsymbol{\sigma}_i^m \right] \\ &= \left(1 - \overline{D}_i^m\right) \mathbf{D}_{ij}^{Mat,m} - \frac{\partial \overline{D}_i^m}{\partial \boldsymbol{\varepsilon}_j} \otimes \boldsymbol{\sigma}_i^m, \end{aligned} \tag{6.20}$$

where symbol $\otimes$ denotes the *dyadic* tensorial product. In the previous equation, tensor $\mathbf{D}_{ij}^{Mat,m}$ consists on the local consistent tangent operator associated to the $m-th$ constitutive material defined by

$$\mathbf{D}_{ij}^{Mat,m} = \frac{\partial \boldsymbol{\sigma}_i^m}{\partial \boldsymbol{\varepsilon}_j}. \tag{6.21}$$

It is important to mention that since the functional of the stress tensor is still local, we conclude that $\mathbf{D}_{ij}^{Mat,m}$ is null whenever $i \neq j$. Finally, the derivative of the non-local damage variable, $\overline{D}_i^m$, in relation to the strain tensor, $\boldsymbol{\varepsilon}_j$ is given by

$$\frac{\partial \overline{D}_i^m}{\partial \boldsymbol{\varepsilon}_j} = \sum_{k=1}^{N_{Gauss}^{nl}} w_k J_k \beta_{ik}^m \frac{\partial D_k^m}{\partial \boldsymbol{\varepsilon}_j}. \tag{6.22}$$

Note that, once again, when $k \neq j$, $\frac{\partial D_k^m}{\partial \boldsymbol{\varepsilon}_j} = \mathbf{0}$. It is also relevant to remark that the fourth order tensor, $\mathbf{D}_{ij}^{Mat,m}$ and the derivative $\frac{\partial D_k^m}{\partial \boldsymbol{\varepsilon}_j}$ are a directly consequence of the local constitutive material and local damage laws.

6.3.5 Extension to finite strains

The derivation of the tangent operator, for a problem enhanced with a non-local approach of integral type presented in the previous section, was carried out in the spirit of infinitesimal strains. However, since this approach will be implemented into a finite element code (***MSP*** code) which uses a hyperelastic-based multiplicative framework proposed by [89, 155], additional algebraic operations are required.

In Section B.2.1 of Appendix B, these algebraic manipulations are described in detail. Here, for convenience, only the final result is presented which consists in the following

expression

$$DG\left\{\boldsymbol{u},\boldsymbol{\eta}\right\}\left[\boldsymbol{d}\right]=\int_{\varphi(\Omega)}\mathbf{a}:\nabla_{\boldsymbol{x},\boldsymbol{\xi}}\boldsymbol{d}:\nabla_{\boldsymbol{x}}\boldsymbol{\eta}dV. \tag{6.23}$$

Note that, in the previous equation, symbols $\nabla_{\boldsymbol{x}}$ and $\nabla_{\boldsymbol{x},\boldsymbol{\xi}}$ denote, respectively, the continuum spatial gradient operator at points $\boldsymbol{y}$ and $\boldsymbol{\xi}$. Moreover, $\varphi\left(\Omega_0\right)$ denotes the spatial configuration of the RVE (deformed domain). Applying the conventional spatial discretization rules to the previous equation and considering the *Gauss* quadrature rule to perform the numerical integration, one can write

$$\boldsymbol{K}_T^{Nl}=\sum_{i=1}^{N_{Gauss}}w_iJ_i\boldsymbol{G}_i^T\sum_{j}^{N_{Gauss}}\mathbf{a}_{ij}^m\boldsymbol{G}_j, \tag{6.24}$$

where $\boldsymbol{G}_i$ and $\boldsymbol{G}_j$ are the discrete gradient operators at the integration *Gauss* points i and j and $\mathbf{a}_{ij}^m$ the spatial tangent modulus. This fourth-order tensor is given by Equation (B.17) in a continuum shape and its local discretized version is given by

$$\mathbf{a}_{ij}^m=\frac{1}{2\det\left(\boldsymbol{F}_i\right)}\mathbf{D}_{ij}^m:\mathbf{L}_j:\mathbf{B}_j-\left[\boldsymbol{\Sigma}_i^m\right]|_{i=j}\,. \tag{6.25}$$

Note that, $\mathbf{D}_{ij}^m$ denotes the tangent modulus at infinitesimal strains defined by Equation (6.20). In the last expression, the fourth-order tensor $\boldsymbol{\Sigma}^m$ is given by

$$\Sigma_i^{ijkl,m}=\sigma_i^{il,m}\delta^{jk}. \tag{6.26}$$

With regard to tensors $\mathbf{L}_j$ and $\mathbf{B}_j$, they are respectively defined by

$$\mathbf{L}_j=\frac{\partial\ln\left[\boldsymbol{B}_{j,n+1}^{e\ trial}\right]}{\partial\boldsymbol{B}_{j,n+1}^{e\ trial}}, \tag{6.27}$$

$$\mathsf{B}_j^{ijkl}=\delta^{ik}\left(\boldsymbol{B}_{j,n+1}^{e\ trial}\right)^{jl}+\delta^{jk}\left(\boldsymbol{B}_{j,n+1}^{e\ trial}\right)^{il}. \tag{6.28}$$

6.3.6 Damage law

In this work, a simple explicit damage law coupled with the *von Mises* elasto-plastic constitutive model is considered. The damage law is simply governed by the evolution of the rate of accumulated plastic strain, $\dot{\overline{\varepsilon}}^p$, affected by a scalar parameter,ε_f, which can be viewed as a critical value of the accumulated plastic strain, $\overline{\varepsilon}^p$. Saying that, it is possible to write

$$\dot{D}=\frac{\dot{\overline{\varepsilon}}^p}{\varepsilon_f}. \tag{6.29}$$

In Section B.3, the derivation of the consistent tangent modulus is presented for this damage law.

6.4 Non-local approach at macro-scale domain

The non-local framework described in the previous section is exclusively dedicated to the micro-scale problem and, therefore, its regularizing effect only takes place exclusively at the RVE domain. Nevertheless, mesh dependence issues may also appear at the macro-scale. Therefore, we conclude that it is also necessary to enhance the formulation at the macro-scale. This is critical in case of *First-Order Coupled Multi-Scale Models*. As a matter of fact, in *Second* order coupled multi-scale problems [38], the mesh dependence issue at the macro-scale is less pronounced. This is due to the fact that, the bridge between macro-to-micro domains and vice-versa is not solely preformed by the macroscopic deformation gradient, $\boldsymbol{F}\{\boldsymbol{x}, t\}$, and homogenized *First Piola-Kirchhoff* stress tensor, $\boldsymbol{P}\{\boldsymbol{x}, t\}$. For this formulation, in addition to these two variables, their gradients are also included. Despite minimizing the mesh dependence pathology, this coupled multi-scale formulation has not gained notable popularity due to the complexity that emerges either from the formulation and numerical implementation. Note that second order finite element codes are rare, only being used to solve very particular problems.

Having in mind the limitation concerned with mesh dependence at the macro-scale that *First* order coupled multi-scale models suffers, we conclude that, this issue should be controlled by means of a suitable numerical scheme. However, due to the nature of the macro-scale problem, where there is a lack of variables at the macro-scale domain which can be considered as non-local variables, the formulation and implementation of non-local approach will different to perform.

As stressed out in Chapter 3, the micro-equilibrium problem can be viewed as the state-update of a standard solid mechanic problem and, hence, at the macro-scale domain there are no internal variables which may be used as non-local variable. Due to this lack of internal variables at the structural level, the implementation of a non-local framework is limited either to the displacements or the deformation gradient. Recently, Wu et al. [54] has proposed a multi-scale method where a non-local framework of gradient type was implemented at both scales. At the RVE level, a standard non-local approach of gradient type was adopted where particular attention was given to the definition of the boundary constraints which may be applied to the non-local variable when different phases exist at the RVE level. However, at the macro-scale, due to the non-existence of internal variables, the non-local variable was defined as being the homogenized accumulated plastic strain over the RVE domain. Then, with this variable at hand, the diffusivity equation, which defines the non-local approach of gradient type, is added to the macroscopic equilibrium problem. Despite of the remarkable results obtained, in view of the author's opinion, the homogenization of internal variables defined at the

RVE level such as accumulated plastic strain, damage, plastic multipliers among several others is questionable. Moreover, the enhancement of the bridge between micro and macro domains with this type of parameters demands additional non-trivial energetic considerations which are still under analysis.

Based on the previous observations, in what follows, a non-local approach of integral type will be proposed for the macroscopic problem where the non-local variable is the macroscopic deformation gradient - a kinematic variable. It is relevant to emphasize that, according to the author's knowledge, a full non-local approach of integral type with a kinematical non-local variable has never been proposed not even within the context of standard solid mechanics problems.

Notwithstanding, in the literature it is possible to find explicit damage models enhanced with a non-local formulation of integral type where the non-local parameter is a kinematical variable: deformation tensor [156] or displacement field [157, 158]. Nevertheless, these two approaches mentioned are clearly different than the scheme herein proposed. Whilst in references [156–158] the non-local variable is exclusively used on the definition of the explicit damage functional (defined in Section 6.3.1), in the present contribution, the non-local macroscopic deformation gradient will be responsible for driving whole micro-equilibrium problem (i.e. state update).

In what follows, this new non-local framework will be introduced where the main differences in relation to the standard coupled multi-scale model will be highlighted. Moreover, special attention will be given to the derivation of the macroscopic tangent operator.

6.4.1 Definition of non-local macroscopic deformation gradient

The mathematical approach followed to define the non-local macroscopic deformation gradient, $\overline{\boldsymbol{F}}\{\boldsymbol{x}\}$, is exactly the same as used for scalar variables (Section 6.3.1). Thus, by using the standard non-local operator previously defined (Equation (6.1)), $\overline{\boldsymbol{F}}\{\boldsymbol{x}\}$, is given by

$$\overline{\boldsymbol{F}}\{\boldsymbol{x}\} = \int_{\Omega_0^{nl}} \beta\{\boldsymbol{x}, \boldsymbol{\xi}\}\, \boldsymbol{F}\{\boldsymbol{\xi}\}\, dV\{\boldsymbol{\xi}\}\,. \tag{6.30}$$

In Figure 6.2, a schematic representation of the *First* order coupled multi-scale model enhanced with a non-local approach of integral type at the macro-scale is introduced. Comparing the strategy described in Chapter 3 and illustrated in Figure 3.3 with the approach schematically presented in Figure 6.2, we observe that the only difference relies on the deformation gradient which is sent to the micro-scale: in this case, the local macroscopic deformation gradient, $\boldsymbol{F}\{\boldsymbol{x}, t\}$, is replaced by its non-local counterpart,

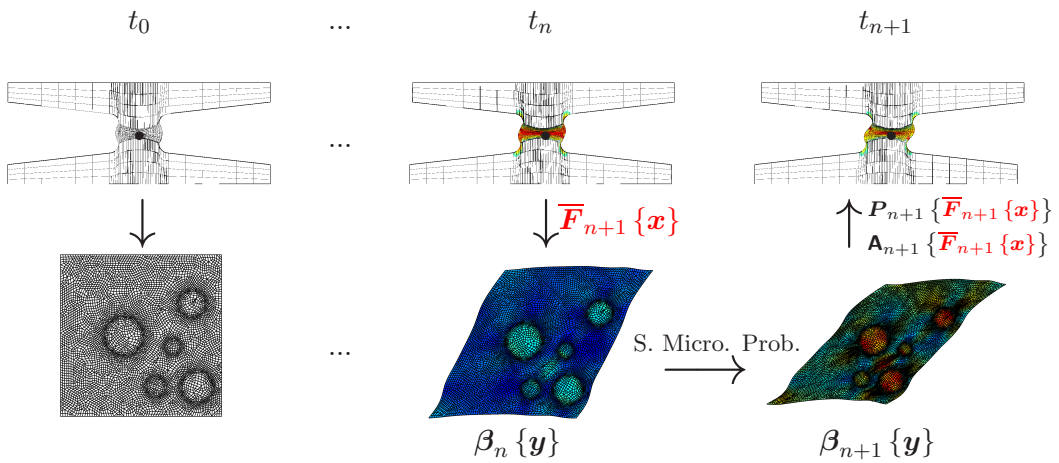

FIGURE 6.2: Schematic illustration of a *First* order coupled multi-scale model enhanced with a non-local framework of integral-type at the macro-scale: macroscopic deformation gradient as non-local parameter, $\overline{\boldsymbol{F}}_{n+1}\{\boldsymbol{x}\}$.

$\overline{\boldsymbol{F}}\{\boldsymbol{x},t\}$. It is noteworthy to mention that, the implementation of this approach does not demand any change in the algorithm employed at the micro-scale, neither on the tangent operator, $\mathbf{A}_{n+1}\left\{\overline{\boldsymbol{F}}_{n+1}\{\boldsymbol{x}\}\right\}$, which corresponds to the derivative of $\boldsymbol{P}_{n+1}\left\{\overline{\boldsymbol{F}}_{n+1}\{\boldsymbol{x}\}\right\}$ in relation to $\overline{\boldsymbol{F}}_{n+1}\{\boldsymbol{x}\}$. Notwithstanding, the macroscopic consistent tangent modulus includes other fourth-order tensors due to the modification of the non-local macroscopic deformation gradient, $\overline{\boldsymbol{F}}_{n+1}\{\boldsymbol{x}\}$. This issue will be discussed in the following section.

6.4.2 Linearization of the macroscopic problem enhanced with a non-local approach of integral type

The linearization of the macroscopic problem enhanced with non-local approach of integral type where the non-local variable is the macroscopic deformation gradient, $\overline{\boldsymbol{F}}\{\boldsymbol{x},\boldsymbol{t}\}$, is a lengthy procedure involving several non-trivial algebraic and mathematical operations. Thus, in Section B.4, all operations are described in detail. The final result of this linearization is given by the following expression

$$\begin{aligned}\mathbf{K}\{\boldsymbol{x}\} = &\int_{\varphi(\Omega_0)} \boldsymbol{G}^T\{\boldsymbol{x}\}\left(\mathbf{q}_1+\mathbf{q}_4\right)\boldsymbol{G}\{\boldsymbol{x}\}\,dV \\ &+\alpha\{\boldsymbol{x},\boldsymbol{\xi}\}\int_{\varphi(\Omega_0)} \boldsymbol{G}^T\{\boldsymbol{x}\}\left(\mathbf{q}_2+\mathbf{q}_3-\mathbf{q}_5\right)\boldsymbol{G}\{\boldsymbol{\xi}\}\,dV,\end{aligned} \tag{6.31}$$

where $\boldsymbol{G}\{\boldsymbol{x}\}$ and $\boldsymbol{G}\{\boldsymbol{\xi}\}$ are the discrete spatial gradient operator at points $\boldsymbol{x}$ and $\boldsymbol{\xi}$ respectively. The scalar, $\alpha\{\boldsymbol{x},\boldsymbol{\xi}\}$ denotes the non-local averaging operator at the macro-scale (introduced in Section 6.2). The fourth order tensors $\mathbf{q}_1$, $\mathbf{q}_2$, $\mathbf{q}_3$, $\mathbf{q}_4$ and $\mathbf{q}_5$ in

Einstein's notation are given by:

$$\mathsf{q}_1^{imkl} = F^{mj}\left[\left(\boldsymbol{\sigma}\left\{\overline{\boldsymbol{F}}\right\}\boldsymbol{F}^{-T}\right)\otimes\boldsymbol{I}\right]^{ijkl}, \tag{6.32a}$$

$$\mathsf{q}_2^{iomp} = \frac{1}{\left(\det\overline{\boldsymbol{F}}\right)}F^{oj}\mathsf{A}^{ilmn}\left(F^{\boldsymbol{\xi}}\right)^{pn}\left(\overline{F}^{lk}\right)^{T}\left(F^{kj}\right)^{-T}, \tag{6.32b}$$

$$\mathsf{q}_3^{iomp} = \frac{1}{\left(\det\overline{\boldsymbol{F}}\right)}F^{oj}\widehat{P}^{ik}\left(\mathsf{I}_T\right)^{klmn}\left(F^{\boldsymbol{\xi}}\right)^{pn}\left(F^{-T}\right)^{lj}, \tag{6.32c}$$

$$\mathsf{q}_4^{iomp} = F^{oj}\sigma^{il}\left(\frac{\partial\boldsymbol{F}^{-T}}{\partial\boldsymbol{F}}\right)^{ljmn}F^{pn}, \tag{6.32d}$$

$$\mathsf{q}_5^{iomp} = F^{oj}\left(\overline{F}^{-T}\right)^{mn}\left(F^{\boldsymbol{\xi}}\right)^{pn}\sigma^{il}\left(F^{-T}\right)^{lj}, \tag{6.32e}$$

where I_T denotes a fourth order tensor defined by

$$\mathsf{I}_T = \frac{\partial\boldsymbol{A}^T}{\partial\boldsymbol{A}}, \tag{6.33}$$

and $\widehat{\boldsymbol{P}}$ is expressed by

$$\widehat{\boldsymbol{P}}\left\{\boldsymbol{x}\right\} = \left(\det\overline{\boldsymbol{F}}\left\{\boldsymbol{x}\right\}\right)\boldsymbol{\sigma}\left\{\boldsymbol{x}\right\}\overline{\boldsymbol{F}}^{-T}\left\{\boldsymbol{x}\right\}. \tag{6.34}$$

6.5 Numerical results

Aiming to assess the efficiency of the non-local frameworks proposed, three numerical examples are used. The first two examples are exclusively devoted to assess the robustness of the non-local approach described in Section 6.3, which is responsible to minimize the mesh dependence pathology that takes place at the micro-scale. Thus, in the first example, a micro-mechanical analysis was carried out where a micro-structure representative of an heterogeneous material was considered. In the second example, this numerical framework was assessed within the context of a *First* order coupled multi-scale problem. Finally, in the last example, the non-local approach formulated specifically for the macroscopic equilibrium problem is analysed by means of a coupled problem where the specimen at the macroscopic domain is a double notched plate.

Remark 6.5. Before proceeding, it is important to note that the author is aware that in the presence of softening behaviours, suitable homogenization procedures should be used in order to guarantee the representativeness of the RVE. Nevertheless, this issue is out of the scope of the present work. Nevertheless, for those who are interested in this research field, references [52, 53] may be consulted.

6.5.1 Micro-mechanical problem

We start the analysis of the non-local framework proposed in Section 6.3 by considering a heterogeneous media which includes different phases and voids with a periodic configuration. In order to construct the geometry of the RVE, two steps were performed. In the first, an algorithm developed by Miranda et al. [133] was used to generate the geometry of the RVE. Basically, this algorithm defines the center of circles (i.e. circular inclusions) over the total domain of the RVE taking into account the concept of periodicity. It is noteworthy to mention that this concept postulates that the total micro-structure may be modelled by successive RVEs positioned side-by-side. For this purpose, some variables were defined: dimension of the square RVE, 40 mm; void volume fraction of inclusions, 40 %; and the diameter of the circular inclusions, 6 mm. Finally, in the second, meshes were created where 8 circles which are completely inside of the RVE were arbitrarily chosen to be voids (the remaining were considered inclusions). This solution was employed in order to promote more severe and visible softening regimes in these type of micro-structures. Note that this softening regime is characterized by a decrease of a specific component of the homogenized *First Piola-Kirchhoff* stress tensor, $\boldsymbol{P}\{\boldsymbol{x}\}$, associated with the preferential mode of deformation considered.

Since the goal is to analyse the mesh dependence pathology, two meshes with different refinement levels were considered, which are introduced in Figure 6.3. In both meshes, quadratic quadrilateral elements were considered with reduced integration (2×2 integration *Gauss* points). As usually, in the present thesis, plane strain condition was considered.

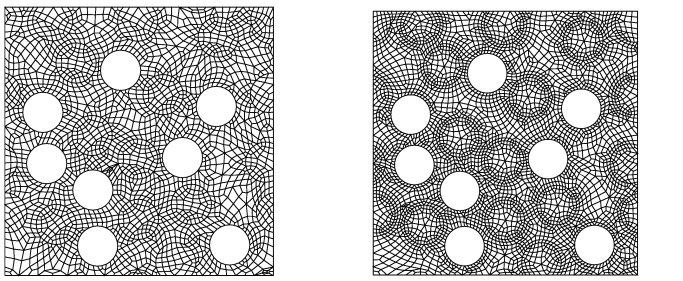

(a) Mesh 1: 2377 quadratic quadrilateral elements.

(b) Mesh 2: 4041 quadratic quadrilateral elements.

FIGURE 6.3: Mesh refinement levels considered for the heterogeneous RVE with periodic configuration.

With regard to the material constitutive models, the matrix of the RVE was modelled by means of the explicit damage model presented in Section 6.3.6 coupled with the standard elasto-plastic *von Mises* constitutive model. On the other hand, the inclusions were modelled by a linear elastic law. The material properties for these two constitutive

models are listed in Table 6.2. Finally, in this problem, the macroscopic deformation

TABLE 6.2: Material properties for the heterogeneous RVE with periodic configuration.

	Matrix	**Inclusion**
Young's Modulus, E (GPa)	30	74
Poisson's ration, v	0.3	0.2
Yield Stress, σ_0 (MPa)	93	-
Hardening Modulus, H (GPa)	0.1	-
Critical accumulated plastic strain, ε_f	0.8	-

gradient enforced to the RVE is given by

$$\boldsymbol{F}\{\boldsymbol{x}\} = \begin{bmatrix} 1.0 & 0.02 \\ 0.02 & 1.0 \end{bmatrix}, \tag{6.35}$$

and *Mortar Periodic* boundary condition was considered.

In Figures 6.4 and 6.5, the contour plots of the damage variable for the two meshes are either for both local or non-local approaches. As it is possible to observe, when the local approach is applied (Figures 6.4(a) and 6.4(b)), the level of damage reached at the same incremental factor is notoriously different for the two meshes considered. As expected, when the number of elements increases (Figure 6.4(b)), the evolution of the damage variable is more pronounced and, as a consequence of this phenomenon, a more severe softening regime results. This softening regime, associated to the fine mesh, is clear in Figure 6.6(a) where the evolution of term P_{12} of the homogenized *First Piola-Kirchhoff*, $\boldsymbol{P}\{\boldsymbol{x}\}$, is plotted.

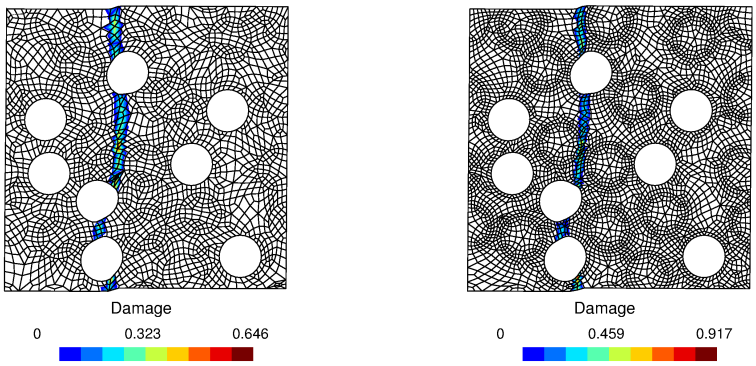

(a) Local result, Mesh 1. (b) Local result, Mesh 2.

FIGURE 6.4: Contour plots of the damage variable for local approach when the incremental factor is equal to 0.4.

However, when the non-local approach described in Section 6.3 is applied to solve the same problem, it is clear that there is a notable attenuation of the mesh dependence pathology. This attenuation is perceptible either from the contour plots of Figure 6.5

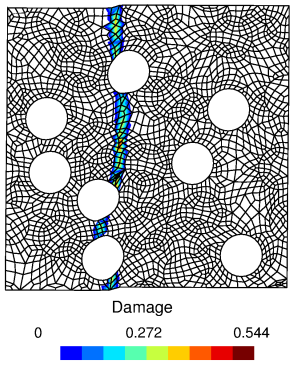

(a) Non-Local result, Mesh 1, $L = 0.5\,mm$, $N^{NL}_{Gauss} = 20$.

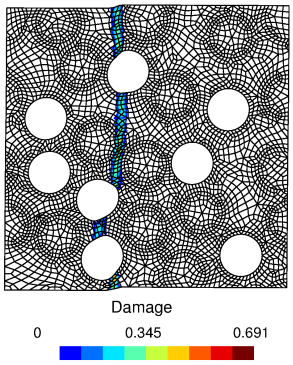

(b) Non-Local result, Mesh 2, $L = 0.5\,mm$, $N^{NL}_{Gauss} = 23$.

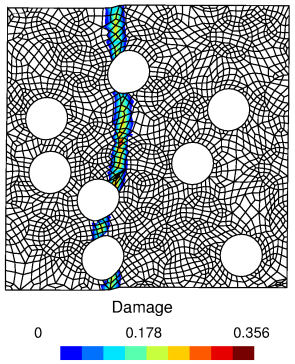

(c) Non-Local result, Mesh 1, $L = 1.0\,mm$, $N^{NL}_{Gauss} = 43$.

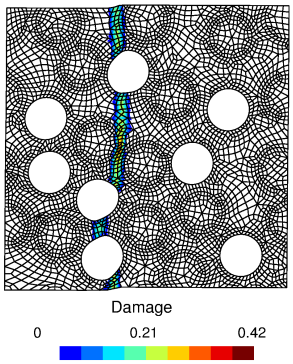

(d) Non-Local result, Mesh 2, $L = 1.0\,mm$, $N^{NL}_{Gauss} = 61$.

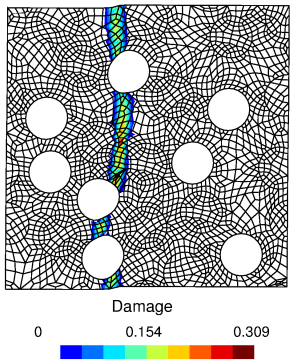

(e) Non-Local result, Mesh 1, $L = 1.25\,mm$, $N^{NL}_{Gauss} = 58$.

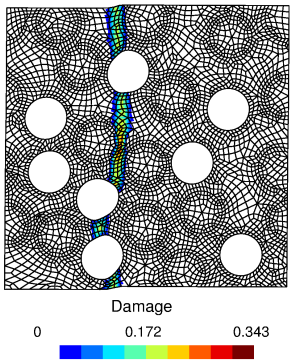

(f) Non-Local result, Mesh 2, $L = 1.25\,mm$, $N^{NL}_{Gauss} = 89$.

FIGURE 6.5: Contour plots of the damage variable for non-local approach when the incremental factor is equal to 0.4.

or evolution of term P_{12} presented in Figure 6.6(b). From the damage plots, it is clear that with the increase of the non-local characteristic length, L, the value of the damage variable attained with the two meshes is closer. This is particularly true for $L = 1.25\ mm$, as it is possible to observe in Figures 6.5(e) and 6.5(f). This conclusion is also corroborated by analysing the evolution of P_{12} term for $L = 1.25\ mm$ in Figure

6.6(b), where both curves (associated to each mesh) are in close agreement throughout the whole deformation process.

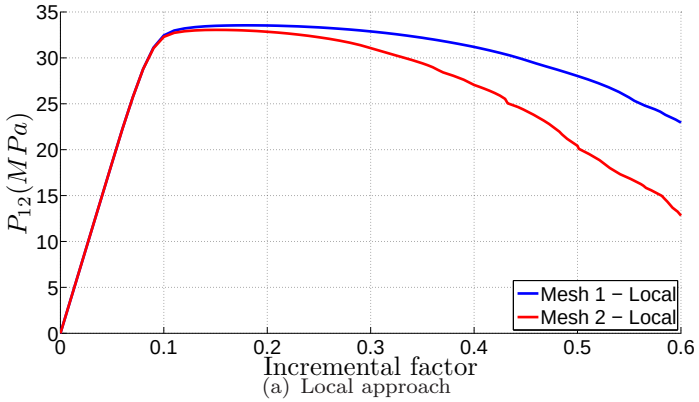

(a) Local approach

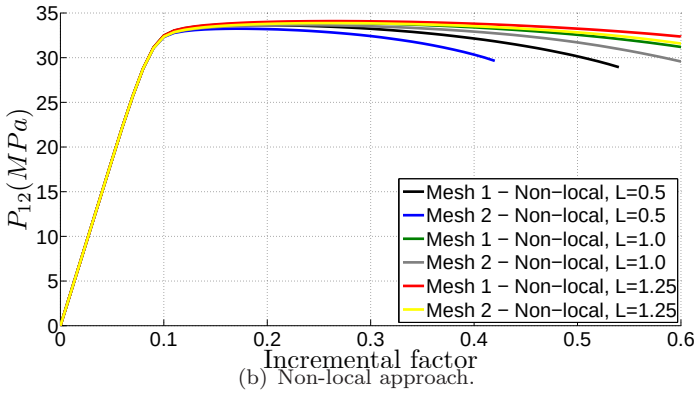

(b) Non-local approach.

FIGURE 6.6: Evolution of term P_{12} of the homogenized *First Piola-Kirchhoff* stress tensor, $\boldsymbol{P}\{\boldsymbol{x}\}$.

From Figure 6.6 it is also possible to conclude that, in general sense, there is a relation between L and the evolution of the P_{12} term of the homogenized *First Piola-Kirchhoff* stress tensor, $\boldsymbol{P}\{\boldsymbol{x}\}$. Thus, it is vital that the user of such numerical tools is aware that unrealistic and non-physical results may appear for large values of L. As pointed out previously, in order to avoid this issue, a calibration procedure for L should be performed for each micro-structure.

In Table 6.3, the convergence behaviour of the *Newton-Raphson* scheme developed to solve the micro-equilibrium problem enhanced with a non-local approach of integral type is illustrated. This convergence was obtained for $L = 1.25\ mm$ when the incremental factor was equal to 0.4. As it is possible to observe, a quadratic asymptotic convergence rate was obtained. This is a clear evidence that the linearization procedure was properly carried out as well as its extension to large strains.

Finally, in Figure 6.7 it is possible to observe the sparsity of the RVE global stiffness matrix for the problem with local and non-local approaches. As expected, the band

TABLE 6.3: Convergence rates obtained with the linearization described in Sections 6.3.4 and 6.3.5 (for incremental factor equal to 0.4 and $L = 1.25\ mm$).

Iteration number	Convergence
1	18.1886
2	9.11023
3	16.4940
4	0.649614
5	$0.884217E-02$
6	$0.303750E-03$
7	$0.361128E-09$

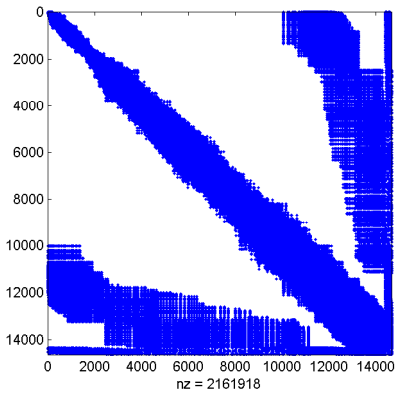

(a) Local approach.

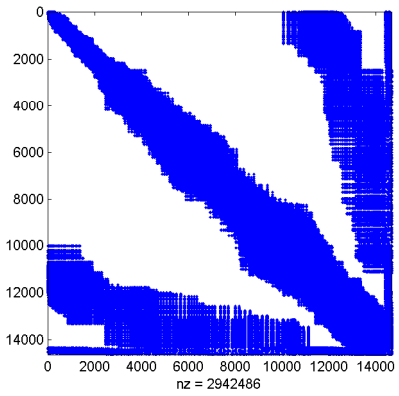

(b) Non-local approach, $L = 0.5\ mm$.

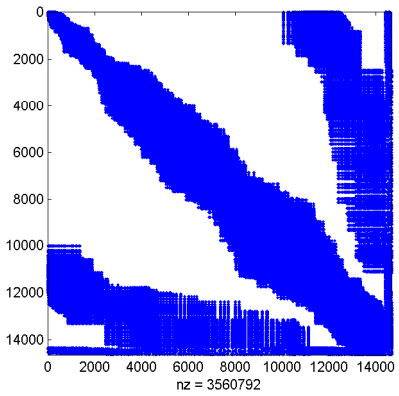

(c) Non-local approach, $L = 1.0\ mm$.

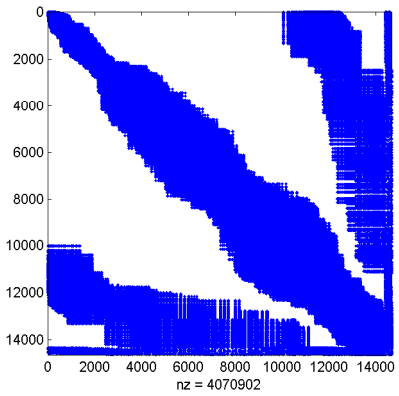

(d) Non-local approach, $L = 1.25\ mm$.

FIGURE 6.7: Sparsity of the RVE global stiffness matrix at incremental factor equal to 0.4 for mesh 1.

width of the matrix is higher when the non-local approach is used compared to the local counterpart. Moreover, inherent with a larger value of the non-local characteristic length, L, a large band width of the matrix was obtained as expected.

6.5.1.1 Periodic integration scheme

Since both the *Periodic* boundary condition and the non-local approach of integral type incorporate geometrical considerations, a different approach to define the non-local integration domain, Ω^{nl}, for integral (6.11) may be used for this boundary condition. This approach is schematically illustrated in Figure 6.8. The main idea consists in

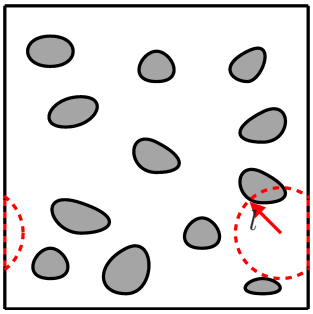

FIGURE 6.8: Schematic representation of the modified non-local averaging scheme for *Periodic* boundary condition.

mirroring the part of Ω^{nl} defined by L which is outside the RVE domain with the sub-domain in the opposite side. Note that this approach is based on the periodicity concept and, therefore, its application is circumscribed to RVEs with periodic configurations.

In Figure 6.9, the results obtained with this approach are introduced for the coarse mesh and $L = 0.5\ mm$. Surprisingly, the final results remained the same, not being possible to observe any difference. After a carefully analysis, it was possible to conclude that this modified approach leads to a redundant constraint imposed to the system of equations which governs the micro-equilibrium problem. This is due to the fact that this modified integration scheme is equivalent to the enforcement of a periodic displacement field over the boundary of the RVE.

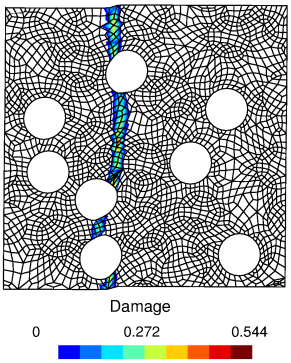

(a) With standard integration scheme.

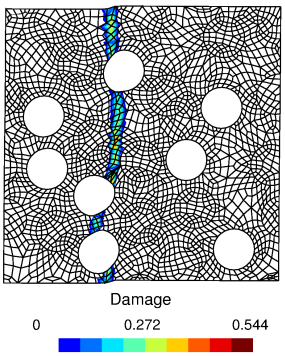

(b) With modified integration scheme.

FIGURE 6.9: Contour plots of the damage variable for different integration schemes for Mesh 1 and $L = 0.5\ mm$ (incremental factor equal to 0.4).

6.5.2 Coupled multi-scale problem: mesh dependence at micro-scale domain

In this section, the robustness of the non-local approach proposed to minimize the mesh dependence at the micro-scale is again assessed. However, in the present case, its efficiency is checked when it is employed within a coupled multi-scale code (***CMSP*** code described in Section 3.3.2.7). For this purpose, a flat grooved specimen at the coarse scale was considered where its geometry is illustrated in Figure 6.10(a). Due to the symmetry of the specimen, only one quarter was modelled by imposing appropriate boundary constraints (Figure 6.10(a)). Aiming to promote a tensile stress state at the critical section of the macroscopic specimen, a vertical displacement of 0.2 mm was prescribed to the top surface of the specimen.

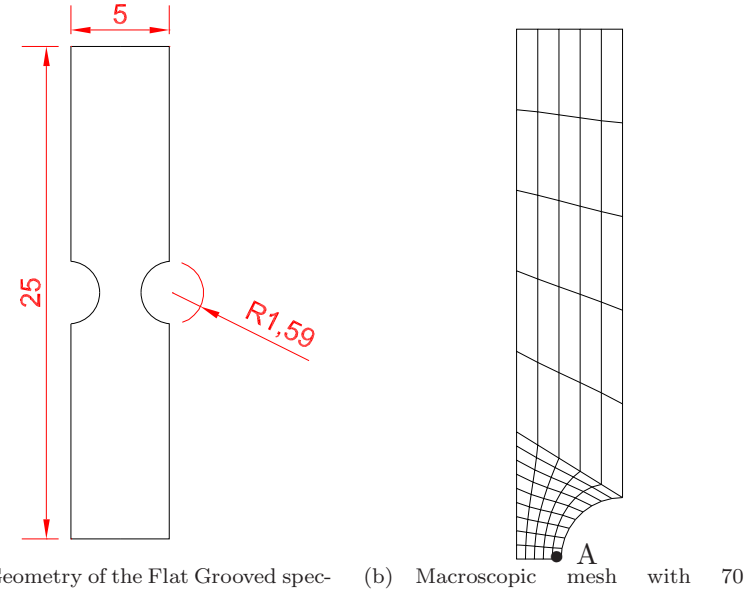

(a) Geometry of the Flat Grooved specimen (units in mm).

(b) Macroscopic mesh with 70 quadratic quadrilateral elements.

FIGURE 6.10: Flat Grooved specimen.

With regard to the micro-structure, a simple RVE with a centered circular void corresponding to a void volume fraction equal to 12.5 % was considered. As a matter of fact, the RVE consists on a square with dimension 1 mm.

Since the main goal of the present numerical example is to assess the micro-scale non-local approach, only one mesh at the macro-scale was considered (Figure 6.10(b)) with quadratic quadrilateral elements and reduced integration (2×2 *Gauss* points). Conversely, at the micro-scale, two refinement mesh levels were considered as illustrated in Figure 6.11 where, once again, quadratic quadrilateral elements with reduced integration scheme were applied. It is noteworthy to mention that, with this approach, involving

only one spatial discretization at the macro-scale, the mesh dependence pathology is restricted to the micro-scale domain. In line with the previous example, plane strain condition was considered as well as *Periodic* boundary condition.

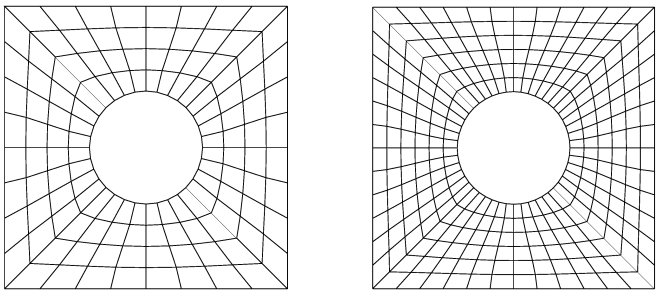

(a) Mesh 1: 128 elements quadratic quadrilateral elements.

(b) Mesh 2: 288 elements quadratic quadrilateral elements.

FIGURE 6.11: Refinement mesh levels at the micro-scale.

With regard to the material constitutive model, the explicit damage model coupled with the elasto-plastic *von-Mises* model described in Section 6.3.6 was considered (at the micro-scale) with the same material properties used for the matrix of the previous numerical example.

In Figure 6.12, the vertical reaction force at the macro-scale is plotted for local and non-local approaches. From the analysis of Figure 6.12(a), it is possible to conclude that there is a clear dependence of the results with the spatial discretization applied at the RVE level and it is convenient to use an appropriate numerical strategy to alleviate the dependence. It is relevant to emphasize that although the source of the mesh dependence is circumscribed at the micro-scale domain, there is a significant repercussion at the macroscopic domain, in particular with regard to the reaction forces. However, surprisingly, there are no appreciable differences between the contour plots of the *von Mises* equivalent stress at macro-scale, which can be observed in Figures 6.13(a) and 6.13(b).

Notwithstanding, it is important to note that, similar to what happens with standard finite element problems involving softening regimes, a more marked localization occurs for a higher number of degrees of freedom at the micro-scale (Figure 6.13(b)).

When the non-local approach is applied at the micro-scale, a regularization of the problem takes place. As pointed out in the previous section, this regularization is deeply dependent on the characteristic length, L. Thus, it is possible to conclude from Figure 6.12(b) that a tenuous regularization for $L = 0.05\ mm$ is obtained, but when this parameter is set up to $L = 0.1\ mm$, quite satisfactory results are achieved. This regularization effect for $L = 0.1\ mm$ is materialized either from closer reaction curves (Figure

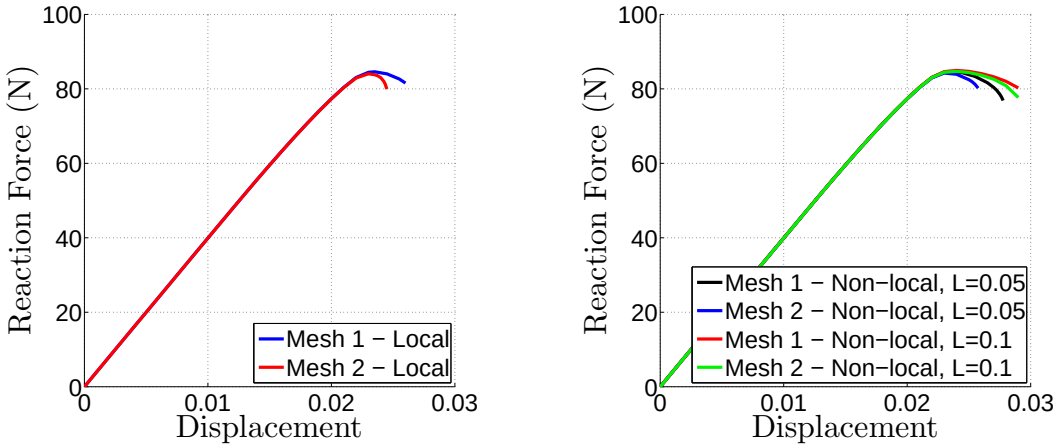

(a) Local result. (b) Non-local result.

FIGURE 6.12: Vertical reaction force curves for local and non-local approaches.

6.12(b)) or from similar contour plots of the accumulated plastic strain at the micro-scale (Figures 6.13(e) and 6.13(f)). Note that despite the fact that the values of the accumulated plastic strain do not perfectly match for the same prescribed displacement (for $u = 0.023\ mm$), they are relatively close.

6.5.3 Coupled multi-scale problem: mesh dependence at the macro-scale domain

Finally, in this section, the non-local approach proposed for the macroscopic domain is assessed by means of a numerical example where the macroscopic specimen is a double notched plate originally proposed by Mediavilla et al. [2]. The geometry of the specimen is given in Figure 6.14. With regard to the spatial discretization of the macro-scale specimen, three refinement levels were considered as illustrated in Figure 6.15. For all cases, quadratic quadrilateral elements with reduced integration scheme (2×2 *Gauss* points) were adopted.

Since the main goal of the present example is exclusively to assess the applicability and reliability of the non-local developed for the macroscopic domain, the micro-scale domain was not changed. This means that, a unique mesh at the micro-scale was considered for all macro-scale meshes as well as the same conditions (i.e. boundary conditions, material constitutive law). With this strategy, it is possible to analyse the macroscopic mesh dependence since the source of the problem is circumscribed to the macroscopic domain. Saying that, the same RVE used in Section 4.3.2 was again considered with the same material parameters. As a matter of fact, plane strain condition was applied in this problem and *Periodic* boundary condition was prescribed. Finally, a displacement equal

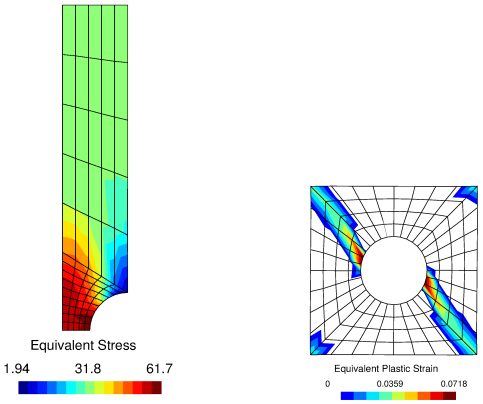

(a) Local result, Mesh 1.

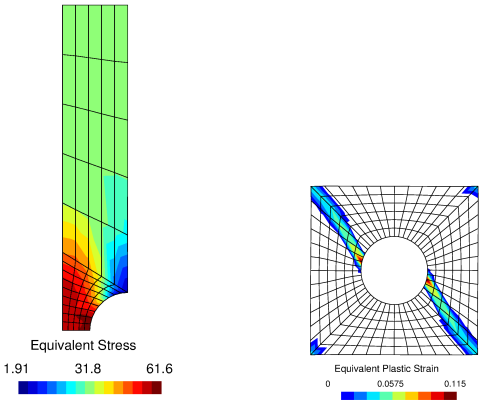

(b) Local result, Mesh 2.

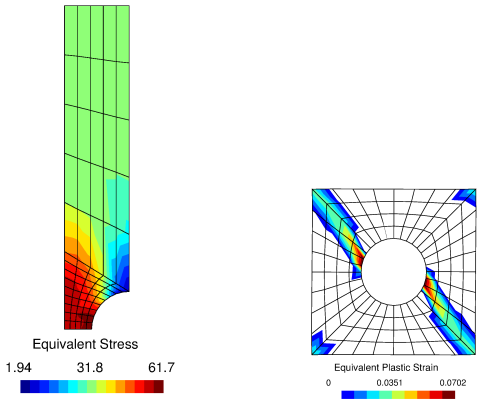

(c) Non-local result, $L = 0.05\ mm$, Mesh 1.

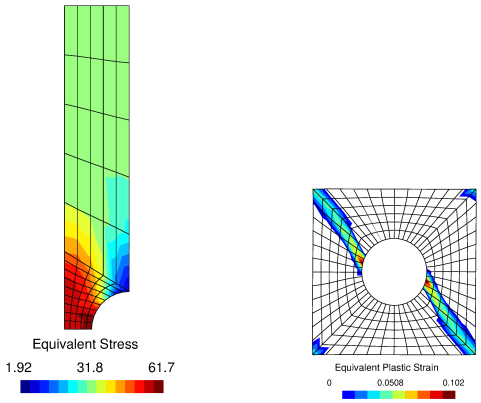

(d) Non-local result, $L = 0.05\ mm$, Mesh 2.

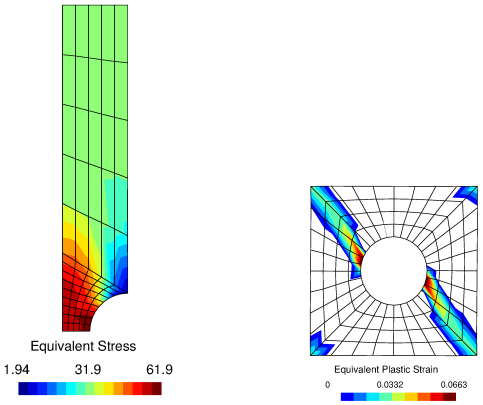

(e) Non-local result, $L = 0.1\ mm$, Mesh 1.

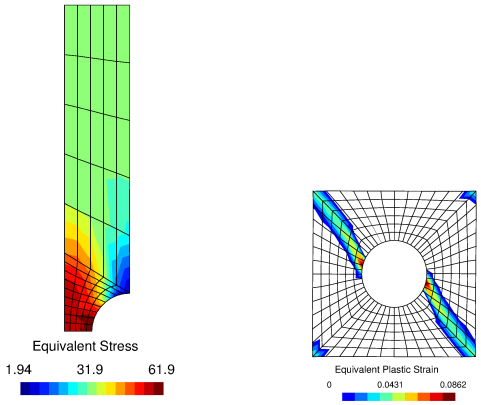

(f) Non-local result, $L = 0.1\ mm$, Mesh 2.

FIGURE 6.13: Contour plots of the *von Mises* equivalent stress at the macro scale and accumulated plastic strain at the RVE level at point A of the flat grooved specimen (defined in Figure 6.10(b)) for prescribed displacement equal to $0.023\ mm$.

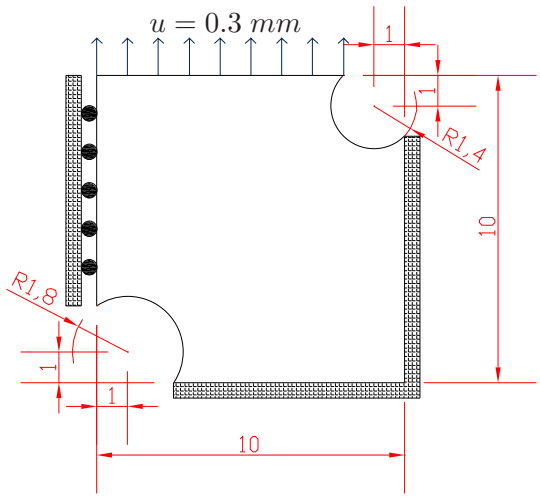

FIGURE 6.14: Geometry of the macroscopic specimen: double notched specimen (units in mm) [2].

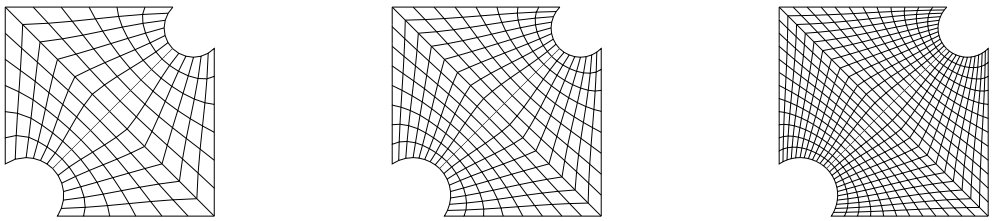

(a) Mesh 1: 144 quadratic quadrilateral elements.

(b) Mesh 2: 256 quadratic quadrilateral elements.

(c) Mesh 3: 576 quadratic quadrilateral elements.

FIGURE 6.15: Mesh refinement considered for the double notched specimen.

to 0.3 m was applied to the top of the macroscopic specimen and 100 equal increments were considered to run this problem.

We start the analysis of this problem by observing the typical convergence behaviour obtained when a non-local approach is used at the macro-scale, which is listed in Table 6.4. As a matter of fact, this convergence evolution was obtained for mesh 3 with L equal to 0.25 mm. As it is possible to observe, the convergence rate is quadratic demonstrating that the linearization of the macroscopic equilibrium problem was correctly performed (Appendix B). It is relevant to emphasize that within the context of an implicit formulation, which is the present case, the correct linearization of the problem plays a critical role since it has a significant impact on the performance of the algorithm.

After the analysis of the efficiency and robustness of the algorithm employed, it is fundamental to analyse the quality of the numerical results. For this purpose, in Figure 6.16, the reaction forces for local and non-local problem are introduced. From Figure 6.16(a), it is clear that at the macro-scale there is an issue concerned with mesh dependence.

TABLE 6.4: Convergence rates at macro-scale for the macroscopic equilibrium problem enhanced with a non-local approach of integral type where the non-local variable is the macroscopic deformation gradient, $\overline{\boldsymbol{F}}\{\boldsymbol{x}, t\}$ - $L = 0.25\ mm$.

Iteration number	Convergence
1	1.67060
2	$0.800135E-01$
3	$0.139756E-03$
4	$0.646328E-09$

It is notorious that when the softening regime is attained, the three reaction curves diverge. However, when the non-local scheme herein proposed is used, this divergence is minimized, as can be observed from Figure 6.16(b). This feature is clear for the curves associated to mesh 1 and 2 for a characteristic length L equal to 0.25 mm. Nevertheless, as highlighted in Figure 6.16(b), for the same characteristic length, hourglass modes appeared for mesh 3. This effect is plainly illustrated in Figure 6.17 where a zoom factor of 10 was considered to highlight this issue. As it is possible to observe from this figure, an irregular shape of the specimen was obtained.

Finally, in Figures 6.18 and 6.19 the contour plots of the *von Mises* equivalent stress are introduced for both local and non-local problems. Unfortunately, it is impossible to withdrawn a definite conclusion from these contour plots.

At the end of the present example, it is important to make some comments. Although the results were not as good as initially expected, it is important to note that it was only possible to run the problem with a very small characteristic length in order to avoid the appearance of hourglass modes. Nevertheless, this formulation has provided positive indications like the improvement of the reaction forces obtained when the non-local approach at macro-scale was used. Saying that, the author believes that different strategies to define the non-local macroscopic deformation gradient should be studied. A possible solution may consist in using a similar strategy as considered on the development of *B-Bar* [159] or *F-Bar* [160, 161] finite element technologies. This means that the use of either the isochoric or volumetric components of the macroscopic deformation gradient as a non-local variable may provide good results.

The second and final remark is concerned with the definition of the present numerical approach. In fact, observing the present non-local formulation from other perspective, it can be understood as the development of a new type of finite element suitable for problems involving softening regimes where mesh dependence pathology is a reality. With this idea in mind and after the elimination of the hourglass modes, it may be possible to extrapolate this framework proposed and developed within the context of coupled multi-scale models to standard finite element codes, which have been used to

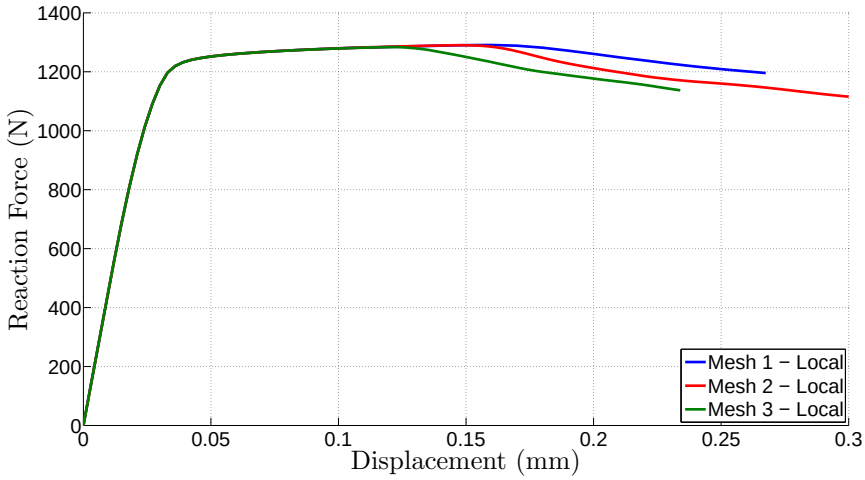

(a) Local approach

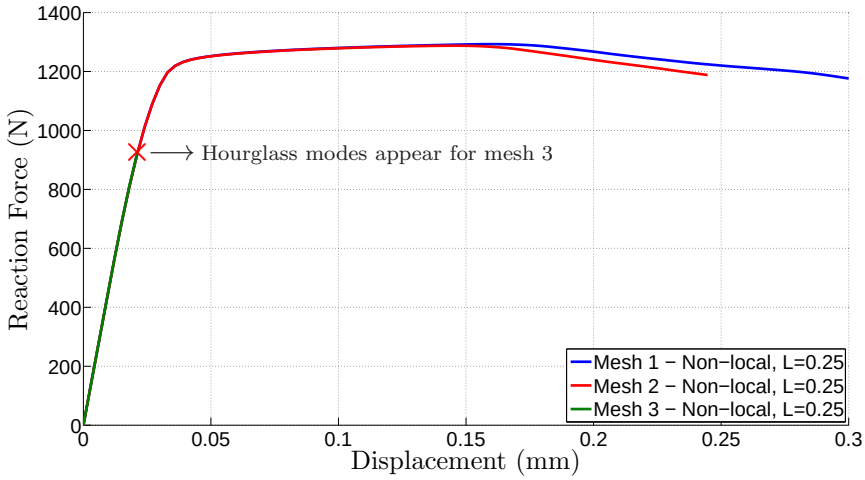

(b) Non-Local approach

FIGURE 6.16: Reaction forces for the double notched specimen.

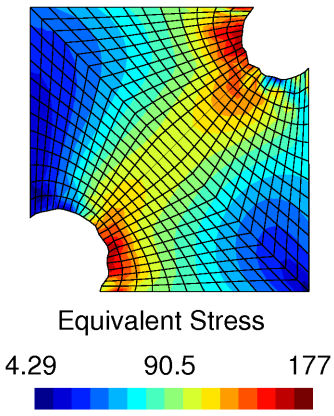

FIGURE 6.17: Hourglass phenomenon which takes place at fine macroscopic mesh for $L = 0.25\,mm$.

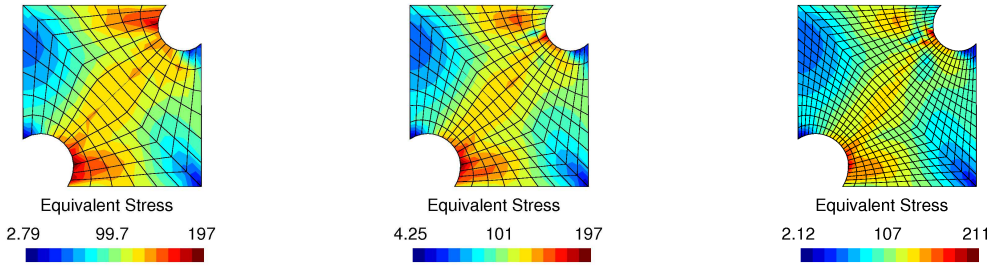

(a) Mesh 1: local. (b) Mesh 2: local. (c) Mesh 3: local.

FIGURE 6.18: Contours plots of the *von Mises* equivalent stress for $u = 0.2\ mm$ for the local problem.

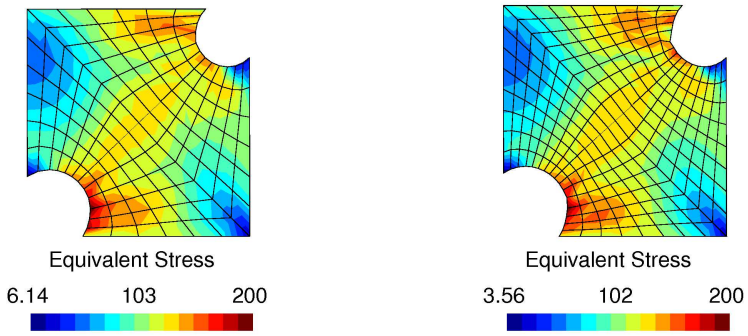

(a) Mesh 1: non-local. (b) Mesh 2: non-local.

FIGURE 6.19: Contours plots of the *von Mises* equivalent stress for $u = 0.2\ mm$ for the non-local approach, $L = 0.25\ mm$.

solve fracture solid mechanics problems. With this approach at hand, it will be avoidable to implement a suitable non-local approach for each material constitutive model.

Remark 6.6. As a matter of fact, a different example was considered in order to assess the robustness of the proposed non-local approach: a tensile test of a notched round bar. Nevertheless, similar conclusions were withdrawn and, hence, it was not included in the present chapter.

6.6 Conclusions

In this chapter, the mesh dependence pathology that inherently affects softening media within the context of coupled multi-scale models was addressed. Based on a set of numerical examples it was clear that coupled multi-scale models are highly affected by this pathology. Moreover, it was demonstrated that this pathology takes place either at the micro or macro domains limiting the range of applicability of this numerical approach to solve fracture solid mechanics problems.

Aiming to minimize this issue, two non-local approaches of integral type were developed for the micro and macro domain. Although both approaches use the same base for their formulation, the resulting frameworks are quite different. While in the former approach, an explicit damage variable was selected to be the non-local parameter, in the latter, due to the lack of internal variables at the macro-scale, the macroscopic deformation gradient was defined as non-local variable. In fact, as stressed out previously, according to the knowledge of the author this is a novelty.

With regard to the formulation and implementation of both non-local approaches, it was demonstrated, by means of a set of numerical examples, that these developments were properly conducted. This is particularly true for the implementation of the tangent operators. However, with regard to the impact of these two numerical approaches, only the one implemented at the micro-scale gave effective results. With this approach, notable results were attained where a significant minimization of the mesh dependence pathology was observed. On the other hand, despite the positive indications provided by the non-local framework implemented at the macro domain, there is still future work to do with this concept. This is due to the fact that, when the non-local characteristic length reaches a certain value, hour-glass modes appear, resulting non-physical results.

Chapter 7

New Periodic boundary condition for strain localization with randomly configurations

7.1 Introduction

There is an enormous expectation around coupled multi-scale models and associated versions with regard to their potential in characterizing complex materials over a wide spectrum of regimes and under arbitrary loading conditions. For instance, the behaviour of an elasto-plastic material under: linear elastic, hardening and softening regimes needs to be understood for the appropriate design and optimization of components. In addition, thermal effects and cyclic loads, which are inevitably associated to creep and fatigue phenomena, are among the most relevant loading conditions that define the applicability of a material. It is noteworthy to mention that the full characterization and numerical simulation of the material over these three regimes and under these two loading conditions are critical within the context of technologically advanced industries such aeronautic or automotive, where complex mechanical systems need to be designed to simultaneously meet high performance criteria and tight safety requirements.

Whilst for linear and hardening regimes coupled multi-scale models have already demonstrated their potential even for complex micro-structure (i.e. [36–38, 44, 45], among several others), for softening regimes and under thermal and cyclic loads there are still some questions without answer. As a matter of fact, according to the knowledge of the author, fatigue and creep phenomena have not been analysed by this particular multi-scale approach even though, some efforts have been directed towards the introduction of

thermals effects into coupled multi-scale models formulation where the work carried out by Özdemir et al. [39], Özdemir et al. [40] and Giusti et al. [162] should be highlighted.

Considering the particular case of softening regimes, one of the most relevant question is concerned with the kinematical boundary condition which should be prescribed over the frontier of the RVE. The difficulty inherent with the selection of an appropriate boundary condition is related to the fact that, when this regime is reached, it is common to observe at the microstructure of the material the appearance of a localization band which consists on a zone where high strains are concentrated. This zone is a consequence of a combination of phenomena such as nucleation, growth and coalescence of voids and small zones with high strain concentrations. Even though the origin of this physical feature (localization band) takes place at the micro-structure of the material, beyond a critical dimension it is also observable at the macroscopic level. Based on these two physical aspects, it is possible to conclude that, in order to use multi-scale models to simulate the behaviour of the material under softening regimes, a suitable kinematical boundary condition needs to be used. This boundary condition should be able to properly tackle the presence of a localization band and, an enhancement of the macro-to-micro "*bridge*" and vice-versa needs to be carried out in order to guarantee the consistency of the presence of a localization band at both scales.

This last issue has been addressed by several authors over the last few years. Among others, the work carried out by Belytschko et al. [55], Song and Belytschko [56], Souza and Allen [57], Coenen et al. [58], Nguyen et al. [59], Nguyen et al. [60], Nguyen et al. [61] and Verhoosel et al. [62] should be highlighted. Despite major differences, all approaches share the idea of increasing the number of variables and parameters that establish the bridge between different scales, which are responsible to define the presence of a localization band (or a discontinuity according to the nomenclature considered) in both scales. Depending on the approach considered, in some cases, a displacement jump or a traction field associated to the localization band is sent from one scale to another and vice-versa, which are a consequence of the evolution of the equilibrium problem.

Nevertheless, the development of kinematical boundary conditions that are able to take into account the presence of localization bands into the global response of the RVE is still limited and, just few efforts have been carried out. As a matter of fact, in [55–57] the *Uniform Traction* has been selected whereas in [59–62] the standard *Periodic* boundary condition was prescribed over the boundary of the RVE. Note that in this case, the discontinuity needs to be parallel to the borders of the RVE (i.e. in case of a square RVE, vertical or horizontal localization band). Thus, the RVE needs to be rotated according to the crack propagation direction, which is a non-physical approach. In addition, it is noteworthy to mention that this strategy is circumscribed to proportional

loads and simple stress states (i.e. pure traction, shear or compression). It is important to mention that the three commonly used boundary conditions, *Linear*, *Periodic* and *Uniform Traction*, have shown some shortcoming to accomplish this task. While *Linear* is to restrictive, not allowing any effect of the localization band into the final shape of the boundary of the RVE, the *Periodic* boundary condition only allows the presence of horizontal or vertical localization bands. Finally, when *Uniform Traction* is prescribed, spurious effects may appear due to the minimal constraint enforced at the frontier of the RVE. Taking into account these issues, Coenen et al. [63] have proposed a new concept of periodicity, which allows the presence of a localization band randomly propagating through the RVE domain. The main idea consists on the alignment of the displacement fluctuation field according to an *average direction* of the localization band. Despite this artificial definition of the localization band, the numerical approach has demonstrated interesting results but it is still limited to some particular cases: proportional loads and simple stress states. Moreover, since the global response of the RVE is dependent on an artificial localization band defined by an *average direction*, the presence of inclusions and phases with non-conventional shape will not be reflected on the final behaviour of the material.

Based on the idea that a more robust kinematical boundary condition, which simultaneously does not suffer from the pathology observed under *Linear* and *Uniform Traction* constrains and able to tackle the presence of a localization band with arbitrary shape, in this chapter, a new concept of *Periodic* boundary condition is proposed. The main idea consists on the definition of arbitrary sub-domains defined by the shape of a localization band. For this purpose, in order to guarantee the correct domain definition and application of *Periodic* boundary conditions over non-standard domains, the *Mortar* decomposition method is used once again. As above pointed out, this new boundary condition consists on an embryonic concept where unfortunately, only the main foundations are described in detail. This is due to the fact that it is quite challenging either from the of formulation or numerical implementation points of view. Nevertheless, the author really believes that in future iterations of the work all potentialities and capacities of the new concept will be explored.

The present chapter has the following architecture: in Section 7.2, the concept of domain decomposition is proposed as well as the proof that the new *Periodic* boundary condition is kinematically admissible. In Section 7.3, the Mortar decomposition method is particularized and elaborated for the new concept. Moreover, attention to all geometric possible cases is given and details of the integration scheme are described. This section is followed by the introduction of a preliminary assessment of the new concept in 7.4. Finally, in Section 7.5 the conclusions of this work are introduced and future iterations are pointed out.

7.2 Periodic boundary condition enhanced with a localization band

In this section, a new admissible kinematical boundary condition based on periodic displacement and anti-periodic traction concepts is introduced. This boundary condition is able to tackle the presence of a localization band which randomly propagates over the domain of the RVE, Ω_0.

In order to start the formulation of the new boundary constraint, we recover the two fundamental equations, which respectively define the micro-equilibrium problem and the *minimal kinematical admissible constraint*,

$$\int_{\Omega_0} \boldsymbol{P}\{\boldsymbol{y},t\} : \nabla_{\boldsymbol{p}}\boldsymbol{\eta} dV - \int_{\Gamma_0} \boldsymbol{T}^{ref}\{\boldsymbol{y},t\}.\boldsymbol{\eta} d\Gamma = 0 \ \ \forall\, \boldsymbol{\eta} \ \in \ \mathcal{V}, \tag{7.1a}$$

$$\int_{\Gamma_0} \widetilde{\boldsymbol{u}}\{\boldsymbol{y},t\} \otimes \boldsymbol{N}\{\boldsymbol{Y}\}\, d\Gamma = \boldsymbol{0}, \tag{7.1b}$$

where, once again, $\mathcal{V}$ denotes the space of the virtual admissible displacement fluctuation field, $\boldsymbol{\eta}$. As pointed out throughout the present document, the equilibrium of the RVE is achieved when both previous equations are satisfied.

Under critical loads and conditions, it is common to observe the appearance of localization bands with high levels of strains in the structure. Inherent to these bands, it is common to observe a reduction of the load capacity of the structure. This physical phenomena is explained by the loss of resistance and strength of the material in the neighbourhood of the band. Thus, based on this physical aspect, in the present formulation, the deformation band will be responsible for splitting the total RVE domain into two semi-dependent domains.

As highlighted in the introduction of the present chapter, this new boundary condition consists on a embryonic concept inspired on the *Mortar* decomposition method. Thus, some assumptions need to be considered at this stage of the work which, in some cases, may not completely represent the physical phenomena involved on the deformation of the material. One of the assumptions consists on the definition of the localization band. In the current stage of the formulation of this kinematical boundary constraint, the localization band needs to intersect to distinct edges of a square RVE in order to have impact on the overall response of the RVE. In other words, before the intersection of two distinct edges of the RVE by the localization band, the micro-structure is modelled using the *Mortar Periodic* boundary condition introduced in Chapter 5 (or standard *Periodic* boundary condition in case of a conform mesh). Nevertheless, the author is completely convinced that with addition work, the new kinematical boundary condition

will be able to tackle the complete evolution of the localization band. This means that, with additional developments, an admissible kinematical boundary condition based on periodicity concepts will be obtained, which is able to properly characterize the propagation of a localization band over the RVE domain.

Taking into account the assumptions above pointed out, it is possible to split the total RVE domain, Ω_0, into two sub-domains, denoted respectively by Ω_0^1 and Ω_0^2, as schematically illustrated in Figure 7.1. Moreover, each domain, Ω_0^1 and Ω_0^2, is confined by boundary Γ_0^1 and Γ_0^2, respectively. These boundaries can also be decomposed into standard, $\overline{\Gamma}^i$, and discontinuity boundaries, Γ_D^i, such that

$$\Gamma_0^1 = \overline{\Gamma}^1 \cup \Gamma_D^1, \tag{7.2a}$$

$$\Gamma_0^2 = \overline{\Gamma}^2 \cup \Gamma_D^2, \tag{7.2b}$$

where the standard boundary, $\overline{\Gamma}^i$, only includes part of the original boundary of the RVE, Γ_0.

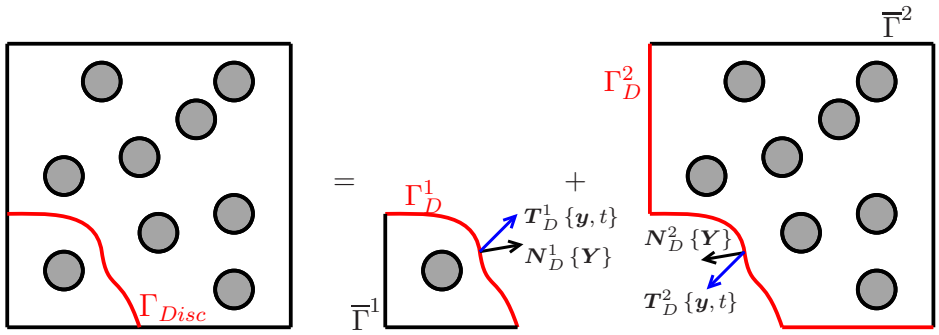

FIGURE 7.1: Decomposition of the RVE considering the discontinuity.

Remark 7.1. In what follows, index $(*)^i$ will denote a variable, parameter associated to sub-domain i.

Nevertheless, it is still necessary to define the discontinuity boundary Γ_D^i. For this purpose, in Figure 7.2, all possible shapes that a localization band may assume are given. As it is possible to observe, this boundary for each sub-domain, Ω_0^i, will not contemplate exclusively the localization band, denoted by Γ_{Disc}^i (see Figure 7.1). In fact, depending on the shape of Γ_{Disc}^i, boundary Γ_D^i may also contemplate part of the initial boundary of the RVE, Γ_0. As a matter of fact, $\Gamma_{Disc}^1 = \Gamma_{Disc}^2$ and $\Gamma_D^i \subset \Gamma_{Disc}^i$.

Remark 7.2. In order to clarify possible incongruities concerned to nomenclature, once again, all integrals used in the formulation of the new kinematical constraint are defined over the undeformed configuration of the RVE. Note that, a finite strains approach has been considered throughout this document.

Based on the decomposition concept above introduced, Equations (7.1a) and (7.1b) can be re-written as:

$$\int_{\Omega_0^1} \boldsymbol{P}\left\{\boldsymbol{y},t\right\} : \nabla_{\boldsymbol{p}}\boldsymbol{\eta} dV - \int_{\Gamma_0^1} \boldsymbol{T}^{ref}\left\{\boldsymbol{y},t\right\}.\boldsymbol{\eta} d\Gamma = 0 \;\; \forall\, \boldsymbol{\eta} \;\in\; \mathcal{V}, \tag{7.3a}$$

$$\int_{\Gamma_0^1} \widetilde{\boldsymbol{u}}\left\{\boldsymbol{y},t\right\} \otimes \boldsymbol{N}\left\{\boldsymbol{Y}\right\} d\Gamma = \boldsymbol{0}, \tag{7.3b}$$

$$\int_{\Omega_0^2} \boldsymbol{P}\left\{\boldsymbol{y},t\right\} : \nabla_{\boldsymbol{p}}\boldsymbol{\eta} dV - \int_{\Gamma_0^2} \boldsymbol{T}^{ref}\left\{\boldsymbol{y},t\right\}.\boldsymbol{\eta} d\Gamma = 0 \;\; \forall\, \boldsymbol{\eta} \;\in\; \mathcal{V}, \tag{7.3c}$$

$$\int_{\Gamma_0^2} \widetilde{\boldsymbol{u}}\left\{\boldsymbol{y},t\right\} \otimes \boldsymbol{N}\left\{\boldsymbol{Y}\right\} d\Gamma = \boldsymbol{0}. \tag{7.3d}$$

Despite of the decomposition considered for Ω_0, both sub-domains, Ω_0^1 and Ω_0^2, are still linked. Hence, an extra constraint needs to be added to the previous system of equations. This relation between the two sub-domains is attained by imposing an anti-periodic traction field over the localization band, Γ^i_{Disc}. Note that this assumption simply consists on the Third Law of *Newton*, commonly called *action-reaction law*. Thus, in the present case, this physical feature is modelled by

$$\boldsymbol{T}^{ref}\left\{\boldsymbol{y}^1_{Disc},t\right\} = -\boldsymbol{T}^{ref}\left\{\boldsymbol{y}^2_{Disc},t\right\}, \tag{7.4}$$

where $\boldsymbol{y}^i_{Disc}$ denotes points located at Γ^i_{Disc} (see Figure 7.1).

7.2.0.1 Kinematical constraints over each sub-domain

Having defined the global problem in the previous section, now, it is time to introduce some constraints to either the displacement fluctuation or to the traction force fields for each sub-domain in order to obtain an admissible kinematical constraint. Note that a boundary condition is only admissible from the kinematical point of view when both *minimal kinematical constraint*, defined by Equation (3.5), and *Hill-Mandel* principle (Section 3.2.4) are simultaneously satisfied for each sub-domain.

For this purpose, consider the equation which governs the equilibrium of sub-domain i (Equation 7.3a or Equation 7.3c) as a function of the fluctuation displacement field, $\widetilde{\boldsymbol{u}}\left\{\boldsymbol{y},t\right\}$,

$$\int_{\Omega_0^i} \boldsymbol{P}\left\{\boldsymbol{y},t\right\} : \nabla_{\boldsymbol{p}}\widetilde{\boldsymbol{u}}\left\{\boldsymbol{y},t\right\} dV - \int_{\Gamma_0^i} \boldsymbol{T}^{ref}\left\{\boldsymbol{y},t\right\}.\widetilde{\boldsymbol{u}}\left\{\boldsymbol{y},t\right\} d\Gamma = 0. \tag{7.5}$$

Taking into account the decomposition previously described for Γ_0^i, it is possible to write

$$\begin{aligned}
&\int_{\Omega_0^i} \boldsymbol{P}\left\{\boldsymbol{y},t\right\} : \nabla_{\boldsymbol{p}} \widetilde{\boldsymbol{u}}\left\{\boldsymbol{y},t\right\} dV - \int_{\Gamma_0^i} \boldsymbol{T}^{ref}\left\{\boldsymbol{y},t\right\} . \widetilde{\boldsymbol{u}}\left\{\boldsymbol{y},t\right\} d\Gamma = 0, \\
\Leftrightarrow &\int_{\Omega_0^i} \boldsymbol{P}\left\{\boldsymbol{y},t\right\} : \nabla_{\boldsymbol{p}} \widetilde{\boldsymbol{u}}\left\{\boldsymbol{y},t\right\} dV - \int_{\overline{\Gamma}^i} \boldsymbol{T}^{ref}\left\{\overline{\boldsymbol{y}}^i,t\right\} . \widetilde{\boldsymbol{u}}\left\{\boldsymbol{y},t\right\} d\Gamma \\
&- \int_{\Gamma_D^i} \boldsymbol{T}^{ref}\left\{\boldsymbol{y}_D^i,t\right\} . \boldsymbol{\eta} d\Gamma = 0,
\end{aligned} \tag{7.6}$$

where $\overline{\boldsymbol{y}}^i$ denotes a point at $\overline{\Gamma}_0^i$.

The concept of *anti-traction* field previously introduced in Section 3.2.6.2 will be properly extrapolated for the current new kinematical constraint. The first change is concerned with the boundary where this constraint is prescribed. Hence, in the current case, it will be prescribed over the boundary of each sub-domain, Γ_0^i, instead to the total RVE frontier, Γ_0. The second change is concerned with how this constraint is applied in each Γ_0^i. Whilst in the standard *Periodic* boundary condition or *Mortar Periodic* boundary condition (see Chapter 5), the opposite boundaries of the RVE are always parallel, in this case, the discontinuity may assume an arbitrary configuration. Therefore, the approach considered to prescribe an *anti-periodic* traction field needs to be modified in order to accommodate the possibility of non-parallel surfaces. Based on these aspects, the *anti-traction* constraint applied to each sub-domain, Ω_0^i, should be such that: the traction force in a generic point, $\boldsymbol{y}_D^i$, of Γ_D^i is equal and symmetric to the traction force in a generic point, $\boldsymbol{y}_*^i$, at $\overline{\Gamma}^i$, which is determined by projecting point $\boldsymbol{y}_D^i$ towards its normal vector, $\boldsymbol{N}\left\{\boldsymbol{Y}_D^i\right\}$. Mathematically, this constraint is expressed

$$\boldsymbol{T}^{ref}\left\{\boldsymbol{y}_D^i,t\right\} = -\boldsymbol{T}^{ref}\left\{\boldsymbol{y}_*^i,t\right\}. \tag{7.7}$$

Following the same approach as used above for the traction field and in agreement with the standard *Periodic* boundary condition, it is possible to write

$$\widetilde{\boldsymbol{u}}\left\{\boldsymbol{y}_D^i,t\right\} = \widetilde{\boldsymbol{u}}\left\{\boldsymbol{y}_*^i,t\right\}. \tag{7.8}$$

Based on the previous two equations, it is possible to conclude that a periodic constraint has been applied to a RVE with arbitrary geometry.

Taking into account Equations (7.7) and (7.8), the equation which defines the equilibrium of sub-domain Ω_0^i (Equation (7.6)) may be re-written into the following fashion

$$\int_{\Omega_0^i} \boldsymbol{P}\left\{\boldsymbol{y},t\right\} : \nabla_{\boldsymbol{p}} \boldsymbol{\eta} dV + \int_{\Gamma_D^i} \boldsymbol{T}^{ref}\left\{\boldsymbol{y}_D^i,t\right\} . \left(\widetilde{\boldsymbol{u}}\left\{\boldsymbol{y}_D^i,t\right\} - \widetilde{\boldsymbol{u}}\left\{\boldsymbol{y}_*^i,t\right\}\right) d\Gamma = 0. \tag{7.9}$$

As it is possible to observe from the previous equation, the *Hill-Mandel* constraint related to the traction force field is enforced with the equation used to define the equilibrium of each sub-domain, Ω_0^i, and, similarly to the *Mortar Periodic* boundary condition (Chapter 5), it is automatically satisfied.

However, it is still necessary to prove that the minimal kinematical constraint is satisfied for sub-domains with non conventional shapes. For this purpose, Equations (7.3b) and (7.3d) need to be satisfied. This proof starts by performing the decomposition of integral (3.5) taking into account, once again, the definition of Γ_0^i (Equation (7.2a) or Equation (7.2b)). Thus, one can write

$$\int_{\Gamma_0^i} \widetilde{\boldsymbol{u}}\left\{\boldsymbol{y},t\right\}\otimes\boldsymbol{N}\left\{\boldsymbol{Y}\right\}d\Gamma = \int_{\overline{\Gamma}^i} \widetilde{\boldsymbol{u}}\left\{\boldsymbol{y}_*^i,t\right\}\otimes\boldsymbol{N}\left\{\boldsymbol{Y}_*^i\right\}d\Gamma + \int_{\Gamma_D^i} \widetilde{\boldsymbol{u}}\left\{\boldsymbol{y}_D^i,t\right\}\otimes\boldsymbol{N}\left\{\boldsymbol{Y}_D^i\right\}d\Gamma = \boldsymbol{0} \tag{7.10}$$

where $\boldsymbol{Y}_*^i$ and $\boldsymbol{Y}_D^i$ denote points at the reference configuration of boundaries $\overline{\Gamma}^i$ and Γ_D^i respectively. Note that in the first surface integral at the right hand side of the previous equation, $\widetilde{\boldsymbol{u}}\left\{\overline{\boldsymbol{y}}^i,t\right\}$ was replaced by $\widetilde{\boldsymbol{u}}\left\{\boldsymbol{y}_*^i,t\right\}$ since both points with coordinates $\overline{\boldsymbol{y}}^i$ and $\boldsymbol{y}_*^i$ belong to the same boundary, $\overline{\Gamma}^i$.

For each sub-domain, Ω^i, there are two orthonormal referentials as illustrated in Figure 7.3. The referential defined by the orthonormal base $\{\boldsymbol{E}_1,\boldsymbol{E}_2\}$ is associated to the reference configuration of the RVE, and the other, defined by $\{\boldsymbol{S}_1,\boldsymbol{S}_2\}$ with the localization band. With regard to this orthonormal referential, direction $\boldsymbol{S}_1$ is always tangent to Γ_D^i, whereas direction $\boldsymbol{S}_2$ is always normal to this boundary. Taking into account these two orthonormal referentials, Equation (7.10) can be redefined such as

$$\begin{aligned}\int_{\Gamma_0^i} \widetilde{\boldsymbol{u}}\left\{\boldsymbol{y},t\right\}\otimes\boldsymbol{N}\left\{\boldsymbol{Y}\right\}d\Gamma = &\int_{\overline{\Gamma}^i} \widetilde{\boldsymbol{u}}\left\{\boldsymbol{y}_*^i,t\right\}\otimes\boldsymbol{N}\left\{\boldsymbol{Y}_*^i\right\}d\Gamma.\left(\overrightarrow{\boldsymbol{S}}_1\otimes\overrightarrow{\boldsymbol{S}}_1\right)\\ &+\int_{\overline{\Gamma}^i} \widetilde{\boldsymbol{u}}\left\{\boldsymbol{y}_*^i,t\right\}\otimes\boldsymbol{N}\left\{\boldsymbol{Y}_*^i\right\}d\Gamma.\left(\overrightarrow{\boldsymbol{S}}_2\otimes\overrightarrow{\boldsymbol{S}}_2\right)\\ &+\int_{\Gamma_D^i} \widetilde{\boldsymbol{u}}\left\{\boldsymbol{y}_D^i,t\right\}\otimes\boldsymbol{N}\left\{\boldsymbol{Y}_D^i\right\}d\Gamma = \boldsymbol{0}.\end{aligned} \tag{7.11}$$

where the first integral at the right hand side of Equation (7.10) was mapped to $\{\boldsymbol{S}_1,\boldsymbol{S}_2\}$ referential. After some tensorial manipulations, the previous equation can be re-written into the following format

$$\begin{aligned}\int_{\Gamma_0^i} \widetilde{\boldsymbol{u}}\left\{\boldsymbol{y},t\right\}\otimes\boldsymbol{N}\left\{\boldsymbol{Y}\right\}d\Gamma = &\int_{\overline{\Gamma}^i} \widetilde{\boldsymbol{u}}\left\{\boldsymbol{y}_*^i,t\right\}\otimes\left[\boldsymbol{S}_1\left(\boldsymbol{N}\left\{\boldsymbol{Y}_*^i\right\}\boldsymbol{S}_1 d\Gamma\right)+\boldsymbol{S}_2\left(\boldsymbol{N}\left\{\boldsymbol{Y}_*^i\right\}\boldsymbol{S}_2 d\Gamma\right)\right]\\ &+\int_{\Gamma_D^i} \widetilde{\boldsymbol{u}}\left\{\boldsymbol{y}_D^i,t\right\}\otimes\boldsymbol{N}\left\{\boldsymbol{Y}_D^i\right\}d\Gamma = \boldsymbol{0}.\end{aligned} \tag{7.12}$$

From the previous equation and taking into account the normal outward directions, it is possible to build a link between $d\overline{\Gamma}^i$ and $d\Gamma^i_D$, which is given by the following equation:

$$\boldsymbol{N}\left\{\boldsymbol{Y}^i_D\right\} d\Gamma^i_D = -\boldsymbol{S}_1\left(\boldsymbol{N}\left\{\boldsymbol{Y}^i_*\right\}\boldsymbol{S}_1 d\overline{\Gamma}^i\right) - \boldsymbol{S}_2\left(\boldsymbol{N}\left\{\boldsymbol{Y}^i_*\right\}\boldsymbol{S}_2 d\overline{\Gamma}^i\right). \tag{7.13}$$

Before proceeding with the proof of admissibility of the present *Periodic* boundary condition, it is relevant to shed some light on the previous result. For this purpose, consider Figure 7.4 where a schematic representation of the simplest shape configuration of a localization band is given: parallel to one pair of edges of the RVE. In this case, since $\boldsymbol{N}\left\{\boldsymbol{Y}^i_*\right\}$ is normal to $\boldsymbol{S}^i_1$ and, in turn, $\boldsymbol{N}\left\{\boldsymbol{Y}^i_*\right\}$ is co-linear with $\boldsymbol{S}^i_2$, the previous equation is dramatically simplified, which gives rise to

$$d\Gamma^i_D = d\overline{\Gamma}^i. \tag{7.14}$$

The previous result is obvious due to the fact that, when $\overline{\Gamma}^i$ and Γ^i_D are parallel to each other, their infinitesimal variation is exactly the same.

Introducing expression (7.13)into (7.12), the initial equation which defines the *minimal kinematical constraint* is re-written as follows

$$\begin{aligned}\int_{\Gamma^i_0}\widetilde{\boldsymbol{u}}\left\{\boldsymbol{y},t\right\}\otimes\boldsymbol{N}\left\{\boldsymbol{Y}\right\}d\Gamma &= -\int_{\Gamma^i_d}\widetilde{\boldsymbol{u}}\left\{\boldsymbol{y}^i_*,t\right\}\otimes\boldsymbol{N}\left\{\boldsymbol{Y}^i_D\right\}d\Gamma \\ &+\int_{\Gamma^i_d}\widetilde{\boldsymbol{u}}\left\{\boldsymbol{y}^i_D,t\right\}\otimes\boldsymbol{N}\left\{\boldsymbol{Y}^i_D\right\}d\Gamma \\ &=\int_{\Gamma^i_D}\left(\widetilde{\boldsymbol{u}}\left\{\boldsymbol{y}^i_D,t\right\}-\widetilde{\boldsymbol{u}}\left\{\boldsymbol{y}^i_*,t\right\}\right)\otimes\boldsymbol{N}\left\{\boldsymbol{Y}^i_D\right\}d\Gamma=\boldsymbol{0}.\end{aligned} \tag{7.15}$$

Since a periodic fluctuation field is considered for each sub-domain (Equation (7.8)), we finally conclude that the new boundary condition based on the concept of decomposition domain is kinematically admissible.

7.2.1 The incremental equilibrium problem

With the previous mathematical manipulation, we are able to redefine up the micro-equilibrium problem when a strain localization band takes place at the micro sample. *Considering a typical time interval (or pseudo-time),* $[t_n, t_{n+1}]$*, and knowing the history of the problem and* $\boldsymbol{F}\left\{\boldsymbol{x},t\right\}$*, find the displacement fluctuation field,* $\widetilde{\boldsymbol{u}}_{n+1}\left\{\boldsymbol{y}\right\}$*, as well as the traction force field acting over the boundary of the RVE,* $\boldsymbol{T}^{ref}_{n+1}\left\{\boldsymbol{y}\right\}$*, by solving the*

following system of equations:

$$\begin{cases} \int_{\Omega_0^1} \boldsymbol{P}_{n+1}\left\{\boldsymbol{y}\right\} : \nabla_{\boldsymbol{p}} \widetilde{\boldsymbol{u}}_{n+1}\left\{\boldsymbol{y}\right\} dV + \int_{\Gamma_D^1} \boldsymbol{T}_{n+1}^{ref}\left\{\boldsymbol{y}_D^1\right\} . \left(\widetilde{\boldsymbol{u}}_{n+1}\left\{\boldsymbol{y}_D^1\right\} - \widetilde{\boldsymbol{u}}_{n+1}\left\{\boldsymbol{y}_*^1\right\}\right) d\Gamma = 0, \\ \int_{\Omega_0^2} \boldsymbol{P}_{n+1}\left\{\boldsymbol{y}\right\} : \nabla_{\boldsymbol{p}} \widetilde{\boldsymbol{u}}_{n+1}\left\{\boldsymbol{y}\right\} dV + \int_{\Gamma_D^2} \boldsymbol{T}_{n+1}^{ref}\left\{\boldsymbol{y}_D^2\right\} . \left(\widetilde{\boldsymbol{u}}_{n+1}\left\{\boldsymbol{y}_D^2\right\} - \widetilde{\boldsymbol{u}}_{n+1}\left\{\boldsymbol{y}_*^2\right\}\right) d\Gamma = 0, \\ \boldsymbol{T}_{n+1}^{ref}\left\{\boldsymbol{y}_{Disc}^1\right\} = -\boldsymbol{T}_{n+1}^{ref}\left\{\boldsymbol{y}_{Disc}^2\right\}, \end{cases} \tag{7.16}$$

where $\widetilde{\boldsymbol{u}}_{n+1}\left\{\boldsymbol{y}\right\}$ *and* $\boldsymbol{T}_{n+1}^{ref}\left\{\boldsymbol{y}_D^i\right\}$ *are the unknowns of the problem.*

Remark 7.3. In what follows, the nomenclature concerned to the time (or pseudo-time) will be dropped down since all variables which will be used are defined at instant t_{n+1}.

7.3 *Mortar* Decomposition Method

Probably, the key feature of the present kinematical boundary condition consists on the domain decomposition approach. It is important to emphasize that this feature is not critical exclusively from the geometrical point of view. In fact, the approach considered needs to be robust enough in order to impose a new concept of *Periodic* boundary constraint over each sub-domain which results from the decomposition of the initial RVE domain into arbitrary sub-domains (in the present stage of the work, only into two sub-domains). Moreover, the framework should be coupled with an integration strategy which guarantees an exact result. Taking into account these requirements, the *Mortar* decomposition method will be applied in the present formulation as used in Chapter 5. In fact, the kinematical constraint introduced in Chapter 5 can be viewed as a particular case of this new kinematical boundary condition enhanced with the possibility of tackling a localization band. Whilst the *Mortar* approach described in Chapter 5 is exclusively used to prescribe a *Periodic* boundary condition over RVEs with non-conform meshes, in the present formulation, the priority of this numerical method is to impose a modified version of the Periodicity constraint described in Section 7.2.0.1 over each sub-domains with eventual non-parallel surfaces (and therefore, with non-conform meshes).

In the spirit of *Mortar* decomposition method, the enforcement of the global constraint described by the boundary integrals of system of equations (7.16), is imposed by means of the *Lagrange* multiplier method. Thus, the traction force field, $\boldsymbol{T}^{ref}\left\{\boldsymbol{y}_D^i\right\}$ is replaced by the *Lagrange* multiplier vector, $\boldsymbol{\lambda}_D^i$. Thus, the equation which establishes the equilibrium of sub-domain i is given by

$$\int_{\Omega_0^i} \boldsymbol{P}\left\{\boldsymbol{y}\right\} : \nabla_{\boldsymbol{p}} \widetilde{\boldsymbol{u}}\left\{\boldsymbol{y}\right\} dV + \int_{\Gamma_D^i} \boldsymbol{\lambda}^i . \left(\widetilde{\boldsymbol{u}}\left\{\boldsymbol{y}_D^i\right\} - \widetilde{\boldsymbol{u}}\left\{\boldsymbol{y}_*^i\right\}\right) d\Gamma = 0. \tag{7.17}$$

Similar to the development of the *Mortar* boundary condition described in Chapter 5, $\boldsymbol{\lambda}_D^i$ consists on a vector which includes normal and tangential traction forces acting over Γ_D^i.

In order to simplify the previous equation as well as forthcoming mathematical expressions, a new function $\boldsymbol{g}$ is defined:

$$\boldsymbol{g}^i = \widetilde{\boldsymbol{u}}\left\{\boldsymbol{y}_D^i\right\} - \widetilde{\boldsymbol{u}}\left\{\boldsymbol{y}_*^i\right\}. \tag{7.18}$$

Introducing the previous relation into Equation (7.17) results

$$\int_{\Omega_0^i} \boldsymbol{P}\left\{\boldsymbol{y}\right\} : \nabla_{\boldsymbol{p}} \widetilde{\boldsymbol{u}}\left\{\boldsymbol{y}\right\} dV + \int_{\Gamma_D^i} \boldsymbol{\lambda}_D^i . \boldsymbol{g}^i d\Gamma = 0. \tag{7.19}$$

With Equations (7.17) and (7.18) at hand, it is possible to arrive to the weak form of the system of equations which governs the micro-equilibrium problem at the micro-scale when the new kinematical boundary condition is prescribed

$$\begin{cases} \int_{\Omega_0^1} \boldsymbol{P}\left\{\boldsymbol{y}\right\} : \nabla_{\boldsymbol{p}} \delta\widetilde{\boldsymbol{u}}\left\{\boldsymbol{y}\right\} dV + \int_{\Gamma_D^1} \delta\boldsymbol{\lambda}_D^1 . \boldsymbol{g}^1 + \boldsymbol{\lambda}_D^1 . \delta\boldsymbol{g}^1 d\Gamma = 0, \\ \\ \int_{\Omega_0^2} \boldsymbol{P}\left\{\boldsymbol{y}\right\} : \nabla_{\boldsymbol{p}} \delta\widetilde{\boldsymbol{u}}\left\{\boldsymbol{y}\right\} dV + \int_{\Gamma_D^2} \delta\boldsymbol{\lambda}_D^2 . \boldsymbol{g}^2 + \boldsymbol{\lambda}_D^2 . \delta\boldsymbol{g}^2 d\Gamma = 0, \\ \\ \boldsymbol{\lambda}_{Disc}^1 = -\boldsymbol{\lambda}_{Disc}^2. \end{cases} \tag{7.20}$$

7.3.1 Spatial discretization of the problem

Inevitably, the spatial discretization of each sub-domain, Ω^i, is performed using the standard finite element method. Therefore, the continuum sub-domain, Ω_0^i, is replaced by a set of finite elements, $\Omega_{e,0}^i$ such that

$$\Omega_0^i \approx \Omega_0^{i,d} = \bigcup_{e=1}^{N_{elem}} \Omega_{e,0}^i, \tag{7.21}$$

where the index, $(*)^d$, denotes the discretized version of a variable/domain, symbol $\bigcup$ represents a suitable assembly operator and N_{elem} the number of elements. Extrapolating this approach to the boundary, it is possible to decompose the different parts of the boundary considered in the present formulation as a sum of segments or surfaces

depending on the problem

$$\overline{\Gamma}^{i} \approx \overline{\Gamma}^{i,d} = \bigcup_{e=1}^{N_s} \overline{\Gamma}_{e}^{i,d}, \tag{7.22a}$$

$$\Gamma_{D}^{i} \approx \Gamma_{D}^{i,d} = \bigcup_{s=1}^{N_s} \Gamma_{D,s}^{i,d}, \tag{7.22b}$$

where N_s denotes the number of segments. In agreement with the spatial discretization, the virtual admissible displacement fluctuation field, $\mathcal{V}$, is replaced by its discretized counterpart, $\mathcal{V}^d$.

Remark 7.4. As mentioned in the introduction of this chapter, this new boundary condition is a concept and therefore, it will be introduced as simple as possible. Thus, in what follows, the formulation will be presented exclusively for two-dimensional analysis.

Based on the above definitions, the discretized version of the system of equations (7.16) is given by

$$\begin{cases} \displaystyle\int_{\Omega_0^{1,d}} \boldsymbol{G}^T \boldsymbol{P}\left\{\boldsymbol{y}\right\} dV \delta\widetilde{\boldsymbol{u}}\left\{\boldsymbol{y}\right\} + \bigcup_{s=1}^{N_s^1} \int_{\Gamma_{D,s}^{1,d}} \delta\boldsymbol{\lambda}_{D,s}^{1}.\boldsymbol{g}_s^1 + \boldsymbol{\lambda}_{D,s}^{1}.\delta\boldsymbol{g}_s^1 d\Gamma = 0, \\ \displaystyle\int_{\Omega_0^{2,d}} \boldsymbol{G}^T \boldsymbol{P}\left\{\boldsymbol{y}\right\} dV \delta\widetilde{\boldsymbol{u}}\left\{\boldsymbol{y}\right\} + \bigcup_{s=1}^{N_s^2} \int_{\Gamma_{D,s}^{2,d}} \delta\boldsymbol{\lambda}_{D,s}^{2}.\boldsymbol{g}_s^2 + \boldsymbol{\lambda}_{D,s}^{2}.\delta\boldsymbol{g}_s^2 d\Gamma = 0, \\ \boldsymbol{\lambda}_{Disc}^{1} = -\boldsymbol{\lambda}_{Disc}^{2}, \end{cases} \tag{7.23}$$

where $\boldsymbol{G}$ denotes the discretized version of the gradient operator, $\nabla_{\boldsymbol{p}}$

The next key step, required for the spatial discretization of the problem, consists on the definition of *Mortar* and *non-Mortar* domains (boundaries). In this case, Γ_D^i will be defined as *non-Mortar* boundary, $\Gamma^{i,nm}$ whereas $\overline{\Gamma}^i$ as *Mortar* frontier, $\overline{\Gamma}^{m,i}$:

$$\Gamma_{D}^{i} \equiv \Gamma^{i,nm}, \tag{7.24a}$$

$$\overline{\Gamma}^{i} \equiv \Gamma^{i,m}. \tag{7.24b}$$

Having defined the *non-Mortar* and *Mortar* boundaries of each sub-domain Ω_0^1 and Ω_0^2, it is necessary to introduce the interpolation scheme inherent with the *Mortar* decomposition method which allows the correct enforcement of a particular condition over non-conform discretized domains. As a matter of fact, this scheme has already been introduced in Section 5.2.2 and, hence, only the vital steps will be restated here.

It is well-known that the interpolation scheme allows us to determine the value of a field in a particular point $\boldsymbol{p}$ within a segment defined by its nodes when the nodal values of this field is known. Based on this concept, for *non-Mortar* and *Mortar* domains it is possible to define the coordinates and displacements for a point $\boldsymbol{p}$ such that

$$\begin{array}{ll} \text{On the } \textit{non-Mortar} \text{ surface, } \Gamma_s^{i,nm}: & \widetilde{\boldsymbol{u}}_p^{i,nm}\{\boldsymbol{\xi}\} = \sum_{i=1}^{N_{nodes}} N_i\left\{\boldsymbol{\xi}_p\right\} \widetilde{\boldsymbol{u}}_{n_i}^{i,nm}, \\ & \boldsymbol{y}_p^{i,nm}\{\boldsymbol{\xi}\} = \sum_{i=1}^{N_{nodes}} N_i\left\{\boldsymbol{\xi}_p\right\} \boldsymbol{y}_{n_i}^{i,nm}, \\ \text{On the } \textit{Mortar} \text{ surface, } \Gamma_s^{i,m}: & \widetilde{\boldsymbol{u}}_p^{m}\{\boldsymbol{\zeta}\} = \sum_{i=1}^{N_{nodes}} N_i\left\{\boldsymbol{\zeta}_p\right\} \widetilde{\boldsymbol{u}}_{n_i}^{i,m}, \\ & \boldsymbol{y}_p^{i,m}\{\boldsymbol{\zeta}\} = \sum_{i=1}^{N_{nodes}} N_i\left\{\boldsymbol{\zeta}_p\right\} \boldsymbol{y}_{n_i}^{i,m}, \end{array} \tag{7.25}$$

where, once again, $N_i\left\{\boldsymbol{\xi}_p\right\}$ and $N_i\left\{\boldsymbol{\zeta}_p\right\}$ denote the interpolation function of node i at *non-Mortar* and *Mortar* boundaries. Once again, $\boldsymbol{\xi}$ and $\boldsymbol{\zeta}$ will denote an integration *Gauss* point at *non-Mortar* and *Mortar* domains. Due to the use of the *Mortar* decomposition method, the *Lagrange multiplier*, $\boldsymbol{\lambda}_{D,p}^i$, is interpolated using "*special*" interpolation functions $M_i\left\{\boldsymbol{\xi}_p\right\}$ defined over the *non-Mortar* boundary, $\Gamma^{i,nm}$ [1].

$$\boldsymbol{\lambda}_{D,p}^i\{\boldsymbol{\xi}\} = \sum_{i=1}^{N_{nodes}} M_i\left\{\boldsymbol{\xi}_p\right\} \boldsymbol{\lambda}_{D,n_i}^i, \tag{7.26}$$

With the previous definition at hand, the *gap* function defined at point $\boldsymbol{p}$ of the *non-Mortar* domain $\boldsymbol{g}_{s,p}^i\{\boldsymbol{\xi}\}$ is defined as

$$\begin{aligned} \boldsymbol{g}_{s,p}^i\{\boldsymbol{\xi}\} &= \widetilde{\boldsymbol{u}}^{i,nm}\left\{\boldsymbol{\xi}_p\right\} - \widetilde{\boldsymbol{u}}^{i,m}\left\{\boldsymbol{\zeta}\left\{\boldsymbol{\xi}_p\right\}\right\} \\ &= \sum_{i=1}^{N_{nodes}} N_i\left\{\boldsymbol{\xi}_p\right\} \widetilde{\boldsymbol{u}}_{n_i}^{i,nm} - \sum_{i=1}^{N_{nodes}} N_i\left\{\boldsymbol{\zeta}\left\{\boldsymbol{\xi}_p\right\}\right\} \widetilde{\boldsymbol{u}}_{n_i}^{i,m}. \end{aligned} \tag{7.27}$$

In the previous equation, $\boldsymbol{\zeta}\left\{\boldsymbol{\xi}_p\right\}$ denotes a point at the *Mortar* surface, which is obtained by projecting the integration *Gauss* point, $\boldsymbol{\xi}_p$, located at the *non-Mortar* segment s towards the associated unit outward normal vector, $\boldsymbol{N}\left\{\boldsymbol{\xi}_p\right\}$. This approach will be carefully explained in Section 7.3.1.1 where the numerical integration scheme for this boundary condition will be introduced. In matrix format, the previous equation is given by

$$\boldsymbol{g}_{s,p}^i\{\boldsymbol{\xi_p}\} = \boldsymbol{w}_{s,p}^{i^T} \boldsymbol{B}_{s,p}^i, \tag{7.28}$$

[1] It is important to note that $(*)^i$ denotes the sub-domain whereas $(*)_i$ the node index of the segment.

where $\boldsymbol{w}_{s,p}^{i}$ and $\boldsymbol{B}_{s,p}^{i}$ are given by

$$\boldsymbol{w}_{s,p}^{i^T} = \left[\begin{array}{cccccccc} \widetilde{\boldsymbol{u}}_{n_1}^{nm^T} & \cdots & \widetilde{\boldsymbol{u}}_{n_{N_{nodes}}}^{nm^T} & \widetilde{\boldsymbol{u}}_{n_1}^{m^T} & \cdots & \widetilde{\boldsymbol{u}}_{n_{N_{nodes}}}^{m^T} & \boldsymbol{\lambda}_{D,n_1}^{T} & \cdots \quad \boldsymbol{\lambda}_{D,n_{N_{nodes}}}^{T} \end{array} \right], \tag{7.29a}$$

$$\boldsymbol{B}_{s,p}^{i^T} = \left[\begin{array}{cccccccc} N_1\left\{\boldsymbol{\xi}_p\right\}\boldsymbol{I} & \cdots & N_{N_{nodes}}\left\{\boldsymbol{\xi}_p\right\}\boldsymbol{I} & -N_1\left\{\zeta\left\{\boldsymbol{\xi}_p\right\}\right\}\boldsymbol{I} & \cdots & -N_{N_{nodes}}\left\{\zeta\left\{\boldsymbol{\xi}_p\right\}\right\}\boldsymbol{I} & \mathbf{0} & \cdots \quad \mathbf{0} \end{array} \right]. \tag{7.29b}$$

Applying the same strategy above introduced to the *Lagrange* multipliers, $\boldsymbol{\lambda}$, (Equation (7.26)), it is possible to write

$$\boldsymbol{\lambda}_{D,p}\left\{\boldsymbol{\xi}\right\} = \boldsymbol{w}_{s,p}^{i^T}\boldsymbol{M}_{s,p}^{i}, \tag{7.30}$$

where matrix $\boldsymbol{M}_{s,p}^{i}$ is given by

$$\boldsymbol{M}_{s,p} = \left[\begin{array}{cccccccc} \mathbf{0} & \cdots & \mathbf{0} & \mathbf{0} & \cdots & \mathbf{0} & M_1\left\{\boldsymbol{\xi}_p\right\}\boldsymbol{I} & \cdots \quad M_{N_{nodes}}\left\{\boldsymbol{\xi}_p\right\}\boldsymbol{I} \end{array} \right]. \tag{7.31}$$

Finally, with the previous relations at hand, it is possible to write the spatial discretized version of system of equations (7.16):

$$\begin{cases} \displaystyle\int_{\Omega_0^{1,d}} \boldsymbol{G}^T\boldsymbol{P}\left\{\boldsymbol{y}\right\} dV\,\delta\widetilde{\boldsymbol{u}}\left\{\boldsymbol{y}\right\} + \bigcup_{s=1}^{N_s^{1,nm}} \sum_{p=1}^{N_{Gauss}} \left[\delta\boldsymbol{w}_{s,p}^{1^T}\left(\boldsymbol{B}_{s,p}^{1}\boldsymbol{M}_{s,p}^{1^T} + \boldsymbol{M}_{s,p}^{1}\boldsymbol{B}_{s,p}^{1^T}\right)\right] J_p w_p = 0, \\ \displaystyle\int_{\Omega_0^{2,d}} \boldsymbol{G}^T\boldsymbol{P}\left\{\boldsymbol{y}\right\} dV\,\delta\widetilde{\boldsymbol{u}}\left\{\boldsymbol{y}\right\} + \bigcup_{s=1}^{N_s^{2,nm}} \sum_{p=1}^{N_{Gauss}} \left[\delta\boldsymbol{w}_{s,p}^{2^T}\left(\boldsymbol{B}_{s,p}^{2}\boldsymbol{M}_{s,p}^{2^T} + \boldsymbol{M}_{s,p}^{2}\boldsymbol{B}_{s,p}^{2^T}\right)\right] J_p w_p = 0, \\ \boldsymbol{\lambda}_{Disc}^{1} = -\boldsymbol{\lambda}_{Disc}^{2}. \end{cases} \tag{7.32}$$

Since the previous equation is satisfied for all admissible $\delta\widetilde{\boldsymbol{u}}\left\{\boldsymbol{y}\right\}$ and $\delta\boldsymbol{w}_p^i$, splitting the total displacement fluctuation field in its *Interior* and *Boundary* counterparts, denoted respectively by $\widetilde{\boldsymbol{u}}^I$ and $\widetilde{\boldsymbol{u}}^B$, and properly modifying matrices $\boldsymbol{B}_{s,p}$, $\boldsymbol{M}_{s,p}$ and $\boldsymbol{w}_{s,p}$, the previous equation can be conveniently expressed as a system of equations:

$$
\begin{cases}
\boldsymbol{f}^{1,I}\left\{\boldsymbol{y}\right\} = \boldsymbol{0}, \\
\boldsymbol{f}^{1,B}\left\{\boldsymbol{y}\right\} + \bigcup_{s=1}^{N_s^{1,nm}} \sum_{p=1}^{N_{Gauss}} \left[\left(\overline{\boldsymbol{B}}_{s,p}\overline{\boldsymbol{M}}_{s,p}^{T}\right)\overline{\boldsymbol{\lambda}}_{s,p}^{1}\right] J_p w_p = \boldsymbol{0}, \\
\bigcup_{s=1}^{N_s^{1,nm}} \sum_{p=1}^{N_{Gauss}} \left[\left(\overline{\boldsymbol{M}}_{s,p}\overline{\boldsymbol{B}}_{s,p}^{T}\right)\overline{\boldsymbol{w}}_{s,p}^{1}\right] J_p w_p = \boldsymbol{0}, \\
\boldsymbol{f}^{2,I}\left\{\boldsymbol{y}\right\} = \boldsymbol{0}, \\
\boldsymbol{f}^{1,B}\left\{\boldsymbol{y}\right\} + \bigcup_{s=1}^{N_s^{2,nm}} \sum_{p=1}^{N_{Gauss}} \left[\left(\overline{\boldsymbol{B}}_{s,p}\overline{\boldsymbol{M}}_{s,p}^{T}\right)\overline{\boldsymbol{\lambda}}_{s,p}^{2}\right] J_p w_p = \boldsymbol{0}, \\
\bigcup_{s=1}^{N_s^{2,nm}} \sum_{p=1}^{N_{Gauss}} \left[\left(\overline{\boldsymbol{M}}_{s,p}\overline{\boldsymbol{B}}_{s,p}^{T}\right)\overline{\boldsymbol{w}}_{s,p}^{2}\right] J_p w_p = \boldsymbol{0}, \\
\boldsymbol{\lambda}_{Disc}^{1} = -\boldsymbol{\lambda}_{Disc}^{2},
\end{cases}
\tag{7.33}
$$

where matrices $\overline{\boldsymbol{M}}_{s,p}^{T}$ and $\overline{\boldsymbol{B}}_{s,p}^{T}$ have been already defined in Section 5.2.2 as well as vectors $\overline{\boldsymbol{w}}_{s,p}^{i}$ and $\overline{\boldsymbol{\lambda}}_{s,p}^{i}$.

Due to the highly non-linear nature of the previous system of equations, a suitable numerical method needs to be considered to solve it. Following the same approach of the previous chapters of the present document, the iterative *Newton-Raphson* will be used. For this purpose, the linearization of the previous system of equations is mandatory which in the present case, leads to:

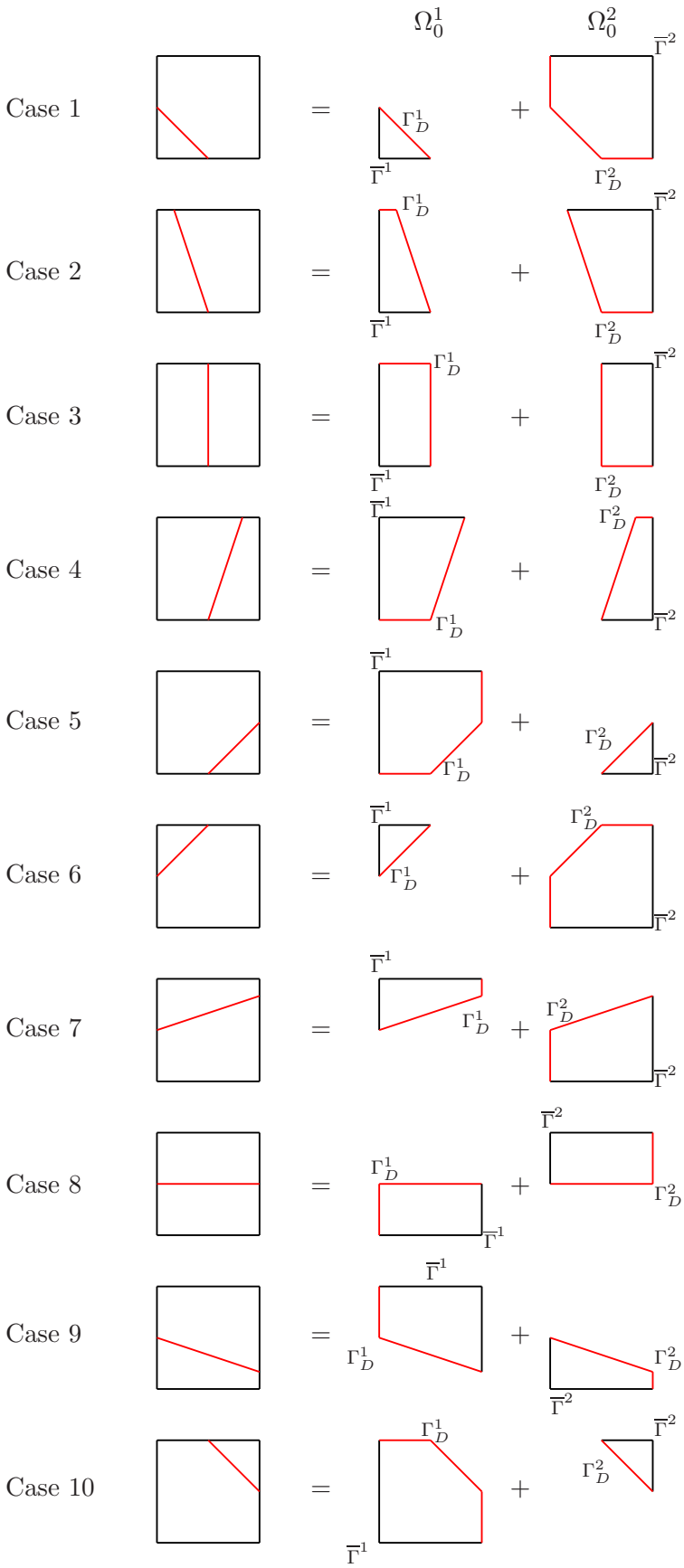

FIGURE 7.2: Schematic illustration of all possible shapes that a localization band may assume.

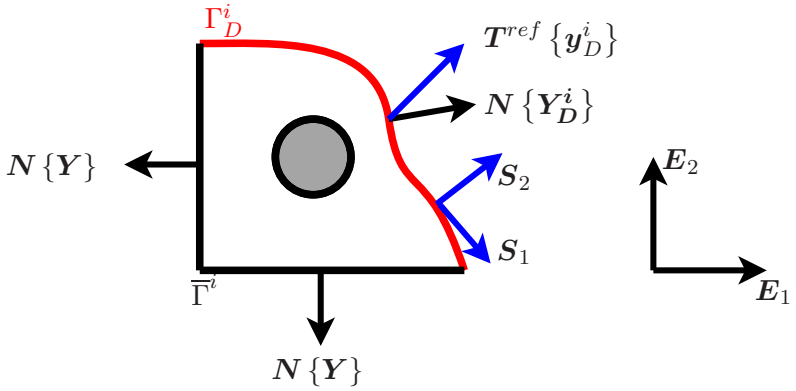

FIGURE 7.3: Domain 1 of the decomposed RVE domain.

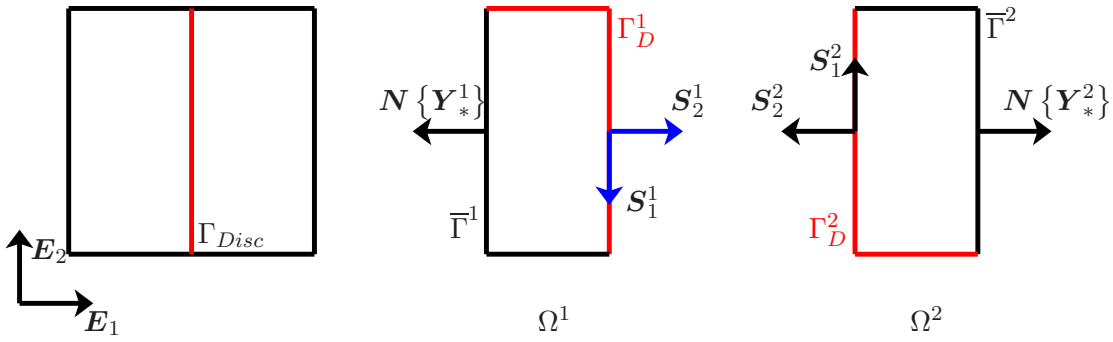

FIGURE 7.4: Simplest shape configuration of the localization band.

$$
\left[\begin{array}{c:c:c|c:c:c|c}
\boldsymbol{K}^{1^{II}} & \boldsymbol{K}^{1^{IB}} & \boldsymbol{0} & \boldsymbol{0} & \boldsymbol{0} & \boldsymbol{0} & \boldsymbol{0} \\
\hdashline
\boldsymbol{K}^{1^{BI}} & \boldsymbol{K}^{1^{BB}} & \bigcup_{s=1}^{N_s^{1,nm}} \sum_{p=1}^{N_{Gauss}} \left[\overline{\boldsymbol{B}}_{s,p}^{1} \overline{\boldsymbol{M}}_{s,p}^{1^T}\right] J_p w_p & \boldsymbol{0} & \boldsymbol{0} & \boldsymbol{0} & \boldsymbol{0} \\
\hdashline
\boldsymbol{0} & \bigcup_{s=1}^{N_s^{1,nm}} \sum_{p=1}^{N_{Gauss}} \left[\overline{\boldsymbol{M}}_{s,p}^{1} \overline{\boldsymbol{B}}_{s,p}^{1^T}\right] J_p w_p & \boldsymbol{0} & \boldsymbol{0} & \boldsymbol{0} & \boldsymbol{0} & \boldsymbol{C}^T \\
\hline
\boldsymbol{0} & \boldsymbol{0} & \boldsymbol{0} & \boldsymbol{K}^{2^{II}} & \boldsymbol{K}^{2^{IB}} & \boldsymbol{0} & \boldsymbol{0} \\
\hdashline
\boldsymbol{0} & \boldsymbol{0} & \boldsymbol{0} & \boldsymbol{K}^{2^{BI}} & \boldsymbol{K}^{2^{BB}} & \bigcup_{s=1}^{N_s^{2,nm}} \sum_{p=1}^{N_{Gauss}} \left[\overline{\boldsymbol{B}}_{s,p}^{2} \overline{\boldsymbol{M}}_{s,p}^{2^T}\right] J_p w_p & \boldsymbol{0} \\
\hdashline
\boldsymbol{0} & \boldsymbol{0} & \boldsymbol{0} & \boldsymbol{0} & \bigcup_{s=1}^{N_s^{2,nm}} \sum_{p=1}^{N_{Gauss}} \left[\overline{\boldsymbol{M}}_{s,p}^{2} \overline{\boldsymbol{B}}_{s,p}^{2^T}\right] J_p w_p & \boldsymbol{0} & -\boldsymbol{C}^T \\
\hline
\boldsymbol{0} & \boldsymbol{0} & \boldsymbol{C} & \boldsymbol{0} & \boldsymbol{0} & -\boldsymbol{C} & \boldsymbol{0}
\end{array}\right]^{(j)}
$$

$$
\left\{\begin{array}{c}
\delta\widetilde{\boldsymbol{u}}^{1^I} \\
\hdashline
\delta\widetilde{\boldsymbol{u}}^{1^B} \\
\hdashline
\delta\boldsymbol{\lambda}^{1} \\
\hline
\delta\widetilde{\boldsymbol{u}}^{2^I} \\
\hdashline
\delta\widetilde{\boldsymbol{u}}^{2^B} \\
\hdashline
\delta\boldsymbol{\lambda}^{2} \\
\hline
\boldsymbol{0}
\end{array}\right\}^{(j+1)}
= -
\left\{\begin{array}{c}
\boldsymbol{f}^{1^I}\{\boldsymbol{y}\} \\
\hdashline
\boldsymbol{f}^{1^B}\{\boldsymbol{y}\} + \bigcup_{s=1}^{N_s^{1,nm}} \sum_{p=1}^{N_{Gauss}} \left[\left(\overline{\boldsymbol{B}}_{s,p}^{1} \overline{\boldsymbol{M}}_{s,p}^{1^T}\right) \overline{\boldsymbol{\lambda}}_{s,p}^{1}\right] J_p w_p \\
\hdashline
\bigcup_{s=1}^{N_s^{1,nm}} \sum_{p=1}^{N_{Gauss}} \left[\left(\overline{\boldsymbol{M}}_{s,p}^{1} \overline{\boldsymbol{B}}_{s,p}^{1^T}\right) \overline{\boldsymbol{w}}_{s,p}^{1}\right] J_p w_p \\
\hline
\boldsymbol{f}^{2^I}\{\boldsymbol{y}\} \\
\hdashline
\boldsymbol{f}^{2^B}\{\boldsymbol{y}\} + \bigcup_{s=1}^{N_s^{2,nm}} \sum_{p=1}^{N_{Gauss}} \left[\left(\overline{\boldsymbol{B}}_{s,p}^{2} \overline{\boldsymbol{M}}_{s,p}^{2^T}\right) \overline{\boldsymbol{\lambda}}_{s,p}^{2}\right] J_p w_p \\
\hdashline
\bigcup_{s=1}^{N_s^{2,nm}} \sum_{p=1}^{N_{Gauss}} \left[\left(\overline{\boldsymbol{M}}_{s,p}^{2} \overline{\boldsymbol{B}}_{s,p}^{2^T}\right) \overline{\boldsymbol{w}}_{s,p}^{2}\right] J_p w_p \\
\hline
\boldsymbol{0}
\end{array}\right\}^{(j)}
. \tag{7.34}
$$

In the previous system of equations, $\boldsymbol{C}$ consists on a matrix fulfilled with 1 and 0 responsible for imposing the condition define by the last expression of (7.32) and (j) denotes the *Newton-Raphson* iteration index.

It is relevant to emphasize that the previous system of equations is generic and does not take into account information concerned with the strategy which may be used to detect and define a localization band. Note that, numerical frameworks exclusively developed to describe the propagation of a localization band (i.e. discontinuity) may be coupled with the previous system of equations. Among several others, remeshing [163], *eXtended Finite Element Method* (X-FEM) [164] and *Partition of Unity Method* (PUM) [165] may be selected.

Nevertheless, probably the simple case consists on the definition of a set of nodes where a specific internal variable (i.e. damage or accumulated plastic strain) reaches a critical value. Despite of being simple, this approach demands additional modifications to (7.34). These modifications are due to the fact that, since the nodes which define the localization band belong simultaneously to both sub-domains, it is necessary to perform the condensation of the system of equations (7.34) in order to obtain a stable and solvable system of equations. Unfortunately, this development has not been yet carried out mainly by two reasons: the elimination of equations from (7.34) is not straightforward and it needs to be performed for each geometric possible case illustrated in Figure 7.2.

7.3.1.1 Integration scheme

From the formulation introduced above for the new concept of periodicity, we recognise that the integration scheme will play a critical role. The fundamental basis of the numerical integration scheme, which will be used in this new boundary condition, has already been introduced in Section 5.2.5. Nevertheless, in Section 5.2.5, this approach was introduced for one particular case: parallel surfaces with non-conform meshes. Since the final objective is to consider localization bands with arbitrary configurations, this method needs to be extended. In what follows, this extension will be addressed.

As a matter of fact, in terms of requirements which the numerical integration scheme should fulfil, they are the same as described in Section 5.2.5: should provide an exact result regardless of the complexity of the boundary; the approach needs to be suitable for a vast variety of finite element types. Despite of being out of the scope of the work, the method should allow the extension of the formulation to 3-dimensional problems.

Expanding the coefficients of the matricial product $\overline{\boldsymbol{B}}^{i}_{s,p}\overline{\boldsymbol{M}}^{i^T}_{s,p}$ and $\overline{\boldsymbol{M}}^{i}_{s,p}\overline{\boldsymbol{B}}^{i^T}_{s,p}$ one can write

$$a^{nm}_{i,j} = \bigcup_{s=1}^{N_s^{i,nm}} \sum_{p=1}^{N_{Gauss}} N_i\left\{\boldsymbol{\xi}_p\right\} M_j\left\{\boldsymbol{\xi}_p\right\} J_p w_p, \tag{7.35a}$$

$$a^{m}_{i,j} = -\bigcup_{s=1}^{N_s^{i,nm}} \sum_{p=1}^{N_{Gauss}} N_i\left\{\zeta\left\{\boldsymbol{\xi}_p\right\}\right\} M_j\left\{\boldsymbol{\xi}_p\right\} J_p w_p. \tag{7.35b}$$

Whilst the numerical integration of Equation (7.35a) is straightforward since all variables are defined at the same *Non-Mortar* surface and, hence, the standard *Gaussian* quadrature can be easily applied, this is not true for Equation 7.35b. In this case, there are terms defined over different boundaries with possible non-conform meshes. Therefore, it is necessary to introduce a numerical approach that is capable to solve this issue.

This is carried out by introducing a segmentation procedure. In this work, the segmentation method considered was proposed by [3–5]. The main idea of this method consists on the definition of a continuous normal field over the *non-Mortar* domain, $\Gamma^{i,nm}$. This procedure is schematically illustrated in Figure 7.5. From a geometric point of view,

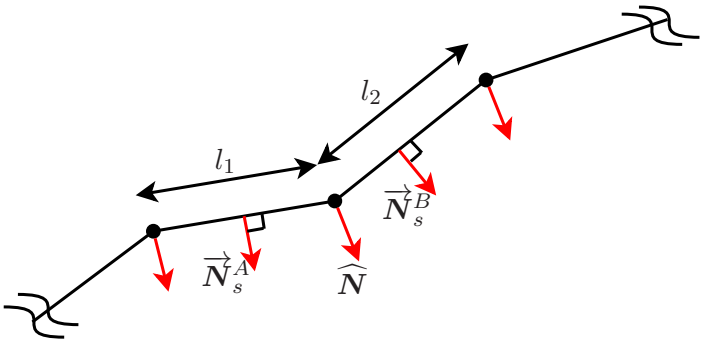

FIGURE 7.5: Definition of the normal vectors at nodes [3–5]

it is possible to define two distinct normal vectors in each node which result from the intersection of two non-collinear lines: each normal vector associated to each segment (not represented in Figure 7.5). Nevertheless, since it is necessary to consider a normal vector for each *non-Mortar* node, in order to define the set of integration segments, it is necessary to choose one. However, this selection is not arbitrary since it may result on discontinuities. In order to avoid this geometrical issue, Yang et al. [3] have proposed a simple but rather effective methodology. The idea is simply consider for each node, the normal vector $\widehat{\boldsymbol{N}}$ which is given by an average of both unit outward normal vectors intrinsic with each segment which define the node. The normal vector, $\widehat{\boldsymbol{N}}$, is given by

$$\widehat{\boldsymbol{N}} = \frac{l_2\overrightarrow{\boldsymbol{N}}^A_s + l_1\overrightarrow{\boldsymbol{N}}^B_s}{\|l_2\overrightarrow{\boldsymbol{N}}^A_s + l_1\overrightarrow{\boldsymbol{N}}^B_s\|}, \tag{7.36}$$

where l_1 and l_2 are the length of the segments in the neighbourhood of the node and $\overrightarrow{\boldsymbol{N}}_s^A$ and $\overrightarrow{\boldsymbol{N}}_s^B$ are the respective outward unit normal vectors.

Having defined for each node a unique normal vector at the *non-Mortar* surface, $\overrightarrow{\boldsymbol{N}}^{nm}$, it is possible to set up a strategy to define the integration segments based exclusively on the *non-Mortar* surface. This approach is performed in two steps. In the first, the projection of a point with coordinates $\boldsymbol{Y}^{nm}$ inside of a s *non-Mortar* segment defined by its outward unit normal vector, $\overrightarrow{\boldsymbol{N}}_s$, onto a *Mortar* segment defined by its nodes, $\boldsymbol{Y}_1^m$ and $\boldsymbol{Y}_2^m$ is determined by the following linear equation

$$\left[N_1\left\{\boldsymbol{\zeta}\right\}\boldsymbol{Y}_1^m + N_2\left\{\boldsymbol{\zeta}\right\}\boldsymbol{Y}_2^m - \boldsymbol{Y}^{nm}\right] \times \overrightarrow{\boldsymbol{N}}_s^{nm} = \boldsymbol{0} \tag{7.37}$$

The second step consists on the projection of a generic node from the *Mortar* discretized boundary with coordinates $\boldsymbol{Y}^m$ onto a *non-Mortar* segment s defined by its nodes with coordinates $\boldsymbol{Y}_1^{nm}$ and $\boldsymbol{Y}_2^{nm}$ and associated unit outward normal vectors $\widehat{\boldsymbol{N}}_1^{nm}$ and $\widehat{\boldsymbol{N}}_2^{nm}$:

$$\left[N_1\left\{\boldsymbol{\xi}\right\}\boldsymbol{Y}_1^{nm} + N_2\left\{\boldsymbol{\xi}\right\}\boldsymbol{Y}_2^{nm} - \boldsymbol{Y}^m\right] \times \left[N_1\left\{\boldsymbol{\xi}\right\}\widehat{\boldsymbol{N}}_1^{nm} + N_2\left\{\boldsymbol{\xi}\right\}\widehat{\boldsymbol{N}}_2^{nm}\right] = \boldsymbol{0}. \tag{7.38}$$

The final result of these two steps are schematically illustrated in Figure 7.6(a).

Performed the segmentation of the surfaces, it possible to numerically determine coefficients $a_{ij}^{i,nm}$ (Equation 7.35b). However, it is necessary to introduce an extra local coordinate system, $\boldsymbol{\eta}_p$, as illustrated in Figure 7.6(b), given rise to

$$a_{ij}^{i,nm} = \bigcup_{s=1}^{N_s^{i,nm}} \sum_{seg=1}^{N_{seg}} \sum_{p=1}^{N_{Gauss}} N_i\left\{\boldsymbol{\zeta}\left\{\boldsymbol{\eta}_p\right\}\right\} M_j\left\{\boldsymbol{\xi}\left\{\boldsymbol{\eta}_p\right\}\right\} J_p w_p, \tag{7.39}$$

where the *jacobian* is given by

$$J_p = \frac{\partial \boldsymbol{Y}}{\partial \boldsymbol{\xi}} \frac{\partial \boldsymbol{\xi}}{\partial \boldsymbol{\eta}}. \tag{7.40}$$

7.3.1.2 General considerations

Despite the potential of this new kinematical boundary condition, there are some assumptions that have to be made with regard to the configuration of the localization band. This is not exclusively related to numerical issues, which may arise due to the complexity of the shape of the localization band, but also, due to the non-physical phenomena which may be modelled. A typical example consists on a localization band which intersects twice the same border of the RVE. Even under quite complex loading conditions, according to the knowledge of the author, this effect is highly unlikely

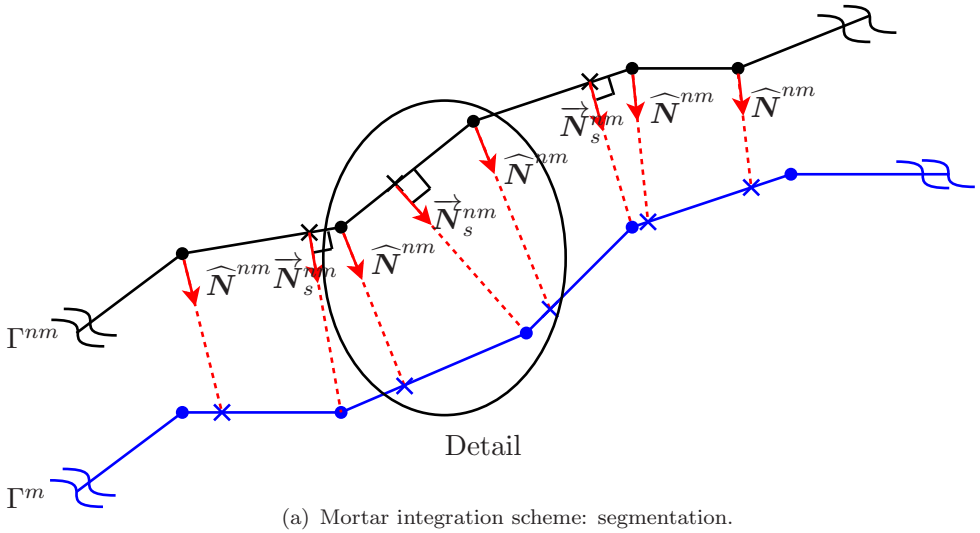

(a) Mortar integration scheme: segmentation.

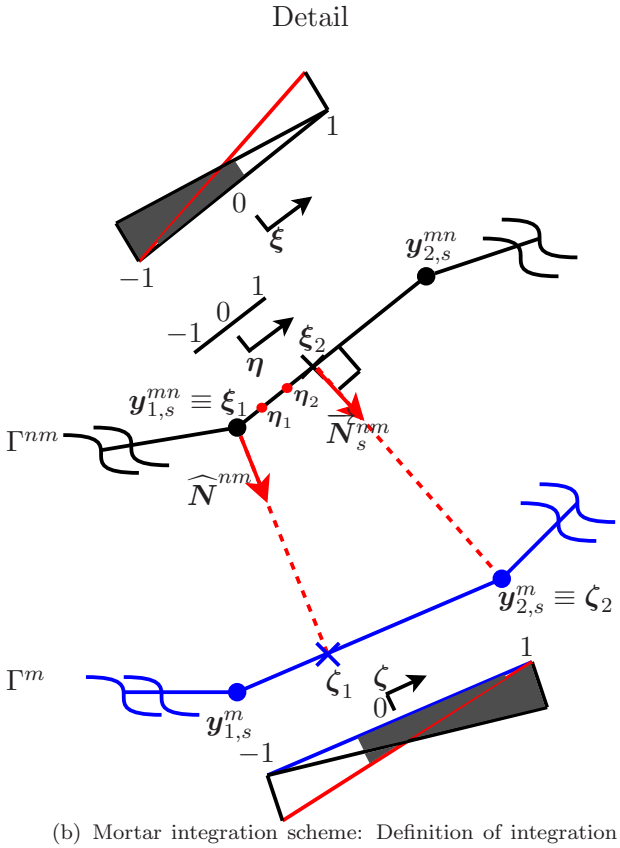

(b) Mortar integration scheme: Definition of integration domain.

FIGURE 7.6: Mortar integration scheme for non-parallel discretized surfaces.

to occur. Probably, other non-sense geometries and considerations inherent with the propagation of the localization band need to be analysed.

Moreover, at this stage of the work, the formulation does not contemplate the evolution of the localization band or the possibility of bifurcation. However, it will be possible to

model these two phenomena in future iterations. For this purpose, the current formulation needs to be enhanced. In particular, the definition of sub-domains which inevitably needs to be extended. For instance, in order to include the possibility of bifurcation, more than two sub-domains will be required.

7.3.2 Activation of the New Periodic boundary condition

Whenever a localization band is not present on the RVE domain, standard *Periodic* boundary condition should be considered. As a matter of fact, the standard enforcement of the *Mortar Periodic* boundary condition proposed in Chapter 5 can be used regardless of the complexity of the geometry modelled at the micro-structure. However, when a localization band develops in the RVE until it intersects two distinct boundaries of the RVE, it is necessary to switch from standard *Periodic* boundary condition to the new concept proposed in this chapter.

In order to detect the presence of a localization band, a suitable criterion needs to be considered. Different approaches may be selected. Probably the most simple one consists on the use of an internal variable such as damage or accumulated plastic strain. In this case, we switch to the new concept above described, which is able to tackle the presence of a localization band, when these variables reach a critical value over a specific path (i.e. localization band). It is also possible to combine this approach with an automatic image analysis as used by Coenen et al. [63].

As previously pointed, the approach proposed throughout this document is a concept and, therefore, it deserves a considerable amount of work to validate as well as to explore all potentialities. However, in order to present a simple and illustrative preliminary example, the above cited approach without an image detection algorithm was considered. This is due to the fact that, it is the simplest approach available at this stage of the work.

7.4 Numerical results

In this final section, a very preliminary result obtained with the new concept of *Periodic* boundary condition is introduced. The main goal of this numerical result, rather than a fully assessment of the new concept, is basically to illustrate on the global behaviour of the RVE in terms of its final shape. Thus, it will be possible to have an idea about the response, which should be expected, with the new concept.

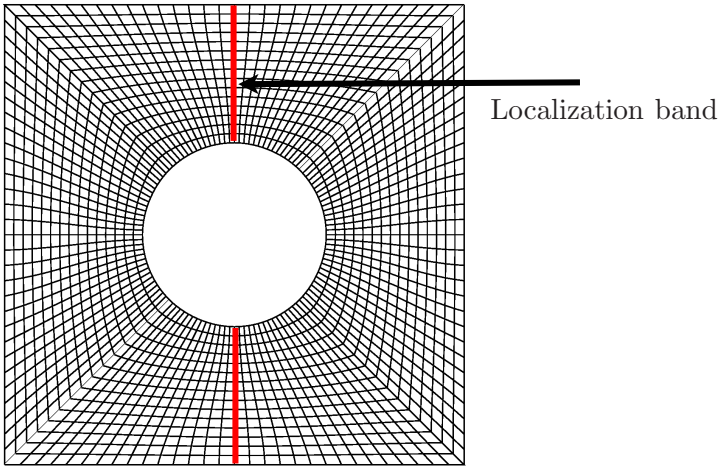

FIGURE 7.7: Mesh of the RVE used on the first preliminary result of the new concept of *Periodic* boundary condition. 1800 linear quadrilateral elements used on the discretization of the RVE. In red, the imposed localization band.

As pointed out in Sections 7.3.1.1 and 7.3.2, some numerical enhancements need to be carried out in order to explore all potentialities of this new concept: fix the issue concerned with the undetermined system of equations (7.34) by performing the condensation for all possible admissible cases (Figure 7.2); implement an algorithm to automatically detect a localization band. Aiming to circumvent these issues, two coarse assumptions were considered. The former is related with the identification of the localization band. In this case, a RVE with a very simple geometry was considered as shown in Figure 7.7. Since the RVE only includes a centered void corresponding to a volume fraction of 12.5%, and considering the following macroscopic deformation gradient, $\boldsymbol{F}\{\boldsymbol{x}\}$,

$$\boldsymbol{F}\{\boldsymbol{x}\} = \begin{bmatrix} 1.2 & 0.0 \\ 0.0 & 1.0 \end{bmatrix}, \tag{7.41}$$

which corresponds to a pure tensile deformation state in direction x, a vertical localization band at the center of the RVE is expected. This particular localization band will be defined by the nodes which belong to the vertical line starting from the middle node at the bottom frontier of the RVE to the top surface. This feature is highlighted in Figure 7.7. The later assumption is associated with the necessity of getting a stable system of equations (7.34). For this purpose, the displacement fluctuation, $\widetilde{\boldsymbol{u}}$, at the nodes which define the localization band will be prescribed. Although this assumption is severe and, in fact, in complete disagreement with the formulation proposed: the localization band is a dynamic feature of a solid and therefore, its shape may change throughout the deformation process of the structure.

As a matter of fact, 1800 linear quadrilateral elements were used on the spatial discretization of the RVE and a linear elastic law was considered with *Young* Modulus

and *Poisson* ration equal to $E = 70$ GPa and $v = 0.3$, respectively. In line with the two-dimensional numerical examples introduced in this document, plane strain condition was considered. Moreover, *Dual* base interpolation functions (see Section 5.2.4.2) were considered.

In Figure 7.8 it is possible to observe the final shapes of the RVE obtained with standard *Periodic* boundary condition, Figure 7.8(a) and with the new concept of periodicity, Figure 7.8(b). As it is possible to observe, the final shapes are notoriously different. Neglecting the final shape of the void, which in the case of the new concept assumes a strange format due the severe constraint applied to the nodes which define the localization band, there is a notable difference on the shapes of left and right borders of the RVE. Whereas standard *Periodic* boundary condition imposes the same fluctuation displacement at left and right surfaces, when the new boundary constraint is considered, a symmetric displacement was obtained from the solution of the micro-equilibrium problem. Apart from the small effect that is observable (the author really believes that it will be much more pronounced when the concept would be completely implemented), the final shape obtained is in agreement with the initial goals proposed at the beginning of this new concept. Considering the definition of a localization band, which roughly consists on a material region that loses its stiffness and load capacity, the left side will no be linked to the right side and vice-versa. Thus, the displacement fluctuation field at the left side will not be dependent on the displacement fluctuation at right side and vice versa. Instead, it will depend on the shape of the localization band. In this case, since the localization band crosses a void, this geometrical feature will influence the deformation of the border of the RVE.

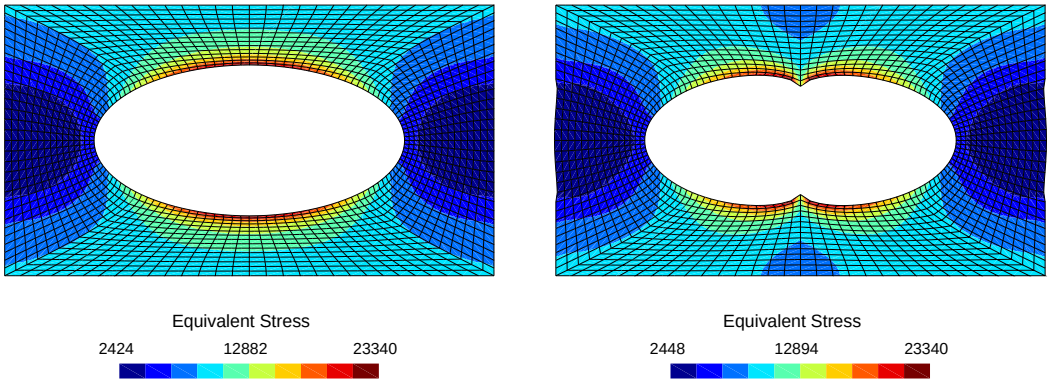

(a) Standard *Periodic* boundary condition . (b) New Periodic boundary Condition.

FIGURE 7.8: Final configuration of the RVE obtained with standard and new *Periodic* boundary conditions. A magnification factor equal to 4 was used to highlight the differences.

7.5 Conclusions

In this chapter, a new concept of a *Periodic* boundary condition that is able to tackle the presence of a localization band was introduced. As pointed out throughout this chapter, this is an embryonic concept and, hence, a significant amount of work needs to be carried out in the future, in particular to improve two issues: unsolvable system of equations which defines the micro-equilibrium problem and an algorithm to detect a localization band taking into account a particular criteria (i.e. critical accumulated plastic strain or critical damage). With regard to the first issue, it may be solved by performing the condensation of the system of equations. This task basically consists on removing from this system of equations repeated unknowns and needs to be carefully carried out for each possible cases.

With regard to the formulation of the new concept, all foundations were consistently introduced either in terms of continuum or discrete approach. Moreover, special attention was given to the numerical framework to implement this new concept.

Unfortunately, due to the complexity of the problem, only one preliminary numerical example was introduced. As previously explained, the idea was not to assess all potentialities of the new concept, but, instead, highlight the main differences compared with standard *Periodic* boundary condition. With this example it was possible to have positive feedback since the final shape of the RVE obtained was in agreement with the expected results.

Chapter 8

Final Remarks

Notwithstanding the huge impact that electronic engineering has had in typical mechanical industries such as automotive and aeronautic over the last three decades, the future of these industries is inevitably linked with the development of new materials, the optimization of their manufacturing processes and their integration into efficient structures. In this context, despite being a recent methodology, coupled multi-scale models will be an allied on the design of complex materials with practical application over a wide spectrum of applications in a near future.

Trying to anticipate the future of this methodology, the author believes that coupled multi-scale models will be widely used in the industry, particularly for the characterization of material properties under a wide range of loading conditions and different regimes (i.e. elastic, hardening, softening, crack propagation, thermal effects, cyclic loads, among several others). Even though it is possible to use this method to fully design a component or a critical part of a mechanical system, the author's opinion is that, for this particular application, its use will be reduced since for the industry, "*time*" is a severe constraint of a project.

The initial goal of the present work was to use coupled multi-scale models to characterize complex materials, which have their global properties deeply dependent on the microstructure, taking into account thermals effects at the fine scale. Nevertheless, since this work started from scratch, it was necessary to develop and implement several routines able to solve coupled multi-scale problems. In the course of the work, some numerical issues arose which led to the change of the focus of the present thesis. As a consequence, particular attention to numerical issues that coupled multi-scale models have shown were discussed. Some of these discussions lead to some scientific contributions. In what follows, a global summary of the present work is introduced chapter by chapter.

Chapter 3

In Chapter 3, the foundations of coupled multi-scale models such as homogenization and *Hill-Mandel* principles as well as boundary constraints, which are kinematically admissible, are introduced. Based on the underlying theory, the formulation of this method was undertaken and a numerical framework was proposed which lead to the development of two finite element codes: ***MSP***, *Micro-Scale Problem* and ***CMSP***, *Coupled Multi-Scale Problem*. The former is exclusively devoted to solve the micro-equilibrium problem when a particular deformation gradient is known, whereas, the latter is able to solve a fully *First-Order Coupled Multi-Scale Model*. As a matter of fact, both codes were implemented in the spirit of finite strains. In this Chapter, special attention was given to the consistent linearization of macro and micro problems.

Chapter 4

Upon the implementation of ***CMSP***, it was verified that the CPU time for the solution of a coupled multi-scale problem is strongly dependent on the efficiency of the *Newton-Raphson* method implemented at the micro-scale. Thus, in order to minimize the computational cost, an adaptive sub-incremental strategy for the micro-equilibrium problem was proposed. This numerical strategy is introduced and described in detail in Chapter 4. The main idea was to enhance the *Newton-Raphson* method at fine scale with *Line-Search* and *Arc-Length* methodologies. With this enhancement, two significant achievements are attained: the minimization of the number of macroscopic cutting increments, leading to a significant computational cost reduction and according to the evolution of the problem, it is possible to automatically perform the incrementation of the microscopic equilibrium problem. These two numerical technologies were developed in order to guarantee perfect quadratic asymptotic convergence rates of the *Newton-Raphson* method at both scales.

As a final result, the two numerical frameworks have dramatically improved the robustness and efficiency of the *Newton-Raphson* scheme at the micro-scale. This is particularly true when both numerical tools are used together.

Chapter 5

In Chapter 5, a new strategy for the enforcement of *Periodic* boundary condition is proposed based on the *Mortar* decomposition method. This approach stands out from standard approaches due to the fact that it does not require conform meshes, i.e. meshes which have adjacent boundaries discretized by means of the same number of nodes and

with the same relative position. This new *Periodic* enforcement was introduced and implemented for two and three-dimensional problems.

The resulting approach has demonstrated a notable robustness in prescribing *Periodic* boundary conditions over non-conform meshes. This conclusion was withdrawn by comparing the results obtained with the new enforcement and the standard *Periodic* boundary constraint when simple benchmarks are analysed. Moreover, as demonstrated by means of the three-dimensional problems introduced in Chapter 5, the new approach provides a significant flexibility to the users of numerical homogenization approaches mainly due to the fact that, when complex three-dimensional RVEs are modelled it is quite complicated or even impossible in some cases to build conform meshes.

Chapter 6

The mesh dependence pathology observed when coupled multi-scale models are used to characterize solids was addressed in Chapter 6. Due to the presence of two spatial scales, micro and macro, the effect of the mesh dependence was investigated at both scales.

In order to minimize this numerical issue inherent to the spatial discretization, two different non-local methodologies of integral type were proposed. Whilst for the fine scale a standard non-local method of integral type was applied, where a scalar internal variable was chosen as non-local variable (i.e. damage variable), at the macroscopic level, a completely different methodology was followed. In this case, due to the lack of internal variables, a tensorial kinematic variable was chosen as non-local variable: the macroscopic deformation gradient, $\boldsymbol{F}\{\boldsymbol{x}, t\}$. Special attention to the numerical implementation of both methods was given, in particular with regard to the consistent linearization of the problems at both scales. It is relevant to emphasize that, once again, the formulation proposed was developed within the context of finite strains which in terms of linearization procedure leads to a greater challenge.

As demonstrated by a set of numerical examples, with the proposed non-local methodology at the micro-scale, the mesh dependence was dramatically minimized. Moreover, when implemented within the context of coupled multi-scale models, it has shown a beneficial impact on the global response of the specimen. It is noteworthy to mention that, the non-local approach at the micro-scale was proposed and developed specifically for heterogeneous media.

Notwithstanding, the non-local approach of integral type specifically developed for the macroscopic domain, has promoted a small improvement to the problem. As it is shown, when the non-local characteristic length reaches a certain value, spurious effects appear

in the final shape of the macroscopic specimen. Probably, with further research with regard to the tensorial kinematic variable, which should be selected as non-local parameter, would lead to a more robust and generic solution. A possible approach consists in splitting the total deformation gradient into volumetric and isochoric counterparts. With this decomposition at hand, it would be possible to consider only one part to be non-local variable.

Chapter 7

In Chapter 7, an embryonic *Periodic* boundary condition that is able to tackle the presence of a localization band with and arbitrary shape was introduced. The main underlying idea of this new concept consists on the decomposition of the total RVE domain into a set of sub-domains, taking into account the shape of the localization band. Having defined this set of sub-domains, the *Periodic* boundary condition is prescribed over each one. For this purpose, once again, the *Mortar* decomposition method is applied. In addition to the foundations required for the formulation of this new concept, attention was given to the proof of admissibility of the new boundary constraint as well as to the numerical integration scheme, which plays a critical role on this development.

Despite demanding a significant amount of work, some positive results were obtained. In particular with regard to the final shape of a RVE with a circular void at its center where a vertical localization band was defined. In contrast with the standard *Periodic* boundary condition, the boundaries of the RVE parallel to the localization band did not assume the same shape at the end but, instead, they attained a non-periodic shape. This is due to the fact that, when a localization band is introduced, the relation between adjacent boundaries is disrupted and, a new one is established taking into account the localization band.

8.1 Future works

At the end of this manuscript, some suggestions for future work are given.

Paralellization of the *CMSP* code

With the level of depth and development achieved in the present work in terms of formulation and numerical implementation, it will be now possible to characterize complex materials taking into account its microstructure for elastic and hardening regimes. In particular, it will be possible to predict and understand the macroscopic behaviour of

the material as a function of the microstructure considered. Nevertheless, although the numerical tools introduced in Chapter 4 have dramatically reduced the CPU time for solving coupled multi-scale problems, the parallelization of ***CMSP*** is still vital. This parallelization coupled with *Line Search* and *Arc-Length* approaches will really increase the speed of ***CMSP*** code.

Being more specific about the parallelization framework, the author suggests that it should be performed at the macroscopic element level. Thus, for each core available on the desktop, or cluster, the whole information concerned to each element (i.e. number of integration *Gauss* points and information linked to each point, nodal displacement of the macroscopic element) is sent for a single CPU (core). Note that, conversely with standard finite element codes where the main computational cost is inevitably associated with the solution of the system of equations, which defines the equilibrium problem of the structure, in this case, the critical feature in terms of CPU time is related to the macroscopic *stress-update*, which solves for each macroscopic integration *Gauss* point the associated micro-equilibrium problem.

Improve the non-local method of integral type at the macro-scale

Despite some positive indications obtained with the non-local approach of integral type at the macro-scale (Chapter 6), it is still necessary to further investigate how a non-local macroscopic deformation gradient should be defined in order to simultaneously guarantee the minimization of the mesh dependence pathology verified at this scale domain and the elimination of spurious effects. A possible solution may be the selective usage of the volumetric and isochoric components of the macroscopic deformation gradient to define the non-local variable.

Conclusion of the implementation of the new concept of Periodic boundary condition

In Chapter 7, only the main foundations of the new concept of *Periodic* boundary condition that is able to tackle the presence of a localization band (or discontinuity) were introduced and, therefore, a significant amount of work should be carried out in order to complete the concept. In what follows, the more urgent tasks to finalise this new kinematical enforcement are listed:

- Perform the condensation of the system of equations which establishes the equilibrium of the RVE for all possible localization band shapes. This task is critical in order to obtain a well-posed system of equations. Note that , this approach is

only valid when the nodes which define the localization band belong to more than two sub-domains;

- Implement an algorithm that is able to automatically detect and define the presence of a localization band considering, for example, the critical value of an internal variable (i.e. accumulated plastic strain or internal damage). Different methodologies may be used however, image analysis that considers the contour map of a specific variable may be a suitable solution.
- Try to validate the new concept if possible with experimental data.

In addition to these three suggestion, others may be pointed out such as

- Enhance the new concept of Periodicity with the capacity of tackle the evolution of the localization band. A possible solution consists in the introduction of X-FEM and PUM methods.
- Implement the new concept into ***CMSP***. For this purpose, as pointed out in Chapter 7, it is necessary to enhance the transition between macro and micro domains and vice-versa.
- Extend the framework to three-dimensional analysis.

Three-dimensional implementation of *CMSP*

As a final suggestion, a three-dimensional version of ***CMSP*** is highly desirable. With this version it would be possible to automatically generate RVEs based on three-dimensional images obtained from image analysis of complex materials (i.e. X-Ray technology). Part of this work has already been carried out being only necessary to extend the algorithm used at the macro-scale domain. At this level, particular attention should be given to the construction of the consistent material tangent operator required to obtain perfect quadratic convergence rates of the *Newton-Raphson* at this scale.

Appendix A

Consistent tangent operators for *First-Order Coupled Multi-Scale Models*

A.1 Microscopic solution problem for different boundary conditions

Linear Boundary Condition

The *Linear* boundary condition imposes that all nodes on the edges of the RVE are prescribed. Thus, for this particular case, Equation (3.27) is defined as:

$$\widetilde{\boldsymbol{u}}\,\{\boldsymbol{y}\}^T = \left\{\ \widetilde{\boldsymbol{u}}^f\ \vdots\ \mathbf{0}\ \vdots\ \mathbf{0}\ \vdots\ \mathbf{0}\ \right\}^T. \tag{A.1}$$

Due to the prescription of all degrees of freedom at the boundary of the RVE, Equation (3.31) can be significantly simplified, resulting:

$$\left[\boldsymbol{k}^{ff}\right]_{n+1}^{(j)} \left\{\delta\widetilde{\boldsymbol{u}}^f\right\}^{(j+1)} = \left\{-\boldsymbol{f}^f\right\}_{n+1}^{(j)}. \tag{A.2}$$

Periodic Boundary Condition

According to the definition of a periodic displacement fluctuation field at the boundary of the RVE (Equation (3.13)) the decomposition of the total displacement fluctuation

field can be carried out in the following fashion:

$$\begin{aligned}\widetilde{\boldsymbol{u}}\{\boldsymbol{y}\}^T &= \left\{ \begin{array}{c:c:c:c} \widetilde{\boldsymbol{u}}^f & \widetilde{\boldsymbol{u}}^i & \widetilde{\boldsymbol{u}}^d & \widetilde{\boldsymbol{u}}^p \end{array} \right\}^T, \\ &= \left\{ \begin{array}{c:c:c:c} \widetilde{\boldsymbol{u}}^f & \widetilde{\boldsymbol{u}}^+ & \widetilde{\boldsymbol{u}}^- & \boldsymbol{0} \end{array} \right\}^T.\end{aligned} \tag{A.3}$$

Since $\{\widetilde{\boldsymbol{u}}^+\} = \{\widetilde{\boldsymbol{u}}^-\}$, we conclude that the dependency matrix is an identity matrix. Taking into account that $\boldsymbol{\alpha} = \boldsymbol{I}$ as well as Equation (A.3), we finally obtain the equation system which governs the equilibrium problem at the micro-scale for *Periodic* boundary condition:

$$\begin{aligned}&\left[\begin{array}{c:c} \boldsymbol{k}^{ff} & \boldsymbol{k}^{f+} + \boldsymbol{k}^{f-} \\ \hdashline \boldsymbol{k}^{+f} + \boldsymbol{k}^{-f} & \boldsymbol{k}^{++} + \boldsymbol{k}^{-+} + \boldsymbol{k}^{+-} + \boldsymbol{k}^{--} \end{array} \right]_{n+1}^{(j)} \left\{ \begin{array}{c} \delta\widetilde{\boldsymbol{u}}^f \\ \hdashline \delta\widetilde{\boldsymbol{u}}^+ \end{array} \right\}^{(j+1)} = \\ &- \left\{ \begin{array}{c} \boldsymbol{f}^f \\ \hdashline \boldsymbol{f}^+ + \boldsymbol{f}^- \end{array} \right\}_{n+1}^{(j)}.\end{aligned} \tag{A.4}$$

Remark A.1. In order to avoid rigid body displacements and rotations, it is necessary to add additional artificial constraints. One possible solution consists in fixing one corner of the RVE plus an additional degree of freedom of any other corner. However, as a consequence of the *Periodic* assumption, all corners are, in practice, completely prescribed. For this reason, and in order to simplify the numerical implementation, all corners of a square RVE are completely fixed. Note that this manipulation is still valid within the *Periodic* boundary hypothesis.

Uniform Traction Condition

As previously stressed out in Section 3.2.6.3, *Uniform Traction* condition is defined by Equation (3.5) which is here recovered for convenience:

$$\int_{\partial\Omega_0} \widetilde{\boldsymbol{u}}\{\boldsymbol{y}, t\} \otimes \boldsymbol{N}\{\boldsymbol{Y}\}\, dA = \boldsymbol{0}. \tag{A.5}$$

The discretized version of previous kinematical constraint is given in matrix format by the following expression

$$\boldsymbol{C}\widetilde{\boldsymbol{u}}^b = \boldsymbol{0}, \tag{A.6}$$

where $\boldsymbol{C}$ is the *constraint matrix* of the degrees of freedom over the boundary of the RVE. In three-dimensional problems, matrix $\boldsymbol{C}$ assumes the form

$$\boldsymbol{C} = \left[\begin{array}{ccc:ccc:c:ccc}
\int N_1\boldsymbol{N}_1 dA & 0 & 0 & \int N_2\boldsymbol{N}_1 dA & 0 & 0 & ... & \int N_n\boldsymbol{N}_1 dA & 0 & 0 \\
0 & \int N_1\boldsymbol{N}_2 dA & 0 & 0 & \int N_2\boldsymbol{N}_2 dA & 0 & ... & 0 & \int N_n\boldsymbol{N}_2 dA & 0 \\
0 & 0 & \int N_1\boldsymbol{N}_3 dA & 0 & 0 & \int N_2\boldsymbol{N}_3 dA & ... & 0 & 0 & \int N_n\boldsymbol{N}_3 dA \\
\int N_1\boldsymbol{N}_2 dA & 0 & 0 & \int N_2\boldsymbol{N}_2 dA & 0 & 0 & ... & \int N_n\boldsymbol{N}_2 dA & 0 & 0 \\
\int N_1\boldsymbol{N}_3 dA & 0 & 0 & \int N_2\boldsymbol{N}_3 dA & 0 & 0 & ... & \int N_n\boldsymbol{N}_3 dA & 0 & 0 \\
0 & \int N_1\boldsymbol{N}_1 dA & 0 & 0 & \int N_2\boldsymbol{N}_1 dA & 0 & ... & 0 & \int N_n\boldsymbol{N}_1 dA & 0 \\
0 & \int N_1\boldsymbol{N}_3 dA & 0 & 0 & \int N_2\boldsymbol{N}_3 dA & 0 & ... & 0 & \int N_n\boldsymbol{N}_3 dA & 0 \\
0 & 0 & \int N_1\boldsymbol{N}_1 dA & 0 & 0 & \int N_2\boldsymbol{N}_1 dA & ... & 0 & 0 & \int N_n\boldsymbol{N}_1 dA \\
0 & 0 & \int N_1\boldsymbol{N}_2 dA & 0 & 0 & \int N_2\boldsymbol{N}_2 dA & ... & 0 & 0 & \int N_n\boldsymbol{N}_2 dA
\end{array}\right], \tag{A.7}$$

and, in case of two-dimensional problems:

$$\boldsymbol{C} = \left[\begin{array}{cc:cc:c:cc}
\int N_1\boldsymbol{N}_1 dA & 0 & \int N_2\boldsymbol{N}_1 dA & 0 & ... & \int N_n\boldsymbol{N}_1 dA & 0 \\
0 & \int N_1\boldsymbol{N}_2 dA & 0 & \int N_2\boldsymbol{N}_2 dA & ... & 0 & \int N_n\boldsymbol{N}_2 dA \\
\int N_1\boldsymbol{N}_2 dA & 0 & \int N_2\boldsymbol{N}_2 dA & 0 & ... & \int N_n\boldsymbol{N}_2 dA & 0 \\
0 & \int N_1\boldsymbol{N}_1 dA & 0 & \int N_2\boldsymbol{N}_1 dA & ... & 0 & \int N_n\boldsymbol{N}_1 dA
\end{array}\right]. \tag{A.8}$$

In the previous two expressions, N_i denotes the $i-th$ shape function and $\boldsymbol{N}_i$ is the $i-th$ direction of the outward unit vector $\boldsymbol{N}$, normal to the boundary $\partial\Omega_0$.

Remark A.2. Within the finite element framework, the global constraint matrix $\boldsymbol{C}$ results from the assembly procedure of each element constraint matrix, $\boldsymbol{C}^e$

$$\boldsymbol{C} = \bigcup_{i=1}^{n_{elem}} \boldsymbol{C}_i^e,$$

where $\bigcup$ denotes a suitable *assembly* operator.

Considering the decomposition proposed for the fluctuation displacement field in Section (3.3.2.2), where the displacement at the boundary of the RVE were divided into *independent*, $\widetilde{\boldsymbol{u}}^i$, *dependent*, $\widetilde{\boldsymbol{u}}^d$, and *prescribed*, $\widetilde{\boldsymbol{u}}^p$ and applying the same decomposition to matrix $\boldsymbol{C}$, Equation (A.6) may be we-written into the following fashion

$$\left[\begin{array}{c:c:c} \boldsymbol{C}^i & \boldsymbol{C}^d & \boldsymbol{C}^p \end{array}\right] \left\{\begin{array}{c} \widetilde{\boldsymbol{u}}^i \\ \widetilde{\boldsymbol{u}}^d \\ \widetilde{\boldsymbol{u}}^p \end{array}\right\} = \boldsymbol{0}. \tag{A.9}$$

Since $\widetilde{\boldsymbol{u}}^p = \boldsymbol{0}$, after a basic algebra manipulation we finally arrive to a closed expression for α matrix when *Uniform Traction* boundary condition is prescribed

$$\boldsymbol{\alpha} = -\left[\boldsymbol{C}^d\right]^{-1} \boldsymbol{C}^f. \tag{A.10}$$

Remark A.3. The dependent degrees of freedom should be selected in order to guarantee that matrix $\boldsymbol{C}^d$ is invertible. In case of a square RVE (two-dimensional problem), it is possible to consider the degrees of freedom of two corners.

A.2 Derivation of the discretized homogenized material tangent modulus

The *Condensation* method starts from the basic definition of the consistent matrix, which is given by the differentiation of the *First Piola-Kirchhoff* stress tensor with regard to the macroscopic deformation gradient:

$$\begin{aligned} \mathbf{A}_{n+1}\{\boldsymbol{x}\} &= \frac{\partial \boldsymbol{P}_{n+1}\{\boldsymbol{x}\}}{\partial \boldsymbol{F}_{n+1}\{\boldsymbol{x}\}} \\ &= \frac{\partial}{\partial \boldsymbol{F}_{n+1}\{\boldsymbol{x}\}}\left(\frac{1}{V_0}\mathbb{D}_b \mathbb{F}_{b_{n+1}}^{int}\right) = \frac{1}{V_0}\mathbb{D}_b \frac{\partial \mathbb{F}_{b_{n+1}}^{int}}{\partial \boldsymbol{F}_{n+1}\{\boldsymbol{x}\}}. \end{aligned} \tag{A.11}$$

According to the variational formulation introduced in Section 3.2, the set of internal forces at the boundary of the RVE are dependent on the displacement field at the fine-scale. In addition, the microscopic displacement is additively composed by two

parts: the former is linear with the macroscopic deformation gradient and the latter is the fluctuation displacement field, which is a consequence of the boundary constraint selected as well as the discretization performed inside the RVE.

Remark A.4. In what follows, the notation related with the time/pseudo-time will be omitted for sake of simplicity since all parameters and variables are defined at the same instant t_{n+1}.

At the fine-scale domain, the total displacement field may be characterized by:

$$\boldsymbol{u}\left\{\boldsymbol{y}\right\} = \mathbb{D}^T\left(\boldsymbol{F}\left\{\boldsymbol{x}\right\} - \boldsymbol{I}\right) + \widetilde{\boldsymbol{u}}\left\{\boldsymbol{y}\right\}, \tag{A.12}$$

where $\mathbb{D}$ is the total nodal coordinate matrix. Extrapolating this result for all sub-sets, which compose the global microscopic displacement $\boldsymbol{u}\left\{\boldsymbol{y}\right\}$, one can write:

$$\boldsymbol{u}\left\{\boldsymbol{y}\right\} = \begin{bmatrix} \mathbb{D}^{f^T}\left(\boldsymbol{F}\left\{\boldsymbol{x}\right\} - \boldsymbol{I}\right) + \widetilde{\boldsymbol{u}}^f \\ \mathbb{D}^{i^T}\left(\boldsymbol{F}\left\{\boldsymbol{x}\right\} - \boldsymbol{I}\right) + \widetilde{\boldsymbol{u}}^i \\ \mathbb{D}^{d^T}\left(\boldsymbol{F}\left\{\boldsymbol{x}\right\} - \boldsymbol{I}\right) + \widetilde{\boldsymbol{u}}^d \\ \mathbb{D}^{p^T}\left(\boldsymbol{F}\left\{\boldsymbol{x}\right\} - \boldsymbol{I}\right) \end{bmatrix} = \begin{bmatrix} \mathbb{D}^{f^T}\left(\boldsymbol{F}\left\{\boldsymbol{x}\right\} - \boldsymbol{I}\right) + \widetilde{\boldsymbol{u}}^f \\ \mathbb{D}^{i^T}\left(\boldsymbol{F}\left\{\boldsymbol{x}\right\} - \boldsymbol{I}\right) + \widetilde{\boldsymbol{u}}^i \\ \mathbb{D}^{d^T}\left(\boldsymbol{F}\left\{\boldsymbol{x}\right\} - \boldsymbol{I}\right) + \boldsymbol{\alpha}\widetilde{\boldsymbol{u}}^i \\ \mathbb{D}^{p^T}\left(\boldsymbol{F}\left\{\boldsymbol{x}\right\} - \boldsymbol{I}\right) \end{bmatrix}. \tag{A.13}$$

With this decomposition of the microscopic displacement field and the internal force vector (Equations (3.27) and (3.29)) at hand and using the chain rule, Equation (A.11) can be re-written as:

$$\begin{aligned} \mathbf{A}\left\{\boldsymbol{x}\right\} &= \frac{\partial \boldsymbol{P}\left\{\boldsymbol{x}\right\}}{\partial \boldsymbol{F}\left\{\boldsymbol{x}\right\}} \\ &= \frac{1}{V_0}\mathbb{D}_b\left[\frac{\partial \mathbb{F}_b^{int}}{\partial \boldsymbol{u}^f\left\{\boldsymbol{y}\right\}}\frac{\partial \boldsymbol{u}^f\left\{\boldsymbol{y}\right\}}{\partial \boldsymbol{F}\left\{\boldsymbol{x}\right\}} + \frac{\partial \mathbb{F}_b^{int}}{\partial \boldsymbol{u}^i\left\{\boldsymbol{y}\right\}}\frac{\partial \boldsymbol{u}^i\left\{\boldsymbol{y}\right\}}{\partial \boldsymbol{F}\left\{\boldsymbol{x}\right\}} + \frac{\partial \mathbb{F}_b^{int}}{\partial \boldsymbol{u}^d\left\{\boldsymbol{y}\right\}}\frac{\partial \boldsymbol{u}^d\left\{\boldsymbol{y}\right\}}{\partial \boldsymbol{F}\left\{\boldsymbol{x}\right\}} + \frac{\partial \mathbb{F}_b^{int}}{\partial \boldsymbol{u}^p\left\{\boldsymbol{y}\right\}}\frac{\partial \boldsymbol{u}^p\left\{\boldsymbol{y}\right\}}{\partial \boldsymbol{F}\left\{\boldsymbol{x}\right\}}\right] \\ &= \frac{1}{V_0}\mathbb{D}_b\left[\frac{\partial \mathbb{F}_b^{int}}{\partial \boldsymbol{u}^f\left\{\boldsymbol{y}\right\}}\left(\mathbb{D}^{f^T} + \frac{\partial \widetilde{\boldsymbol{u}}^f}{\partial \boldsymbol{F}\left\{\boldsymbol{x}\right\}}\right) + \frac{\partial \mathbb{F}_b^{int}}{\partial \boldsymbol{u}^i\left\{\boldsymbol{y}\right\}}\left(\mathbb{D}^{i^T} + \frac{\partial \widetilde{\boldsymbol{u}}^i}{\partial \boldsymbol{F}\left\{\boldsymbol{x}\right\}}\right)\right. \\ &\quad \left. + \frac{\partial \mathbb{F}_b^{int}}{\partial \boldsymbol{u}^d\left\{\boldsymbol{y}\right\}}\left(\mathbb{D}^{d^T} + \boldsymbol{\alpha}\frac{\partial \widetilde{\boldsymbol{u}}^i}{\partial \boldsymbol{F}\left\{\boldsymbol{x}\right\}}\right) + \frac{\partial \mathbb{F}_b^{int}}{\partial \boldsymbol{u}^p\left\{\boldsymbol{y}\right\}}\mathbb{D}^{p^T}\right]. \end{aligned} \tag{A.14}$$

The derivatives of the internal forces over the boundary of the RVE, $\mathbb{F}_b^{int}$, with regard to the different sub-sets of the fluctuation displacement field are, by definition, sub-matrices of the global microscopic stiffness matrix:

$$\frac{\partial \mathbb{F}_b^{int}}{\partial \boldsymbol{u}^f\left\{\boldsymbol{y}\right\}} = \boldsymbol{k}^{bf}, \tag{A.15a}$$

$$\frac{\partial \mathbb{F}_b^{int}}{\partial \boldsymbol{u}^i\left\{\boldsymbol{y}\right\}} = \boldsymbol{k}^{bi}, \tag{A.15b}$$

$$\frac{\partial \mathbb{F}_b^{int}}{\partial \boldsymbol{u}^d\left\{\boldsymbol{y}\right\}} = \boldsymbol{k}^{bd}, \tag{A.15c}$$

$$\frac{\partial \mathbb{F}_b^{int}}{\partial \boldsymbol{u}^p\{\boldsymbol{y}\}} = \boldsymbol{k}^{bp}. \tag{A.15d}$$

Thus, after straightforward algebraic manipulations, Equation (A.14) may be rewritten:

$$\begin{aligned}\mathbf{A}\{\boldsymbol{x}\} &= \frac{1}{V_0}\mathbb{D}_b\left[\boldsymbol{k}^{bf}\frac{\partial \widetilde{\boldsymbol{u}}^f}{\partial \boldsymbol{F}\{\boldsymbol{x}\}} + \boldsymbol{k}^{bi}\frac{\partial \widetilde{\boldsymbol{u}}^i}{\partial \boldsymbol{F}\{\boldsymbol{x}\}} + \boldsymbol{k}^{bd}\boldsymbol{\alpha}\frac{\partial \widetilde{\boldsymbol{u}}^i}{\partial \boldsymbol{F}\{\boldsymbol{x}\}} + \boldsymbol{K}^b\mathbb{D}_{Total}^T\right] \\ &= \frac{1}{V_0}\mathbb{D}_b\left[\begin{bmatrix}\boldsymbol{k}^{bf} \\ \boldsymbol{k}^{bi} + \boldsymbol{k}^{bd}\boldsymbol{\alpha}\end{bmatrix}^T \begin{Bmatrix}\frac{\partial \widetilde{\boldsymbol{u}}^f}{\partial \boldsymbol{F}\{\boldsymbol{x}\}} \\ \frac{\partial \widetilde{\boldsymbol{u}}^i}{\partial \boldsymbol{F}\{\boldsymbol{x}\}}\end{Bmatrix} + \left[\boldsymbol{K}^B\right]\left[\mathbb{D}_{Total}\right]^T\right],\end{aligned} \tag{A.16}$$

where $\boldsymbol{K}^B$ is defined by

$$\boldsymbol{K}^B = \left[\begin{array}{c:c:c:c} \left[\boldsymbol{k}^{bf}\right] & \left[\boldsymbol{k}^{bi}\right] & \left[\boldsymbol{k}^{bd}\right] & \left[\boldsymbol{k}^{bp}\right] \end{array}\right], \tag{A.17}$$

and $\mathbb{D}_{Total}$ is the total reference nodal coordinate matrix of the RVE:

$$\mathbb{D}_{Total} = \left[\begin{array}{c:c:c:c} \left[\mathbb{D}^f\right] & \left[\mathbb{D}^i\right] & \left[\mathbb{D}^d\right] & \left[\mathbb{D}^p\right] \end{array}\right]. \tag{A.18}$$

In order to conclude this process, it is necessary to compute the partial derivatives $\partial \widetilde{\boldsymbol{u}}^f / \partial \boldsymbol{F}\{\boldsymbol{x}\}$ and $\partial \widetilde{\boldsymbol{u}}^i / \partial \boldsymbol{F}\{\boldsymbol{x}\}$. When the equilibrium of the RVE is satisfied, by definition, we have

$$\left\{\begin{array}{c} \frac{\partial \mathbb{F}_f^{int}}{\partial \boldsymbol{F}\{\boldsymbol{x}\}} \\ \hdashline \frac{\partial \mathbb{F}_i^{int}}{\partial \boldsymbol{F}\{\boldsymbol{x}\}} + \boldsymbol{\alpha}^T\frac{\partial \mathbb{F}_d^{int}}{\partial \boldsymbol{F}\{\boldsymbol{x}\}} \end{array}\right\} = \{\boldsymbol{0}\}. \tag{A.19}$$

Therefore, following the same procedure, it is possible to find out a closed-form to compute the missing relations.

$$\begin{aligned}\frac{\partial \mathbb{F}_f^{int}}{\partial \boldsymbol{F}\{\boldsymbol{x}\}} &= \frac{\partial \mathbb{F}_f^{int}}{\partial \boldsymbol{u}^f\{\boldsymbol{y}\}}\left(\mathbb{D}^f + \frac{\partial \widetilde{\boldsymbol{u}}^f\{\boldsymbol{y}\}}{\partial \boldsymbol{F}\{\boldsymbol{x}\}}\right) + \frac{\partial \mathbb{F}_f^{int}}{\partial \boldsymbol{u}^i\{\boldsymbol{y}\}}\left(\mathbb{D}^i + \frac{\partial \widetilde{\boldsymbol{u}}^i\{\boldsymbol{y}\}}{\partial \boldsymbol{F}\{\boldsymbol{x}\}}\right) \\ &+ \frac{\partial \mathbb{F}_f^{int}}{\partial \boldsymbol{u}^d\{\boldsymbol{y}\}}\left(\mathbb{D}^d + \boldsymbol{\alpha}\frac{\partial \widetilde{\boldsymbol{u}}^i\{\boldsymbol{y}\}}{\partial \boldsymbol{F}\{\boldsymbol{x}\}}\right) + \frac{\partial \mathbb{F}_f^{int}}{\partial \boldsymbol{u}^p\{\boldsymbol{y}\}}\mathbb{D}^p \\ &= \boldsymbol{k}^{ff}\left(\mathbb{D}^f + \frac{\partial \widetilde{\boldsymbol{u}}^f\{\boldsymbol{y}\}}{\partial \boldsymbol{F}\{\boldsymbol{x}\}}\right) + \boldsymbol{k}^{fi}\left(\mathbb{D}^i + \frac{\partial \widetilde{\boldsymbol{u}}^i\{\boldsymbol{y}\}}{\partial \boldsymbol{F}\{\boldsymbol{x}\}}\right) \\ &+ \boldsymbol{k}^{fd}\left(\mathbb{D}^d + \boldsymbol{\alpha}\frac{\partial \widetilde{\boldsymbol{u}}^i\{\boldsymbol{y}\}}{\partial \boldsymbol{F}\{\boldsymbol{x}\}}\right) + \boldsymbol{k}^{fp}\mathbb{D}^p\end{aligned} \tag{A.20}$$

$$\begin{aligned}\frac{\partial \mathbb{F}_i^{int}}{\partial \boldsymbol{F}\{\boldsymbol{x}\}} &= \frac{\partial \mathbb{F}_i^{int}}{\partial \boldsymbol{u}^f\{\boldsymbol{y}\}}\left(\mathbb{D}^f + \frac{\partial \widetilde{\boldsymbol{u}}^f\{\boldsymbol{y}\}}{\partial \boldsymbol{F}\{\boldsymbol{x}\}}\right) + \frac{\partial \mathbb{F}_i^{int}}{\partial \boldsymbol{u}^i\{\boldsymbol{y}\}}\left(\mathbb{D}^i + \frac{\partial \widetilde{\boldsymbol{u}}^i\{\boldsymbol{y}\}}{\partial \boldsymbol{F}\{\boldsymbol{x}\}}\right) \\ &+ \frac{\partial \mathbb{F}_i^{int}}{\partial \boldsymbol{u}^d\{\boldsymbol{y}\}}\left(\mathbb{D}^d + \boldsymbol{\alpha}\frac{\partial \widetilde{\boldsymbol{u}}^i\{\boldsymbol{y}\}}{\partial \boldsymbol{F}\{\boldsymbol{x}\}}\right) + \frac{\partial \mathbb{F}_i^{int}}{\partial \boldsymbol{u}^p\{\boldsymbol{y}\}}\mathbb{D}^p \\ &= \boldsymbol{k}^{if}\left(\mathbb{D}^f + \frac{\partial \widetilde{\boldsymbol{u}}^f\{\boldsymbol{y}\}}{\partial \boldsymbol{F}\{\boldsymbol{x}\}}\right) + \boldsymbol{k}^{ii}\left(\mathbb{D}^i + \frac{\partial \widetilde{\boldsymbol{u}}^i\{\boldsymbol{y}\}}{\partial \boldsymbol{F}\{\boldsymbol{x}\}}\right) \\ &+ \boldsymbol{k}^{id}\left(\mathbb{D}^d + \boldsymbol{\alpha}\frac{\partial \widetilde{\boldsymbol{u}}^i\{\boldsymbol{y}\}}{\partial \boldsymbol{F}\{\boldsymbol{x}\}}\right) + \boldsymbol{k}^{ip}\mathbb{D}^p\end{aligned} \tag{A.21}$$

$$\begin{aligned}\boldsymbol{\alpha}^T\frac{\partial \mathbb{F}_d^{int}}{\partial \boldsymbol{F}\{\boldsymbol{x}\}} &= \boldsymbol{\alpha}^T\frac{\partial \mathbb{F}_d^{int}}{\partial \boldsymbol{u}^f\{\boldsymbol{y}\}}\left(\mathbb{D}^f+\frac{\partial \widetilde{\boldsymbol{u}}^f\{\boldsymbol{y}\}}{\partial \boldsymbol{F}\{\boldsymbol{x}\}}\right)+\boldsymbol{\alpha}^T\frac{\partial \mathbb{F}_d^{int}}{\partial \boldsymbol{u}^i\{\boldsymbol{y}\}}\left(\mathbb{D}^i+\boldsymbol{\alpha}^T\frac{\partial \widetilde{\boldsymbol{u}}^i\{\boldsymbol{y}\}}{\partial \boldsymbol{F}\{\boldsymbol{x}\}}\right)\\ &+\boldsymbol{\alpha}^T\frac{\partial \mathbb{F}_d^{int}}{\partial \boldsymbol{u}^d\{\boldsymbol{y}\}}\left(\mathbb{D}^d+\boldsymbol{\alpha}\frac{\partial \widetilde{\boldsymbol{u}}^i\{\boldsymbol{y}\}}{\partial \boldsymbol{F}\{\boldsymbol{x}\}}\right)+\boldsymbol{\alpha}^T\frac{\partial \mathbb{F}_d^{int}}{\partial \boldsymbol{u}^p\{\boldsymbol{y}\}}\mathbb{D}^p\\ &=\boldsymbol{\alpha}^T\boldsymbol{k}^{df}\left(\mathbb{D}^f+\frac{\partial \widetilde{\boldsymbol{u}}^f\{\boldsymbol{y}\}}{\partial \boldsymbol{F}\{\boldsymbol{x}\}}\right)+\boldsymbol{\alpha}^T\boldsymbol{k}^{di}\left(\mathbb{D}^i+\frac{\partial \widetilde{\boldsymbol{u}}^i\{\boldsymbol{y}\}}{\partial \boldsymbol{F}\{\boldsymbol{x}\}}\right)\\ &+\boldsymbol{\alpha}^T\boldsymbol{k}^{dd}\left(\mathbb{D}^d+\boldsymbol{\alpha}\frac{\partial \widetilde{\boldsymbol{u}}^i\{\boldsymbol{y}\}}{\partial \boldsymbol{F}\{\boldsymbol{x}\}}\right)+\boldsymbol{\alpha}^T\boldsymbol{k}^{dp}\mathbb{D}^p\end{aligned} \tag{A.22}$$

Finally, after a rearrangement of the previous equations we obtain a system of equations that allow us to compute the terms $\frac{\partial \widetilde{\boldsymbol{u}}^f}{\partial \boldsymbol{F}\{\boldsymbol{x}\}}$ and $\frac{\partial \widetilde{\boldsymbol{u}}^i}{\partial \boldsymbol{F}\{\boldsymbol{x}\}}$:

$$\begin{aligned}&\left[\begin{array}{c:c}\boldsymbol{k}^{ff} & \boldsymbol{k}^{fi}+\boldsymbol{k}^{fd}\boldsymbol{\alpha}\\ \hdashline \boldsymbol{k}^{if}+\boldsymbol{\alpha}^T\boldsymbol{k}^{df} & \boldsymbol{k}^{ii}+\boldsymbol{k}^{id}\boldsymbol{\alpha}+\boldsymbol{\alpha}^T\boldsymbol{k}^{di}+\boldsymbol{\alpha}^T\boldsymbol{k}^{dd}\boldsymbol{\alpha}\end{array}\right]\left\{\begin{array}{c}\frac{\partial \widetilde{\boldsymbol{u}}^f}{\partial \boldsymbol{F}\{\boldsymbol{x}\}}\\ \frac{\partial \widetilde{\boldsymbol{u}}^i}{\partial \boldsymbol{F}\{\boldsymbol{x}\}}\end{array}\right\}=\\ &-\left[\begin{array}{c:c}\left[\boldsymbol{K}^{\boldsymbol{f}}\right] & \\ \hdashline \left[\boldsymbol{K}^{\boldsymbol{i}}\right]+\boldsymbol{\alpha}^T\left[\boldsymbol{K}^{\boldsymbol{d}}\right] & \end{array}\right]\cdot\left[\mathbb{D}^{Total}\right]^T,\end{aligned} \tag{A.23}$$

where the matrices $\boldsymbol{K}^f$, $\boldsymbol{K}^i$ and $\boldsymbol{K}^d$ are respectively defined by:

$$\boldsymbol{K}^f=\left[\begin{array}{c:c:c:c}\left[\boldsymbol{k}^{ff}\right] & \left[\boldsymbol{k}^{fi}\right] & \left[\boldsymbol{k}^{fd}\right] & \left[\boldsymbol{k}^{fp}\right]\end{array}\right], \tag{A.24a}$$

$$\boldsymbol{K}^i=\left[\begin{array}{c:c:c:c}\left[\boldsymbol{k}^{if}\right] & \left[\boldsymbol{k}^{ii}\right] & \left[\boldsymbol{k}^{id}\right] & \left[\boldsymbol{k}^{ip}\right]\end{array}\right], \tag{A.24b}$$

$$\boldsymbol{K}^d=\left[\begin{array}{c:c:c:c}\left[\boldsymbol{k}^{df}\right] & \left[\boldsymbol{k}^{di}\right] & \left[\boldsymbol{k}^{dd}\right] & \left[\boldsymbol{k}^{dp}\right]\end{array}\right]. \tag{A.24c}$$

Linear Boundary Condition

With the RVE in equilibrium and for *Linear Boundary Condition*, the *macroscopic tangent modulus* may be computed by the following expression

$$\mathbf{A}\{\boldsymbol{x}\}=\frac{1}{V_0}\mathbb{D}_b\left[\left[\begin{array}{c}\boldsymbol{k}^{bf}\end{array}\right]\left\{\begin{array}{c}\frac{\partial \widetilde{\boldsymbol{u}}^f}{\partial \boldsymbol{F}\{\boldsymbol{x}\}}\end{array}\right\}+\left[\boldsymbol{K}^B\right]\left[\mathbb{D}_{Total}\right]^T\right], \tag{A.25}$$

where the derivative $\frac{\partial \widetilde{\boldsymbol{u}}^f}{\partial \boldsymbol{F}\{\boldsymbol{x}\}}$ is computed by solving following equation system

$$\left[\begin{array}{c}\boldsymbol{k}^{ff}\end{array}\right]\left\{\begin{array}{c}\frac{\partial \widetilde{\boldsymbol{u}}^f}{\partial \boldsymbol{F}\{\boldsymbol{x}\}}\end{array}\right\}=-\left[\boldsymbol{K}^f\right]\left[\mathbb{D}_{Total}\right]^T. \tag{A.26}$$

Periodic Boundary Condition

With the RVE in equilibrium and for *Periodic Boundary Condition*, the *macroscopic tangent modulus* may be computed by the following expression

$$\mathbf{A}\{\boldsymbol{x}\}=\frac{1}{V_0}\mathbb{D}_b\left[\left[\begin{array}{c}\boldsymbol{k}^{bf}\\ \boldsymbol{k}^{b+}+\boldsymbol{k}^{b-}\end{array}\right]^T\left\{\begin{array}{c}\frac{\partial \widetilde{\boldsymbol{u}}^f}{\partial \boldsymbol{F}\{\boldsymbol{x}\}}\\ \frac{\partial \widetilde{\boldsymbol{u}}^+}{\partial \boldsymbol{F}\{\boldsymbol{x}\}}\end{array}\right\}+\left[\boldsymbol{K}^B\right]\left[\mathbb{D}_{Total}\right]^T\right], \tag{A.27}$$

where the derivatives $\frac{\partial \widetilde{\boldsymbol{u}}^f}{\partial \boldsymbol{F}\{\boldsymbol{x}\}}$ and $\frac{\partial \widetilde{\boldsymbol{u}}^+}{\partial \boldsymbol{F}\{\boldsymbol{x}\}}$ are computed by solving following equation system

$$\begin{aligned}&\left[\begin{array}{c|c} \boldsymbol{k}^{ff} & \boldsymbol{k}^{f+}+\boldsymbol{k}^{f-} \\ \hline \boldsymbol{k}^{+f}+\boldsymbol{k}^{-f} & \boldsymbol{k}^{++}+\boldsymbol{k}^{+-}+\boldsymbol{k}^{-+}+\boldsymbol{k}^{--} \end{array}\right]\left\{\begin{array}{c} \frac{\partial \widetilde{\boldsymbol{u}}^f}{\partial \boldsymbol{F}\{\boldsymbol{x}\}} \\ \frac{\partial \widetilde{\boldsymbol{u}}^+}{\partial \boldsymbol{F}\{\boldsymbol{x}\}} \end{array}\right\}= \\ &-\left[\begin{array}{c} \boldsymbol{K}^f \\ \hline \boldsymbol{K}^+ + \boldsymbol{K}^- \end{array}\right][\mathbb{D}_{Total}]^T\,.\end{aligned} \tag{A.28}$$

Appendix B

Tangent operators for the non-local approach

In this Appendix, the linearization of the weak equilibrium equations at both scales, micro and macro, enhanced with a non-local strategies of integral type will be described. In addition, the tangent moduli for the explicit damage model introduced in Section 6.3.6 will be also described. It is important to emphasize that within the context of implicit finite element codes, it is only possible to obtain quadratic rates of convergence with a correct linearization of the problem.

B.1 Definition of directional derivative

Before to proceed, it is mandatory to introduce the definition of directional derivative. In fact, from the mathematical point of view, the linearization of a problem consists in determining the directional derivative of a function which models it [166]. Considering a generic function

$$f\left(\boldsymbol{x}\right) = 0, \tag{B.1}$$

its linearisation with respect to the unknown $\boldsymbol{x}$ about an arbitrary argument $\boldsymbol{x}^*$ consists in finding the *directional* field $\boldsymbol{d}$ such that:

$$L_{x^*}\left(\boldsymbol{d}\right) = f\left(\boldsymbol{x}^*\right) + Df\left(\boldsymbol{x}^*\right).\boldsymbol{d} = 0, \tag{B.2}$$

where L is the linearised functional of equation f and

$$Df(\boldsymbol{x}^*).\boldsymbol{d} = \left.\frac{d}{d\varepsilon}\right|_{\varepsilon=0} f(\boldsymbol{x}^* + \varepsilon\boldsymbol{d}) \tag{B.3}$$

is the directional derivative of f at $\boldsymbol{x}^*$ in the direction $\boldsymbol{d}$.

B.2 Linearization of the weak equilibrium problem enhanced with a non-local strategy at the micro-scale

At the micro-scale, the weak equilibrium equation for the micro-scale problem enhanced with the non-local strategy of integral type is given by

$$G\left\{\boldsymbol{u}\left\{\boldsymbol{y},t\right\},\boldsymbol{\eta}\right\}=\int_{\Omega_0}\boldsymbol{P}\left\{\boldsymbol{F}\left\{\boldsymbol{\xi},t\right\}\right\}:\nabla_{\boldsymbol{p}}\boldsymbol{\eta}dV=0 \tag{B.4}$$

where $\boldsymbol{\xi}$ denotes the coordinate of points which affect the stress state of point with coordinate $\boldsymbol{y}$. In other words, $\boldsymbol{\xi}$ are inside to the non-local circumference with radius defined by the non-local length, L, and centred at point $\boldsymbol{y}$. In the limit case, when the non-local length parameter is equal to 0 the last expression recover the standard local weak equilibrium equation.

Remark B.1. For sake of simplicity, in this section, information about scale domain and time will be omitted. Note that all variables are defined at the micro-scale domain and defined at the same instant.

Considering the concept of directional derivative above defined, one can write

$$DG\left\{\boldsymbol{u},\boldsymbol{\eta}\right\}\left[\boldsymbol{d}\right]=\left.\frac{d}{d\varepsilon}\right|_{\varepsilon=0}\int_{\Omega_0}\boldsymbol{P}\left\{\boldsymbol{F}_{\varepsilon}\left\{\boldsymbol{\xi}\right\}\right\}:\nabla_{\boldsymbol{p}}\boldsymbol{\eta}dV, \tag{B.5}$$

where $\boldsymbol{F}_{\varepsilon}\left\{\boldsymbol{\xi}\right\}$ denotes the perturbed microscopic deformation gradient at point $\boldsymbol{\xi}$ defined by

$$\boldsymbol{F}_{\varepsilon}\left\{\boldsymbol{\xi}\right\}=\boldsymbol{I}+\nabla_{\boldsymbol{p}}\left(\boldsymbol{u}^*\left\{\boldsymbol{\xi}\right\}+\varepsilon\boldsymbol{d}\right)=\boldsymbol{F}^*\left\{\boldsymbol{\xi}\right\}+\varepsilon\nabla_{\boldsymbol{p}}\boldsymbol{d}. \tag{B.6}$$

Applying the chain rule, one can write

$$DG\left\{\boldsymbol{u},\boldsymbol{\eta}\right\}\left[\boldsymbol{d}\right]=\int_{\Omega_0}\mathbf{A}:\nabla_{\boldsymbol{p},\boldsymbol{\xi}}\boldsymbol{d}:\nabla_{\boldsymbol{p}}\boldsymbol{\eta}dV, \tag{B.7}$$

where $\mathbf{A}$ denotes the material tangent modulus (fourth-order tensor) defined by

$$\mathbf{A}=\frac{\partial\boldsymbol{P}}{\partial\boldsymbol{F}\left\{\boldsymbol{\xi}\right\}}. \tag{B.8}$$

B.2.1 Map the linearized expression to the spatial configuration

With the linearized expression of the weak equilibrium problem at the micro-scale enhanced with non-local strategy of integral type at the material configuration, it is necessary to map expression (B.7) to the spatial configuration. Introducing expressions (2.28b) and (2.29) into Equation B.7 results

$$DG\left\{\boldsymbol{u},\boldsymbol{\eta}\right\}\left[\boldsymbol{d}\right]=\int_{\varphi(\Omega_0)}\mathbf{a}:\nabla_{\boldsymbol{x},\boldsymbol{\xi}}\boldsymbol{d}:\nabla_{\boldsymbol{x}}\boldsymbol{\eta}dV \tag{B.9}$$

where $\mathbf{a}$ denotes the spatial tangent modulus, which is given by the following expression in *Einstein*'s notation:

$$a^{ijkl}=\frac{1}{\det\left(\boldsymbol{F}\right)}A^{imkn}F^{jm}F^{ln}_{\boldsymbol{\xi}}. \tag{B.10}$$

In the previous equation, the fourth-order tensor A^{imkn} is given by

$$A^{imkn}=\frac{P_{im}}{F_{kn}\left\{\boldsymbol{\xi}\right\}}. \tag{B.11}$$

Based on basic concepts of *Continuum Solid Mechanics*, the *First Piola-Kirchhoff* stress tensor, $\boldsymbol{P}$, can be re-written as function of the *Kirchhoff* stress tensor, $\boldsymbol{\tau}$

$$\boldsymbol{P}=\boldsymbol{\tau}\boldsymbol{F}^{-T}. \tag{B.12}$$

With this relation at hand, Equation (B.11) can be re-written as follows

$$\mathsf{A}^{imkn}=\frac{\partial}{\partial F_{kn}\left\{\boldsymbol{\xi}\right\}}\left[\tau^{ip}\left(F^{mp}\right)^{-1}\right] \tag{B.13}$$

Applying the chain rule to the previous equation, one can write

$$\mathsf{A}^{imkn}=\frac{\partial\tau^{ip}}{\partial F^{kn}\left\{\boldsymbol{\xi}\right\}}\left(F^{mp}\right)^{-1}+\tau^{ip}\frac{\partial\left(F^{mp}\right)^{-1}}{\partial F^{kn}\left\{\boldsymbol{\xi}\right\}}. \tag{B.14}$$

There are two possible results for the derivative of the last term of the right hand side on the previous equation. If point $\boldsymbol{\xi}=\boldsymbol{y}$ results [167]

$$\left.\frac{\partial\left(F^{mp}\right)^{-1}}{\partial F^{kn}\left\{\boldsymbol{\xi}\right\}}\right|_{\boldsymbol{y}=\boldsymbol{\xi}}=-\left(F^{mk}\right)^{-1}\left(F^{np}\right)^{-1}. \tag{B.15}$$

However, when $\boldsymbol{\xi}\neq\boldsymbol{y}$, the derivative is equal to zero.

Substituting the previous result into Equation (B.14) results

$$\mathsf{A}^{imkn} = \frac{\partial \tau^{ip}}{\partial F^{kn}\{\boldsymbol{\xi}\}} (F^{mp})^{-1} - \tau^{ip} \left(F^{mk}\right)^{-1} (F^{np})^{-1}\Big|_{\boldsymbol{y}=\boldsymbol{\xi}}. \tag{B.16}$$

Finally, the substitution of the previous result into Equation (B.10) and after some straightforward algebraic manipulation, we finally arrive to the spatial tangent modulus for the weak equilibrium problem enhanced with a non-local approach of integral-type:

$$\mathsf{a}^{ijkl} = \frac{1}{\det(\boldsymbol{F})} \frac{\partial \tau^{ij}}{\partial F^{km}\{\boldsymbol{\xi}\}} F^{lm}\{\boldsymbol{\xi}\} - \sigma^{ik}\delta^{jk}\Big|_{\boldsymbol{y}=\boldsymbol{\xi}}. \tag{B.17}$$

B.3 Tangent operator for the local explicit damage model

In the spirit of small strains theory, by definition, the consistent tangent operator is given by

$$\mathbf{D}^{ep}_{n+1} = \frac{\partial \boldsymbol{\sigma}_{n+1}}{\partial \boldsymbol{\varepsilon}^{e\,Trial}_{n+1}}, \tag{B.18}$$

where $\boldsymbol{\varepsilon}$ denotes the logarithmic deformation tensor at instant $t = t_{n+1}$. Applying this definition to the effective stress tensor $\boldsymbol{\sigma}^{*}_{n+1}$, Equation (6.7), results:

$$\begin{aligned} \mathbf{D}^{*}_{n+1} &= \frac{\partial \boldsymbol{\sigma}^{*}_{n+1}}{\partial \boldsymbol{\varepsilon}^{e\,Trial}_{n+1}} \\ &= (1 - D_{n+1})\,\mathbf{D}^{ep}_{n+1} - \boldsymbol{\sigma}_{n+1} \otimes \frac{\partial D_{n+1}}{\partial \boldsymbol{\varepsilon}^{e\,Trial}_{n+1}}. \end{aligned} \tag{B.19}$$

In the previous equation, $\mathbf{D}^{ep}$ denotes the consistent tangent operator intrinsic with the constitutive model coupled with the explicit damage law introduced in Section 6.3.6. Since the *von Mises* elasto-plastic constitutive model was considered, the elasto-plastic tangent operator of this model is given by [6]:

$$\begin{aligned} \mathbf{D}^{ep}_{n+1} = {} & 2G \left(1 - \frac{3G\Delta\gamma}{q^{Trial}_{n+1}}\right) \left(\mathsf{I} - \frac{1}{3}\boldsymbol{I} \otimes \boldsymbol{I}\right) \\ & + 6G^2 \left(\frac{\Delta\gamma}{q^{Trial}_{n+1}} - \frac{1}{3G + H}\right) \boldsymbol{N}_{n+1} \otimes \boldsymbol{N}_{n+1} + K\boldsymbol{I} \otimes \boldsymbol{I}, \end{aligned} \tag{B.20}$$

where

$$\boldsymbol{N}_{n+1} = \frac{\boldsymbol{s}^{Trial}_{n+1}}{\| \boldsymbol{s}^{Trial}_{n+1} \|}. \tag{B.21}$$

In Equation (B.20), parameters G and K corresponds to the shear and *Bulk* modulus of the material and H corresponds to the derivative of the hardening curve of the material in relation of the accumulated plastic strain.

The derivative of the damage variable, D_{n+1}, in relation to the the logarithmic elastic trial deformation tensor, $\boldsymbol{\varepsilon}_{n+1}^{e\,Trial}$, is given by:

$$\frac{\partial D_{n+1}}{\partial \boldsymbol{\varepsilon}_{n+1}^{e\,Trial}} = \frac{1}{\varepsilon_f} \frac{\partial \Delta\gamma}{\partial \boldsymbol{\varepsilon}_{n+1}^{e\,Trial}}. \tag{B.22}$$

As previously pointed out, the explicit damage model is coupled with the *von Mises* elasto-plastic model, and, therefore, the plastic multiplier, $\Delta\gamma$, is dependent on $\boldsymbol{\varepsilon}_{n+1}^{e\,Trial}$. Thus, it is possible to write:

$$\frac{\partial \Delta\gamma}{\partial \boldsymbol{\varepsilon}_{n+1}^{e\,Trial}} = -\left[\frac{\partial res_{\Delta\gamma}}{\partial \Delta\gamma}\right]^{-1} \frac{\partial res_{\Delta\gamma}}{\partial \boldsymbol{\varepsilon}_{n+1}^{e\,Trial}}, \tag{B.23}$$

where

$$res_{\Delta\gamma} = \sigma_{eq_{n+1}}^{Trial} - 3G\Delta\gamma - \sigma_y\left(\overline{\varepsilon}^p + \Delta\gamma\right), \tag{B.24}$$

and

$$\frac{\partial res_{\Delta\gamma}}{\partial \boldsymbol{\varepsilon}_{n+1}^{e\,Trial}} = \sqrt{\frac{3}{2}} \frac{2G}{\parallel \boldsymbol{\varepsilon}_{d_{n+1}}^{e\,Trial} \parallel} \boldsymbol{\varepsilon}_{d_{n+1}}^{e\,Trial} : \left(\mathsf{I} - \frac{1}{3}\boldsymbol{I} \otimes \boldsymbol{I}\right). \tag{B.25}$$

B.4 Linearization of the macroscopic equilibrium problem enhanced with a non-local formulation of integral type

We start this section by recovering the definition of the *First Piola-Kirchoff* stress tensor

$$\begin{aligned} \boldsymbol{P}\left\{\boldsymbol{x}\right\} &= \left(\det \boldsymbol{F}\left\{\boldsymbol{x}\right\}\right) \boldsymbol{\sigma}\left\{\overline{\boldsymbol{F}}\left\{\boldsymbol{x}\right\}\right\} \boldsymbol{F}^{-T}\left\{\boldsymbol{x}\right\} \\ &= \frac{\left(\det \boldsymbol{F}\left\{\boldsymbol{x}\right\}\right)}{\left(\det \overline{\boldsymbol{F}}\left\{\boldsymbol{x}\right\}\right)} \widehat{\boldsymbol{P}}\left\{\overline{\boldsymbol{F}}\left\{\boldsymbol{x}\right\}\right\} \overline{\boldsymbol{F}}^{T}\left\{\boldsymbol{x}\right\} \boldsymbol{F}^{-T}\left\{\boldsymbol{x}\right\} \end{aligned} \tag{B.26}$$

where

$$\widehat{\boldsymbol{P}}\left\{\overline{\boldsymbol{F}}\left\{\boldsymbol{x}\right\}\right\} = \left(\det \overline{\boldsymbol{F}}\left\{\boldsymbol{x}\right\}\right) \boldsymbol{\sigma}\left\{\overline{\boldsymbol{F}}\left\{\boldsymbol{x}\right\}\right\} \overline{\boldsymbol{F}}^{-T}\left\{\boldsymbol{x}\right\} \tag{B.27}$$

Remark B.2. For sake of simplicity, information related to the scale where the variables are defined will be omitted. It is noteworthy to mention that all variables used throughout the linearization of the present problem are defined at the macro-scale domain as well as at the some instant t.

With the previous definition of the *First Piola-Kirchoff*, the material version of the internal virtual work functional of the First Order non-local multi-scale model with the deformation gradient as non-local variable is given by

$$G^{int}\left(\boldsymbol{u}, \boldsymbol{\eta}\right) = \int_{\Theta_0} \nabla_{\boldsymbol{p}} \boldsymbol{\eta} : \left[\frac{\left(\det \boldsymbol{F}\right)}{\left(\det \overline{\boldsymbol{F}}\right)} \widehat{\boldsymbol{P}}\left\{\overline{\boldsymbol{F}}\right\} \overline{\boldsymbol{F}}^{T} \boldsymbol{F}^{-T}\right] dV \tag{B.28}$$

In order to linearize the problem it is necessary to consider the definition of the *directional derivative* introduced in Section B.1 which demands the definition of the perturbed deformation gradient (either local and its non-local counterpart). The perturbed non-local deformation gradient, $\overline{\boldsymbol{F}}_{\epsilon}\{\boldsymbol{x}\}$, is given by:

$$\overline{\boldsymbol{F}}_{\epsilon}\{\boldsymbol{x}\} = \int_{\Omega_0^{nl}} \alpha\{\boldsymbol{x},\boldsymbol{\xi}\}\,\boldsymbol{F}_{\epsilon}\{\boldsymbol{\xi}\}\,dV\{\boldsymbol{\xi}\} \tag{B.29}$$

where $\boldsymbol{F}_{\epsilon}\{\boldsymbol{\xi}\}$ is given by

$$\boldsymbol{F}_{\epsilon}\{\boldsymbol{\xi}\} = \boldsymbol{I} + \nabla_{\boldsymbol{p},\boldsymbol{\xi}}\left(\boldsymbol{u}^{*} + \epsilon\boldsymbol{d}\right) = \boldsymbol{F}^{*} + \epsilon\nabla_{\boldsymbol{p},\boldsymbol{\xi}}\boldsymbol{d} \tag{B.30}$$

Considering the definition of *directional derivative* it is possible to write

$$DG^{int}(\boldsymbol{u},\boldsymbol{\eta})[\boldsymbol{d}] = \left.\frac{d}{d\varepsilon}\right|_{\varepsilon=0}\int_{\Theta_0}\nabla_{\boldsymbol{p}}\boldsymbol{\eta} : \left[\frac{(\det\boldsymbol{F}_{\varepsilon})}{(\det\overline{\boldsymbol{F}}_{\varepsilon})}\widehat{\boldsymbol{P}}\left\{\overline{\boldsymbol{F}}_{\varepsilon}\right\}\overline{\boldsymbol{F}}_{\varepsilon}^{T}\boldsymbol{F}_{\varepsilon}^{-T}\right]dV \tag{B.31}$$

Applying the chain rule to the previous equation results

$$\begin{aligned}
DG^{int}(\boldsymbol{u},\boldsymbol{\eta})[\boldsymbol{d}] = &\int_{\Theta_0}\nabla_{\boldsymbol{p}}\boldsymbol{\eta} : \left[\frac{\left((\det\boldsymbol{F})\,\boldsymbol{F}^{-T} : \nabla_{\boldsymbol{p}}\boldsymbol{d}\right)}{(\det\overline{\boldsymbol{F}})}\widehat{\boldsymbol{P}}\left\{\overline{\boldsymbol{F}}\right\}\overline{\boldsymbol{F}}^{T}\boldsymbol{F}^{-T}\right]dV \\
&+\int_{\Theta_0}\nabla_{\boldsymbol{p}}\boldsymbol{\eta} : \left[\frac{(\det\boldsymbol{F})}{(\det\overline{\boldsymbol{F}})}\left(\mathbf{A} : \int_{\Omega_0^{nl}}\beta\{\boldsymbol{x},\boldsymbol{\xi}\}\,\nabla_{\boldsymbol{p},\boldsymbol{\xi}}\boldsymbol{d}dV\right)\overline{\boldsymbol{F}}^{T}\boldsymbol{F}^{-T}\right]dV \\
&+\int_{\Theta_0}\nabla_{\boldsymbol{p}}\boldsymbol{\eta} : \left[\frac{(\det\boldsymbol{F})}{(\det\overline{\boldsymbol{F}})}\widehat{\boldsymbol{P}}\left\{\overline{\boldsymbol{F}}\right\}\left(\mathbf{I}_4^{T} : \int_{\Omega_0^{nl}}\beta\{\boldsymbol{x},\boldsymbol{\xi}\}\,\nabla_{\boldsymbol{p},\boldsymbol{\xi}}\boldsymbol{d}dV\right)\boldsymbol{F}^{-T}\right]dV \\
&+\int_{\Theta_0}\nabla_{\boldsymbol{p}}\boldsymbol{\eta} : \left[\frac{(\det\boldsymbol{F})}{(\det\overline{\boldsymbol{F}})}\widehat{\boldsymbol{P}}\left\{\overline{\boldsymbol{F}}\right\}\overline{\boldsymbol{F}}^{T}\left(\frac{\partial\boldsymbol{F}^{-T}}{\partial\boldsymbol{F}} : \nabla_{\boldsymbol{p}}\boldsymbol{d}\right)\right]dV \\
&-\int_{\Theta_0}\nabla_{\boldsymbol{p}}\boldsymbol{\eta} : \left[\frac{(\det\boldsymbol{F})}{(\det\overline{\boldsymbol{F}})}\left(\overline{\boldsymbol{F}}^{-T} : \int_{\Omega_0^{nl}}\beta\{\boldsymbol{x},\boldsymbol{\xi}\}\,\nabla_{\boldsymbol{p},\boldsymbol{\xi}}\boldsymbol{d}dV\right)\widehat{\boldsymbol{P}}\left\{\overline{\boldsymbol{F}}\right\}\overline{\boldsymbol{F}}^{T}\boldsymbol{F}^{-T}\right]dV.
\end{aligned} \tag{B.32}$$

B.4.1 Map the linearised expression to the spatial configuration

Before to proceed with this mapping, it is convenient to introduce a tensorial relation for second-order tensors

$$\left(\boldsymbol{M}\otimes\boldsymbol{F}^{-T}\right) : \nabla_{\boldsymbol{p}}\boldsymbol{d} = \left(\boldsymbol{F}^{-T} : \nabla_{\boldsymbol{p}}\boldsymbol{d}\right)\boldsymbol{M} = \left(\boldsymbol{I} : \nabla_{\boldsymbol{p}}\boldsymbol{d}\boldsymbol{F}^{-1}\right)\boldsymbol{M} = (\boldsymbol{M}\otimes\boldsymbol{I}) : \nabla_{\boldsymbol{x}}\boldsymbol{d}. \tag{B.33}$$

It is also important to note that, in order to perform this mapping, once again, expressions (2.28b) and (2.29) will be used.

We start from the first on the right side of Equation (B.32):

$$
\begin{aligned}
&\int_{\Theta_0} \nabla_{\boldsymbol{p}}\boldsymbol{\eta} : \left[\frac{\left(\left(\det \boldsymbol{F}\right)\boldsymbol{F}^{-T} : \nabla_{\boldsymbol{p}}\boldsymbol{d}\right)}{\left(\det \overline{\boldsymbol{F}}\right)}\widehat{\boldsymbol{P}}\left\{\overline{\boldsymbol{F}}\right\}\overline{\boldsymbol{F}}^{T}\boldsymbol{F}^{-T}\right] dV = \\
&= \int_{\Theta_0} \nabla_{\boldsymbol{p}}\boldsymbol{\eta} : \left[\frac{\left(\det \boldsymbol{F}\right)}{\left(\det \overline{\boldsymbol{F}}\right)}\left(\boldsymbol{F}^{-T} : \nabla_{\boldsymbol{p}}\boldsymbol{d}\right)\left(\widehat{\boldsymbol{P}}\left\{\overline{\boldsymbol{F}}\right\}\overline{\boldsymbol{F}}^{T}\boldsymbol{F}^{-T}\right)\right] dV \\
&= \left(\det \boldsymbol{F}\right)\int_{\Theta_0} \nabla_{\boldsymbol{p}}\boldsymbol{\eta} : \left[\left(\boldsymbol{F}^{-T} : \nabla_{\boldsymbol{p}}\boldsymbol{d}\right)\left(\boldsymbol{\sigma}\left\{\overline{\boldsymbol{F}}\right\}\boldsymbol{F}^{-T}\right)\right] dV \\
&= \left(\det \boldsymbol{F}\right)\int_{\Theta_0} \nabla_{\boldsymbol{p}}\boldsymbol{\eta} : \left[\left(\boldsymbol{\sigma}\left\{\overline{\boldsymbol{F}}\right\}\boldsymbol{F}^{-T}\right)\otimes\boldsymbol{I}\right] : \nabla_{\boldsymbol{x}}\boldsymbol{d}dV \\
&= \left(\det \boldsymbol{F}\right)\int_{\Theta_0} \nabla_{\boldsymbol{p}}\eta^{ij}\left[\left(\boldsymbol{\sigma}\left\{\overline{\boldsymbol{F}}\right\}\boldsymbol{F}^{-T}\right)\otimes\boldsymbol{I}\right]^{ijkl}\nabla_{\boldsymbol{x}}d^{kl}dV \\
&= \int_{\varphi(\Theta_0)} \nabla_{\boldsymbol{x}}\eta^{im}F^{mj}\left[\left(\boldsymbol{\sigma}\left\{\overline{\boldsymbol{F}}\right\}\boldsymbol{F}^{-T}\right)\otimes\boldsymbol{I}\right]^{ijkl}\nabla_{\boldsymbol{x}}d^{kl}dV \\
&= \int_{\varphi(\Theta_0)} \nabla_{\boldsymbol{x}}\eta^{im}\mathsf{q}_1^{imkl}\nabla_{\boldsymbol{x}}d^{kl}dV \\
&= \int_{\varphi(\Theta_0)} \nabla_{\boldsymbol{x}}\boldsymbol{\eta} : \mathbf{q}_1 : \nabla_{\boldsymbol{x}}\boldsymbol{d}dV
\end{aligned}
\tag{B.34}
$$

where $\mathbf{q}_1$ is a fourth-order tensor defined by

$$
\mathsf{q}_1^{imkl} = F^{mj}\left[\left(\boldsymbol{\sigma}\left\{\overline{\boldsymbol{F}}\right\}\boldsymbol{F}^{-T}\right)\otimes\boldsymbol{I}\right]^{ijkl} \tag{B.35}
$$

With regard to the second term on the right side of Equation (B.32), one can write

$$
\begin{aligned}
&\int_{\Theta_0} \nabla_{\boldsymbol{p}}\boldsymbol{\eta} : \left[\frac{\left(\det \boldsymbol{F}\right)}{\left(\det \overline{\boldsymbol{F}}\right)}\left(\mathbf{A} : \int_{\Omega_0^{nl}} \beta\left\{\boldsymbol{x},\boldsymbol{\xi}\right\}\nabla_{\boldsymbol{p},\boldsymbol{\xi}}\boldsymbol{d}dV\right)\overline{\boldsymbol{F}}^{T}\boldsymbol{F}^{-T}\right] dV = \\
&= \frac{\left(\det \boldsymbol{F}\right)}{\left(\det \overline{\boldsymbol{F}}\right)}\int_{\Theta_0} \nabla_{\boldsymbol{p}}\boldsymbol{\eta} : \left[\left(\mathbf{A} : \int_{\Omega_0^{nl}} \beta\left\{\boldsymbol{x},\boldsymbol{\xi}\right\}\nabla_{\boldsymbol{p},\boldsymbol{\xi}}\boldsymbol{d}dV\right)\overline{\boldsymbol{F}}^{T}\boldsymbol{F}^{-T}\right] dV \\
&= \frac{\left(\det \boldsymbol{F}\right)}{\left(\det \overline{\boldsymbol{F}}\right)}\int_{\Theta_0} \nabla_{\boldsymbol{p}}\eta^{ij}\left[\left(\mathsf{A}^{ilmn}\int_{\Omega_0^{nl}} \beta\left\{\boldsymbol{x},\boldsymbol{\xi}\right\}\nabla_{\boldsymbol{p},\boldsymbol{\xi}}d^{mn}dV\right)\left(\overline{F}^{T}\right)^{lk}\left(F^{-T}\right)^{kj}\right]^{ij} dV \\
&= \frac{1}{\left(\det \overline{\boldsymbol{F}}\right)}\int_{\varphi(\Theta_0)} \nabla_{\boldsymbol{x}}\eta^{io}F^{oj}\left[\left(\mathsf{A}^{ilmn}\int_{\Omega_0^{nl}} \beta\left\{\boldsymbol{x},\boldsymbol{\xi}\right\}\nabla_{\boldsymbol{x},\boldsymbol{\xi}}d^{mp}\left(F^{\boldsymbol{\xi}}\right)^{pn}dV\right)\left(\overline{F}^{T}\right)^{lk}\left(F^{-T}\right)^{kj}\right]^{ij} dV \\
&= \int_{\varphi(\Theta_0)} \nabla_{\boldsymbol{x}}\eta^{io}\mathsf{q}_2^{iomp}\left[\int_{\Omega_0^{nl}} \beta\left\{\boldsymbol{x},\boldsymbol{\xi}\right\}\nabla_{\boldsymbol{x},\boldsymbol{\xi}}d^{mp}dV\right] dV \\
&= \int_{\varphi(\Theta_0)} \nabla_{\boldsymbol{x}}\boldsymbol{\eta} : \mathbf{q}_2 : \left[\int_{\Omega_0^{nl}} \beta\left\{\boldsymbol{x},\boldsymbol{\xi}\right\}\nabla_{\boldsymbol{x},\boldsymbol{\xi}}\boldsymbol{d}dV\right] dV
\end{aligned}
\tag{B.36}
$$

where $\mathbf{q}_2$ is given by

$$
\mathsf{q}_2^{iomp} = \frac{1}{\left(\det \overline{\boldsymbol{F}}\right)}F^{oj}\mathsf{A}^{ilmn}\left(F^{\boldsymbol{\xi}}\right)^{pn}\left(\overline{F}^{T}\right)^{lk}\left(F^{-T}\right)^{kj} \tag{B.37}
$$

The map of the third term on the right side of Equation (B.32) is given by

$$\begin{aligned}
&\int_{\Theta_0} \nabla_{\boldsymbol{p}}\boldsymbol{\eta} : \left[\frac{(\det \boldsymbol{F})}{(\det \overline{\boldsymbol{F}})}\widehat{\boldsymbol{P}}\left\{\overline{\boldsymbol{F}}\right\}\left(\mathbf{I}_T : \int_{\Omega_0^{nl}} \beta\left\{\boldsymbol{x},\boldsymbol{\xi}\right\}\nabla_{\boldsymbol{p},\boldsymbol{\xi}}\boldsymbol{d}dV\right)\boldsymbol{F}^{-T}\right]dV = \\
&= \frac{(\det \boldsymbol{F})}{(\det \overline{\boldsymbol{F}})}\int_{\Theta_0}\nabla_{\boldsymbol{p}}\eta^{ij}\left[\widehat{P}^{ik}\left(\left(\mathsf{I}_T\right)^{klmn}\int_{\Omega_0^{nl}}\beta\left\{\boldsymbol{x},\boldsymbol{\xi}\right\}\nabla_{\boldsymbol{p},\boldsymbol{\xi}}d^{mn}dV\right)\left(F^{-T}\right)^{lj}\right]^{ij}dV \\
&= \frac{1}{(\det \overline{\boldsymbol{F}})}\int_{\varphi(\Theta_0)}\nabla_{\boldsymbol{x}}\eta^{io}F^{oj}\left[\widehat{P}^{ik}\left(\left(\mathsf{I}_T\right)^{klmn}\int_{\Omega_0^{nl}}\beta\left\{\boldsymbol{x},\boldsymbol{\xi}\right\}\nabla_{\boldsymbol{x},\boldsymbol{\xi}}d^{mp}\left(F^{\boldsymbol{\xi}}\right)^{pn}dV\right)\left(F^{-T}\right)^{lj}\right]dV \\
&= \int_{\varphi(\Theta_0)}\nabla_{\boldsymbol{x}}\eta^{io}\mathsf{q}_3^{iomp}\left[\int_{\Omega_0^{nl}}\beta\left\{\boldsymbol{x},\boldsymbol{\xi}\right\}\nabla_{\boldsymbol{x},\boldsymbol{\xi}}d^{mp}dV\right]dV \\
&= \int_{\varphi(\Theta_0)}\nabla_{\boldsymbol{x}}\boldsymbol{\eta} : \mathbf{q}_3 : \left[\int_{\Omega_0^{nl}}\beta\left\{\boldsymbol{x},\boldsymbol{\xi}\right\}\nabla_{\boldsymbol{x},\boldsymbol{\xi}}\boldsymbol{d}dV\right]dV
\end{aligned} \tag{B.38}$$

where $\mathbf{q}_3$ is given by

$$\mathsf{q}_3^{iomp} = \frac{1}{(\det \overline{\boldsymbol{F}})}F^{oj}\widehat{P}^{ik}\left(\mathsf{I}_T\right)^{klmn}\left(F^{\boldsymbol{\xi}}\right)^{pn}\left(F^{-T}\right)^{lj} \tag{B.39}$$

Considering the fourth term of the right side of Equation (B.32), its map to the spatial configuration is given by

$$\begin{aligned}
&\int_{\Theta_0}\nabla_{\boldsymbol{p}}\boldsymbol{\eta} : \left[\frac{(\det \boldsymbol{F})}{(\det \overline{\boldsymbol{F}})}\widehat{\boldsymbol{P}}\left\{\overline{\boldsymbol{F}}\right\}\overline{\boldsymbol{F}}^T\left(\frac{\partial \boldsymbol{F}^{-T}}{\partial \boldsymbol{F}} : \nabla_{\boldsymbol{p}}\boldsymbol{d}\right)\right]dV = \\
&= \frac{(\det \boldsymbol{F})}{(\det \overline{\boldsymbol{F}})}\int_{\Theta_0}\nabla_{\boldsymbol{p}}\eta^{ij}\left[\widehat{P}^{ik}\left(\overline{F}^T\right)^{kl}\left(\left(\frac{\partial \boldsymbol{F}^{-T}}{\partial \boldsymbol{F}}\right)^{ljmn}\nabla_{\boldsymbol{p}}d^{mn}\right)\right]^{ij}dV \\
&= \frac{1}{(\det \overline{\boldsymbol{F}})}\int_{\varphi(\Theta_0)}\nabla_{\boldsymbol{x}}\eta^{io}F^{oj}\left[\widehat{P}^{ik}\left(\overline{F}^T\right)^{kl}\left(\left(\frac{\partial \boldsymbol{F}^{-T}}{\partial \boldsymbol{F}}\right)^{ljmn}\nabla_{\boldsymbol{x}}d^{mp}F^{pn}\right)\right]^{ij}dV \\
&= \int_{\varphi(\Theta_0)}\nabla_{\boldsymbol{x}}\eta^{io}\mathsf{q}_4^{iomp}\nabla_{\boldsymbol{x}}d^{mp}dVdV \\
&= \int_{\varphi(\Theta_0)}\nabla_{\boldsymbol{x}}\boldsymbol{\eta} : \mathbf{q}_4 : \nabla_{\boldsymbol{x}}\boldsymbol{d}dV
\end{aligned} \tag{B.40}$$

where $\mathbf{q}_4$ is given by

$$\begin{aligned}
\mathsf{q}_4^{iomp} &= \frac{1}{(\det \overline{\boldsymbol{F}})}F^{oj}\widehat{P}^{ik}\left(\overline{F}^T\right)^{kl}\left(\frac{\partial \boldsymbol{F}^{-T}}{\partial \boldsymbol{F}}\right)^{ljmn}F^{pn} \\
&= F^{oj}\sigma^{il}\left(\frac{\partial \boldsymbol{F}^{-T}}{\partial \boldsymbol{F}}\right)^{ljmn}F^{pn}
\end{aligned} \tag{B.41}$$

Finally, the map of the last term on the right side of Equation (B.32) is given by

$$
\begin{aligned}
&-\int_{\Theta_0}\nabla_{\boldsymbol{p}}\boldsymbol{\eta}:\left[\frac{(\det\boldsymbol{F})}{(\det\overline{\boldsymbol{F}})}\left(\overline{\boldsymbol{F}}^{-T}:\int_{\Omega_0^{nl}}\beta\left\{\boldsymbol{x},\boldsymbol{\xi}\right\}\nabla_{\boldsymbol{p},\boldsymbol{\xi}}\boldsymbol{d}dV\right)\widehat{\boldsymbol{P}}\left\{\overline{\boldsymbol{F}}\right\}\overline{\boldsymbol{F}}^{T}\boldsymbol{F}^{-T}\right]dV=\\
&=-\frac{(\det\boldsymbol{F})}{(\det\overline{\boldsymbol{F}})}\int_{\Theta_0}\nabla_{\boldsymbol{p}}\boldsymbol{\eta}:\left[\left(\overline{\boldsymbol{F}}^{-T}:\int_{\Omega_0^{nl}}\beta\left\{\boldsymbol{x},\boldsymbol{\xi}\right\}\nabla_{\boldsymbol{p},\boldsymbol{\xi}}\boldsymbol{d}dV\right)\widehat{\boldsymbol{P}}\left\{\overline{\boldsymbol{F}}\right\}\overline{\boldsymbol{F}}^{T}\boldsymbol{F}^{-T}\right]dV\\
&=\frac{(\det\boldsymbol{F})}{(\det\overline{\boldsymbol{F}})}\int_{\Theta_0}\nabla_{\boldsymbol{p}}\eta^{ij}\left[\left(\left(\overline{F}^{-T}\right)^{mn}\int_{\Omega_0^{nl}}\beta\left\{\boldsymbol{x},\boldsymbol{\xi}\right\}\nabla_{\boldsymbol{p},\boldsymbol{\xi}}d^{mn}dV\right)\widehat{P}^{ik}\left(\overline{F}^{T}\right)^{kl}\left(F^{-T}\right)^{lj}\right]^{ij}dV\\
&=-\frac{1}{(\det\overline{\boldsymbol{F}})}\int_{\varphi(\Theta_0)}\nabla_{\boldsymbol{x}}\eta^{io}F^{oj}\left[\left(\left(\overline{F}^{-T}\right)^{mn}\int_{\Omega_0^{nl}}\beta\left\{\boldsymbol{x},\boldsymbol{\xi}\right\}\nabla_{\boldsymbol{x},\boldsymbol{\xi}}d^{mp}\left(F^{\boldsymbol{\xi}}\right)^{pn}dV\right)\widehat{P}^{ik}\left(\overline{F}^{T}\right)^{kl}\left(F^{-T}\right)^{lj}\right]^{ij}dV\\
&=-\int_{\varphi(\Theta_0)}\nabla_{\boldsymbol{x}}\eta^{io}\mathsf{q}_5^{iomp}\left[\int_{\Omega_0^{nl}}\beta\left\{\boldsymbol{x},\boldsymbol{\xi}\right\}\nabla_{\boldsymbol{x},\boldsymbol{\xi}}d^{mp}dV\right]dV\\
&=-\int_{\varphi(\Theta_0)}\nabla_{\boldsymbol{x}}\boldsymbol{\eta}:\mathbf{q}_5:\left[\int_{\Omega_0^{nl}}\beta\left\{\boldsymbol{x},\boldsymbol{\xi}\right\}\nabla_{\boldsymbol{x},\boldsymbol{\xi}}\boldsymbol{d}dV\right]dV
\end{aligned}
\tag{B.42}
$$

where $\mathbf{q}_5$ is given by

$$
\begin{aligned}
\mathsf{q}_5^{iomp}&=\frac{1}{(\det\overline{\boldsymbol{F}})}F^{oj}\left(\overline{F}^{-T}\right)^{mn}\left(F^{\boldsymbol{\xi}}\right)^{pn}\widehat{P}^{ik}\left(\overline{F}^{T}\right)^{kl}\left(F^{-T}\right)^{lj}\\
&=F^{oj}\left(\overline{F}^{-T}\right)^{mn}\left(F^{\boldsymbol{\xi}}\right)^{pn}\sigma^{il}\left(F^{-T}\right)^{lj}
\end{aligned}
\tag{B.43}
$$

With the different terms of Equation (B.32) mapped to the spatial configuration, the global expression for the stiffness tangent matrix is given by

$$
\begin{aligned}
\mathsf{K}\left\{\boldsymbol{x}\right\}=&\int_{\varphi(\Theta_0)}\boldsymbol{G}^{T}\left\{\boldsymbol{x}\right\}\left(\mathbf{q}_1+\mathbf{q}_4\right)\boldsymbol{G}\left\{\boldsymbol{x}\right\}dV\\
&+\alpha\left\{\boldsymbol{x},\boldsymbol{\xi}\right\}\int_{\varphi(\Theta_0)}\boldsymbol{G}^{T}\left\{\boldsymbol{x}\right\}\left(\mathbf{q}_2+\mathbf{q}_3-\mathbf{q}_5\right)\boldsymbol{G}\left\{\boldsymbol{\xi}\right\}dV
\end{aligned}
\tag{B.44}
$$

where $\boldsymbol{G}\left\{\boldsymbol{x}\right\}$ and $\boldsymbol{G}\left\{\boldsymbol{\xi}\right\}$ are the discrete gradient operator at points $\boldsymbol{x}$ and $\boldsymbol{\xi}$ respectively. Finally, the term $\alpha\left\{\boldsymbol{x},\boldsymbol{\xi}\right\}$ is a scalar parameter related to the non-local integral.

Bibliography

[1] B. I. Wohlmuth. *Discretization methods and iterative solvers based on domain decomposition*. Springer-Verlag, Heidelberg, 2001.

[2] J. Mediavilla, R.H.J. Peerlings, and M.G.D Geers. A robust and consistent remeshing-transfer operator for ductile fracture simulations. *Computer and Structures*, 84:604–623, 2006.

[3] Bin Yang, T. A. Laursen, and Xiaonong Meng. Two dimensional mortar contact methods for large deformation frictional sliding. *International Journal for Numerical Methods in Engineering*, 62:1183–1225, 2005.

[4] Bin Yang. *Mortar Finite Element Method for Large Deformation Contact Mechanics*. PhD thesis, 2006.

[5] Bin Yang and T. A. Laursen. A large deformation mortar formulation of self contact with finite sliding. *Computer Methods in Applied Mechanics and Engineering*, 197:756–772, 2008.

[6] E. A. de Souza Neto, D. Perić, and D. R. Owen. *Computational Methods for Plasticity: Theory and Application*. 2008.

[7] J. D. Eshelby. The determination of the elastic field of an ellipsoidal inclusion and related problems. *Proceedings of the Royal Society of London A*, 241:376–396, 1957.

[8] Z. Hashin. The elastic moduli of heterogeneous materials. *Journal of Applied Mechanics*, 29:143–150, 1962.

[9] T. Mori and K. Tanaka. Average stress in the matrix and average elastic energy of materials with misfitting inclusions. *Acta Metallurgica*, 21:571–574, 1973.

[10] J. M. Duva and J. W. Hutchinson. Constitutive potentials for dilutely voided nonlinear materials. *Mechanics of Materials*, 3:41–54, 1984.

[11] S. Nemat-Nasser. Multi-inclusion method for finite deformations: exact results and applications. *Computer Methods in Applied Mechanics and Engineering*, A285: 239–245, 2000.

[12] R. Hill. A self-consistent mechanics of composite materials. *Journal of the Mechanics and Physics of Solids*, 4:213–222, 1965.

[13] Z. Hashin and S. Shtrikman. A variational approach to the theory of the elastic behaviour of multiphase materials. *Journal of the Mechanics and Physics of Solids*, 11:127–140, 1963.

[14] J. R. Willis. The overall response of composite materials. *ASME Journal of Applied Mathematics and Mechanics*, 50:1202–1209, 1983.

[15] P. Ponte Castaneda. The effective mechanical properties of nonlinear isotropic composites. *Journal of the Mechanics and Physics of Solids*, 39:45–71, 1991.

[16] P. Ponte Castaneda. New variational mechanical properties of nonlinear isotropic composites. *Journal of the Mechanics and Physics of Solids*, 40:1757–1788, 1991.

[17] D. R. S. Talbot and J. R. Willis. Some explicit bounds for the overall behaviour of nonlinear composites. *International Journal of Solids and Structures*, 29:1981–1987, 1992.

[18] P. M. Suquet. Overall potentials and extremal surfaces of power law or ideally plastic materials. *Journal of the Mechanics and Physics of Solids*, 36:29–58, 1993.

[19] A. Bensoussan, J. L. Lions, and G. Papanicolaou. *Asymptotic analysis for periodic structures.* North-Holland, Amsterdam, 1978.

[20] E. Sanchez-Palencia. *Non-homogeneous media and vibration theory. Lecture notes in physics.* Springer-Verlag, Berlin, 1980.

[21] F. Devries, H. Dumontet, G. Duvaut, and F. Lene. Homogenization and damage for composite structures. *International Journal for Numerical Methods in Engineering*, 27:285–298, 1989.

[22] S. J. Hollister and N. Kikuchi. A comparison of homogenization and standard mechanics analysis for periodic porous composite. *Computational Mechanics*, 10: 73–95, 1992.

[23] J. Fish, Q. Yu, and K. Shek. Computational damage mechanics for composite materials based on mathematical homogenization. *International Journal for Numerical Methods in Engineering*, 45:1657–1679, 1999.

[24] S. Nemat-Nasser and M. Hori. *Micromechanics: overall properties of heterogeneous materials*. North-Holland, second edition, 1999.

[25] R. Hill. Elastic properties of reinforced solids: Some theoretical principles. *Journal of the Mechanics and Physics of Solids*, 11:357–372, 1963.

[26] H. Moulinec and P. M. Suquet. A numerical method for computing the overall response of non-linear composites with complex microstructures. *Computer Methods in Applied Mechanics and Engineering*, 157:69–94, 1998.

[27] S. Ghosh and S. Moorthy. Particle fracture simulation in non-uniform microstructures of metal-matrix composites. *Acta Materialia*, 46:965–982, 1998.

[28] J. C. Michel, H. Moulinec, and P. M. Suquet. Effective properties of composite materials with periodic microstructure: a computational approach. *Computer Methods in Applied Mechanics and Engineering*, 172:109–143, 1999.

[29] I. Temizer and P. Wriggers. A multiscale contact homogenization technique for the modeling of third bodies in the contact interface. *Comput. Methods Appl. Mech. Engrg.*, 198:377–396, 2008.

[30] P. M. Suquet. Local and global aspects in the mathematical theory of plasticity. In A. Sawczuk and G. Bianchi, editors, *Plasticity today: modelling, methods and applications*, pages 279–310. Elsevier Applied Science Publishers, 1985.

[31] J. M. Guedes and N. Kikuchi. Preprocessing and postoprocessinf for materials based on the homogenization method with adaptative finite element methods. *Computer Methods in Applied Mechanics and Engineering*, 83:143–198, 1990.

[32] K. Terada and N. Kikuchi. Nonlinear homogenization method for practical application. In S. Ghosh and M. Ostoja-Starzewski, editors, *Proceedings of 1995 ASME International Mechanical Engineering Congress and Exposition*, volume 212, pages 1–16, 1995.

[33] S. Ghosh, K. Lee, and S. Moorthy. Multiple scale analysis of heterogeneous elastic structures using homogenisation theory and Voronoi cell finite element method. *International Journal of Solids and Structures*, 32:27–62, 1995.

[34] S. Ghosh, K. Lee, and S. Moorthy. Two scale analysis of heterogeneous elastic-plastic materials with asymptotic homogenisation and Voronoi cell finite element model. *Computer Methods in Applied Mechanics and Engineering*, 132:63–116, 1996.

[35] V. G. Kouznetsova and M. G. D. Geers. A multi-scale model of martensitic transformation plasticity. *Mechanics of Materials*, 40:641–657, 2008.

[36] C. Miehe, J. Schotte, and J. Schröder. Computational micro-macro transitions and overall moduli in the analysis of polycrystals at large strains. *Computational Materials Science*, 16:372–382, 1999.

[37] C. Miehe and A. Koch. Computational micro-to-macro transitions of discretized microstructures undergoing small strains. *Archive of Applied Mechanics*, 72:300–317, 2002.

[38] V.G. Kouznetsova, M. G. D. Geers, and W. A. M. Brekelmans. Multi-scale second-order computational homogenization of multi-phase materials: a nested finite element solution strategy. *Comput. Methods Appl. Mech. Engrg.*, 193:5525–5550, 2004.

[39] I. Özdemir, W. A. M. Brekelmans, and M. G. D. Geers. Computational homogenization for heat conduction in heterogeneous solids. *International Journal for Numerical Methods in Engineering*, 73:185–204, 2008.

[40] I. Özdemir, W. A. M. Brekelmans, and M. G. D. Geers. FE computational homogenization for the thermo-mechanical analysis of heterogeneous solids. *Comput. Methods Appl. Mech. Engrg.*, 198:602–613, 2008.

[41] T. J. Massart, R. H. J. Peerlings, and M. G. D. Geers. An enhanced multi-scale approach for masonry wall computations with localization of damage. *International Journal for Numerical Methods in Engineering*, 69:1022–1059, 2006.

[42] T. J. Massart, R. H. J. Peerlings, and M. G. D. Geers. Structural damage analysis of masonry walls using computational homogenization. *International Journal of Damage Mechanics*, 16(2):199–226, 2007.

[43] B. C. N. Mercatoris, Ph. Bouillard, and T. J. Massart. Multi-scale detection of failure in planar masonry thin shells using computational homogenisation. *Engineering Fracture Mechanics*, 79:479–499, 2009.

[44] E. W. C. Coenen, V. G. Kouznetsova, and M. G. D. Geers. Computational homogenization for heterogeneous thin sheets. *International Journal for Numerical Methods in Engineering*, 83:1180–1205, 2010.

[45] D. C. D. Speirs, E. A. de Souza Neto, and D. Perić. An approach to the mechanical constitutive modelling of arterial tissue based on homogenization and optimization. *Journal of Biomechanics*, 41(12):2673–2680, 2008.

[46] Thomas Hettich, Andrea Hund, and Ekkehard Ramm. Modeling of failure in composites by X-FEM and level sets within a multiscale framework. *Computer Methods in Applied Mechanics and Engineering*, 197:414–424, 2008.

[47] J. Ghanbari and R. Naghdabadi. Nonlinear hierarchical multiscale modeling of cortical bone considering its nanoscale microstructure. *Journal of Biomechanics*, 42:1560–1565, 2009.

[48] Naoki Takano, Ken Fukasawa, and Kazuaki Nishiyabu. Structural strength prediction for porous titanium based on micro-stress concentration by micro-CT image-based multiscale simulation. *International Journal of Mechanical Sciences*, 52: 229–235, 2010.

[49] F. Feyel and J. L. Chaboche. FE^2 multiscale approach for modelling the elastoviscoplastic behaviour of long fiber SiC/Ti composite materials. *Computer Methods in Applied Mechanics and Engineering*, 183:309–330, 2000.

[50] K. Matsui, K. Terada, and K. Yuge. Two-scale finite element analysis of heterogeneous solids with periodic microstructures. *Computers and Structures*, 82:593–606, 2004.

[51] S. Ghosh, K. Lee, and P. Raghavan. A multi-level computational model for multi-scale damage analysis in composite and porous materials. *International Journal of Solids and Structures*, 38:2335–2385, 2001.

[52] I.M. Gitman, H. Askes, and L. J. Sluys. Representative volume: Existence and size determination. *Engineering Fracture Mechanics*, 74:2518–2534, 2007.

[53] I.M. Gitman, H. Askes, and L. J. Sluys. Coupled-volume multi-scale modelling of quasi-brittle material. *European Journal of Mechanics A/Solids*, 27:302–327, 2008.

[54] L. Wu, L. Noels, L. Adam, and I. Doghri. A multiscale mean-field homogenization method for fiber-reinforced composites with gradient-enhanced damage models. *Computer Methods in Applied Mechanics and Engineering*, 233-236:164–179, 2012.

[55] Ted Belytschko, S. Loehnert, and JH. Song. Multiscale aggregating discontinuities: a method for circumventing loss of material stability. *International Journal for Numerical Methods in Engineering*, 73:869–894, 2008.

[56] Jeong-Hoon Song and Ted Belytschko. Multiscale aggregating discontinuities method for micro-macro failure of composites. *Composites: Part B*, 40:417–426, 2009.

[57] Flavio V. Souza and David H. Allen. Multiscale modeling of impact on heterogeneous viscoelastic solids containing evolving cracks. *International Journal for Numerical Methods in Engineering*, 82:464–504, 2010.

[58] E.W.C. Coenen, V.G. Kouznetsova, and M.G.D. Geers. Multi-scale continuous-discontinuous framework for computational-homogenization-localization. *Journal of the Mechanics and Physics of Solids*, 60:1486–1507, 2012.

[59] V. P. Nguyen, O. Lloberas-Valls, M. Stroeven, and L. J. Sluys. Computational homogenization for multiscale crack modeling. Implementation and computational aspects. *International Journal for Numerical Methods in Engineering*, 89:192–226, 2012.

[60] V. P. Nguyen, M. Stroeven, and L.J. Sluys. Multiscale failure modelling of concrete: micromechanical modelling, discontinuous homogenization and parallel computations. *Computer Methods in Applied Mechanics and Engineering*, 201-204: 139–156, 2012.

[61] V. P. Nguyen, M. Stroeven, and L.J. Sluys. An enhanced continuous-discontinuous multiscale method for modeling mode-I cohesive failure in random heterogeneous quasi-brittle materials. *Engineering Fracture Mechanics*, 79:78–102, 2012.

[62] Clemens V. Verhoosel, Joris J. C. Remmers, Miguel A. Gutiérrez, and René de Borst. Computational homogenization for adhesive and cohesive failure in quasi-brittle solids. *International Journal for Numerical Methods in Engineering*, 83:1155–1179, 2010.

[63] E. W. C. Coenen, V. G. Kouznetsova, and M. G. D. Geers. Novel boundary conditions for strain localization analyses in microstructural volume elements. *International Journal for Numerical Methods in Engineering*, 2011.

[64] G. A. Holzapfel. *Nonlinear solid mechanics: a continuum approach for engineering.* John Wiley & Sons, Chichester, 2000.

[65] M. A. Crisfield. *Non-linear finite element analysis of solids and structures*, volume 1: Essentials. John Wiley & Sons, 2000.

[66] A. Bertram. *Elasticity and plasticity of large deformations. An introduction.* Springer-Verlag, Berlin, 2005.

[67] J. Bonet and R. D. Wood. *Nonlinear continuum mechanics for finite element analysis.* Cambridge University Press, 2 edition, 2008.

[68] A. A. Shabana. *Computational continuum mechanics.* Cambridge University Press, 2008.

[69] M. A. Crisfield. *Non-linear finite element analysis of solids and structures*, volume 2: Advanced topics. John Wiley & Sons, 2000.

[70] O. C. Zienkiewicz, R. L. Taylor, and J. Z. Zhu. *The Finite Element Method. Its Basics & Fundamentals*. Elsevier Butterworth Heinemann, 6 edition, 2005.

[71] O. C. Zienkiewicz and R. L. Taylor. *The Finite Element Method for Solid and Structural Mechanics*. Elsevier Butterworth Heinemann, 6 edition, 2005.

[72] M. E. Gurtin. *An Introduction to Continuum Mechanics*. 1981.

[73] O. Kintzel and Y. Basar. Fourth-order tensors - tensor differentiation with applications to continuum mechanics. Part I: Classical tensor analysis. *Journal of Applied Mathematics and Mechanics*, 86(4):291–311, 2006.

[74] C. Miehe. Strain-driven homogenization of inelastic microstructures and composites based on an incremental variational formulation. *International Journal for Numerical Methods in Engineering*, 55:1285–1322, 2002.

[75] A. J. C. Molina. *Computational Homogenization for Multi Scale Finite Element Simulation*. PhD thesis, Swasea University, 2007.

[76] S. M. Giusti. *Análise de sensibilidade topológica em modelos constitutivos multi-escalas*. PhD thesis, LNCC, Rio de Janeiro, Brasil, 2009.

[77] S. M. Giusti, A. A. Novotny, E. A. de Souza Neto, and R. A. Feijóo. Sensitivity of the macroscopic elasticity tensor to topological microstructural changes. *Journal of the Mechanics and Physics of Solids*, 57:555–570, 2009.

[78] D. Perić, E.A. de Souza Neto, R.A. Feijóo, M. Partovi, and A.J. Carneiro Molina. On micro-to-macro transitions for multi-scale analysis of non-linear heterogeneous materials: unified variational basis and finite element implementation. *International Journal for Numerical Methods in Engineering*, 87:149–170, 2011.

[79] J. D. Clayton and D. L. McDowell. A multiscale multiplicative decomposition for elastoplasticity of polycrystals. *International Journal of Plasticity*, 19(3):1401–1444, 2003.

[80] J. D. Clayton and D. L. McDowell. Homogenized finite elastoplasticity and damage: theory and computations. *Mechanics of Materials*, 36:799–824, 2004.

[81] S. Graham and N. Yang. Representative volumes of materials based on microstructural statistics. *Scripta Materialia*, 48:269–274, 2003.

[82] M. Stroeven, H. Askes, and L. J. Sluys. Numerical determination of representative volumes for granular materials. *Computer Methods in Applied Mechanics and Engineering*, 193:3221–3238, 2004.

[83] M. Ostoja-Starzewski. Scale effects in plasticiy of random media: status and challenges. *International Journal of Plasticity*, 21:1119–1160, 2005.

[84] V. P. Nguyen, O. L. Valls, M. Stroeven, and L. J. Sluys. On the existence of representative volumes for softening quasi-brittle materials - A failure zone averaging scheme. *Computer Methods in Applied Mechanics and Engineering*, 199: 3028–3038, 2010.

[85] J. Mandel. Plasticité Classique et Viscoplasticité. CISM Lecture Notes, Udine, Italy, Springer-Verlag, 1971. $infrench$.

[86] E. A. de Souza Neto and R. A. Feijóo. *Variational Foundations of Large Strain Multiscale Solid Constitutive Models: Kinematical Formulation*, chapter 9, pages 341–378. WILEY-VCH, 2010.

[87] K. Terada, M. Hori, T. Kyoya, and N. Kikuchi. Simulation of the multi-scale convergence in computational homogenization approaches. *International Journal of Solids and Structures*, 37:2285–2311, 2000.

[88] T. Kanit, S. Forest, I. Galliet, V. Mounoury, and D. Jeulin. Determination of the size of the representative volume element for random composites: statistical and numerical approach. *International Journal of Solids and Structures*, 40:3647–3679, 2003.

[89] J. C. Simo and T. J. R Hughes. *Computational Inelasticity*. 1998.

[90] T. Belytschko, W.K. Liu, and B. Moran. *Nonlinear Finite Elements for Continua amd Structures*. Wiley, New York, 2000.

[91] P. Wriggers. *Nonlinear Finite Element Methods*. Springer, Berlin, 2008.

[92] C. Miehe. Computational micro-to-macro transitions for discretized microstructures of heterogeneous materials at finite strains based on the minimization of averaged incremental energy. *Computer Methods in Applied Mechanics and Engineering*, 192:559–591, 2003.

[93] S. Nemat-Nasser. Averaging theorems in finite deformation plasticity. *Mechanics of Materials*, 31:493–523, 1999.

[94] E. A. de Souza Neto and R. A. Feijóo. On the equivalence between spatial and material volume averaging of stress in large strain multi-scale solid constitutive models. *Mechanics of Materials*, 40:803–811, 2008.

[95] K. Terada, I. Saiki, K. Matsui, and Y. Yamakawa. Two-scale kinematics and linearization for simultaneous two-scale analysis of periodic heterogeneous solids

at finite strain. *Computer Methods in Applied Mechanics and Engineering*, 192: 3531–3563, 2003.

[96] V. G. Kouznetsova, W. A. M. Brekelmans, and F. P. T. Baaijens. An approach to micro-macro modeling of heterogeneous materials. *Computational Mechanics*, 27:37–48, 2001.

[97] D. Deniz Somer. *Computational Strategies For Multi-Scale Analysis of Solids: Small and Large Strain Formulations*. PhD thesis, University of Wales, Swansea, 2010.

[98] İ. Temizer and P. Wriggers. On the computation of the macroscopic tangent for the multiscale volumetric homogenization problems. *Computer Methods in Applied Mechanics and Engineering*, 198:495–510, 2008.

[99] Assyr Abdulle and Achim Nonnenmacher. A short and versatile finite element multiscale code for homogenization problems. *Computer Methods in Applied Mechanics and Engineering*, 198:2839–2859, 2009.

[100] Sonia Marfia and Elio Sacco. Multiscale damage contact-friction model for periodic masonry walls. *Computer Methods in Applied Mechanics and Engineering*, 2011.

[101] J. C. Michel and P. Suquet. Nonuniform transformation fields analysis. *International Journal of Solids and Structures*, 40:6937–6955, 2003.

[102] J. C. Michel and P. Suquet. Computational analysis of nonlinear composite structures using the nonuniform transformation fields analysis. *Computer Methods in Applied Mechanics and Engineering*, 193((48-51)):5477–5502, 2004.

[103] J. Yvonnet and Q.-Ce. He. The reduced model multiscale method (R^3M) for the non-linear homogenization of hyperlastic media at finite strains. *Journal of Computational Physics*, 223:341–368, 2007.

[104] J. Yvonnet, H. Zahrouni, and M. Potier-Ferry. A model reduction method for the post-buckling analysis of cellular microstructures. *Computer Methods in Applied Mechanics and Engineering*, 197:265–280, 2007.

[105] M. A. Crisfield. An arc-length method including line searches and accelerations. *International Journal for Numerical Methods in Engineering*, 19:1269–1289, 1983.

[106] M. G. D. Geers. Enhanced solution control for physically and geometrically non-linear problems. Part I - The subplane control approach. *International Journal for Numerical Methods in Engineering*, 46:177–204, 1999.

[107] M. G. D. Geers. Enhanced solution control for physically and geometrically non-linear problems. Part II - Comparative performance analysis. *International Journal for Numerical Methods in Engineering*, 46:205–230, 1999.

[108] M. A. Gutiérrez. Energy release control for numerical simulations of failure in quasi-brittle solids. *Communications in Numerical Methods in Engineering*, 20: 19–29, 2004.

[109] M. A. Crisfield. *Non-linear Finite Element Analysis of Solids and Structures. Volume 1: Essentials*. John Wiley & Sons, 1991.

[110] Agustí Pérez-Foguet, Antonio Rodríguez-Ferran, and Antonio Huerta. Consistent tangent matrices for substepping schemes. *Computer Methods in Applied Mechanics and Engineering*, 190:4627–4647, 2001.

[111] D. Deniz Somer, E. A. de Souza Neto, W.G. Dettmer, and D. Perić. A sub-stepping scheme for multi-scale analysis of solids. *Computer Methods in Applied Mechanics and Engineering*, 198:1006–1016, 2009.

[112] I. Saiki, K. Terada, K. Ikeda, and M. Hori. Appropriate number of unit cells in a representative volume element for micro-structural bifurcation encountered in a multi-scale modeling. *Computer Methods in Applied Mechanics and Engineering*, 191:2561–2585, 2002.

[113] F.J.P. Reis and F.M. Andrade Pires. An adaptive sub-incremental strategy for the solution of homogenization-based multi-scale problems. *Computer Methods in Applied Mechanics and Engineering*, 257:164–182, 2013.

[114] Cécile Dobrzynski, Maxime Melchior, Laurent Delannay, and Jean-François Remacle. A mesh adaptation procedure for periodic domains. *International Journal for Numerical Methods in Engineering*, 86:1396–1412, 2011.

[115] R. Wentorf, R. Collar, M.S. Shephard, and J. Fish. Automated modeling for complex woven mesostructures. *Computer Methods in Applied Mechanics and Engineering*, 172:273–291, 1999.

[116] Zheng Yuan and Jacob Fish. Toward realization of computational homogenization in practice. *International Journal for Numerical Methods in Engineering*, 73:361–380, 2007.

[117] J. M. Tyrus, M. Gosz, and E. DeSantiago. A local finite element implementation for imposing periodic boundary conditions on composite micromechanical models. *International Journal of Solids and Structures*, 44:2972–2989, 2007.

[118] V.-D Nguyen, E. Béchet, C. Geuzaine, and L. Noels. Imposing periodic boundary condition on arbitrary meshes by polinomial interpolation. *Computational Materials Science*, 55:390–406, 2012.

[119] F. Larsson, K. Runesson, S. Saroukhani, and R. Vafadari. Computational homogenization based on a weak format of micro-periodicity for RVE-problems. *Computer Methods in Applied Mechanics and Engineering*, 200:11–26, 2011.

[120] B. I. Wohlmuth. A mortar finite element method using dual spaces for the lagrange multiplier. *SIAM Journal of Numerical Analysis*, 38:989–1012, 2000.

[121] Michael A. Puso and T. A. Laursen. A mortar segment-to-segment contact method for large deformation solid mechanics. *Comput. Methods Appl. Mech. Engrg.*, 193: 601–629, 2004.

[122] K. A. Fischer and P. Wriggers. Frictionless 2D contact formulations for finite deformations based on the mortar method. *Computer Mechanics*, 36:226–244, 2005.

[123] Michael A. Puso, T. A. Laursen, and Jerome Solberg. A segment-to-segment mortar contact method for quadratic elements and large deformations. *Computer Methods in Applied Mechanics and Engineering*, 197:555–566, 2008.

[124] T. Cichosz and M. Bischoff. Consistent treatment of boundaries with mortar contact formulations using dual Lagrange multipliers. *Computer Methods in Applied Mechanics and Engineering*, 200:1317–1332, 2011.

[125] T. A. Laursen, Michael A. Puso, and Jessica Sanders. Mortar contact formulations for deformable-deformable contact: Past contributions and new extensions for enriched and embedded interface formulations. *Computer Methods in Applied Mechanics and Engineering*, pages 3–15, 2012.

[126] Thomas Kloppel, Alexander Popp, Ulrich Kuttler, and Wolfgang A. Wall. Fluid-structure interaction for non-conforming interfaces based on a dual mortar formulation. *Computer Methods in Applied Mechanics and Engineering*, 200:3111–3126, 2011.

[127] Nagi El-Abbasi and Klaus-Jürgen Bathe. Stability and patch test performance of contact discretizations and a new solution algorithm. *Computer and Structures*, 79:1473–1486, 2001.

[128] P. Wriggers. *Computational Contact Mechanics*. Springer, Berlin, Heidelberg, second edition, 2006.

[129] S. Hartmann, S. Brunssen, E. Ramm, and B. I. Wohlmuth. Unilateral non-linear dynamic contact of thin-walled structures using a primal-dual active set strategy. *International Journal for Numerical Methods in Engineering*, 70:883–912, 2007.

[130] Alexander Popp, Markus Gitterle, Michael W. Gee, and Wolfgang A. Wall. A dual mortar approach for 3D finite deformation contact with consistent linearization. *International Journal for Numerical Methods in Engineering*, 83:1428–1465, 2010.

[131] J. D. Foley, A. vanDam, S. K. Feiner, and J. F. Hughes. *Computer Graphics, Principles and Practice*. Addison-Wesley, Boston, MA, 2nd edition, 1990.

[132] G. R. Cowper. Gaussian quadrature formulas for triangles. *International Journal for Numerical Methods in Engineering*, 70:405–408, 1973.

[133] H.D. Miranda, F.M. Andrade Pires, and A.T. Marques. Generation of micro mechanical models with random distribution of circular inclusions. *(submitted for publication)*, 2013.

[134] A.L. Gurson. Continuum Theory of Ductile Rupture by Void Nucleation and Growth - Part I: Yield Criteria and Flow Rule for Porous Media. *Journal of Engineering Materials and Technology*, 99:2–15, 1977.

[135] V Tvergaard and A. Needleman. Analysis of Cup-Cone Fracture in a Round Tensile Bar. *Acta Metallurgica*, 32:157–169, 1984.

[136] J. Lemaitre. Coupled elasto-plasticity and damage constitutive equation. *Comp. Meth. Applied Mech. Engng*, 51:31–49, 1985.

[137] Z.P. Bažant and F.-B. Lin. Nonlocal yield-limit degradation. *International Journal for Numerical Methods in Engineering*, 26:1805–1823, 1988.

[138] Z.P. Bažant and G. Pijaudier-Cabot. Nonlocal Continuum Damage, Localization Instability and Convergence. *Journal of Applied Mechanics*, 55:287–290, 1988.

[139] M. Jirásek and Z.P. Bazant. Nonlocal integral formulations of plasticity and damage: Survey of progress. *Jornal of Engineering Mechanics*, 128(11):4133–4145, 2002.

[140] M. Jirásek. Nonlocal models for damage and fracture: comparison of approaches. *International Journal of Solids and Structures*, 35:4133–4145, 1998.

[141] M. Jirásek and S. Rolshoven. Comparison of integral-type nonlocal plasticity models for strain-softening materials. *International Journal of Engineering Science*, 41:1553–1602, 2003.

[142] G. Pijaudier-Cabot and Z.P Bazant. Nonlocal damage theory. *Jornal of Engineering Mechanics*, 113(10):1512–1533, 1987.

[143] R. De Borst and H. Mühlhaus. Gradient-dependent plasticity: formulation and algorithmic aspects. *International Journal for Numerical Methods in Engineering*, 35:521–539, 1992.

[144] R.H.J. Peerlings, R. De Borst, W.A.M. Brekelmans, and J.H.P. De Vree. Gradient-enhanced damage for quasi-brittle materials. *International Journal for Numerical Methods in Engineering*, 39:1512–1533, 1996.

[145] R.H.J. Peerlings, M.G.D. Geers, R. De Borst, and W.A.M. Brekelmans. A critical comparison of nonlocal and gradient-enhanced softening continua. *International Journal of Solids and Structures*, 38(44–45):7723–7746, 2001.

[146] M. Jirásek and B. Patzák. Consistent tangent stiffness for nonlocal damage models. *Computers and Structures*, 80:1279–1293, 2002.

[147] F.X.C. Andrade, F.M. Andrade Pires, J.M.A. César de Sá, and L. Malcher. Nonlocal Integral Formulation for a Plasticity-Induced Damage Model. *Computer Methods in Material Science*, 9(1):49–54, 2009.

[148] F.X.C. Andrade, J.M.A. Cesar de Sa, and F.M. Andrade Pires. A ductile damage nonlocal model of integral-type at finite strains: formulation and numerical issues. *International Journal of Damage Mechanics*, 20:515–557, 2011.

[149] F.X.C. Andrade, F.M. Andrade Pires, and J.M.A. César de Sá. Consistent tangent operators for implicit non-local models of integral-type. *Computer and Structures - In Press*, 2013.

[150] Jacob Fish, Tao Jiang, and Zheng Yuan. A staggered nonlocal multiscale model for heterogeneous medium. *International Journal for Numerical Methods in Engineering*, 91(2):142–157, 2012.

[151] G. Borino, B. Failla, and C. Polizzotto. A symmetric nonlocal damage theory. *International Journal of Solids and Structures*, 40:3621–3645, 2003.

[152] F. X. C. Andrade. *Non-local Modelling of Ductile Damage. Formulation and Numerical Issues.* PhD thesis, Faculty of Engineering of University of Porto, 2012.

[153] J. Lemaitre. *A Course on Damage Mechanics.* Springer, New York, 1996.

[154] F.J.P. Reis, L. Malcher, F.M. Andrade Pires, and J.M.A. César de Sá. A comparation of Shear Mechanisms for the Prediction of Ductile Failure under Low Stress Triaxiality. *International Journal of Structural Integrity*, 2010.

[155] J. C. Simo, R. L. Taylor, and P. Wriggers. A perturbed lagrangian formulation for the finite element solution of contact problems. *Computer Methods in Applied Mechanics and Engineering*, 50:163–180, 1985.

[156] Z.P. Bažant and T.-P. Chang. Instability of nonlocal continuum and strain averaging. *Journal of Engineering Mechanics*, ASCE 110:1441–1450, 1984.

[157] Antonio Rodríguez-Ferran, Irene Morata, and Antonio Huerta. A new damage model based on non-local displacements. *International Journal for Numerical Methods in Engineering*, 29:473–493, 2005.

[158] M. Jirásek and S. Marfia. Non-local damage model based on displacement averaging. *International Journal for Numerical Methods in Engineering*, 63:77–102, 2005.

[159] T.J.R. Hughes. Generalization of selective integration procedures to anisotropic and nonlinear media. *International Journal for Numerical Methods in Engineering*, 15:1413–1418, 1980.

[160] E.A. de Souza Neto, D. Perić, M. Dutko, and D. R. Owen. Design of simple low order finite elements for large strains analysis of nearly incompressible solids. *International Journal of Solids and Structures*, 33:3277–3296, 1996.

[161] E.A. de Souza Neto, F.M. Andrade Pires, and D. R. Owen. F-bar-based linear triangles and tetrahedra for finite strain analysis of nearly imcompressible solids. Part I: formulation and benchmarking. *International Journal for Numerical Methods in Engineering*, 62:353–383, 2005.

[162] S. M. Giusti, A. A. Novotny, E. A. de Souza Neto, and R. A. Feijóo. Sensitivity of the macroscopic thermal conductivity tensor to topological microstructural changes. *Comput. Methods Appl. Mech. Engrg.*, 198:727–739, 2009.

[163] P.O. Bouchard, F. Bay, Y. Chastel, and I. Tovena. Crack propagation modelling using an advanced remeshing technique. *Computer Methods in Applied Mechanics and Engineering*, 189 (3):723–742, 2000.

[164] T. Belytschko and T Black. Elastic crack growth in finite elements with minimal remeshing. *International Journal for Numerical Methods in Engineering*, 45:601–620, 1999.

[165] G.N. Wells and L.J. Sluys. A new method for modelling cohesive cracks using finite elements. *International Journal for Numerical Methods in Engineering*, 50 (12):2667–2682, 2001.

[166] Jerrold E. Marsden and Thomas J.R. Hughes. *Mathematical Foundations of Elasticity*. Dover Publications, 1983.

[167] Mikkail Itskov. *Tensor Algebra and Tensor Analysis for Engineers*. Springer, second edition, 2009.